Title
Search for the low lying transition in the 229Th Nucleus

Author
Jeet, Justin

Publication Date
2018

Peer reviewed|Thesis/dissertation

UNIVERSITY OF CALIFORNIA
Los Angeles

Search for the low lying transition in the ^{229}Th Nucleus

A dissertation submitted in partial satisfaction
of the requirements for the degree
Doctor of Philosophy in Physics

by

Justin Jeet

2018

ABSTRACT OF THE DISSERTATION

Search for the low lying transition in the ^{229}Th Nucleus

by

Justin Jeet
Doctor of Philosophy in Physics
University of California, Los Angeles, 2018
Professor Eric R Hudson, Chair

This dissertation presents a search for the low lying transition in the ^{229}Th nucleus. This nucleus is expected to have an exceptionally low energy and long-lived isomeric level just above the ground state which could be amenable to laser spectroscopy. We utilize ^{229}Th doped $LiSrAlF_6$ crystals to achieve high densities adequate for broadband synchrotron excitation. The charge state of the doped thorium atoms (4^+) ensures a radiative decay upon de-excitation of the nucleus, necessary for fluorescence detection. Additionally; we built a pulsed VUV laser system, utilizing four wave difference frequency mixing in Xe, to continue interrogation of the ^{229}Th:$LiSrAlF_6$ crystals with improved sensitivities to longer lifetimes for the decay from the isomeric level. And finally, we utilize a ^{233}U source along with superconducting single photon nanowire detectors (SNSPD's) in attempt to measure the internal conversion (IC) decay channel available to neutral ^{229}Th. If successful, the experiment can provide the lifetime of the IC decay and can potentially provide energy bounds on the isomeric level.

The dissertation of Justin Jeet is approved.

Chee Wei Wong

Paul Hamilton

Eric R Hudson, Committee Chair

University of California, Los Angeles

2018

Table of Contents

List of Figures

List of Tables

Acknowledgments

I would like to thank everyone..... But in particular, I would like to thank Eric Hudson for the wonderful opportunity to be a part of his research group here at UCLA; Christian Schneider for all the things he has taught me, Scott Sullivan for welcoming me into the lab when I first joined the group; and many others including Wade Rellergert, Steven Schowalter, Prateek Puri, Kuang Chen, Alex Dunning, and Mike Mills. Outside of the Hudson group, I would like to thank everyone that comprises the UCLA AMO team including Wes Campbell and Paul Hamilton and the members of their respective groups. Outside of AMO, I would like to thank: Bob Cousins for expert advice in data analysis; Craig Reaves for all the help over the years in setting up equipment in the labs; Aldrich Rivera for help with radiation safety issues; and Patrice Tonnis.

A huge thanks to everyone outside of UCLA involved in the ^{229}Th project. This includes: Eugene Tkalya for the collaborations and expert knowledge in nuclear structure; Saed Mirzadeh (ORNL) for making the ^{229}Th available for our experiments; Hans Jenssen and Arlete Cassanho (AC Materials) for growing such beautiful ^{229}Th:LiSrAlF$_6$ crystals for our experiments; Yih-Chung Chang and Cheuk Ng (UCD) for introducing us to pulsed VUV laser systems; Sae Woo Nam, Varun Verma, and Galen O'Neil (NIST) for introducing us to SNSPD's; Bruce Rude (ALS) for all the help in setting up our experiments; Adam Larson and Brant Jones (Spectra-Physics) for helping us keep our Nd:YAG laser in operation; Nan Yu, Thanh Le, and Guoping Lin (JPL) for introducing us to WGMR's; and many, many others.

I would also like to thank my family and friends for everything!!!!

Vita

2008-2009	Undergraduate research under Prof.Mike Crommie, Condensed Matter Physics, Nanomachines
2009-2010	Undergraduate research under Prof.John Clarke, Condensed Matter Physics, Microstrip SQUID Amplifiers
2009	B.S. (Engineering/Physics), UC Berkeley.
2011	Intern at Jet Propulsions Laboratory under Nan Yu, Whispering Gallery Mode Resonators
2011-2013	Teaching Assistant, Department of Physics and Astronomy, UCLA
2013-present	Graduate Student Research, UCLA, Atomic, Molecular and Optical Physics with Prof. Eric R. Hudson
2017	Fellowship, Dissertation Year Fellowship (DYF)

Publications

T. Le et al.: Opt. Lett. 37, 4961-4963 (2012).

J. Jeet et al.: Phys. Rev. Lett. 114, 253001 (2015).

E. V. Tkalya et al.: Phys. Rev. C 92, 054324 (2015).

CHAPTER 1

Prelude: Low-threshold ultraviolet solid-state laser based on a Ce3+:LiCaAlF6 crystal resonator

A low-threshold solid-state ultraviolet (UV) laser using a whispering gallery mode (WGM) resonator constructed from UV transparent crystalline material is demonstrated. Using a Ce^{3+}:$LiCaAlF_6$ resonator, we observe broad bandwidth lasing (280-330 nm) with a low threshold intensity of $7.5\times109W/m^2$ and an effective slope efficiency of 25%. The lasing time delay dynamics in the pulsed operation mode are also observed and analyzed. Additionally, a $LiCaAlF_6$ WGM resonator with $Q = 2 \times 10^7$ at 370 nm is realized. The combination of this high Q and the small WGM mode volume significantly lowers the pump power threshold compared to traditional cavity designs, opening the door for both tunable continuous-wave and mode-locked operation.

Mode-locked and tunable continuous-wave (cw) ultraviolet (UV) laser sources are highly desirable for a number of important applications, including molecular spectroscopy, detection of atmospheric constituents, and remote sensing [MSA90, Kim10]. Further, stabilized UV lasers play a key role in current [RHS08] and planned [RDG10] optical clocks. Despite these demands, most current UV laser systems operate either in pulsed mode or are obtained through nonlinear frequency conversion [PDF09, WWT12], as few viable UV gain media are known [CM04], making them inappropriate for the aforementioned applications. Of the known UV gain media, trivalent cerium-doped colquiriites, such as Ce^{3+}:$LiCaAlF_6$, possess several intriguing features, such as a convenient pumping wavelength (266 nm) and a gain bandwidth of 280-330 nm [MSP94, LSC08, ATV06], allowing in principle both tunable cw and mode-locked operation. However, to date, neither cw nor broadband mode-locked lasing has been demonstrated in these systems [GCS09], as the short lifetime of the upper state in

the crystal requires pump power in excess of 1 W to reach the lasing threshold in traditional cavity designs [ATV05]. An alternative approach, which should dramatically reduce the stringent requirement on pump power, is to utilize a resonator based on whispering gallery modes (WGM) in a circular dielectric medium. In a WGM resonator, light is trapped near the surface of the dielectric by repeated total internal reflection, and, as long as a low absorption material is used, a high quality (Q) factor can be realized. This high-Q together, with the small mode volume of a WGM resonator, leads to a significant reduction of the lasing pump power threshold [San96, HCA09, OV09, SZF07].

In this letter, we report the first demonstration of a UV WGM laser. Using crystalline $LiCaAlF_6$ (LiCAF) as the host material, we have fabricated a WGM resonator with a Q in excess of 10^7 at 370 nm. We have also experimentally investigated the properties of a Ce:LiCAF WGM laser with pulsed pumping and observed both low threshold lasing, as well as pulsed lasing time delay dynamics. Both the threshold measurements and delay dynamics were found in good agreement with our theoretical analysis. From these results, we calculate that a cw Ce:LiCAF WGM UV laser with a threshold pump power of 20 mW is possible.

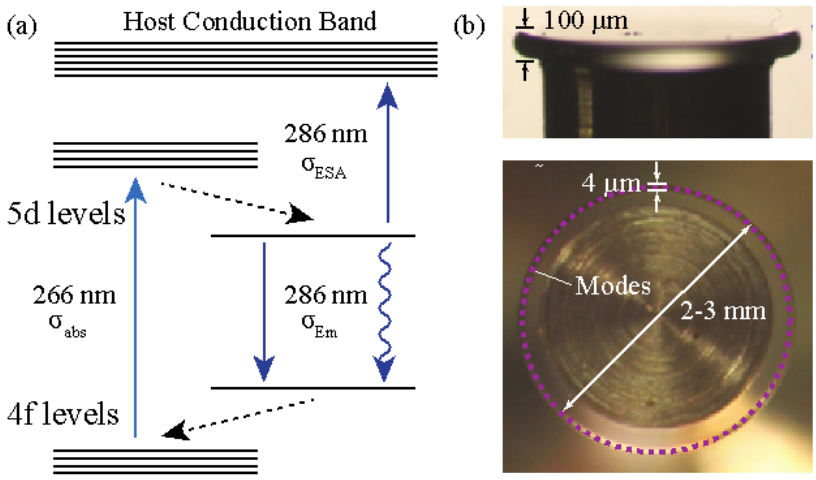

Figure 1.1: (a) Schematic of the energy level structure in Ce:LiCAF crystal and related parameter designation. (b) Side and top view images of WGM resonator.

The WGM resonators used in this work were fabricated from bulk LiCAF and Ce:LiCAF crystalline materials with techniques similar to those described in Ref. [MSS07]. The bulk

crystals (AC Materials) were cut into thin disks, preformed, and polished to optical smoothness. The finished resonator disks had diameters of 2 - 3 mm and thicknesses of $\sim$ 100 um. The Q factors of these resonators were measured with a 370 nm laser, evanescently coupled to the resonator via a prism, and found to be as high as Q = 2.6×10^7 and Q = 2×10^6 for LiCAF and Ce:LiCAF resonators, respectively.

The pump laser threshold intensity for a four-level lasing system like the Ce^{3+} color center (shown in Fig. 1.1) is given as: $I_{th} = 2\pi hc/(\tau_f Q \sigma_e \sigma_{abs} N_o \lambda_s \lambda_P)$, where σ_{abs} is the pump laser absorption cross-section; $\lambda_s(\lambda_p)$ is the laser (pump) wavelength; N_o is the Ce^{3+} number density; τ_f is the lifetime associated with the lasing transition; and $\sigma_e = \sigma_{Em} - \sigma_{ESA}$, where $\sigma_{Em} = 9.6 \times 10^{-22}\ m^2$ is the laser transition absorption cross-section and $\sigma_{ESA} = 3.6 \times 10^{-22}$ m^2 is the absorption cross-section from the excited 5d level into the host conduction band. Given the demonstrated UV Q and a typical Ce^{3+} concentration of 1 mol%, the theoretical lasing threshold occurs for a pump intensity of $1.3 \times 109\ W/m^2$, two orders of magnitude lower than that reported in [LSC08].

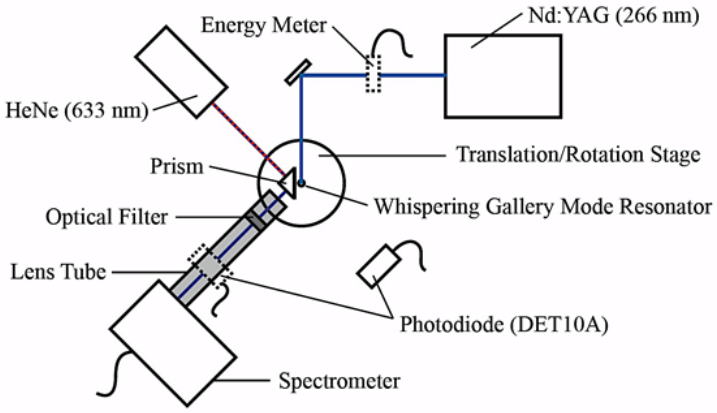

Figure 1.2: Schematic of the UV laser experimental setup. The 266 nm pump laser beam is projected from the top of the resonator disk.

To experimentally verify this lasing threshold, we used a quadrupled, pulsed Nd:YAG laser (266 nm, 2 mJ at 2 Hz, 6 ns pulse) to pump the Ce:LiCAF WGM resonators, as shown in Fig. 1.2. The pump light was focused on the top surface of the resonator disk with

a Gaussian spot size maximally overlapped with the WGM. The WGM lasing signal was observed by evanescent wave coupling to a prism and measured with a photodiode and a spectrometer situated behind a set of optical filters to block the 266 nm pump light. Figure 3 shows the measured out-coupled laser power as a function of pump laser energy. Also shown in Fig. 3 is the result of a simple 4-level laser rate equation model using a Ce3+ number density of $N_o = 5.5 \times 10^2 3\ m^{-3}$ and probability of spontaneous emission into the laser mode of $\beta \sim 0.01$.

The lasing threshold observed in Fig. 3 corresponded to an applied total pump energy of 800 uJ. Due to mismatch between the pump laser spatial mode and the WGM lasing modes, only a small fraction of this pump energy was actually absorbed in the gain medium. Calculating this fraction and the actual pump intensity in the WGM volume requires knowledge of the WGM laser profile inside the crystal resonator, where the lasing modes reside. In the present experiment we cannot differentiate the various lasing modes, however, typically only equatorial WGMs contribute to the observed lasing signal as they exhibit the highest Q and are more strongly out-coupled via the prism. With this approximation, we find that the fraction of the pump pulse energy that is incident upon the volume containing the lasing modes is 0.002, leading to an actual pump energy threshold of 1.6 uJ as shown in Fig. 1.3. This corresponds to a laser threshold pump intensity of $7.5 \times 109\ W/m^2$. This is consistent with the theoretical estimate when we consider that the definition for the threshold intensity is the intensity at which the resonant photon number becomes undamped, whereas the measured threshold intensity is taken to be the intensity at which the photon number becomes experimentally measureable and increases linearly with pump power.

Taking into account geometric factors and losses, the overall slope efficiency is found to be 1.1% in this top-pumped configuration. However, due to an absorption coefficient of $\alpha = 4.1\ cm^{-1}$ only $\sim 4\%$ of the pump energy incident upon the mode volume is absorbed in the 100 $\hat{\text{I}}\frac{1}{4}$m thick active medium, resulting in an effective slope efficiency of $\sim 25\%$.

Figure 1.4 shows the spectrum of the UV WGM laser for several pump energies using a UV spectrometer with ~ 0.1 nm resolution. Consistent with previous observations [LSC08], the laser displayed a dominant emission peak centered at 286 nm with a secondary peak around

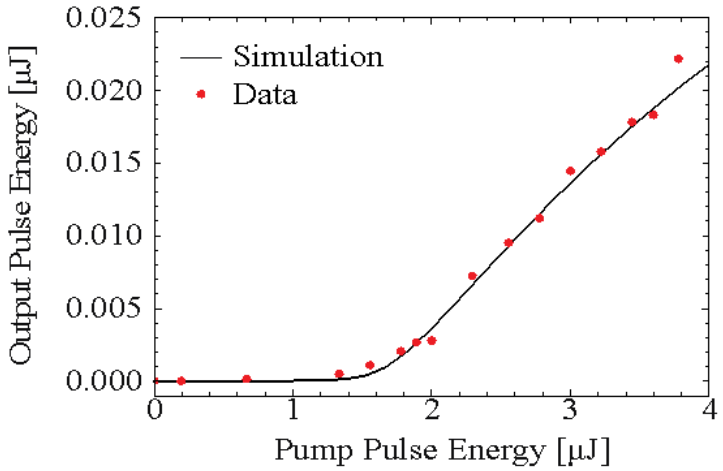

Figure 1.3: Experimental and simulated laser output as a function of the total pump energy, showing the lasing threshold of 1.6 Î¼J.

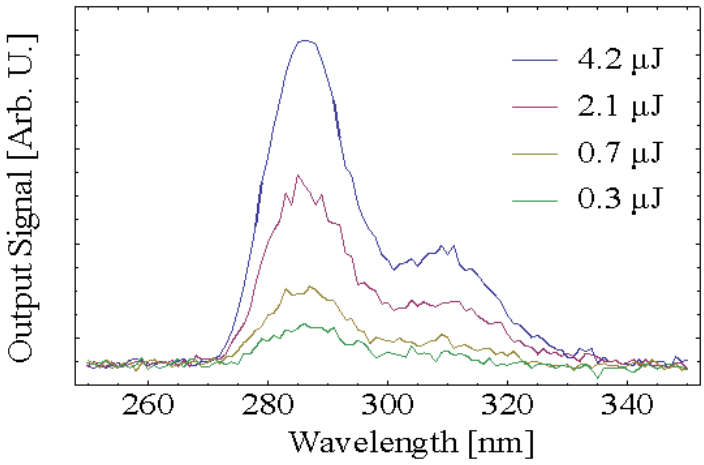

Figure 1.4: UV WGM laser spectrum at several pump energies.

310 nm, showing that both tunable cw and mode-locked operation in the WGM laser are possible in principle. Finally, a control experiment was also performed using an undoped LiCAF host, which confirmed that no spurious emission from the crystal contaminated the measured laser spectrum.

In pulsed mode operation, the competition between the creation of an inversion by the pump pulse and the depletion of the inversion by the lasing pulse leads to rich dynamics in the time domain, which have been explored in [ATV05]. The result of a simple four-level rate equation model of the laser time dynamics is shown in Fig. 1.5a, where it is seen that there is a finite time for the gain medium to build up the population inversion. The build-up time is pump power dependent. Once sufficient inversion is reached, the number of laser photons rapidly increases, resulting in the sudden overtaking of spontaneous emission by stimulated emission and a marked decrease in excited state density. Together these effects lead to a time delay between the pump pulse and the laser pulse that depends on the total pump energy. We have measured this delay dependence on pump energy and it is shown in Fig. 1.5b alongside the result of the simple rate equation model. Considering the idealization of the four-level model, the agreement is reasonable. However, the fact that the experimental data shows a peak time delay at larger energies, as well a slower decrease in delay with energy, compared to simulation indicates that the simulation may be overestimating the real excited state density participating in the observed lasing signal.

In summary, we have demonstrated that WGM resonators with a high-Q in the UV range can be fabricated from $LiCaALF_6$ crystalline material. With a Ce^{3+}:$LiCaAlF_6$ resonator pumped by a 266 nm pulsed laser, we have also shown the operation of a wide-bandwidth laser ($280nm - 330nm$) with a threshold intensity of $7.5 \times 109\ W/m^2$ and an effective slope efficiency of $\sim 25\%$.

Finally, there is significant potential for further reducing the lasing threshold. For example, if a narrow-band 266 nm pump laser is resonantly coupled to a WGM resonator similar in size to those used in our current experiment, the pump mode almost completely overlaps the laser mode volume. This can be accomplished by reducing the dopant concentration so as to have a reasonable resonator Q, e.g. 106, at the pump wavelength. (The decrease in

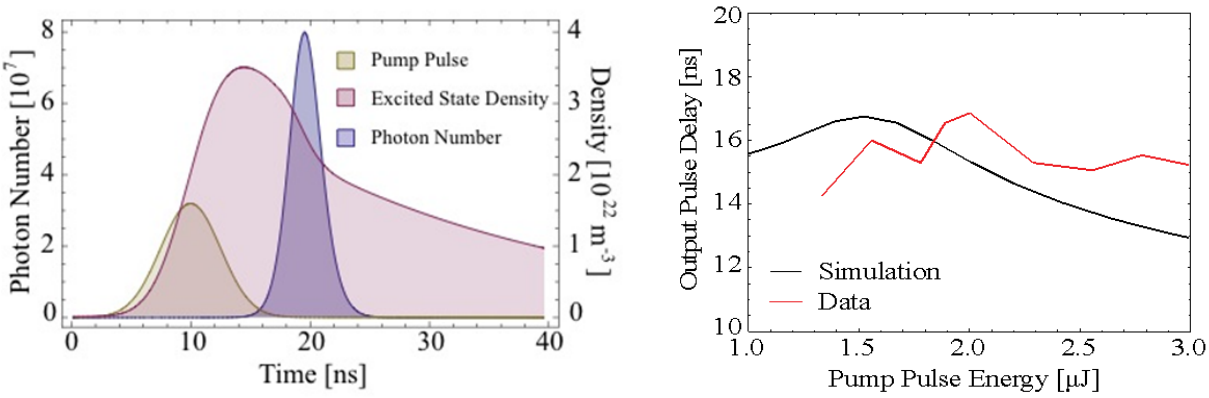

(a) **(b)**

Figure 1.5: (a) The simulated lasing pulse dynamics above threshold at 3.2 uJ pump energy. (b) Experimental and simulated delays as a function of the pump energy.

total pump photon absorption due to the smaller dopant concentration is compensated by the corresponding cavity buildup of the pump intensity inside the resonator.) This improved pump coupling and the fact that we have recently demonstrated LiCAF resonators with Q factors exceeding 107, results in a predicted cw laser pump power threshold of 20 mW. Currently, we are pursuing the development of such a device in an effort to enable both tunable cw and mode-locked operation in the UV spectral range.

Part of this work was performed at the Jet Propulsion Laboratory, California Institute of Technology, under a contract with NASA. The research is supported in part by JPL Strategic University Research Partnerships Program. UCLA also acknowledges support from the DARPA QuASAR program.

CHAPTER 2

Introduction

2.1 The Structure of Things

2.2 Atoms

The structure of atomic electrons around a nucleus is very well understood. Quantum mechanics has proven to be an indispensable tool for describing electronic orbitals around a nucleus. It is well understood that these orbitals consist of mostly open space in contrast to the density of nucleons in nuclei. The small, compact nucleus provides a radially symmetric potential through the Coulomb interaction. In the case of a single electron around a nucleus, the Schrodinger equation which dictates quantum behavior can be solved exactly.

Consider hydrogenic type atoms in which there is one electron and a nucleus with total positive charge Z. The hamiltonian may be written down as:

$$H = -\frac{\hbar^2}{2\mathrm{m}}\nabla^2_{cm} - \frac{\hbar^2}{2\mu}\nabla^2 - \frac{Ze^2}{4\pi\epsilon_o \mathrm{r}}, \tag{2.1}$$

with $\mathrm{m} = \mathrm{m}_e + \mathrm{m}_A$ being the total mass of the electron and nucleus system with ∇^2_{cm} acting on the corresponding center of mass coordinate, which we can ignore for now. μ is the reduced mass of the system with ∇^2 acting on the relative coordinate with this mass. Considering a separable solution of the form:

$$\psi(r,\theta,\phi) = R(r)Y(\theta,\phi), \tag{2.2}$$

and utilizing some familiar tricks, an effective potential results which applies for the radial solution with the form:

$$V_{eff} = -\frac{Ze^2}{4\pi\epsilon_o \mathrm{r}} + \frac{\ell(\ell+1)\hbar^2}{2\mu \mathrm{r}^2}. \tag{2.3}$$

We recognize the original attractive Coulomb potential but there is also the centrifugal term which is repulsive and is simply due to the motion of the electron around the nucleus. The solutions to these sets of differential equations are well-known. The angular part of the solution reduces to the spherical harmonics and the radial part to Laguerre polynomials with the individual orbitals of the overall wavefunction described by the familiar quantum numbers n,l, and m. As electrons are fermions with spin $\frac{1}{2}$, the actual wavefunctions describing the electrons will need an extra multiplicative term accounting for this intrinsic spin. We briefly introduce term symbols to describe the state of an electron which has the form:

$$^{2S+1}\{L\}_J, \tag{2.4}$$

where S is the spin angular momentum, and L is the orbital angular momentum which takes on letters of $(S, P, D, F, ...)$ corresponding to values of $(0, 1, 2, 3, ...)$. But these orbitals and their corresponding energies are not entirely accurate. There is of course the fine structure that must be accounted for arising from spin-orbit angular momentum coupling, and there is also the hyperfine structure due to interactions with the nuclear magnetic moment. While the labelling of the levels remains in accord with the defined spectroscopic notation, the corresponding energies may differ due to the additional interactions. And for the case of strong spin-orbit coupling versus weak, the total angular momentum (J) is determined differently. Relativistic effects can be considered in these systems and Quantum Electro-Dynamics (in which charged particles are allowed to interact with the quantized electromagnetic fields) can be applied to obtain the most precise solutions. For these reasons, hydrogenic systems are ideal for experiments involving precision measurements to determine certain fundamental quantities relevant in theory.

In this sense, the single-electron system is solved, but what happens as more electrons are added to the system? With the use of the Pauli Exclusion principle and given the orbitals described by the quantum numbers n, l, and m; the orbitals of lowest energies can be filled out with the available electrons. The solutions cannot be solved exactly with the additional electron-electron interactions taken into account however. There are techniques that can be utilized to obtain approximate solutions. One of them being the orbital approximation which

can be applied to systems such as He in which the electrons are assumed to be non-interacting such that the total wavefunction is a product of the individual electron wavefunctions and the electron-electron interaction is treated as a small distortion to the system. In general, there are several methods available to approximate solutions to these more complex systems: Variational Principle, Semi-Classical Approximations, Perturbation Theory, Numerical Solutions, Self Consistent Field Procedures, and Density Functional Procedures. These methods have been very successful in describing multi-electron systems.

As a final thought on atomic structure, we consider the patterns noticed in the first ionization energies across the periodic table. Atoms with a filled shell have larger first ionization energies as compared to neighboring atoms. This is a consequence of the shell structure that exists in atoms and is accurately described by the Schrodinger equation and a Coulomb central potential (and of course modified by a host of other interactions). And so atoms with filled shells are typically more stable and less reactive than other atoms, as we know from the behavior of the noble gases.

2.3 Nuclei

Just as atoms with filled shells are more stable relative to their neighbors, a similar behavior is noticed in nuclei. There exist nuclei with magic numbers of either neutrons and/or protons (nucleons) which tend to be more stable than neighboring nuclei. The binding energy of the last nucleon, or the energy to remove the last nucleon to infinity, in these nuclei tend to be large compared to neighboring nuclei. There are some other facts that are worth mentioning about the nucleus and the nuclear force:

- Nuclei tend to be small, on the order of 1-10 fm in diameter.
- The density of nuclei is relatively constant and independent of the number of nucleons contained, as shown by electron scattering experiments.
- The strong nuclear force is a residual force resulting from the interaction of quarks. It is this residual force that is responsible for holding together nucleons in nuclei. It is a

charge independent force.

- The strong nuclear force is a short range attractive force and is relatively weak when considering the scale of separation of nucleons in nuclei.
- When considering the motion of electrons in atoms and molecules, the nuclear force can be neglected.
- Experiments suggest that nucleons can move independently inside a nucleus.

Independent nucleon motion can be justified by considering several different effects. As just mentioned, the nuclear force holding together nucleons is relatively weak, especially when compared to the kinetic energies of these nucleons. In addition to the attractive strong force between nucleons, there is also the repulsive Coulomb force between protons which can help support an independent nucleon motion theory. If we assume that quantized levels in the nuclei exist and we demand that the nucleons, as fermions, must obey the Pauli Exclusion principle, then this further promotes independent nucleon motion. No two nucleons with the same quantum numbers can share the same orbital, which forces them further apart in space.

2.3.1 Shell Model

To motivate an independent particle model, a Hamiltonian for the nucleus can be expressed:

$$H = T + V = \sum_{i=1}^{A} \frac{\vec{p}_i^{\,2}}{2m} + \sum_{i>k}^{A} V_{ik}(\vec{r}_i - \vec{r}_k). \tag{2.5}$$

Along with the kinetic energy term (T), there is also a potential energy term (V) which includes the interactions between all nucleons. For simplicity, the Coulomb potential is not included here as it is a longer range force and plays a more important role in heavier nuclei. It can be advantageous to represent the nucleon-nucleon interactions term as an effective potential that describes individual non-interacting nucleons. This requirement can

be approximately enforced:

$$H = \sum_{i=1}^{A} \{ \frac{\vec{p}_i^2}{2m} + U_i(\vec{r}) \} + \sum_{i>k}^{A} V_{ik}(\vec{r}_i - \vec{r}_k) - \sum_{i=1}^{A} U_i(\vec{r})$$
$$H = H_o + H_{residual}$$
$$\text{with}$$
$$H_{residual} = \sum_{i>k}^{A} V_{ik}(\vec{r}_i - \vec{r}_k) - \sum_{i=1}^{A} U_i(\vec{r}). \tag{2.6}$$

H_o containing the effective potential can be solved given that the quantity $H_{residual}$ is minimal. The effective potential should in general represent a convolution of the independent nucleon-nucleon interactions over the nuclear density:

$$U_i(\vec{r}) = \int V_{ik}(\vec{r}_i - \vec{r}_k)\rho(\vec{r})\mathrm{d}\vec{r} = \sum_k \int \psi_k^*(\vec{r}) V_{ik}(\vec{r}_i - \vec{r}_k)\psi_k(\vec{r})\mathrm{d}\vec{r} \tag{2.7}$$

But V_{ik} is not typically known. Self consistent field procedures such as the Hartree-Fock technique can be utilized to tackle these problems. For a given V_{ik}, ψ_k is guessed and used to calculate $U(\vec{r})$, which is then used to recalculate ψ_k in an iterative process.

With an effective mean field potential established or guessed, ideally a central one, the Schrodinger equation can be solved for the case of a single nucleon in this effective potential. A central potential allows for solutions to the Schrodinger equation which are separable. A harmonic oscillator potential has often been used historically. As in the case of the hydrogenic system, an effective centrifugal potential arises. The resulting differential equation for the radial part of the equation can be solved. A Hamiltonian of this form does not exactly reproduce the magic numbers ([2,8,20,28,50,82,126,...]) and other interaction terms are necessary. Consider a larger nuclei with radius (R_A) larger than the range of the nuclear force, indicated by R_N. Due to an approximately constant nuclear density, it can be assumed that a nucleon at some radii $R_N < r < R_A$ is surrounded uniformly by nucleons in either direction and should be screened by any non-uniformity that may exist near the nuclear surface. The addition of an ℓ^2 term to the Hamiltonian promotes a flatter central potential near the center of the nuclear radius by producing a stronger attractive force on nucleons with larger ℓ, effectively lowering their energies. Another term added to the Hamiltonian involves

a spin-orbit coupling term. This force will affect nucleons with larger angular momentum more significantly and also has some preference between the relative alignment of the spin and angular momentum. A nucleon near the center of the radius should not experience a net force, and so this coupling term should be more of a nuclear surface phenomenon. The total Hamiltonian of the system can now be expressed as:

$$H_{\text{shell}} = T + V_{\text{cen}} + V_{\ell^2}\ell^2 - V_{\ell\text{s}}\frac{\partial V}{\partial r}\vec{\ell}\cdot\vec{s}, \tag{2.8}$$

with T being the kinetic energy of the single nucleon, and V_{cen} is the effective central potential due to all other nucleons. This form of the Hamiltonian does in fact reproduce the magic numbers. And it is important to note that the additional terms are not simply added to make the solutions agree with experiment, but do arise from more fundamental principles beyond the scope of the thesis.

The solutions for the single particle levels with the described Hamiltonian can be represented by:

$$H_{\text{shell}}\phi_j(\vec{r}) = E_j\phi_j(\vec{r}). \tag{2.9}$$

The ϕ_j's are the spherical shell model wavefunctions for a nucleon occupying the orbit denoted by j, which represents some arbitrary set of quantum numbers. Nucleons can be filled up according to the lowest energy orbitals to form different nuclei. The Coulomb force and Pauli Exclusion principle work against the nuclear force to allow independent nucleon motion. Collisions can occur between nucleons in different orbitals, but only in the case that these collisions are energetic enough to put a nucleon in an unoccupied orbital will such collisions have any effect, which can typically occur only for nucleons near the nuclear surface. The spherical shell model for nuclei works great for a single nucleon outside of a filled shell, where the effect of an inner filled shell only contributes to the overall radial potential felt by the valence nucleon [CC00].

2.3.2 Collective Motions and the Nilsson Model

For nuclei with an increasing number of nucleons outside of a closed shell, the shell model description becomes inadequate. Configuration mixing of the spherical shell orbitals occur

as valence nucleons can scatter to different orbitals through the residual interaction. As the number of nucleons is increased, different types of macroscopic collective motions of the nucleus become possible from spherical harmonic vibrations near a closed shell to axially asymmetric and symmetric rotors near midshell.

For nuclei near closed shells whose ground states are spherical, vibrational excitations are common. The residual interaction can be expressed in terms of a multipole expansion. The different terms in the expansion can correspond to the different excitation modes available for multi-nucleon configurations. A magnetic dipole (M1) excitation typically exists for heavier nuclei which corresponds to the oscillations of the proton and neutron distributions with respect to one another and can display a scissors type motion. The electric quadrupole (E2) component is a common vibrational mode which describes oscillations in the shape of the nucleus, in this case taking on time-varying quadrupole distortions [CC00]. These and other terms in the expansion of the residual interaction can represent both low and higher energy excitation modes.

As nucleon numbers are further increased past closed shells, the strength of the residual interaction becomes sufficient to alter the underlying structure of the nucleus. The ground-state levels are no longer spherically symmetric. These nuclei have permanent deformations with the lowest order component consisting of a quadrupole distortion. Most nuclei far from a closed shell, with a static quadrupole deformation, are typically axially symmetric in their ground state. Prolate and oblate shapes of the nucleus are possible which permit rotations, about an axis perpendicular to the symmetry axis, in addition to the vibrational motion [CC00].

The Nilsson model is a natural extension of the single nucleon shell model description and provides the microscopic basis to the macroscopic collective motions of the nucleus. It is a single particle model and provides the description for the motion of a single nucleon in a potential due to a deformed nuclear core with collective rotational motion. As in the case for molecules in which the Born-Oppenheimer approximation can be applied to separate the motions of nuclei and electrons, the motions of a rotating core (about an axis perpendicular to the deformation symmetry axis) and that of an orbiting nucleon can also be separated.

This is possible when the frequency of rotation of the nuclear core is much less than that of the orbiting nucleon. With higher rotational frequencies of the core, separations of the core and single nucleon motions can become poor approximations and effects including Coriolis mixing should be taken into account.

Most permanently deformed nuclei are prolate with the exception of those near major closed shells, which are typically oblate [CC00]. Consider a prolate deformed nuclei with a deformation symmetry axis along the z-axis, see Fig. 2.1. The appropriate Hamiltonian can be expressed as:

$$\begin{aligned} H_{\text{Nils}} &= T + V_{\text{def}} + V_{\ell^2}\ell^2 - V_{\ell\text{s}}\frac{\partial V}{\partial r}\vec{\ell}\cdot\vec{s} \\ &= \frac{\vec{p}^2}{2m} + \frac{1}{2m}\left[\omega_o^2(x^2+y^2) + \omega_z^2 z^2\right] + V_{\ell^2}\ell^2 - V_{\ell\text{s}}\frac{\partial V}{\partial r}\vec{\ell}\cdot\vec{s}. \end{aligned} \tag{2.10}$$

T is the kinetic energy and V_{def} is the deformed potential due to the deformed nuclear core. The $V_{\ell^2}\ell^2$ term promotes a flatter potential in the nuclear core and the $V_{\ell\text{s}}\frac{\partial V}{\partial r}\vec{\ell}\cdot\vec{s}$ term accounts for spin orbit coupling. A deformed harmonic oscillator potential is used for V_{def} but a Wood-Saxon potential is also appropriate. The Nilsson Hamiltonian is often written in terms of a deformation parameter (β) which is related ω_o and ω_z. In the limit where the deformation parameter approaches zero, the Hamiltonian becomes that of the shell model described by the spherical shell orbitals. As β increases, configuration mixing of the spherical shell orbitals occur.

A spherical potential yields orbitals with degenerate magnetic substates. A preference for a non-uniform magnetic substate distribution is characteristic of deformed nuclei. The appropriate quantum numbers are given by the projections along the deformation symmetry axis. The Nilsson single particle levels in this case are given by:

$$\psi_i = K^\pi[Nn_Z\Lambda]. \tag{2.11}$$

K is the total angular momentum projection on the deformation axis (z). π is the parity of the level. N is the principle quantum number and n_Z is the number of nodes in the wavefunction along deformation axis. Λ is the orbital angular momentum projection along the symmetry axis. The Nilsson orbitals can be expanded in the spherical shell basis:

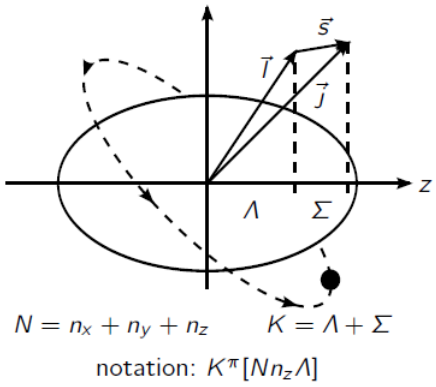

Figure 2.1: Nilsson model schematic. The intrinsic Nilsson levels are denoted by $K^{\pi}[Nn_Z\Lambda]$ where K is the total angular momentum projection on the deformation axis (z). π is the parity of the level. N is the principle quantum number and n_Z is the number of nodes along deformation axis. Λ is the orbital angular momentum projection along the symmetry axis.

$$\psi_i = \sum_j C_j^i \phi_j. \tag{2.12}$$

The C_j^i's are the configuration mixing coefficients and the ϕ_j's are the spherical shell orbitals.

It is important to point out that the Nilsson levels are the intrinsic levels describing a single nucleon in a potential due to a fixed nuclear core. The intrinsic motion must be superimposed onto the rotational motion of the core for a true description of the actual nuclear state. The effects of the rotational motion of the nuclear core introduces additional rotational levels for a given intrinsic Nilsson state, creating a rotational band. Such rotational bands are shown in Figure. 2.2 for the lowest energy Nilsson states in the ^{229}Th nucleus.

2.4 A low lying Transition in the ^{229}Th Nucleus

The ^{229}Th nucleus can be considered as a single nucleon outside of the ^{228}Th nucleus, which has all paired nucleons. The nuclear core is quadrupole-octopole deformed and can support vibrational and rotational motion. A Coriolis interaction should be taken into account between the even-even core and the single unpaired nucleon. ^{229}Th is expected to have the lowest-energy nuclear isomeric transition between the Nilsson levels $\frac{3}{2}^+\frac{3}{2}[631] \leftrightarrow \frac{5}{2}^+\frac{5}{2}[633]$.

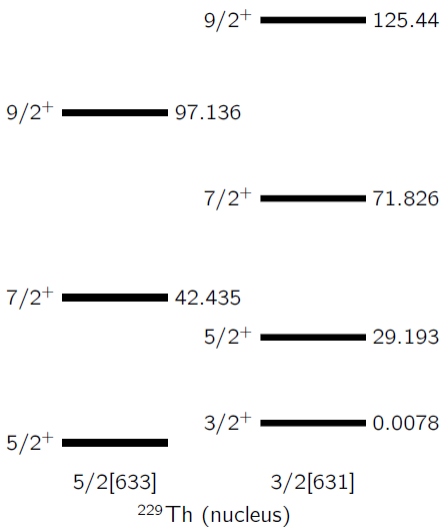

Figure 2.2: The lowest energy intrinsic Nilsson states are shown for ^{229}Th. The rotational motion of the nuclear core leads to additional rotational bands on top of the Nilsson states.

The transition energy between these levels can be thought of as a sum of two terms: a change in the Coulomb configuration energy and a change in the strong nuclear configuration energy ($\Delta E_{i \leftrightarrow f} = \Delta E_{\text{Coulomb}} + \Delta E_{\text{Strong Nuclear}}$). While the change in these configuration energies can be individually large, the sum of the two terms happen to nearly cancel resulting in a peculiarly low nuclear transition energy.

Almost four decades ago, the existence of the low-lying isomeric level was first indirectly established [KR76]. Since then, several other spectroscopy measurements have been conducted. The currently accepted value of the transition energy is at $7.8 \pm 0.5\,\text{eV}$ [BWB09], which also results from indirect measurements. The ^{229}Th nucleus is currently a subject of intense experimental and theoretical research. Efforts are ongoing to better to resolve the energy and lifetime of the transition. The prospects of a laser-accessible nuclear transition has inspired numerous proposals to utilize this apparently unique nuclear transition to study several interesting physical phenomenon as well as for applications with significant technological impact. Some of these will be mentioned in the following sections.

2.4.1 History of the Transition

The work of Kroger and Reich ([KR76]), which was conducted over 40 years ago, led to the discovery of a low lying isomeric state in ^{229}Th. In this experiment, γ-singles and $\gamma\gamma$ coincident measurements were taken following the α-decay of ^{233}U using a variety of Ge and Si detectors. This lead to the identification of 91 distinct lines belonging to ^{229}Th. Using these lines, a limit for the energy of the isomeric level $\frac{3}{2}^{+}\frac{3}{2}[631]$, which we will label $I^p = 3/2^+$ for brevity, was established at $< 100\,\text{eV}$ above the ground state.

In addition to γ ray spectroscopy, the ^{230}Th(d,t)^{229}Th nuclear reaction has also confirmed the existence of the low lying isomeric level in ^{229}Th [BGQ90]. In this work, deuteron beams were used to carry out the reaction and the products were then analyzed using a split pole magnetic spectograph and photographic plates. This experiment provides strong evidence that the $3/2^+[631]$ bandhead is located very close to the ground state. Although these measurements did not resolve the energy difference between the ground and isomeric levels, they did support its existence and fueled further investigations.

Later in 1993 in the work of Helmer and Reich ([HR94]), a thorough gamma spectroscopy measurement was conducted on ^{229}Th. More γ-rays were studied utilizing detectors with better energy resolution, and more reference lines were used for calibration. These measurements put the $I^p = 3/2^+$ level at $3.5 \pm 1.0\,\text{eV}$ above the ground state. These results led to efforts to spectroscopically resolve the expected ultraviolet (UV) emission from the isomeric level, which is expected to be populated with a 2% branching ratio upon α decay of ^{233}U. Despite initial claims of observation [IK97, RBE98], these searches were unsuccessful [UBB99, SYC99, MAB04].

Over the decades, many notable experiments have been carried out to investigate the structure of the ^{229}Th nucleus ([BMF88, GKA02, RPZ06, BAB03]). A relatively recent work by Beck ([BBB07]) has set the currently most accepted value of the isomeric transition energy. In this work gamma spectroscopy was conducted with a microcalorimeter xray spectrometer (XRS) developed by NASA and installed at the Lawrence Livermore National Labs Electron Beam Ion Trap (EBIT) facility [PBB09]. An isotopically pure sample of ^{233}U

is mounted in the vicinity of the XRS which is cooled to 90 mK for an energy resolution of 26 eV at full width half maximum. These results, along with a follow-up experiment ([BWB09]), result in the currently accepted value of 7.8 ± 0.5 eV for the isomeric energy level.

Attempts have also been made to measure the lifetime of this transition [ZER12]. In this experiment, ^{229}Th recoils from a $^{233}UO_2$ source are collected onto an MgF_2 substrate. As the small fraction of the implanted ^{229}Th expected to be at the isomeric level de-excite to the ground state, fluorescence is detected with the use of photomultiplier tubes. The result of this experiment reports a half life of 6.1 ± 1 h. This work also suggests that the transition energy is actually < 7.75 eV, which is a subject of controversy [PZ13].

In very recent experiments, the internal conversion (IC) decay from the isomeric level was directly measured along with its lifetime [WSL16, SWT17]. In internal conversion, γ-ray emission upon de-excitation of a nucleus is suppressed and the energy is instead carried away with the ejection of a core electron. These experiments confirm theoretical predictions regarding the IC decay channel in ^{229}Th [ST91, KT07].

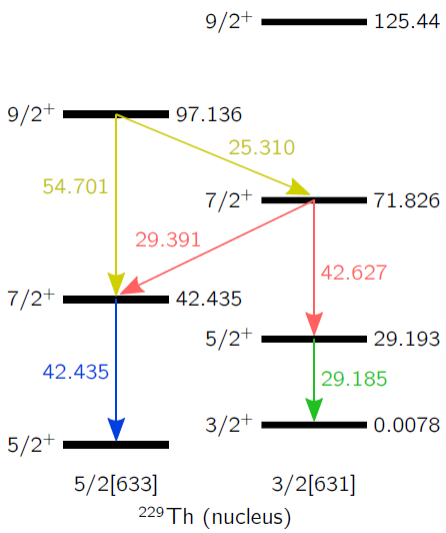

Figure 2.3: The energy of ceratin transitions in ^{229}Th provided by experimental measurements are shown. The transition energies are in keV.

Despite the tremendous experimental efforts over the decades to better determine the energy and lifetime of the radiative decay from the isomeric level, there is more research to be done.

2.4.2 Nuclear Isomeric Decay Processes

The isomeric level in ^{229}Th ($I^p = 3/2^+$) has different decay modes available to it which are dependent upon its charge state and chemical environment. For a radiative decay involving emission of a γ in relaxation to the ground level, a charge state of greater than three is necessary ($^{229}Th^{4+}$ or higher ionization states). The radiative decay is expected to have a long lifetime on the order of $10^3 - 10^4$ sec [DT98, RPZ06, TSJ15, MP17]. This can make experiments looking for long-lived fluorescence from the decay difficult. We have been conducting experiments that aim to detect the radiative decay after direct excitation, however, we utilize a large bandgap crystal doped with ^{229}Th (as $^{229}Th^{4+}$) to achieve large densities facilitating fluorescence detection.

The internal conversion decay channel is available to neutral ^{229}Th. This process was mentioned previously and will be described in more detail in a later chapter. But in brief, the excited nuclear level couples to that of an inner shell atomic electron promoting its ejection upon relaxation from the excited nuclear level. The internal conversion lifetime is $\sim$ 10 usec [TSJ15, SWT17]. We are conducting experiments utilizing superconductiong nanowire single photon detectors (SNSPD's) and a ^{233}U source which are sensitive to the IC decay from the isomeric level in ^{229}Th.

Additionally, decay from the nuclear isomeric level is possible via the electronic bridge mechanism (EB). This decay mode is expected for charge states of ^{229}Th up to the third ionization state ($^{229}Th^{(1-3)+}$) [ST91, PF10a]. In the EB decay process, relaxation from the nuclear isomeric level is coupled to an electronic excitation. Subsequent relaxation from the excited electronic level than leads to the emission of a γ. See Fig. 2.4c. There have been proposals to utilize the reverse process to search for the isomeric energy level [PF10b,BPP18]. An advantage of such a method stems from the availability of optical laser sources which

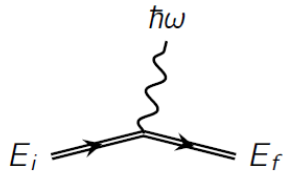

(a) Radiative Decay.

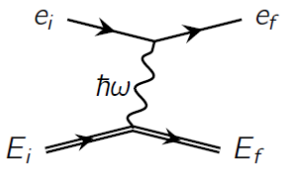

(b) Internal Conversion.

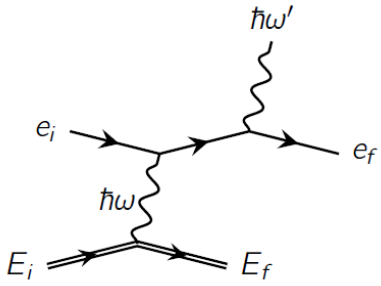

(c) Electronic Bridge Decay.

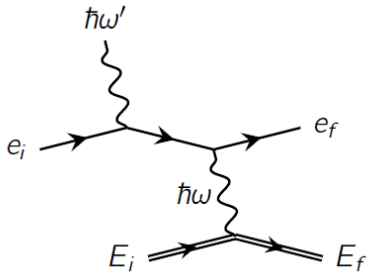

(d) Electronic Bridge Excitation.

Figure 2.4: Decay and excitation modes available to the isomeric level in ^{229}Th.

can be used to drive multi-photon electronic transitions, eliminating the need for a tuneable VUV light source necessary for direct excitation to the nuclear isomeric level. Experiments using trapped $^{229}Th^{+}$ [HOZ12,OMP15] or $^{229}Th^{3+}$ [CSC09,Bel14,CRK11,RCK12] ions aim at exploiting the EB excitation process. Experiments have advanced rapidly in recent years and it is expected that with recent high-resolution electronic spectra [OMP15, CRK11, RCK12, HNO13], electronic bridge excitation rates can be better calculated in the near future.

2.4.3 Motivations and Potential Applications

The low lying transition in the ^{229}Th nucleus is expected to provide access to a number of interesting physical effects, including the decay of the nuclear isomeric level via the electronic bridge in certain chemical environments [ST91], cooperative spontaneous emission [Dic54] in a system of excited nuclei, the Mossbauer effect in the optical range [Tka11], sensitive tests of the variation of the fine structure constant α and the strong interaction parameter [Fla06], a check of the exponentiality of the decay law of an isolated metastable state at long times

[DT98], and accelerated decay of the ^{229}Th nuclei via the low energy isomeric state [DET96]. In addition, two applications that may have a significant technological impact were proposed: a new metrological standard for time [TVL96] or the "nuclear clock" [PT03,RDG10,CRK12], and a nuclear laser (or gamma ray laser) in the optical range [Tka11].

2.5 Our Goal

It is desirable to perform a measurement of the energy of the nuclear isomeric level in ^{229}Th, which involves direct excitation by an external source of electromagnetic radiation and monitoring of the resulting fluorescence, to conclusively measure the energy of the nuclear transition. However, given that the nuclear transition is expected to have a narrow linewidth and is only constrained to within a 40 nm band in the VUV region of the electromagnetic spectrum, such a direct search is daunting.

We utilize VUV transparent crystals doped with ^{229}Th to provide a high density sample suitable for a search using a broadband synchrotron light source, which can easily tune over the requisite 40 nm portion of the VUV spectrum. In addition to utilizing a synchrotron source for the direct excitation of ^{229}Th, we also built a pulsed VUV laser system for continued interrogation of the ^{229}Th doped crystals. The pulsed VUV laser system provides orders of magnitude improvement in spectral irradiance compared to synchrotron sources and improves our sensitivity to longer transition lifetimes. In tandem, we are conducting experiments utilizing SNSPD's (superconducting nanowire single photon detectors) along with a ^{233}U source. These experiments are sensitive to the internal conversion decay channel and can potentially provide energy bounds on the low-lying isomeric level.

...

CHAPTER 3

A Solid State Approach

A novel route to directly measure the isomeric transition energy to higher precision by interrogating ^{229}Th doped into a VUV transparent crystal was proposed. The chief advantage of this technique is that it allows the use of samples containing densities as high as 10^{18} ^{229}Th nuclei/cm^3. By comparison, ion trapping based techniques are limited to densities roughly 10 orders of magnitude smaller [PT03, CRK12]! The ability to address such large numbers of absorbers leads to fluorescence rates sufficient for the use of a synchrotron light source, which are typically broadband and tunable, to directly observe the transition. Given that the transition energy is only known with ~ 40 nm accuracy and is in the VUV region, this is a dramatic experimental simplification.

3.1 Mossbauer Spectroscopy

In fluorescence spectroscopy involving electronic transitions, the narrow band of energies being absorbed by a species typically matches the distribution of energies being emitted. Free atoms and molecules, such as in a gas, will undergo a recoil upon the absorption or emission of a γ ray, due to conservation of momentum. Transitions between different electronic levels in atomic and molecular species are typically low in energy (eV range) however. As γ's with larger energies have more momentum, the process of relaxation of a nucleus ($> keV$ typically) can result in a significant recoil of the atom/molecule [Her65].

Consider a nucleus at rest which de-excites from an excited energy level to the ground state and in the process emits a γ. In the following equations E_R is the recoil energy of a nucleus of mass M with an imparted velocity v after the recoil. The momentum of the

nucleus is given by p. As the nucleus was initially at rest, its momentum is equal to that of the emitted γ-ray, whose energy is given by E_γ. With these expressions, the recoil energy of the nucleus can be expressed as a function of its mass and the emitted γ energy.

$$\begin{aligned} E_R &= \frac{1}{2}\mathrm{Mv}^2 = \frac{\mathrm{p}^2}{2\mathrm{M}} \\ E_\gamma &= \mathrm{pc} \\ E_R &= \frac{(\mathrm{E}_\gamma)^2}{2\mathrm{Mc}^2}. \end{aligned} \tag{3.1}$$

Now consider two free nuclei of the same species at rest. One of them is at the exited energy level (the source) and the other is in the ground state (the absorber). When the source nucleus de-excites, the emitted γ will have an energy that is $\mathrm{E_R}$ less than the natural transition energy and will be $2\mathrm{E_R}$ off resonant from the absorber due to the recoil it will experience upon absorption. In the case where there are separate collections of nuclei making up the source and absorber, such as gaseous species for example, the nuclei in each collection can have a distribution of velocities arising from thermal motion. And this will lead to a Doppler broadened emission and absorption spectrum. Fig. 3.1 depicts an example of absorption and emission spectra for some arbitrary gaseous nuclear species. The width of each distribution is given by $\mathrm{E_D}$ (the Doppler broadened width) and the peaks are separated by $2\mathrm{E_R}$. The overlapping region represents the distribution of γ energies that can be emitted by the source and absorbed by the absorber. In actuality this region only accounts for a very small fraction of the total γ's emitted and explains why past measurements involving free nuclei have either been inconclusive or witnessed very small resonance absorption features [Her65].

A better overlap between the source and absorber spectra can be achieved. Either the emitter or the absorber can be mechanically moved as to attain some velocity which can shift one of the spectra relative to the other. In the case of a source moving at speed v_d in the direction of propagation of the emitted γ, an amount of energy $\mathrm{E_d}$ is imparted to that γ which is given by:

$$\mathrm{E}_d = \frac{\mathrm{v_d E}_\gamma}{c}. \tag{3.2}$$

This imparted velocity can be used to attain a relative shift of $2\mathrm{E_R}$ between the absorption

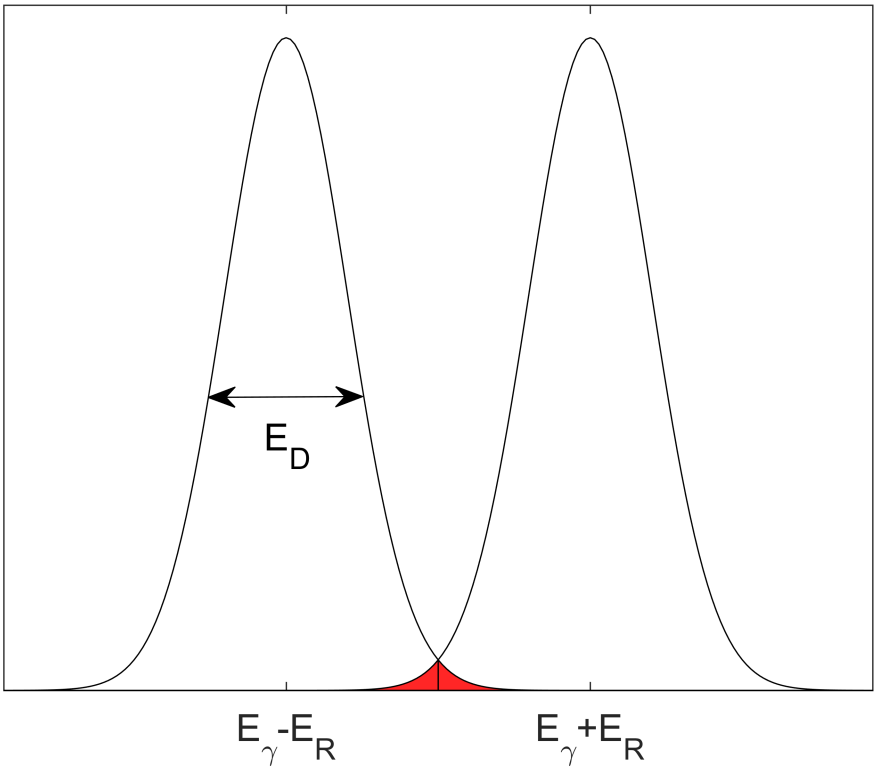

Figure 3.1: Absorption and emission spectra for some arbitrary gaseous nuclear species. The width of each distribution is given by E_D (the Doppler broadened width) and the peaks are separated by $2E_R$. The overlapping region represents the distribution of γ energies that can be emitted by the source and absorbed by the absorber.

and emission spectra for optimal overlap. Another means of achieving a better overlap is by inducing a Doppler broadening by heating the sample. The translational energy of a monoatomic gas can be related to its energy by the equipartition theorem.

$$\frac{1}{2}\mathrm{Mv}^2 = \frac{3}{2}\mathrm{k}_b\mathrm{T}$$
$$\text{with} \tag{3.3}$$
$$\mathrm{v} = \left[\frac{3\mathrm{k}_b\mathrm{T}}{M}\right]^{\frac{1}{2}}.$$

And with the requirement that $\mathrm{E_d}$ be equal to $2\mathrm{E_R}$, this yields a temperature of

$$\mathrm{T} = \frac{4\mathrm{Mc}^2\mathrm{E}_\mathrm{R}^2}{\mathrm{E}_\gamma^2\mathrm{k_b}}, \tag{3.4}$$

which is required such that the root-mean-square velocity will compensate for the recoil losses.

Mossbauer discovered that nuclei in a solid substrate, such as when frozen or doped in a crystal, do not show similar results as the gaseous case. When nuclei are frozen onto a substrate or bound in a solid, the effective mass is equal to that of the whole solid. The Mossbauer line then corresponds to the γ's which are absorbed or emitted elastically with respect to the crystal as a whole, or as Mossbauer put it, the zero phonon mode. In the case of the ^{229}Th nucleus, E_γ is expected to be small for the isomeric transition. And for ^{229}Th doped into a large band gap dielectric, the effective mass is significantly increased, reducing the recoil energy to zero.

Generally speaking, Mossbauer spectroscopy is an excellent tool to probe the local environment of nuclei. As nuclear transitions tend to be of high energy and narrow linewidth, and mainly unaffected by recoil losses when the nuclei are doped in solids or frozen, they can be utilized to look for shifts and splittings in the nuclear energy levels that may arise from different types of interactions or other phenomenon. Some of these interactions include the isomer shift, quadrupole splitting, and magnetic hyperfine splitting. There are several applications for Mossbauer spectroscopy such as in geology and bioinorganic chemistry, which usually involves the identification of iron-containing specimens.

3.2 The ^{229}Th:LiSrAlF$_6$ Crystal

The development of a suitable ^{229}Th-doped crystal has been a significant challenge of this work [RSD10b, HGR13]. A variety of VUV transparent crystals doped with the common ^{232}Th isotope have been grown and tested to find a material which satisfies all of the requirements of this experiment, which include: high VUV transparency; absence of long-lived VUV induced fluorescence; resistance to the effects of nuclear radiation; and low radiation-induced scintillation.

To determine the most suitable host for ^{229}Th, a number of different crystals were obtained commercially from AC Materials including Na_2ThF_6, Th:LiCAF, Th:LiSAF, Th:YLF, and some others. These crystals were grown using the more abundant isotope of thorium, ^{232}Th. And while this dopant does not reveal information about radiation induced scintillation, it does provide information about VUV induced backgrounds [RSD10a].

The host crystal must be VUV transparent such that some external source (such as synchrotron radiation) can be used to excite the doped ^{229}Th inside the crystal. And for similar reasons, the band gap of the host crystal must exceed the energy of the isomeric level. Another important consideration is the charge state of the dopant nuclei. To expect radiative decay from the transition versus internal conversion, the dopant must be accepted as $^{229}Th^{4+}$. Computer modeling was carried out for the case of LiSAF and LiCAF host crystals and $^{229}Th^{4+}$ as the dopant [JAV09]. For different dopant sites, the form of charge compensation is obtained. The end result is that $^{229}Th^{4+}$ will substitute at the Ca^{2+} and Sr^{2+} sites, but F^- interstitial ions must be taken into account when considering the full effect of the crystal lattice on the isomeric transition in ^{229}Th. While many of the tested crystals have band gaps of over 10 eV, color centers and impurities in the host crystal can cause residual absorption which can interfere with spectroscopy of the isomeric transition in ^{229}Th [RSD10a]. For these reasons, the impurities in the host crystal must be at the part per billion level. Based on these past works, LiSrAlF$_6$ was eventually chosen as the host crystal.

After determination of the crystal host, the most significant challenge that the project faced was obtaining a sufficient quantity (a few mg) of the rare ^{229}Th to produce the final

crystals. (For reference, the first quote from a commercial supplier for 3 mg of ^{229}Th was priced at 6 millon dollars!). Fortunately, Oak Ridge National Laboratory and DARPA helped secure a sample of 3 mg of ^{229}Th. This sample was received in the middle of 2011 and the first-ever ^{229}Th doped crystal was grown in December of that year. Due to unknown contamination in the material received from Oak Ridge, the first generation of crystals were of an inferior quality in both transmission and thorium content ($\sim 10^{16}$ nuclei/cm^3). Since then, the original ^{229}Th material has been reprocessed at Oak Ridge National Labs to remove the impurities and then sent back to AC Materials for another round of crystal growth. The new crystals show a much-improved quality and thorium content ($\sim 10^{17}$ nuclei/cm^3), see Fig. 3.2.

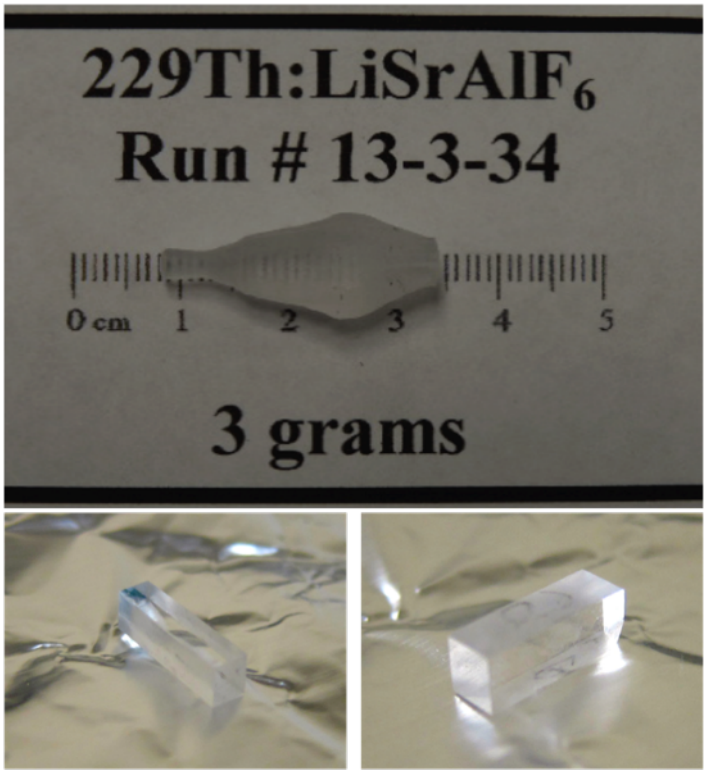

Figure 3.2: Second crystal growth run. Two crystals were produced with activities of ~ 292 and 2150 nCi, which corresponds to densities of $\sim 10^{17} - 10^{18}$ nuclei/cm^3.

A huge thanks to Hans Jenssen and Arlete Cassanho from AC Materials for growing such beautiful crystals. Also a big thanks to Saed Mirzadeh from Oakridge National Labs for making the ^{229}Th available to us.

3.3 A Solid State Frequency Reference

Atomic clock experiments have provided some of the most sensitive measurements on the variations of fundamental constants [RHS08, HLT14, GNJ14] and perhaps the most stringent tests of General Relativity [AHJ07]. Atomic transitions however, utilized as high-Q oscillators, are sensitive to its environment making traditional atomic clock experiments cumbersome. Modern clock experimenters routinely employ complicated interrogation schemes, e.g., atomic fountains or 3-dimensional optical lattice confinement to mitigate environmental influences. Just as in atomic clocks, the nuclear transition in ^{229}Th can be addressed by laser spectroscopic techniques, if the transition energy is accessible with current laser technology. This would allow the transition to be driven as a high-Q oscillator with the added benefit of reduced sensitivity to the environment due to shielding from atomic electrons. As nuclear transitions are less sensitive to the local environment as compared to atomic transitions, ^{229}Th atoms doped into a suitable host crystal can retain a narrow transition linewidth. This feature can help realize a solid-state optical frequency reference with better short-term stability than current optical clocks [RDG10].

^{229}Th atoms in a crystal lattice are confined to the Lamb-Dicke regime [Dic53] in which the recoil energy is much less than the energy required to create a phonon in the lattice such that the internal and external degrees of freedom are decoupled. This essentially means that the transition energy will not be sensitive to recoil or first order Doppler effects, however, there are a variety of effects that must be accounted for.

The Hamiltonian for a ^{229}Th nucleus in a crystal can be written as

$$\mathrm{H} = \mathrm{H}_0 + \mathrm{H}_{FS} + \mathrm{H}_{HFS}, \tag{3.5}$$

where H_0 is the single-particle Nilsson Hamiltonian, and H_{FS} and H_{HFS} are the Hamiltonians describing the fine and hyperfine interactions arising from the crystal environment. This Hamiltonian is in the absence of external fields. In ionically bonded crystals with no unpaired electron spins, the fine-structure interaction vanishes and the hyperfine interactions are the dominant source of shifts and broadenings of the nuclear transition. A multipole expansion

of the hyperfine Hamiltonian can be written as:

$$\mathrm{H}_{HFS} = \mathrm{H}_{E0} + \mathrm{H}_{M1} + \mathrm{H}_{E2} + ... \tag{3.6}$$

These effects are similar to those that arise in Mossbauer and NMR spectroscopy, and can be reliably estimated using previous measurements. The effects of the first few terms in the Hamiltonian for a generic lattice environment can be explained.

$\mathrm{H_{E0}}$ represents the electric monopole term which describes the contact interaction between the nucleus and its electron cloud. Changes in the size of the electron cloud or the nucleus will affect the transition energy. Because the electron density at a given lattice site is temperature dependent, this is a temperature dependent effect. Temperature gradients across the crystal can lead to inhomogeneous line broadening. Experiments involving Mossbauer spectroscopy indicate that this shift should be $\sim<$ 100 MHz compared to free ions, with the temperature dependence of the shift on the order of 10 kHz/K [DSL, RS83, Gib76]. If the ^{229}Th reliably substitute for a single species in a crystal, the shift will be consistent for all nuclei. In addition, established techniques can lead to a temperature stability better than 0.1 mK across the crystal [Dav96] such that this contributes $\sim$ 1 Hz to the linewidth.

In the presence of a magnetic field at the nucleus, $\mathrm{H_{M1}}$ will give rise to shifts and splittings of the ground and excited state energies. Crystals that transmit in the VUV will be free of spurious currents due to the large band gap energy. Additionally, in ionically bonded crystals of interest such as $\mathrm{LiSrAlF_6}$, thorium substitutes as a $\mathrm{Th^{4+}}$ ion such that all electron spins are paired. And so the only magnetic fields in the crystal will be due to the magnetic moments of surrounding nuclei. One nuclear magneton at the shortest typical distance of $\sim$ 2.5 angstrom in a crystal produces a magnetic field of $\sim$ 400 mG. The magnetic dipole moments of the $5/2^+$ and $3/2^+$ states are estimated to be $0.45\mu_\mathrm{N}$ and $-0.08\mu_\mathrm{N}$, respectively [DT98]. This can lead to a broadening of the transition energy by up to $\sim$ 400 Hz. Considering the contributions of all the neighboring nuclei, this could cause a broadening of up to 1-10 kHz [RDG10].

If an electric field gradient is present, the electric quadrupole term (H_{E2}) can also give rise to a shift and splitting of the transition energy. Because both ground and excited states have spin I $>1/2$, they can support an electric quadrupole moment. The structure of the

host crystal has a significant effect on the electric field gradient felt by the nucleus. An estimate for the size of the effect can be estimated by considering only the ground state shift. The ground state quadrupole moment of ^{229}Th is known (4.3 barns [GL74]). Typical field gradients in crystals range from $10^{16} - 10^{21}$ V/m^2 [Ram66, PRF]. This can lead to transition energy shifts of $1kHz$ - $100MHz$. If the ^{229}Th nuclei substitute into a single lattice site consistently, the quadrupole interaction will result in a constant shift of the transition frequency with a temperature (T) dependence given by:

$$\frac{\Delta \mathrm{f}}{\mathrm{f}} = \alpha \Delta \mathrm{T}, \tag{3.7}$$

where α is the coefficient of linear expansion for the crystal. For host crystals with cubic or icosahedral symmetry, H_{E2} is minimized [KPR75].

Nuclei can vibrate in their lattice sites. These vibrations could lead to a broadening of the transition frequency if the zero-phonon transitions are mode dependent. This is likely only for optical phonon modes where the ^{229}Th nuclei are vibrating relative to their nearest neighbors. These modes are expected be frozen out however at room temperatures [Sla61]. Such an effect could lead to resolvable sidebands if the shift is more than the linewidth. The vibrations of the nuclei can also lead to second order Doppler effects which can also cause a shift in the transition energy. Using a simple harmonic oscillator model, this effect can be estimated as:

$$\frac{\Delta \mathrm{f}}{\mathrm{f}} = \frac{3\mathrm{k}_B\mathrm{T}}{2\mathrm{Mc}^2} \tag{3.8}$$

[Gib76], resulting in a temperature dependent shift on the order of $1\frac{\mathrm{Hz}}{K}$; $\Delta \mathrm{f} \leq 0.1\mathrm{mHz}$ across the sample for the assumed temperature stability.

While the discussed effects show that the crystal lattice environment can cause large shifts in the transition frequency, these shifts are a consequence of the lattice molecular binding and are constant in time. The modified nuclear transition frequency can therefore be utilized for time-keeping purposes. Table 3.1 summarizes the broadenings and shifts limiting the usefulness of this transition as a primary frequency standard assuming a LiCAF ($\mathrm{LiCaAl_6}$) host crystal [RDG10]. The broadenings will impact the precision of the frequency measurement, while the shifts will impact its accuracy. Considering even the worst case

Interaction	Effect on $^{229}Th4^{+}$
Electric Monopole (Isomer Shift)	$\phi \leq 100$ MHz. Estimate based on typical Mossbauer observations. $\Delta = 10$ Hz per 1 mK gradient across sample.
Magnetic Dipole	$\phi \leq 1\frac{Hz}{mG}$. $\Delta = 1\frac{Hz}{mG}$. $1 - 10$ kHz given the contributions from nearest neighbors.
Electric Quadrupole	$\phi \leq 100$ MHz. Estimate is based solely on the quadrupole moment of the ground state as the quadrupole moment of the $I^P = \frac{3}{2}^+$ level is not known.
2nd Order Doppler	$\phi \leq 300$ Hz at 300 K. $\Delta = 1$ mHz per 1 mK gradient across sample.

Table 3.1: Effect of the Crystal Lattice Environment on ^{229}Th. These effects can be attributed to a hyperfine Hamiltonian, typical in Mossbauer spectroscopy and NMR. The interaction along with its effects on the transition are stated. [RDG10]

scenario in which there is a 10kHz broadening due to the magnetic dipole term, the frequency can be measured with a greater precision than current clocks due to the large number of absorbers. Standard laboratory techniques allow the suppression of electric and magnetic fields to below $1\frac{\text{mV}}{\text{cm}}$ and 1μG, respectively. And so the most significant environmental effect arises from the crystal temperature. A 1mK temperature difference results in a fractional shift of the frequency by 6x10^{-15} [RDG10]. Even with state of the art thermometer accuracies of 0.04mK [Pre90], a clock based on this architecture may not possess the necessary accuracy to be a primary standard.

And while the effects of the crystal environment on the low-lying transition in ^{229}Th are by no means negligible, the ^{229}Th:LiSrAlF$_6$ crystal is adequate to serve as a short term frequency reference, making it useful as a flywheel oscillator. It is especially ideal for a coarse scan via a broadband synchrotron source.

CHAPTER 4

A Coarse Scan via The Advanced Light Source

As the ^{229}Th:LiSrAlF$_6$ crystals can achieve a high concentration of thorium per volume, broadband synchrotron sources should be sufficient for a coarse scan over the transition frequency. Although there are some broadenings and shifts of the natural linewidth due to the crystal environment as discussed in the previous chapter, these broadenings can actually be beneficial for a relatively quick interrogation using a broadband synchrotron source. We utilize the Advanced Light Source (ALS) in Berkeley CA which provides a tunable source of photons which can probe much of the region of interest near 7.8 eV. In the following sections we will provide a brief intro on synchrotron sources then discuss some specifics regarding the ALS and the beamline of interest. And then we will discuss our experiment including instrumentation, characterizations, and results.

4.1 Synchrotrons

Although synchrotron sources were originally produced as very powerful x-ray sources, modern research facilities are designed to generate electromagnetic radiation which is tunable from the far infrared to the hard x-ray regime and with intensities many orders of magnitude greater than those typically produced by laboratory-based sources [Wil11].

Synchrotrons sources utilize electrons accelerating in a circular path, at relativistic speeds, to generate electromagnetic radiation. The electrons are typically generated via thermionic emission with an electron gun and then accelerated up to energies of $\sim$100 MeV with a linear accelerator (linac). Upon exit from the linac, the electrons are introduced into a booster ring. Acceleration is achieved in the booster ring through RF cavities which impart longitudinal

kicks to the electrons, producing a spatially bunched electron beam. The electron beam is then injected (at the injection energy) into the storage ring where it should achieve its target energy (or beam energy). Modern synchrotrons typically operate at the same injection and beam energies allowing a continuous feed of electrons from the booster into the storage rings.

A well-behaved circulating electron beam is maintained in the booster and storage rings with the use of magnets. Dipole or bending magnets are used to steer the beam in a circular path. Quadrupole magnets are used for focusing of the electron beam which is necessary to counteract the Coulomb repulsion. As electrons are continuously lost in the storage ring due to collisions with residual gases and through unwanted photoemission, RF cavities are typically utilized in the storage rings to make up for round-trip energy losses.

Straight sections in the storage ring allow insertion of different devices, called insertion devices. These can consist of undulator and wiggler magnets, which are composed of permanent magnets arranged in a periodic structure. These insertion devices force the electrons to perform undulations and wiggles as they pass through the periodic magnetic structures, which stimulates the generation of brilliant electromagnetic radiation in the direction of propagation. The spatial period of the magnetic structure influences the range of wavelengths that can be produced. The beamlines typically run off tangentially to the storage ring from the insertion devices. A front end station often serves as a safety and monitoring station for the beamline output. This station can block unwanted radiation such as higher harmonics and can monitor useful beam parameters.

4.2 The Advanced Light Source

The Advanced Light Source is a government sponsored synchrotron providing scientists and students with a wide variety of stations to run experiments. The synchrotron at the ALS is typically operated at 1.9 GeV beam and injection energies. The beam current is 500 mA in multibunch mode. The bunch spacing is 2 ns with a pulse length of 60 ps. The circumference of the synchrotron is 196.8 m. It has 12 straight sections for insertion devices. Each straight section is followed by a bending sector composed of three bending magnets

to form a "Triple Bend Achromat". As the high speed electrons are forced to bend, they lose significant amounts of energy. A couple of RF cavities, operated at $\sim$ 500 MHz, help replenish this lost energy. At the ALS, we utilize the Chemical Dynamic Beamline 9.0.2.

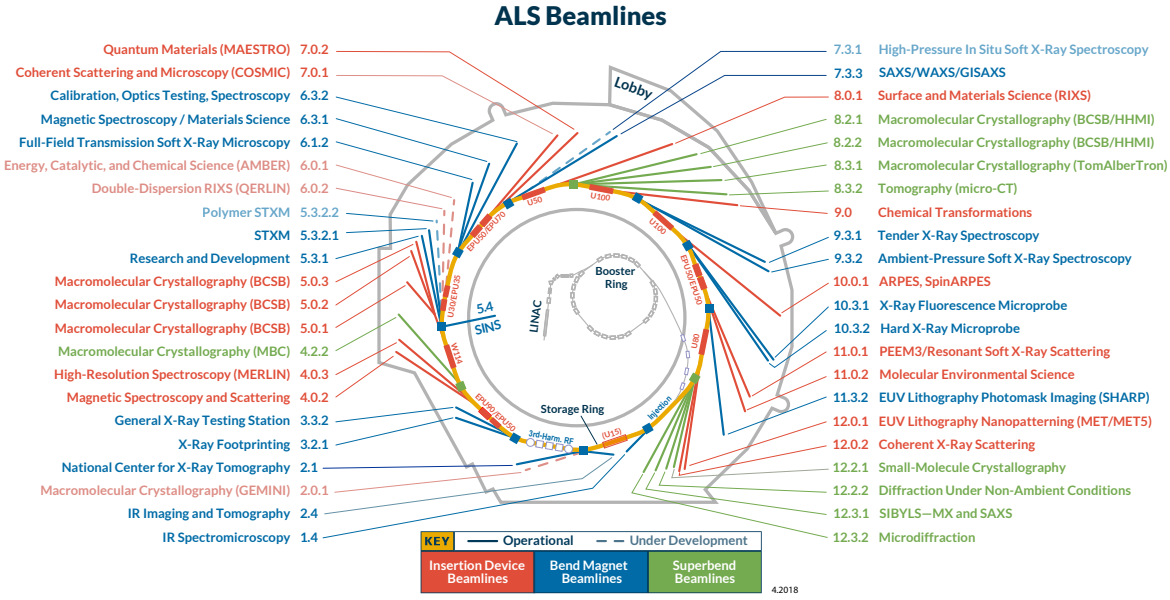

Figure 4.1: ALS synchrotron and beamlines. Image taken from LBL.gov.

4.2.1 Chemical Dynamics Beamline 9.0.2.1

The chemical dynamics beamline at the ALS provides an output that is tunable from $\sim$ $7.4 - 30$ eV. Producing such low energy photons with a synchrotron source requires small undulator gaps and the large magnetic fields required give rise to intense higher harmonics. The Chemical Dynamics beamline utilizes a differentially pumped gas filter to help reduce the higher harmonic contaminants [HKH97]. The rare gases contained in the filter absorb the higher harmonics, effectively reducing the intensities by five orders of magnitude. There are a total of 4 terminals available at the chemical dynamics beamline. Terminals 1 and 2 provide a broadband high flux output with a photon flux of $\sim 10^{15}$ s^{-1}. While terminal 1 can provide access to roll-up endstations, terminal 2 is equipped with a permanent imaging endstation. Terminals 3 and 4 provide monochromatized light with a lower photon flux of $\sim 10^{13}$ s^{-1}. Our experiments, which have included several visits for characterizations as

well as the interrogation of the ^{229}Th:LiSrAlF$_6$ crystals, have primarily utilized beamline terminal 9.0.2.1 (terminal 1). We prefer the broadband and higher flux for a course search for the transition. This endstation also allows an MgF_2 window to be placed into the beam path which serves as an additional filter for higher harmonics. The access allowed for roll-up endstations has made it relatively simple to set up our experimental apparatus.

4.3 The Experiment

Conceptually, the experimental protocol is simple. A VUV transparent, ^{229}Th-doped crystal is illuminated for time T_e with VUV photons. If the VUV photons are resonant with the isomeric transition, a fraction of the ^{229}Th nuclei are excited to the ($I^p = 3/2^+$) isomeric state. Following the excitation period, the VUV photon source is shuttered and any subsequent fluorescence, which results from spontaneous decay back to the ($I^p = 5/2^+$) ground state, is recorded by opening two low-profile shutters to expose two photomultiplier tubes (PMTs) to the crystal for a time T_d. See Fig. 4.2. For a tunable source of VUV photons, we utilize beamline 9.0.2.1. Several trips have been made to the ALS to conduct our experiments. Excluding trips made for characterization purposes, a total of three actual visits were made for interrogation of the ^{229}Th:LiSrAlF$_6$ crystals. The methods and apparatus have evolved since our initial visit. Only details of the most recent experimental run at the ALS will be discussed as these results are the most relevant.

4.3.1 Instrumentation

We will briefly describe some of the instrumentation involved in the experiments at the ALS. Fortunately, the ALS provides the VUV beam. There have been occasional losses of beamtime, due to different reasons, but this has never been a major hindrance to our experiment. And in fact, the staff at the ALS as well as other scientists utilizing the beamline have been more than accommodating and we typically get more beamtime than is allotted to us. On our end, the instrumentation used at the ALS primarily consists of a spectroscopy chamber. The chamber housing all of the components including the ^{229}Th:LiSrAlF$_6$ crystal and the

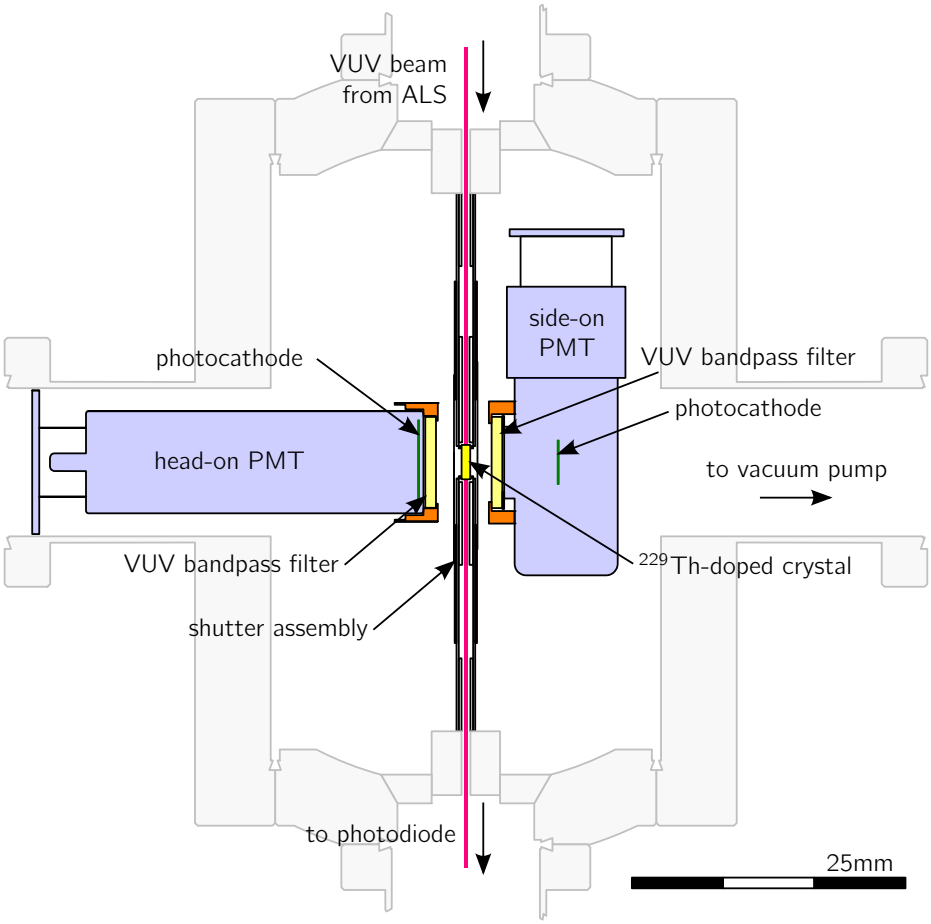

Figure 4.2: Spectroscopy chamber schematic. The chamber is an 8" spherical octagon manufactured by Kimball Physics. It houses two photomultiplier tubes during the experimental runs, a head-on and a side-on type. The ^{229}Th:LiSrAlF$_6$ crystal is housed at the center of the chamber. Two low-profile shutters (VS35), manufactured by Uniblitz, protect the PMT's during illumination of the crystal with the ALS beam. The shutters are then opened after illumination for fluorescence detection.

photomultiplier tubes is an 8 inch spherical octagon manufactured by Kimball Physics. The chamber is equipped with several ports for electrical and other types of feedthroughs. In prior experiments at the ALS, the apparatus for fluorescence detection was not optimized. Through trial and error and eventually with the help of ray-tracing software such as Zemax, we constructed an optimized VUV fluorescence detection system, which basically involves putting the detectors as close as possible to the crystal. The inside of the spectroscopy chamber is shown in Figure 4.2. The chamber can house two PMT's during the experimental runs. To protect the PMT's during illumination of the crystal, a low profile shuttering system is used. The VS35 shutters are manufactured by Uniblitz and allow the PMT's to be placed within millimeters of the crystal for optimized collection efficiencies. The up-close configuration is beneficial in that it obviates the need of lenses and other optics which could have frequency dependence and require accurate alignment. These VS35 shutters are of a unistable design and require an applied voltage to keep them open during fluorescence detection. This leads to heating of the actuator coils in the shutters which produces black body radiation that increases the dark count rate of some of our photomultiplier tubes. To prevent this effect, Uniblitz was kind of enough to modify their shutters and add a heat exchange link to the actuator coils. And by coupling a heat sink to the links on the actuator coils, we are able to prevent the increased count rates. The ^{229}Th:LiSrAlF$_6$ crystal is housed at the center of the chamber where it can be interrogated by the ALS beam.

We have a variety of photomultiplier tubes available to us for fluorescence detection after illumination. We typically utilize a cathode grounded voltage divider circuit for our PMT's. The cathode grounded configuration allows us to put the photomultiplier tubes very close to grounded surfaces in the vacuum chamber. In the typical anode grounded voltage divider boards, the signal is read with respect to ground which is safer but would put the cathode at a large negative voltage. In this scenario, electrons can flow from the cathode to nearby grounded surfaces. This leakage current can increase the dark countrate of the PMTs which can reduce the signal to noise ratio (SNR). We also have a variety of narrowband and broadband VUV bandpass filters available to us, manufactured by eSource Optics and Acton Optics. These can be beneficial in reducing unwanted background fluorescence.

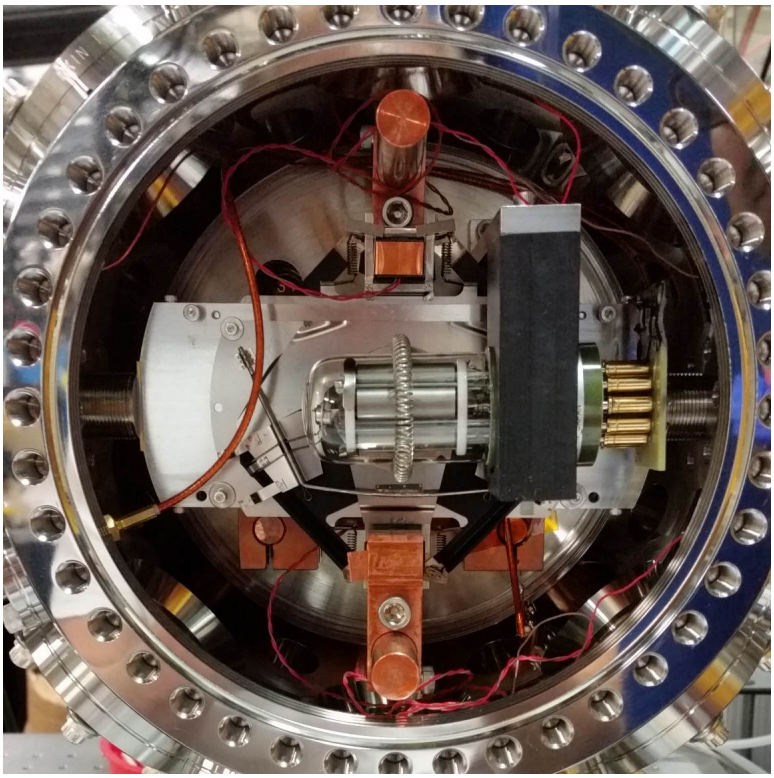

Figure 4.3: Spectroscopy chamber picture. The actual innards of the spectroscopy chamber are shown. The side-on PMT is clearly visible (R7639) along with the one of the VS35 shutters. The Cu pieces are the thermal links which allow for cooling of shutter actuator coils, and also for cooling of the head-on PMT, which is on the back-side of the shutter assembly.

Additionally, we have the ability to cool down our head-on photomultiplier tubes. Cooling the photocathode and dynodes can reduce the dark count rate of the PMT's. We achieve the cooling utilizing thermo-electric coolers (TEC's) which operate based on the Peltier effect. The TEC's are attached to Cu feedthroughs which thermally link the TEC's to the PMT's housed inside of the vacuum chamber. By cooling the hot side of the TEC's against a reservoir at a fixed temperature of $\sim -10C$, we can cool our PMT's down to $\sim -25C$. And finally, with the use of waveform digitization, we have the ability to post-process the data which allows us to discriminate noise and other unwanted effects (which will be discussed in more detail in chapter 5).

Beamline 9.0.2.1 is a roll-up endstation, which allows us to setup our spectroscopy chamber downstream of the beam. To facilitate the experiment, we constructed a portable table on wheels, as can be seen in Figure 4.4. The spectroscopy chamber is mounted to the table. All of the necessary electronics and additional hardware is contained on the racks of this table. The portable spectroscopy rack has made our experiments at the ALS easier to set up and operate. We are literally able to roll right up to endstation and then metaphorically set up shop.

4.3.2 Characterizations

4.3.2.1 Thorium Crystals

The ^{229}Th dopant used in this work was purchased from Isotope Distribution Office, U.S. Department of Energy and was extracted from ORNL mass-separated ^{233}U, batch UTHX001, which contains only ppb levels of ^{232}U. The mass distribution of thorium isotopes in this sample was: ^{229}Th (75.6%), ^{228}Th ($< 0.1\%$), ^{230}Th (0.48%) and ^{232}Th (23.8%). During the time of the most recent experimental run at the ALS, a total of three ^{229}Th-doped $LiSrAlF_6$ crystals with dimensions $\approx 3\,\text{mm} \times 3\,\text{mm} \times 10\,\text{mm}$ were available to us. The amount of ^{229}Th in each crystal was assayed by γ-ray spectroscopy (Ortec GMX-50220-P) [ARM02] and found to be $(115 \pm 5)\,\text{nCi}$, $(290 \pm 40)\,\text{nCi}$, and $(2.2 \pm 3)\,\mu\text{Ci}$ (see Fig. 4.5). For these experiments at the ALS, we used only the latter two crystals, referred to as crystal B and C,

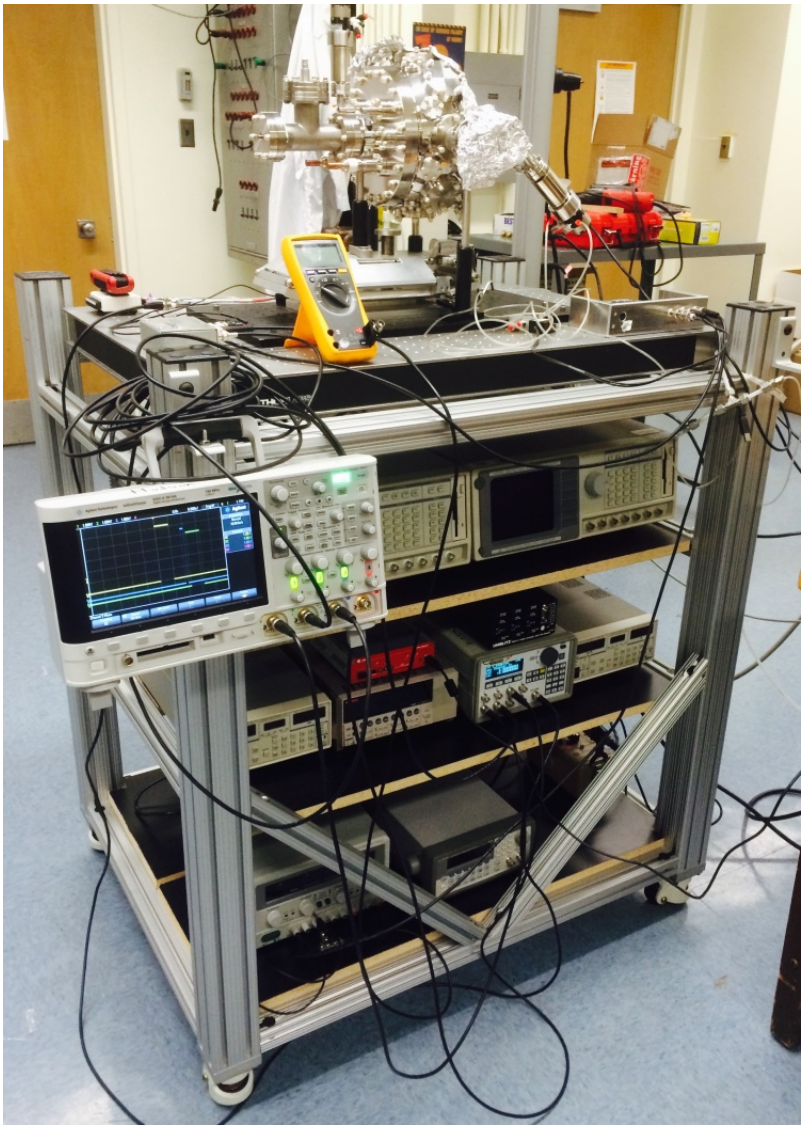

Figure 4.4: Portable spectroscopy table. The table was constructed to help facilitate our experiments at the ALS.

which have a thorium atomic density of $n_{\mathrm{Th}} \approx 5.8 \times 10^{16}\,\mathrm{cm}^{-3}$ and $n_{\mathrm{Th}} \approx 4.1 \times 10^{17}\,\mathrm{cm}^{-3}$, respectively. The first experiments at the ALS involved a ^{229}Th:LiSrAlF$_6$ crystal of inferior

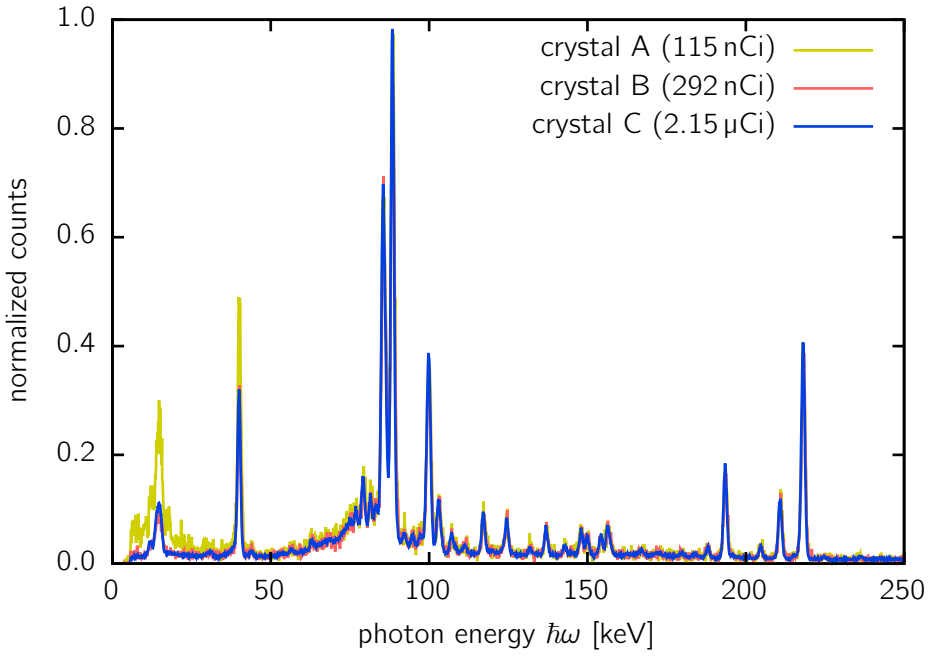

Figure 4.5: Gamma spectra of ^{229}Th:LiSrAlF$_6$ crystals. These were taken using the Ortec GMX-50220-P. Three crystals were available to us at the time of the most recent ALS experiments. These are labelled A, B, and C and their activities were found to be $(115 \pm 5)\,\mathrm{nCi}$, $(290 \pm 40)\,\mathrm{nCi}$, and $(2.2 \pm 3)\,\mu\mathrm{Ci}$, respectively.

quality, and the corresponding results of that search will not be discussed.

4.3.2.2 ALS Parameters

In normal operation (1.9 GeV electron energy), the chemical dynamics beamline can be tuned within $\hbar\omega \approx (7.4\text{–}30)\,\mathrm{eV}$. We characterize the photon flux ϕ_{p} of the beamline with a Opto Diode Corporation (ODC) SXUV-100 VUV damage resistant photodiode, calibrated against a NIST-calibrated ODC AXUV-100G photodiode, and find the photon flux to be $\phi_{\mathrm{p}} = (1.0\text{–}1.25) \times 10^{15}\,\mathrm{s}^{-1}$ (see Fig. 4.6a). The VUV spectrum is nearly Lorentzian with linewidth $\hbar\Gamma \approx 0.19\,\mathrm{eV}$ and exhibits a constant "tail" up to $\approx 10\,\mathrm{eV}$ (see inset Fig. 4.6(a)). We reduce the photon flux to $\xi \approx 0.7$ of its measured value to account for the fraction of

ALS photons which are contained in this tail.

4.3.2.3 Signal Detection

The determination of the total collection efficiency ($\eta(\omega)$) for each fluorescence detection configuration used requires knowledge of the PMT quantum efficiency (η_{PMT}), its solid angle fraction (η_{SAF}), and the transmission of a VUV bandpass filter (η_{filter}), optionally used to reduce the UV background. Both η_{PMT} and η_{filter} are characterized using a McPherson 234/302 monochromator, deuterium lamp, and the SXUV-100 and AXUV-100G photodiodes. The currents produced by these photodiodes are read out using a Keithley 6485 picoammeter. Our measurements agree with the calibrations provided by the respective manufacturers. The different η_{SAF} are determined using commercial (Zemax) ray-tracing software and independently verified with homemade ray-tracing software. Due to scintillation following the radioactive decay of ^{229}Th (4.8 MeV α-decay with a half-life of (7917$\pm$48) y [VNM14]) and its daughter isotopes, the crystals emit photons in the UV region. The spectrum of the scintillation in each crystal is shown in Fig. 4.6(b). All spectra show a maximum at $\approx 300\,\mathrm{nm}$ and drop to 50 % at $\sim 250\,\mathrm{nm}$. This UV fluorescence together with scintillation induced directly in the PMTs by the crystal radioactivity is the dominant background in our measurements.

To better discriminate any ^{229}Th nuclear fluorescence from spurious PMT signals, we simultaneously employ two PMTs of differing technology for each measurement. Specifically, three overall configurations, listed in Tab. 4.1, were used in the measurements at the ALS and their resulting total detection efficiencies are shown in Fig. 4.6(c). Finally, the PMT electronic signals are (optionally) amplified (Stanford Research SR445A) and recorded using a digitizer (CAEN DT5751), which stores the waveform of every detected event for off-line analysis.

4.3.2.4 Error Budget

There are sources of error in the experiment which must be accounted for. As we use a NIST calibrated AXUV100 photodiode to determine the efficiencies of other detectors, the error

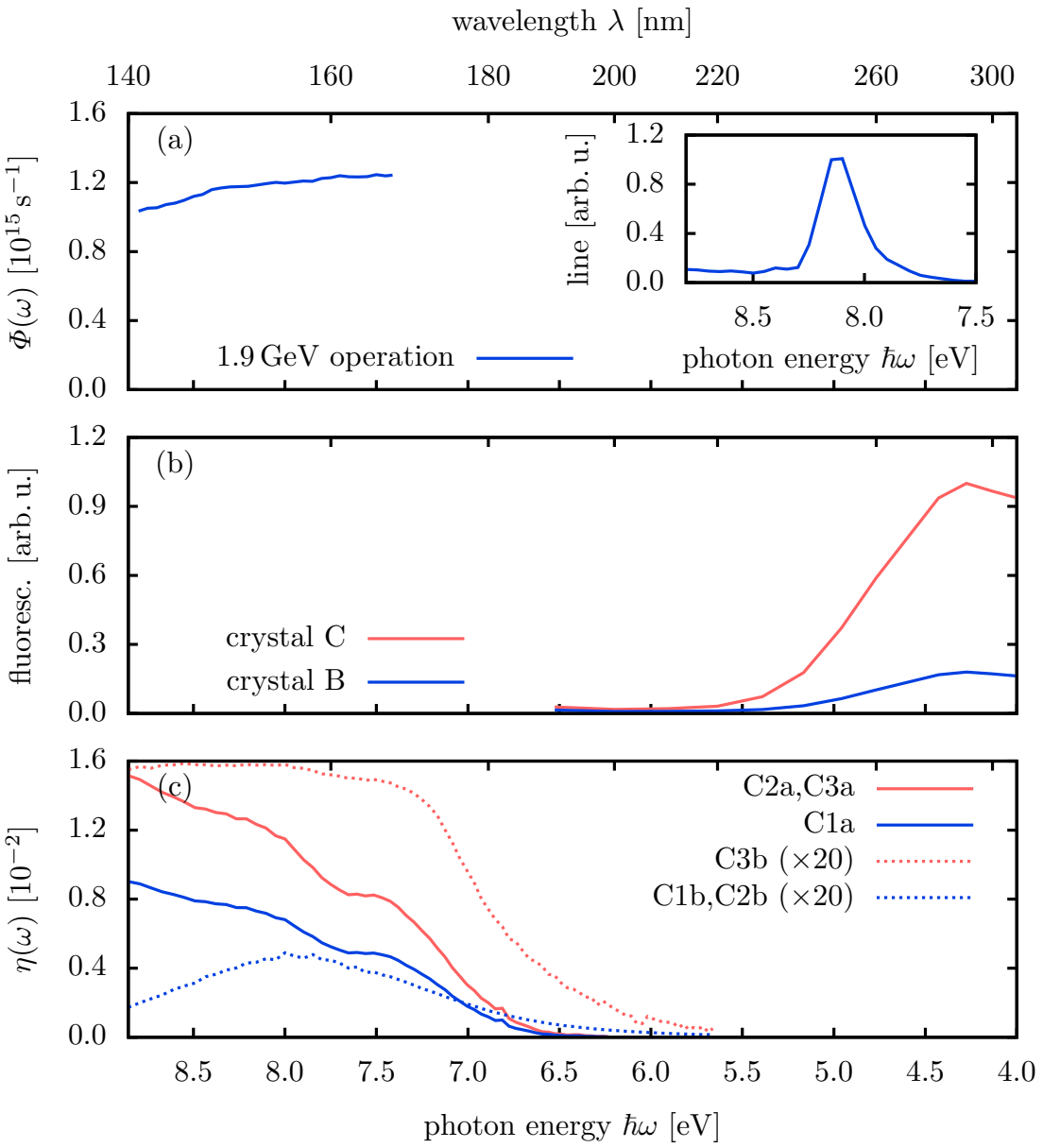

Figure 4.6: ALS experimental parameters. (a) shows the measured photon flux of the ALS beam over the scan range, along with the lineshape at a particular undulator setting. (b) depicts the crystal background as measured with the McPherson 234/302 monochromator. It is supected that this background is due to Cherenkov radiation and/or scintillation. (c) shows the overall detection efficiencies for different configurations used at the ALS, see Tab. 4.1.

config.		crystal	PMTs	filter	d [mm]	$\hbar\omega_{\mathrm{L}}$ [eV]
C1	a	C	R6835	no	12	7.4–8.8
	b		R8486	yes	25	
C2	a	B	R6835	no	5–6	7.4–8.8
	b		R8486	yes	25	
C3	a	B	R6835	no	6–7	7.4–8.25
	b		R7639	no	25	

Table 4.1: Relevant configurations of the experimental system (see Fig. 4.2) and searched VUV photon energy range. All PMTs are manufactured by Hamamatsu, the VUV bandpass filter ((150 ± 27) nm) is an Acton Research Corporation 150-N-MF-1D, and d denotes the distance of the photocathode to the crystal center.

in this calibration must be propagated to determine the errors of the other detectors. These other detectors include the SXUV100 used to characterize the ALS photon flux and the different PMT's used in fluorescence detection. Other sources of error include the absolute activities of the ^{229}Th:LiSrAlF$_6$ crystals and the determined thorium nuclei density. And additionally, the exact placement of the thorium crystal with respect to the PMT photocathodes produces an additional error which manifests in the form of an error in the solid angle fraction for photon collection.

Considering all of the experimental parameters and the errors due to each, a total error budget can be constructed. See Table. 4.2. This total error budget can be taken into account in the excitation model. It does have an effect on the total collection efficiency of our system. And this will ultimately affect a comparison of the experimental data to what is expected given the experimental parameters.

4.4 Analysis and Results

Using the chemical dynamics beamline at the ALS (Fig. 4.1)) and the apparatus as described earlier, our most recent experiments at the Advanced Light Source in Berkeley California

parameter	symbol	rel. error
ALS VUV energy	$\hbar\omega_{\mathrm{L}}$	0.02
ALS VUV linewidth	Γ_{L}	0.10
ALS VUV spectrum	ξ	0.40
photon flux	ϕ_{p}	0.15
solid angle fraction	η_{SAF}	0.15
PMT quantum efficiencies	η_{PMT}	0.15
(eff.) crystal length	l	0.10
^{229}Th density	n_0	0.15
total		≈ 0.52

Table 4.2: Statistical and systematic errors for the individual contributions to N_0 in Eq. (4.3). We estimate bounds for the systematic error, which are significantly larger than statistical errors for most parameters. For the statistical errors, we report 1.64 standard errors (corresponding to a 90 % CL). The total is estimated using standard error propagation, because the parameters (except for Φ and η_{PMT}) are independent. The configurations involving a VUV filter were inferior and did not enter in the final results such that η_{filter} is not listed.

were conducted in August and September of 2014. Results from a couple of experiments conducted prior to this will not be discussed. As mentioned previously, the quality of the ^{229}Th:LiSrAlF$_6$ crystal was not ideal and our apparatus for fluorescence detection was not optimized. For these reasons we will discuss the results of the latest experiments at the ALS. The actual experiment was comprised of beamtime allotments ranging in between 8 and 16 hours from August 20 to September 5, 2014 and spanned a total of 96 hours . We performed a search in the range (7.412–8.8) eV with step size $\leq$ 0.1 eV. We chose an illumination time $T_\mathrm{e} = 2000\,\mathrm{s}$ for each VUV energy and a detection time $T_\mathrm{d} = 1000\,\mathrm{s}$ ($T_\mathrm{d} = 1800\,\mathrm{s}$) for configurations C1 and C2 (C3).

4.4.1 Excitation Model

To determine the rate of excitation of the ^{229}Th nuclei in the crystal, we will need to develop an excitation model. We can begin with a two level system as the next excited levels in the ^{229}Th nuclei are of significantly larger energies in excess of 20 keV. The rate equation governing the excited state population can be expressed as:

$$\frac{dN_2}{dt} = (N_1 - \frac{g_1}{g_2}N_2)\int \sigma(\omega)\Phi(\omega)\mathrm{d}\omega - N_2\Gamma. \tag{4.1}$$

N_2 and N_1 represent the excited and ground states, respectively. g_2 and g_1 are the corresponding multiplicities and Γ is the transition strength of the excited state. $\Phi(\omega)$ is the spectral irradiance of the excitation source whose integral yields the total photon flux. We know this to be of a Lorentzian profile with a width defined in the previous section. The absorption cross section $\sigma(\omega)$ can be expressed as:

$$\begin{gathered}\sigma(\omega) = \frac{g_2}{g_1}\Gamma\frac{\lambda_o^2}{4}g_\Gamma(\omega) \\ \text{with} \\ g_\Gamma(\omega) = \frac{2}{\pi\Gamma}\frac{1}{1+4(\frac{w-w_o}{\Gamma})^2}.\end{gathered} \tag{4.2}$$

$g_\Gamma(\omega)$ is the normalized lineshape function with λ_o and ω_o representing the unknown transition wavelength and frequency, respectively. This result is derived from a semi-classical treatment of the two level system interacting with coherent radiation.

Given the parameters of the experiment, the rate equations can be solved to determine the number of fluorescence photons we can expect to detect. At a given ALS beam energy, $\hbar\omega$, in the limit of weak excitation, the number of detected photons from the nuclear fluorescence, N_d, in a time interval $\{t_1, t_2\}$ is given as:

$$\begin{gathered} N_d = N_0 \left(1 - \mathrm{e}^{-T_\mathrm{e}/\tau'}\right) \left(\mathrm{e}^{-t_1/\tau'} - \mathrm{e}^{-(t_1+t_2)/\tau'}\right) \\ \text{with} \\ N_0 = \frac{2}{3}\,\eta(\omega)\,\frac{\lambda_0^2}{2\pi}\,\frac{\xi\phi_p'(\omega)\,n_\mathrm{Th}\,l}{\Gamma_\mathrm{L}}\,\frac{1}{1+4\left(\frac{\omega-\omega_0}{\Gamma_\mathrm{L}}\right)^2}, \end{gathered} \tag{4.3}$$

where τ' is the lifetime of the ^{229}Th transition inside the crystal, ϕ_p' is the photon flux transmitted through the crystal, t_0 is the time between closing the ALS beam shutter and opening the PMT shutters (typically $t_0 = 2\,\mathrm{s}$), $\eta(\omega)$ is the total efficiency of the detection system, l is the length of the crystal, and $\Gamma_\mathrm{L} \approx 0.19\,\mathrm{eV}$ is the bandwidth of the ALS beam at beamline 9.0.2.1.

There are a few other factors that should be considered when considering the excitation of the ^{229}Th nuclei and the subsequent fluorescence detection. One of them is the effect of the dielectric medium on the lifetime of the transition. The vacuum lifetime is given by [RK95]:

$$\tau = n^3(\omega)\tau', \tag{4.4}$$

where n is the index of refraction. This means that the transition rate or strength is effectively enhanced by the dielectric medium which is advantageous for fluorescence detection.

Another effect is superradiance. As the ^{229}Th density in the $LiSrAlF_6$ crystals can be rather large, we can expect that the number of ^{229}Th nuclei in a volume defined by λ_o^3 to be greater than 250. In this regime, the fluorescence pattern of the decay from the excited level can be irregular [Dic54]. But as the transition is broadened by 10 kHz [RSD10b], we can expect an effective reduction in this number by a factor of $\frac{n^3(\omega_o)\tau}{\Gamma_B}$ which can extinguish the effect. Additionally, superradiance has shown to favor enhanced optical effects in a direction parallel to the excitation source which does not affect our perpendicular detection scheme.

We should also consider the effects of radiation trapping. In this phenomenon, light that is emitted by one species in a medium can be absorbed by another. If this process occurs

repeatedly, it can be thought of as a "trapping" effect. We will need to consider the two level optical system analog of Beer's law:

$$\frac{dI}{dz} = -\kappa(\omega)I(\omega) = -(N_1 - \frac{g_1}{g_2}N_2)\sigma(\omega)I(\omega). \tag{4.5}$$

In this equation, I is the intensity of the excitation source and z the direction of propagation into a medium of absorbers. We can once again utilize the weak excitation limit as the ^{229}Th density is so high. We can express this equation a bit differently:

$$\begin{gathered} \frac{dI}{I} = -\kappa(\omega)dz \\ \text{with} \\ \kappa(\omega) = \mathrm{n}_{Th}\sigma(\omega). \end{gathered} \tag{4.6}$$

The solution of this should be familiar with κ^{-1} being a measure of the absorption length into the medium. n_{Th} is the ^{229}Th nuclei density in the crystal and $\sigma(\omega)$ is the optical cross section due to the naturally broadened linewidth only. We will need to consider the effects of the inhomogenously broadened linewidth (Γ_B) due to the crystal field. We can assume a Gaussian form for the density of modes distribution within the crystal centered about the true transition frequency:

$$\eta(\omega, \omega_o) = \frac{2}{\Gamma_B}\sqrt{\frac{ln2}{\pi}}\exp\big\{-4ln2\frac{(\omega-\omega_o)^2}{\Gamma_B^2}\big\}. \tag{4.7}$$

We will need to consider the convolution of $\sigma(\omega, \omega')$, which is the absorption cross section for individual nuclei at a particular site with center frequency ω', and $\eta(\omega, \omega_o)$. κ can then be expressed as:

$$\kappa = \int \mathrm{n}_{Th}\sigma(\omega, \omega')\eta(\omega, \omega_o)d\omega. \tag{4.8}$$

As the natural linewidth should be orders of magnitude lower than that of the broadened, we can express $\sigma(\omega, \omega')$ with a Dirac delta function instead of a Lorentzian lineshape. And this can be easily solved to yield an expression for the absorption length in the crystal as a function of the vacuum lifetime τ:

$$L_{res} = \left(\mathrm{n}_{Th}\frac{n^3(\omega)}{\Gamma_B\tau}\frac{\lambda_o^2}{3}\sqrt{\frac{ln2}{\pi}}\right)^{-1}. \tag{4.9}$$

We see that radiation trapping has a larger effect if the transition lifetime is short. Shorter ^{229}Th lifetimes will cause photons to be absorbed more readily in the crystal which reduces the effective length of the crystal from which we can expect fluorescence photons. As our crystal length is on the order of 10 mm with the photomultiplier photocathodes aligned with respect to the center of the crystal, this does hurt the solid angle collection efficiency. But it has been shown through analytical models as well as with Monte Carlo simulations, through successive absorption and emission processes, that we still have sensitivity to relatively short lifetimes. Figure. 4.7 and Figure. 4.8 show the results of the Monte carlo simulations compared to the analytical model that does not take radiation trapping into account. It is clear that this only affects fluorescence detection at shorter lifetimes, which is not expected from the decay of the low-lying isomeric level in ^{229}Th.

4.4.2 Parameter Estimation: Maximum Likelihood Method and Chi-Squared Statistics

With no clear indication of fluorescence decay, we look to establish bounds on the transition lifetime as a function of the excitation energy. Figure 4.9 shows representative data taken at the ALS. As we have characterized the conditions of the experiment such as photon flux and light collection efficiencies, we can begin to make predictions on what kind of signal to expect for a given transition lifetime. At a particular excitation energy, if the measured signal is inconsistent with an analytical model described by a particular lifetime, then we can claim that the transition cannot have such a lifetime at the given excitation energy. And this provides us with a means of defining an exclusion region, which will be outlined shortly. But the general procedure will involve estimating the parameters, such as the lifetime, that our theoretical model is dependent upon; and then determining confidence intervals for the parameters. We begin by breaking up the data into separate time bins as can be seen in Figure 4.9. The actual data is then compared to the analytical model as described earlier. Along with the experimental conditions corresponding to the given data, assuming a fixed lifetime for the transition will then determine the number of counts expected in each of these bins according to Eq. (4.3). The number of counts in each bin can be considered a random

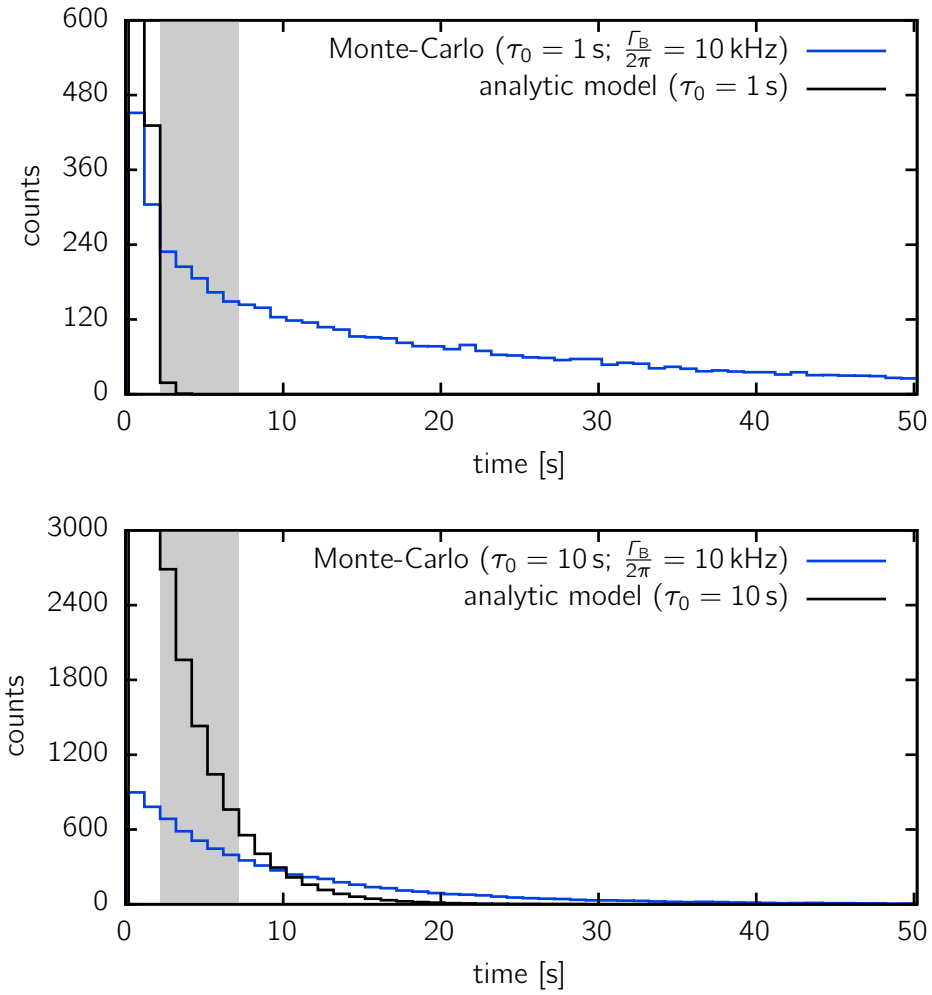

Figure 4.7: Optical trapping in the short lifetime limit. A broadening of 10 kHz is considered. Monte carlo simulations are compared to an analytical model. It is evident that the model and simulations differ.

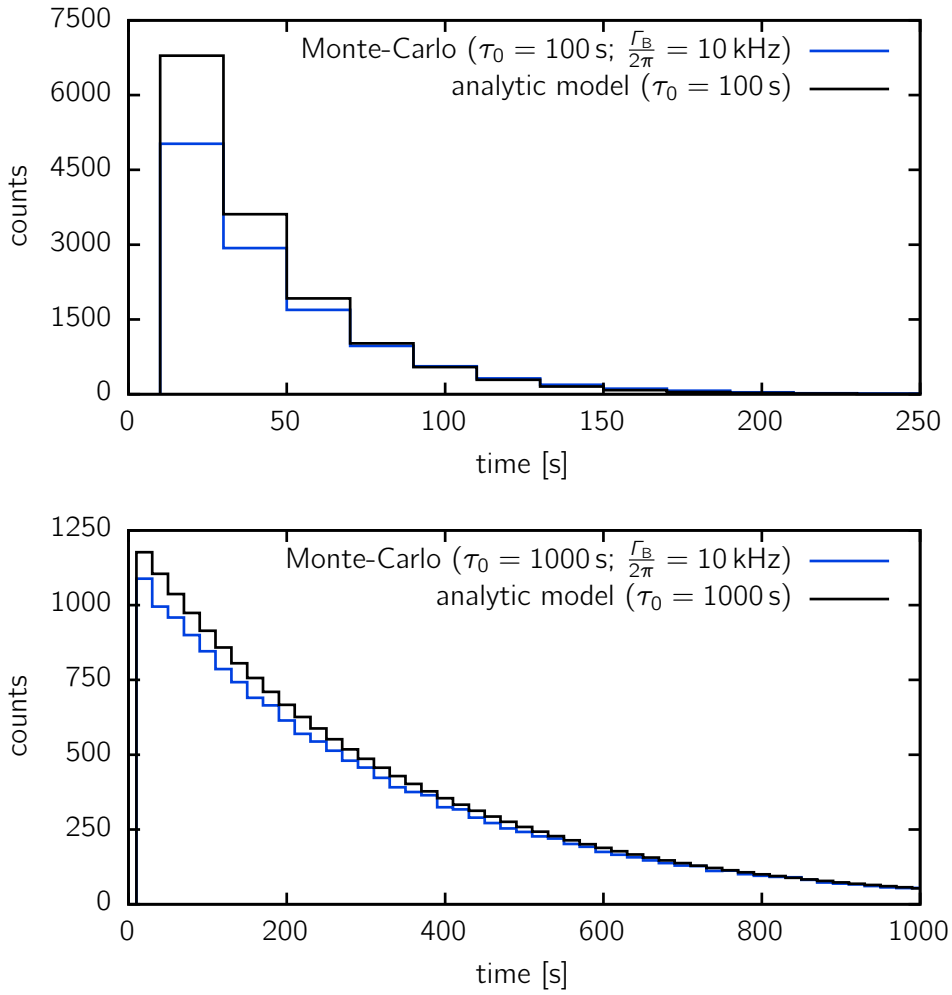

Figure 4.8: Optical trapping in the long lifetime limit. A broadening of 10 kHz is considered. Monte carlo simulations are compared to an analytical model. The model and simulations yield similar results.

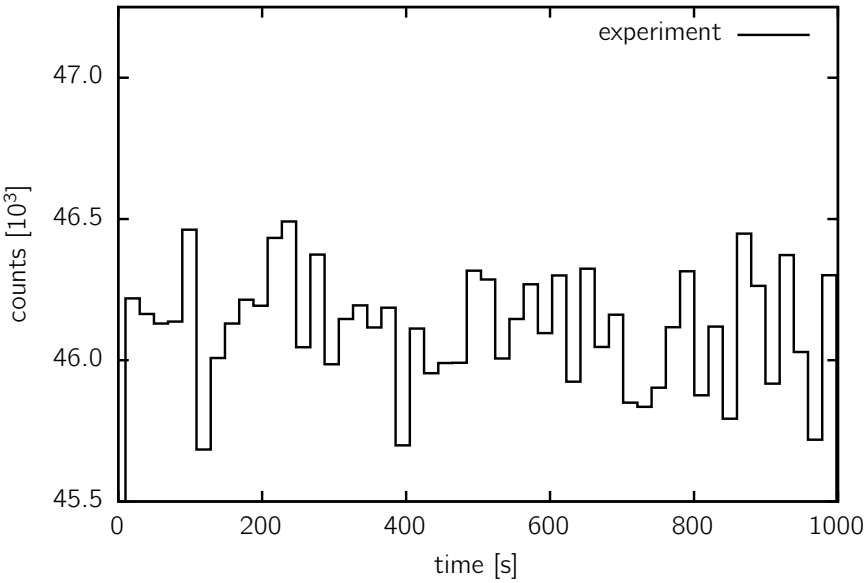

Figure 4.9: ALS data. The counts are grouped into time bins with a width of 20 seconds. This is representative of all the data taken at the ALS.

variable. In general, the counts in any arbitrary time bin (denoted by $\imath$) can be described by a Poissonian distribution.

$$f(\mathrm{k}_i) = \exp(-\mu_i)\frac{\mu_i^{\mathrm{k}_i}}{\mathrm{k}_i!} \tag{4.10}$$

In this equation, $f(\mathrm{k}_i)$ represents the probability of measuring k_i events in time bin $\imath$, or equivalently the probability distribution function for the outcome of a single arbitrary bin. And μ_i represents the actual number of events that can be expected in that time bin according to the model and the true lifetime of the transition. As we do not know the true lifetime, our goal is to estimate it or put bounds on it, according to the data and given the experimental conditions. To achieve this, we will look to methods of parameter estimation, and in particular, the method of Maximum Likelihood.

We have defined the number of counts in any particular time bin (k_i) as a random variable. And the probability to measure k_i is $\mathrm{P}(\mathrm{k}_i)$ with μ_i determined in each bin according to the lifetime of the transition and experimental conditions. For a given data set, the experimental conditions are known, and therefore μ_i is a function of the lifetime of the transition only. Actually, when considering the longer lifetime limits of the transition in

^{229}Th, the background can also be a parameter. So in general $\mu_i = \mu_i(\Gamma, b)$, where Γ is the transition strength (or inverse of the lifetime τ), and b represents the background counts. As our background is considerable due to a Cherenkov spectrum and radiation induced scintillation, the Poisson probability distribution describing the number of expected counts in a time bin can be approximated with a Gaussian distribution. In this limit, the random variable k_i can be replaced with the random variable x_i, and the probability distribution describing the counts in time bin i becomes:

$$f(\mathrm{x}_i) = \frac{1}{\sqrt{2\pi\sigma_i^2}} \exp - \frac{(x_i - \mu_i)^2}{2\sigma_i^2}, \tag{4.11}$$

where σ_i is the variance which is given by $\sqrt{\mu_i}$ for a Poissonian process. With the probability of a particular measurement x_i in the arbitrary bin i defined, we can go ahead and define the joint probability of obtaining the whole measurement. Let $f(x_i; \boldsymbol{\theta})$ represent the same probability distribution function (p.d.f) for the outcome of a single arbitrary bin as defined previously but with $\boldsymbol{\theta}$ representing all of the parameters involved in the model. The joint p.d.f. ($F(\mathrm{X})$) can be written as:

$$\begin{gathered} F(\mathrm{X}) = \prod_{i=1}^{n} f(x_i; \boldsymbol{\theta}) \\ \text{with} \\ \boldsymbol{\theta} = (\Gamma, b) \end{gathered} \tag{4.12}$$

which represents the probability of obtaining a set of counts per bin (x_i) comprising the complete measurement (X). This joint p.d.f. can be interpreted as a measure of the parameters which we wish to estimate. If the model and parameters are consistent with the experimental data, one can expect a larger value for the joint p.d.f. This joint p.d.f. is also known as the Likelihood function $L(\boldsymbol{\theta})$:

$$L(\boldsymbol{\theta}) = \prod_{i=1}^{n} f(x_i; \boldsymbol{\theta}). \tag{4.13}$$

In the function $L(\boldsymbol{\theta})$, the x_i's are fixed after the experiment has been conducted. The maximum value of the Likelihood function corresponds to parameters which lead to the least discrepancy between the theoretical model and the data. These maximizing parameter

values are known as the Maximum Likelihood (ML) estimators. They can be found by optimizing the Likelihood function with respect to the parameters.

$$\frac{\partial L}{\partial \theta_i} = 0, \quad \text{for} \quad i = 1, 2, 3... \tag{4.14}$$

Let us look more carefully at the Likelihood function as applied to our experiment.

$$L(\boldsymbol{\theta}) = \prod_{i=1}^{n} \frac{1}{\sqrt{2\pi\sigma_i^2}} \exp - \frac{(x_i - \mu(t, \Gamma, b))^2}{2\sigma_i^2}. \tag{4.15}$$

In this, we have re-written μ_i as $\mu(t, \Gamma, b)$ to reflect that the counts in each bin are also dependent on the time in which the bin is centered. The counts in each bin actually depend on the bin width as well as any possible time delay between illumination and collection. For now we omit to write down these factors, and additionally all of these extra variables are fixed and typically held constant throughout the experiment. And so the lifetime and background, which we wish to estimate or bound, are the only remaining parameterizing variables. And in general, along with the statistical error, the variances (σ_i^2) can also contain a component due to systematic errors such that:

$$\sigma^2_{i,\text{total}} = \sigma^2_{i,\text{statistical}} + \sigma^2_{i,\text{systematic}}. \tag{4.16}$$

In the expression for $L(\boldsymbol{\theta})$, the variances are considered to be known or should be possible to calculate. It is only the parameters of the modeling function and their variances which we wish to estimate. An analytical determination of the estimators for the lifetime (Γ) and the background (b) will be a little complicated given the form of our Likelihood function. Sometimes the log of the Likelihood function can simplify matters.

$$\log L(\boldsymbol{\theta}) = \sum_{i=1}^{n} \log(\frac{1}{\sqrt{2\pi}}) + \log(\frac{1}{2\sigma_i^2}) - \frac{(x_i - \mu(t, \Gamma, b))^2}{2\sigma_i^2} \tag{4.17}$$

The log of the Likelihood function will have the same maximum as the original function, and this will occur when the parameters are given by the ML estimators $\hat{\boldsymbol{\theta}}$. There are some p.d.f.'s in general for which the estimators can be solved for analytically. And in other cases, there are other methods available to estimate them. And of course, the solutions can be determined numerically.

For the Likelihood function as described under the context of our experiment, we are assuming that the μ is described by a particular number of parameters (call it m for now) which can contain the "true" values or the ones we wish to estimate. We can call this the test hypothesis or HT with a corresponding Likelihood function L_{HT}. Now consider another Likelihood function, but this time utilizing a maximum of n parameters such that the $(x_i - \mu_i)$'s are zero. Lets call this the saturated hypothesis (HS) with L_{HS} given by:

$$L_{HS} = \prod_{i=1}^{n} \frac{1}{\sqrt{2\pi\sigma_i^2}}. \tag{4.18}$$

The errors or variances given in HT are the same as in HS, since in our case, we are considering the same time bins whose total counts will be the same in both hypotheses. Now consider the log of the ratio of L_{HT} to L_{HS}, which we will call the Likelihood ratio (Λ). It can be recognized that the remaining term in the expression is just proportional to the chi-squared test statistic.

$$\log(\frac{L_{HT}}{L_{HS}}) = \log(\Lambda) = \sum_{i=1}^{n} -\frac{(x_i - \mu_i)^2}{2\sigma_i^2}$$

$$\text{and} \tag{4.19}$$

$$\chi^2 = -2\log(\Lambda) = \sum_{i=1}^{n} \frac{(x_i - \mu_i)^2}{\sigma_i^2}$$

Wilks' theorem states that if the measurement is repeated under similar conditions, even for non-Gaussian measurement uncertainties, the p.d.f. for $-2\log(\Lambda)$ will have a chi-squared distribution with the degrees of freedom being the difference in the number of free parameters between HS and HT; if the modeling function $\mu(t, \Gamma, b)$ is appropriate, and if certain conditions apply. For the test hypothesis, the number of free parameters is given by m in general; and as for the saturated hypothesis, the number of free parameters is n since the maximal number is utilized. This yields a chi-squared distribution with n-m degrees of freedom. If we compare the expression for $-2\log(\Lambda)$ to $\log L(\boldsymbol{\theta})$, the only difference is that the summation contains terms not dependent on the data and of course the remaining term has an opposite sign. As the extra terms do not depend on the measurements, they will have no effect on optimizing the parameters. Additionally, it is just an overall additive factor. The overall sign change means that instead of maximizing the log of the Likelihood function

to obtain the estimators, we can instead minimize $-2\log(\Lambda)$, which is just the chi-squared statistic with known degrees of freedom and therefore a known distribution.

For cases in which the counts in each bin are Poissonian distributed, and where we only consider the statistical error, $\sigma_i^2 = \mu_i$, the expected counts in each bin, chi-squared becomes:

$$\chi^2 = \sum_{i=1}^{n} \frac{(x_i - \mu_i)^2}{\mu_i}. \tag{4.20}$$

In this form, the χ^2 value can also be interpreted as a measure of the level of agreement between observations(x_i's) and a hypothesis or model(μ_i's). This is known as Pearson's chi-squared statistic and is one of the most commonly used goodness of fit tests. This test, and others, can be used to test whether a model is acceptable or not. The chi-squared values, in the limit of large data, will have a chi-squared distribution with degrees of freedom given by the number of bins subtracted by the number of free parameters. And this will be true regardless of the distribution of the μ_i's but does require that the x_i's are at least approximately Gaussian distributed, that is if the measurements are repeated many times. And this is true by the central limit theorem. Often p-values are associated to these goodness-of-fit tests and used to determine whether to accept or reject some hypothesis or model. Another test statistic that can be considered is the reduced chi-squared statistic, given by:

$$\begin{gathered} \chi^2_\nu = \frac{\chi^2}{\nu} \\ \text{with} \\ \nu = n - m, \end{gathered} \tag{4.21}$$

where the degrees of freedom is given by ν. A value of the reduced chi-squared statistic of $\sim$1 is typical of good agreement between the model and measurements. Values of the reduced chi-squared statistic that are much greater than 1 signify that the errors in the model are underestimated. And χ^2_ν values much less than 1 signify that errors in the model are overestimated or that noise is not appropriately accounted for by the model. When considering our model and some particular data, we typically see values close to unity for χ^2_ν when the parameters are $\sim \hat{\boldsymbol{\theta}}$. Before continuing on to estimate the variances of the estimators, it is assuring to know that model is reasonable according to this statistic.

To determine the variances of the estimators, we will look again at the log of the Likelihood function. This function can be expanded about its minimum $\hat{\theta}$, this time just considered to be a single parameter. If similar measurements are repeated and tested against the same model, the distribution of $\hat{\theta}$ generated by all of the experiments should be at least approximately Gaussian distributed, just as the individual x_i's will be in repeated measurements. The log of the Likelihood function can be expanded about its maximum value, given by the estimators. We will refer to the variance of the estimator as $\hat{\sigma}_{\hat{\theta}}$.

$$\log L(\theta) = \log L(\hat{\theta}) + (\frac{\partial \log L}{\partial \theta})\Big|_{\hat{\theta}}(\theta - \hat{\theta}) + \frac{1}{2!}\frac{\partial^2 \log L}{\partial \theta^2}\Big|_{\hat{\theta}}(\theta - \hat{\theta})^2 + ...$$

$$\text{with}$$

$$(\frac{\partial \log L}{\partial \theta})\Big|_{\hat{\theta}} = 0$$

$$\text{and} \tag{4.22}$$

$$(\frac{\partial^2 \log L}{\partial \theta^2})\Big|_{\hat{\theta}} = -\frac{1}{\hat{\sigma}^2_{\hat{\theta}}}$$

$$\rightarrow$$

$$\log L(\theta) \approx \log L_{max} - \frac{(\theta - \hat{\theta})^2}{2\hat{\sigma}^2_{\hat{\theta}}}$$

The first and second partial derivatives can be easily solved from Eq. (4.17). And just as a note, since $\mu = \mu(\theta)$:

$$\frac{\partial}{\partial \theta} = \frac{\partial \mu}{\partial \theta}\frac{\partial}{\partial \mu}$$

$$\text{and} \tag{4.23}$$

$$\frac{\partial^2}{\partial \theta^2} = \frac{\partial^2 \mu}{\partial \theta^2}\frac{\partial}{\partial \mu} + (\frac{\partial \mu}{\partial \theta})^2\frac{\partial^2}{\partial \mu^2}.$$

The 1st and 2nd derivatives of μ with respect to theta need not to vanish or have any other constraint. Its actually the derivatives of the log of the Likelihood function with respect to μ evaluated at the estimator values that yield the results in Eq. (4.22). If we evaluate the last expression in the same equation for $\theta = \hat{\theta} \pm \hat{\sigma}_{\hat{\theta}}$, then this yields:

$$\log L(\hat{\theta} \pm \hat{\sigma}_{\hat{\theta}}) \approx \log L_{max} - \frac{1}{2} \tag{4.24}$$

This means that when the parameter is shifted from the estimator value by an amount equal to its standard deviation (or variance), the log of the Likelihood function will have decreased

by 1/2. This is excellent because it provides a way of approximating the variance of the estimator by looking at the behavior of the log of the Likelihood function near its maximum. It can be very beneficial to cast this in terms of chi-squared. To do that we can once again consider that minimizing the quantity $-2\log(\frac{L_{HT}}{L_{HS}}) = \chi^2$ will yield the same estimator as maximizing the log of the Likelihood function. And according to equation. (4.17), these quantities will have the same functional form only shifted and inverted such that they yield the same variance on the estimator. So instead of expanding $\log L_{HT}$, which has the free parameter, we will expand $-2\log(\frac{L_{HT}}{L_{HS}})$ about the estimator. There are some subtle differences in the expansion and those are outlined in the following:

$$
\begin{gathered}
-2\log(\frac{L_{HT}}{L_{HS}}) \approx \chi^2_{min} + (\frac{\partial\chi^2}{\partial\theta})\Big|_{\hat{\theta}}(\theta-\hat{\theta}) + \frac{1}{2!}\frac{\partial^2\chi^2}{\partial\theta^2}\Big|_{\hat{\theta}}(\theta-\hat{\theta})^2 \\
\text{with} \\
(\frac{\partial\chi^2}{\partial\theta})\Big|_{\hat{\theta}} = 0 \\
\text{and} \\
(\frac{\partial^2\chi^2}{\partial\theta^2})\Big|_{\hat{\theta}} = \frac{1}{\hat{\sigma}^2_{\hat{\theta}}} \\
\rightarrow \\
\chi^2(\theta) \approx \chi^2_{max} + \frac{(\theta-\hat{\theta})^2}{\hat{\sigma}^2_{\hat{\theta}}}
\end{gathered}
\tag{4.25}
$$

For $\theta = \hat{\theta} \pm \hat{\sigma}_{\hat{\theta}}$, this yields:

$$
\chi^2(\hat{\theta} \pm \hat{\sigma}_{\hat{\theta}}) \approx \chi^2_{min} + 1. \tag{4.26}
$$

And there it is. Minimizing χ^2 yields the estimator, and where the quantity deviates from the minimal value by 1, signifies the 1 standard deviation bounds on the parameter. And this can be used to define confidence intervals (CI) on the parameter which we are trying to estimate, which is the lifetime of the transition in our case. Instead of using $\pm 1\hat{\sigma}_{\hat{\theta}}$ for the CI, any value can be used to report an estimation of the parameter with the desired level of confidence. The actual meaning of such a CI is that, if the experiment is to be repeated many times, you can expect that the true value of the parameter ($\bar{\theta}$) will be contained in your CI a fraction of the time determined by the confidence level. In the case of a single

experiment, a Gaussian is formed centered around the estimated $\hat{\theta}$ which may contain the true value $\bar{\theta}$.

We mentioned before that the chi-squared distribution resulting from $-2\log(\Lambda)$ will have degrees of freedom equal to the number of bins minus the number of free parameters. Now consider subtracting χ^2_{min} from both sides of the above equation. Recall that χ^2_{min} is the value of chi-squared evaluated with the estimators. This can also be written as a ratio of the log of Likelihood functions. Let H1 represent another hypothesis in which there is still the same number of bins, but the parameters are fixed to the values of the estimators.

$$\begin{gathered}
\chi^2(\hat{\theta} \pm \hat{\sigma}_{\hat{\theta}}) - \chi^2_{min} = 1 \\
\text{but} \\
\chi^2_{min} = -2\log\left(\frac{L_{H1}}{L_{HS}}\right) \\
\text{so} \\
\chi^2(\hat{\theta} \pm \hat{\sigma}_{\hat{\theta}}) - \chi^2_{min} = -2\log\left(\frac{(\frac{L_{HT}}{L_{HS}})}{(\frac{L_{H1}}{L_{HS}})}\right) \\
\text{yielding} \\
\chi^2(\hat{\theta} \pm \hat{\sigma}_{\hat{\theta}}) - \chi^2_{min} = -2\log\left(\frac{L_{HT}}{L_{H1}}\right).
\end{gathered} \tag{4.27}$$

The resulting chi-squared distribution, which is really just the difference between two different chi-squared distributions, will have degrees of freedom given by (n) - (n-m), which is just the number of parameters which we are trying to estimate. Lets call this quantity $\Delta\chi^2$. We will refer to it later.

This case was done for a single parameter. We will need to consider the case of multiple parameters so that it can be generally applied to our experiment to consider the lifetime and background. We will also need to consider the form of the log of the Likelihood function. We can make use of the fact that the joint p.d.f. for the estimators can be represented by a multidimensional Gaussian, as can be expected if the experiment is repeated many times. In general, $\hat{\boldsymbol{\theta}}$ is a vector of parameters. Let us define the quantity $\boldsymbol{Q}$ such that:

$$Q(\hat{\boldsymbol{\theta}}, \bar{\boldsymbol{\theta}}) = (\hat{\boldsymbol{\theta}} - \bar{\boldsymbol{\theta}})^T V^{-1} (\hat{\boldsymbol{\theta}} - \bar{\boldsymbol{\theta}}). \tag{4.28}$$

In this equation, $\hat{\boldsymbol{\theta}}$ represent the estimators obtained from repeated experiments and $\bar{\boldsymbol{\theta}}$ represent the true values which we are trying to estimate. V^{-1} is the inverse of the covariance error matrix whose components are given by:

$$V_{i,j} = E\big[(\theta_i - \bar{\theta}_i)(\theta_j - \bar{\theta}_j)\big] = E[\theta_i\theta_j] - \bar{\theta}_i\bar{\theta}_j, \tag{4.29}$$

with $E[]$ representing the expectation values of the respective quantities and $\imath$ and $\jmath$ represent the rows and columns of the matrix containing the different parameters. For m parameters, this will be an m by m matrix. The joint p.d.f. of the parameters can then be expressed as:

$$g(\hat{\boldsymbol{\theta}}|\bar{\boldsymbol{\theta}}) = \frac{1}{(2\pi)^{\frac{m}{2}}\left|V\right|^{\frac{1}{2}}}\exp(-\frac{1}{2}Q(\hat{\boldsymbol{\theta}},\bar{\boldsymbol{\theta}})). \tag{4.30}$$

This is a multi-dimensional Gaussian centered around the true values which we are trying to estimate. This allows the log of the Likelihood function to be expressed as:

$$\begin{gathered}\log L(\boldsymbol{\theta}) = \log(L_{max}) - \frac{Q_\gamma}{2} \\ \text{with} \\ Q_\gamma = F^{-1}(1-\gamma;q).\end{gathered} \tag{4.31}$$

F^{-1} is the inverse of a chi-squared distribution with q degrees of freedom and Q_γ is the quantile of order $(1-\gamma)$. The same statement can be expressed as:

$$\int_0^{Q_\gamma} f(z,q) = 1-\gamma, \tag{4.32}$$

where $f(z,q)$ is the chi-squared distribution with q degrees of freedom, the confidence level is given by $(1-\gamma)$. We can recast the log of the Likelihood function into an expression involving chi-squared by once again considering the ratio of the log of the Likelihood functions for the test and saturated hypothesis. An extra factor of -2 will then yield the following expressions:

$$\begin{gathered}\chi^2 = \chi^2_{min} + Q_\gamma \\ \text{or} \\ \Delta\chi^2 = Q_\gamma.\end{gathered} \tag{4.33}$$

The last expression above results from subtracting χ^2_{min} from both sides. The resulting $\Delta\chi^2$ statistic has degrees of freedom given by the number of parameters which we are trying

to estimate, or similarly, the number of parameters in our model. For a given confidence level of $(1-\gamma)$ and q degrees of freedom, Q_γ can be determined from standard tables. And there it is for the general case. Under the assumptions discussed, χ^2 can be written down and minimized with respect to the parameters to obtain their estimators. By examining the resulting χ^2 function near its minimum and generating a hyper-ellipsoid contour at the appropriate confidence level, a confidence interval can be constructed which can contain the true values of the parameters. For the case of two parameters, the contour of equal $\Delta\chi^2$ at the appropriate confidence level will create an ellipse centered around the estimator values.

4.4.3 The Exclusion Bounds

Using the methods described in the last section, we can determine the estimators for the parameters in our model, and we can construct confidence intervals based on them. But we are not here to claim that we have clear evidence of the transition, and so we are not interested in simply reporting our value of the estimators along with some interval at the appropriate confidence level. Fig. 4.9 was pointed out earlier showing (binned) crystal fluorescence after ALS illumination at $\hbar\omega = 7.7\,\mathrm{eV}$ using configuration C2. This data is representative of all recorded data. From data such as these, we can establish both an upper lifetime exclusion bound as well as the lower lifetime exclusion bound, at each given excitation energy.

Let us first consider the case of the short lifetime exclusion bound. For this limit, the background doesn't need to be a parameter as a typical photon collection cycle following illumination of the crystal is at least 1000 seconds in duration. In considering the short lifetime limit (large Γ), the adequate collection times allow us to fix the background to levels given by data near the end of the collection cycle. By then, any signal due to a short lifetime decay should be insignificant. So in this case, our function can be appropriately modeled with just the lifetime as a parameter. And we follow the same procedure as outlined in the previous section. We obtain the estimator value for the lifetime (actually for Γ) by minimizing chi-squared using the test and saturated hypothesis. Once determined, the approximate form of χ^2 near its minimum can be examined. This reduces down to the delta chi-squared

statistic described by a chi-squared distribution with degrees of freedom given by the number of parameters in the model. And based on the level of confidence desired (%90) and the appropriate degrees of freedom (1), we can determine the appropriate confidence interval. As we are trying to define the short lifetime exclusion bound, we consider the CI for Γ and we look to the smallest value of Γ contained in the interval. This defines the short lifetime exclusion bound. Values of Γ smaller than this should yield an appreciable detected signal which our experiment would have been sensitive to. But of course if Γ continues to get significantly smaller, it will reach a point where the produced signal is comparable to the noise in our experiment. As this limit is approached, an appropriate way to define the long lifetime exclusion bound must be established.

As we are limited in beamtime at the ALS, we cannot simply collect fluorescence photons for an indefinite amount of time following an illumination cycle. For very long lifetimes of the isomeric level, we cannot know what the true background is in a limited detection window. And so μ in each bin will be a function of the transition width Γ and the background b. Although characterization of the background in terms of defining its estimator and variance is not a major concern in our experiment, we will need to let it be a varying parameter to define the appropriate longer lifetime exclusion bounds. We follow the same guidelines as described earlier. We minimize χ^2 with respect to both parameters to obtain the estimators. We examine χ^2 near its minimum and obtain an expression for a contour of $\Delta\chi^2$ according to the appropriate confidence level (%90) and degrees of freedom (1). For this analysis, the background count-rate is a nuisance parameter [MV00]. The first 10 s of each data trace are omitted to mitigate the effect of any scattered light and/or short-lived UV/VIS fluorescence. The resulting %90 contour can be seen in figure. 4.10. It is a tilted ellipsoid, but becomes deformed as the parameter values approach the sensitivity limit (longer lifetimes, smaller transition strengths). We are interested in the most conservative longer lifetime exclusion bound. As can be seen in the contour (indicated by the border to the white region), this is achieved where the background (b) is minimal and the transition strength (Γ) is the largest. And so the upper left tip of the deformed ellipsoid represents the longer lifetime exclusion bound. For each experimentally probed VUV energy, we analyze the data assuming

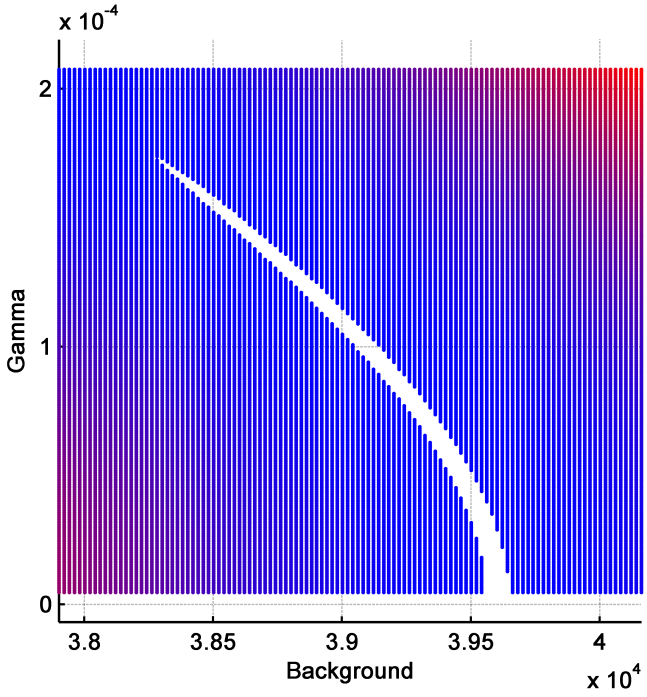

;

Figure 4.10: Delta Chi Squared contour for a particular data point. The border to the white region represents the %90 confidence level contour, for 1 degree of freedom. The upper left tip represents the longer lifetime exclusion bound for this particular excitation energy.

detunings of the ALS beam from the thorium transition by $-0.2\,\mathrm{eV}$ to $+0.2\,\mathrm{eV}$ in $0.01\,\mathrm{eV}$ steps and present the most excluding lifetime bounds as just described, both long and short, obtained from all configurations. Figure. 4.11 shows data which is plotted together with the theoretical model using the estimators (red dashed line) as well as Γ and b determined from the %90 confidence level contour (solid blue line) for the longer lifetime limit.

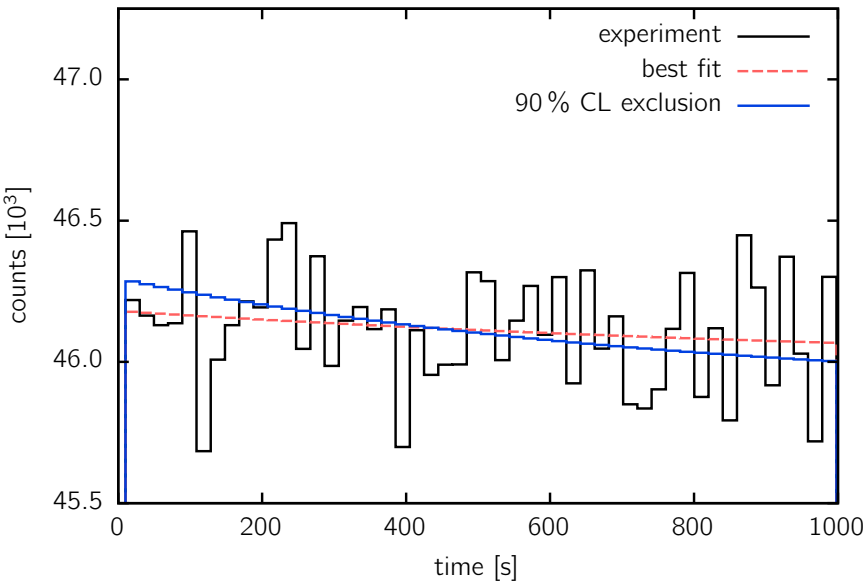

Figure 4.11: ALS data w/ exclusion. The red dashed line represents the best fit solution, or estimators, for the longer lifetime bound. And the blue dashed line represents the %90 CL longer lifetime exclusion bound.

The range of lifetimes in between the short and long lifetime exclusion bounds defines the exclusion region at a particular excitation energy. Since this data is recorded in a dielectric medium with refractive index n, which varies from $1.46 \leq n \leq 1.51$ over the scanned photon energy range, the M1 transition rate is enhanced, as described earlier. Therefore, to compare our results to the expected lifetime range, we convert our lifetime exclusion bounds to vacuum lifetimes, $\tau = n^3\,\tau'$. The resulting $90\,\%$ confidence level (CL) excluded region, which comes from configurations C2a and C3a, is shown in Fig. 4.12 (red shaded area between solid red lines). These are exclusion regions obtained from all of the different excitation energies. The exclusion region includes effects resulting from the total error budget

(see Table. 4.2), the varying VUV photon flux, the discrete ALS VUV energies $\hbar\omega$ used for the scan, UV background fluctuations, and statistical fluctuations. In conclusion, barring

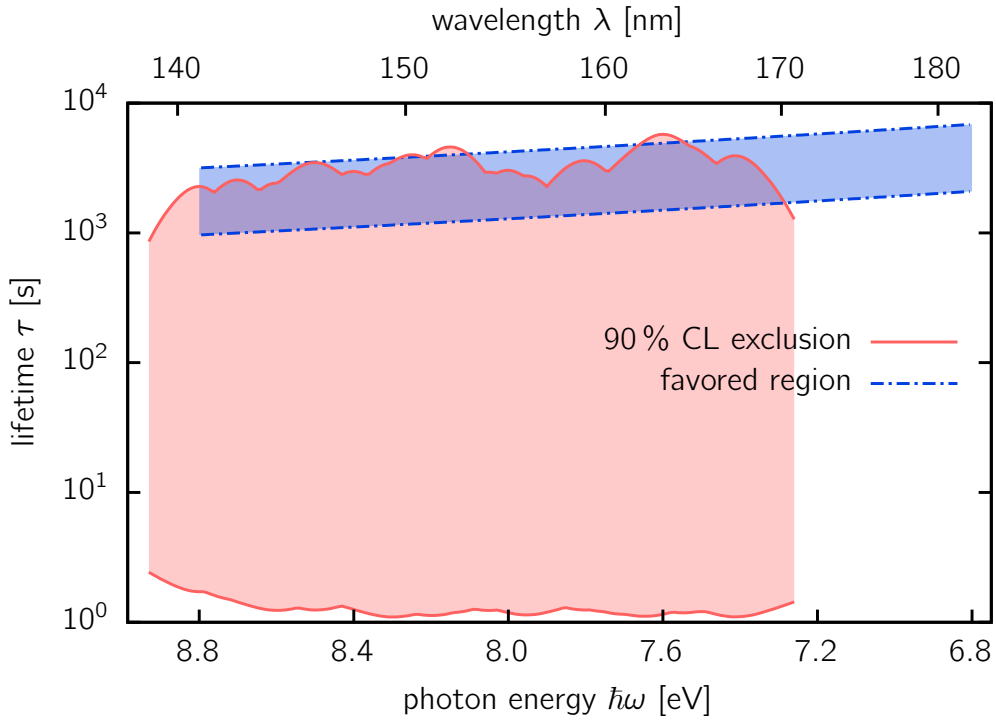

Figure 4.12: The ALS exclusion region. This is determined from all of the excitation energies. The solid red region represents the lifetimes, at the corresponding excitation energies, for which we claim the transition does not exist. The blue shaded region is the "favored region" which is the range of lifetimes that are expected for the transition, which will be described in more detail in the next chapter.

the presence of unknown systematic effects, such as an unexpected non-radiative relaxation channel or optical trapping [RDG10], the present result excludes the existence of the ^{229}Th isomeric transition with a vacuum lifetime $(1\text{–}2)\,\mathrm{s} \lesssim \tau \lesssim (2000\text{–}5600)\,\mathrm{s}$ for the energy range $\hbar\omega = (7.3\text{–}8.8)\,\mathrm{eV}$ at the 90 % CL. This experiment did not probe energies below 7.4 eV because in normal operation the ALS beamline cannot reach these energies.

We thank David DeMille for useful discussions; Bruce Rude, Kevin Wilson, Musahid Ahmed, Oleg Kostko, and Sarah Ferrell for their support at the ALS; Alyssa Ruiz and James Hefley for help with γ-ray spectroscopy; and Richard Greco, Markus Hehlen, and

Justin Torgerson for help with crystal characterization. The ALS is supported by the U.S. DOE under Contract No. DE-AC0205CH11231. This work was supported by the DARPA QuASAR program and the ARO under W911NF-11-1-0369:P00004, NIST PMG, and DOE Office of Nuclear Physics, Isotope Program. And much love to Scott Sullivan and Wade Rellergert for all of their efforts in making these results possible.

4.4.4 Feldman Cousins Prescription

And while the exclusion region determined from the procedures outlined in the previous section should be approximately accurate, more caution should be taken in general when defining confidence intervals and bounds. In general, there can be many approaches towards defining confidence intervals. One of them is the classical approach defined by Neyman which requires knowledge of the form of the p.d.f. for the estimators. The details will not be outlined here, but can be found in texts [Cow98]. For Gaussian distributed estimators, the methods of chi-squared are adequate. And we will utilize this approach.

Recently, there has been much dissatisfaction with the standard methods for constructing upper confidence limits. The issues arise when the result is an empty set or unphysical. The Feldman-Cousins prescription utilizes the freedom in Neyman's construction to obtain a unified set of confidence intervals for defining upper limits and two-sided intervals. This method involves ordering based on likelihood ratios [FC98].

Often is the case where an experiment is performed and the actual results then determine whether a central confidence interval is reported or a one sided limit. This is the classic problem of "flip-flopping" and can be avoided altogether. In cases like a Gaussian near a boundary (i.e. a null result) or zero counts in a Poissonian process when a background is present, care should be taken in defining the confidence interval. In cases like these, the bounds of the confidence interval should be established in a more sophisticated way. And this can be done according to a likelihood ratio, which orders the importance of the different $\boldsymbol{\theta}$'s in a way that is different than treating them all equally.

In the Feldman Cousins prescription, points in the confidence interval are constructed by

determining how likely is that particular result relative to the most likely it could have been with a physically allowed $\boldsymbol{\theta}$. The likelihood ratio can be defined in terms of the joint p.d.f. for the measurement of X:

$$R = \frac{P(X|\boldsymbol{\theta})}{P(X|\boldsymbol{\theta}_{best})}. \tag{4.34}$$

$\boldsymbol{\theta}$ represents the complete parameter space and $\boldsymbol{\theta}_{best}$ are the particular set of parameters (which must be physically allowed) that maximize the likelihood ratio for any arbitrary $\boldsymbol{\theta}$. With the likelihood ratio R, the confidence interval is constructed in a systematic and ordered manner. The space of $\boldsymbol{\theta}$, or at least a subset of it, is ordered according to the largest R values. The CI is then simply built up according to these largest likelihood ratios until the sum of the probabilities $P(X|\boldsymbol{\theta})$ reaches the desired confidence level. This space of $\boldsymbol{\theta}$, which corresponds to the largest likelihood ratios, is the proper confidence interval.

With a given and fixed data set, the likelihood ratio is just a function of parameters. An expression for the log of the likelihood ratio is then given by:

$$\log(R) = \log\left(\frac{L(X|\boldsymbol{\theta})}{L(X|\boldsymbol{\theta}_{best})}\right). \tag{4.35}$$

Multiplication by a factor of -2 yields the delta chi-squared distribution:

$$\Delta\chi^2 = -2\log(R). \tag{4.36}$$

And this results in a distribution with the degrees of freedom given by the number of free parameters. Instead of filling out the confidence interval according to parameters with the largest R values, we can fill out the interval according to minimum delta chi-squared values. In practice, this would be done such that $\sum P(X|\boldsymbol{\theta})$ covers the appropriate confidence level. For a multi-parameter model with non-discrete parameters, an integral must be performed to fill out the probabilities such that the confidence interval is properly constructed. Another way to do this involves utilizing Monte Carlo simulations and the delta chi-squared statistics. The idea behind this approach is to essentially simulate the likelihood ratios across the space of parameters relevant to the problem, given the analytical model and other details of the experiment. This is achieved through generating fake data for all the parameter values in the space of interest. At each particular parameter value in the space, several MC simulations

must be generated. And for each generated simulation, a delta chi-squared statistic is produced which yields a chi-squared value. With repeated simulations at a particular parameter value, a chi-squared distribution is generated. The critical chi-squared value in the distribution marks the position such that a fraction of the simulations given by the confidence level fall below this critical value. By repeating this procedure across the space of all parameters, the corresponding critical values are generated. Then by producing a delta chi-squared statistic with the actual data, across the same space of parameters, $\Delta\chi^2_{\text{data}}$ can be compared to $\Delta\chi^2_{\text{critical}}$. And comparing the values across the space of parameters, wherever the former is less than the latter signifies that the data is adequately described by the analytical model given those particular parameter values. Therefore, these particular parameter values must be included in the confidence interval.

In the context of our experiment, we do the following:

- Consider a two dimensional grid of the parameters, the transition strength (Γ) and the background (b), such that the range covered by each is adequate for our experiment.
- First generate fake data for a fixed and physically allowed (Γ, b) on the grid, according to the analytical model. Then find the estimators to this fake data, which we will call (Γ_o, b_o).
- Calculate χ^2 given this fake data and the same fixed parameters on the grid, $\chi^2(\Gamma, b)$. For the case of a nuisance parameter (b), first optimize the nuisance parameter by minimizing the chi-squared statistic involving the fake data and the fixed non-nuisance parameter (Γ) given at the position on the grid. Lets call this optimal nuisance parameter b'. Then calculate chi-squared, $\chi^2(\Gamma, b')$.
- Calculate χ^2 with the estimators for the fake data, $\chi^2(\Gamma_o, b_o)$.
- Now calculate $\Delta\chi^2$: $\Delta\chi^2 = \chi^2(\Gamma, b) - \chi^2(\Gamma_o, b_o)$. In the case of the nuisance parameter, calculate: $\Delta\chi^2 = \chi^2(\Gamma, b') - \chi^2(\Gamma_o, b_o)$.
- Do this over and over again until you build up a histogram of $\Delta\chi^2$ at (Γ, b). Then report $\Delta\chi^2_C$ which has the property that γ, the confidence level, of the 'fake experiments' had

a $\Delta\chi^2 < \Delta\chi^2_C$. In the case where we "profile" the nuisance parameter, the delta chi-squared distributions to obtain the critical values have reduced degrees of freedom.

- This process should be repeated with all the points on the grid to obtain the critical delta chi-squared value for the entire parameter space of interest. We now have $\Delta\chi^2_C(\Gamma, b)$.

- Now consider the actual experimental data. After minimizing chi-squared against the data and the analytical model to obtain the estimators, calculate $\Delta\chi^2$ everywhere on the grid. That is, calculate at each (Γ, b) the statistic: $\Delta\chi^2_{data} = \chi^2(\Gamma, b) - \chi^2(\hat{\Gamma}, \hat{b})$, where $(\hat{\Gamma}, \hat{b})$ are the estimators.

- If $\Delta\chi^2_{data}(\Gamma, b) < \Delta\chi^2_C(\Gamma, b)$ then you must accept (Γ, b) as part of your confidence interval at the γ confidence level.

Figure. 4.13 shows a sample delta chi-squared histogram created from running several Monte Carlo simulations at a particular set of parameter values. In this example, the parameter values were chosen to be near the estimators for the data. The resulting chi-squared distribution has only one degree of freedom as can be expected and the critical value is determined based on a 90% confidence level.

Figure. 4.14 shows the critical chi-squared values determined from a set of parameter values. Also depicted is the delta chi-squared values as determined from the data. Where the delta chi-squared values according to the data fall below the critical surface, defines the confidence interval as determined from FC.

It can be seen in figure. 4.15 that the critical chi-squared values are not exactly 2.71 as assumed in the previous section. There are several reason why this could be the case, but the most significant reason for this is due to the fact that we are approaching the unphysical region and the limits of our experimental sensitivity.

And finally, figure. 4.16 shows that the CI determined from FC and by the standard means described earlier do in fact agree, roughly.

We thank Robert Cousins for expert advice on data analysis.

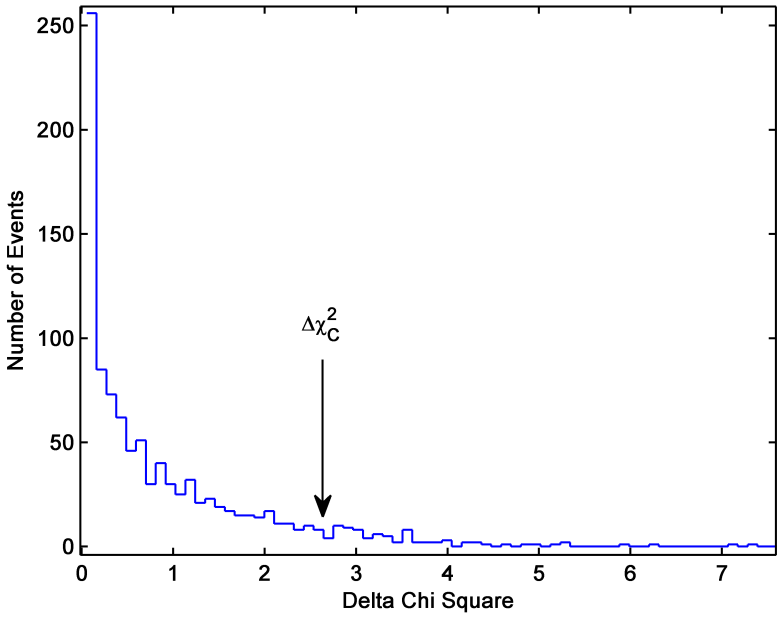

;

Figure 4.13: Delta chi-squared distribution. Monte Carlo simulations were conducted (1000 of them) at a particular set of parameter values. The delta chi-squared value is determined for each simulation and a histogram of all the resulting delta chi-squared values produces a chi-squared distribution. The position in the distribution which contains γ of the values obtained from the simulations marks the critical delta chi-squared value $\Delta\chi^2_C$.

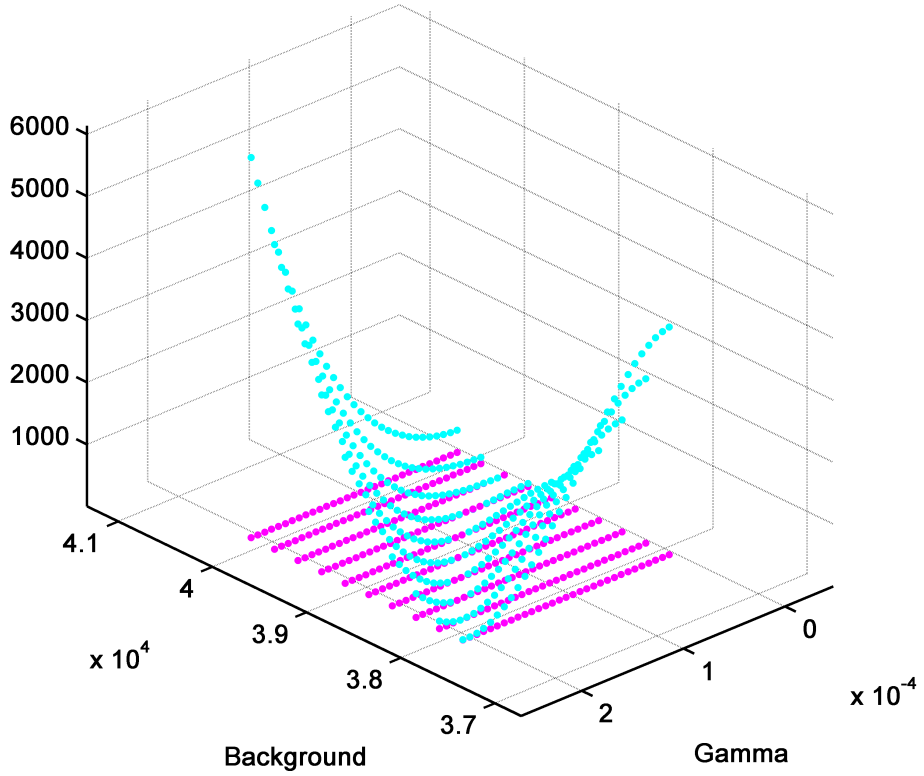

;

Figure 4.14: Delta chi-squared and delta chi-squared critical surfaces. The delta chi-squared surface obtained form the data is represented in cyan. The delta chi-squared critical surface generated from the MC simulation is represented in magenta. Where the former falls below the latter marks values of the parameters which should be included in the confidence interval.

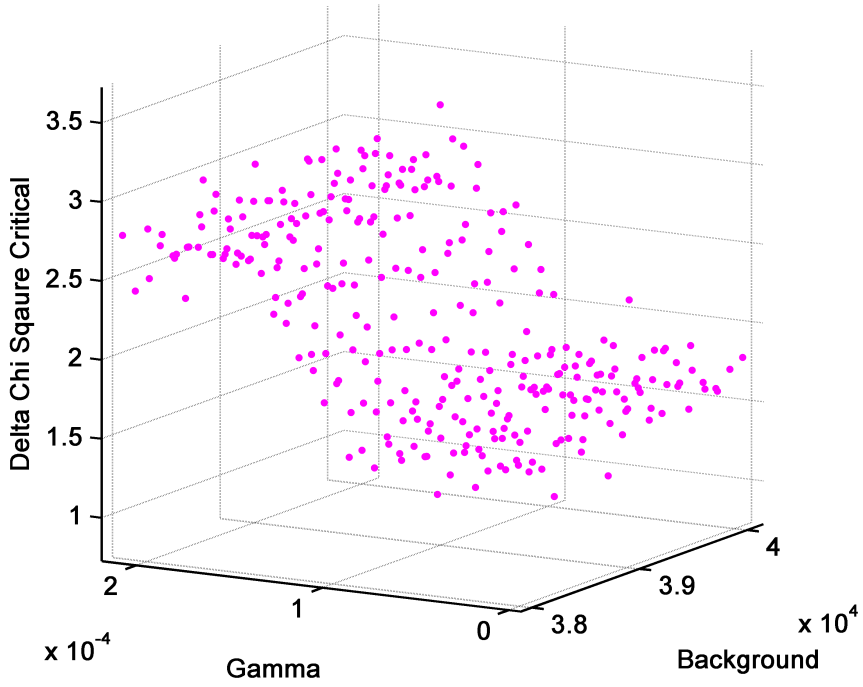

;

Figure 4.15: Delta chi-squared critical values. These are determined from 1000 MC simulations at each point on the parameter space grid. It is noticed that the critical values are not exactly 2.71 as expected for perfect chi-squared distributions. The discrepancy can be attributed to the unphysical region of the parameter space and also the limits of our experimental sensitivity.

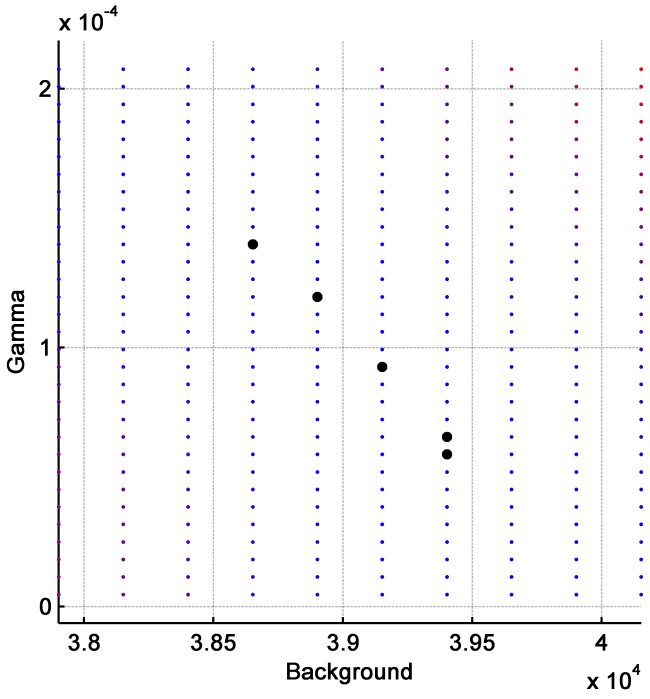

;

Figure 4.16: Feldman-Cousins solution. The border to the black circles mark the FC CI contour at %90 CL. This approximately overlaps with the standard solution obtained which is shown in Fig. 4.10.

CHAPTER 5

Aftermath of the ALS Scans

In conclusion of our ALS experiments, we claim that there was no clear evidence of a strong fluorescence signature. In any experiment searching for the nuclear energy level, two key parameters in the preparation of the experiment are the isomeric state lifetime and energy. Therefore, the aim of this chapter is to provide a critical assessment and estimation of these parameters to aid future experiments. Experimental data based on the nuclear matrix elements of transitions between states belonging to rotational bands K^{π} $[Nn_z\Lambda] = \frac{5}{2}^{+}[633]$ and $\frac{3}{2}^{+}[631]$ both in ^{229}Th only and in comparable nuclei will be analyzed. Then an estimate for the radiative lifetime of the isomeric state can be made using available experimental data for the transition rates of the interband M1 and E2 γ transitions between excited levels of the ^{229}Th nucleus. The importance of the internal conversion (IC) decay channel will be considered later in Chapter 6, but in brief, these processes will dominate the isomer radiative decay in cases where they are possible. In addition, the possible range of branching coefficients for levels in ^{229}Th will be analyzed. It will be shown how this range affects the determination of the isomeric energy in the experiments of Refs. [BBB07, BWB09], which provide the currently accepted isomeric transition energy range.

5.1 Matrix Element of the Isomeric Transition

Together with the energy of the isomeric level, the magnitude of the nuclear transition matrix element determines the half-life $T_{\frac{1}{2}}$ or the radiative lifetime τ, where $\tau = T_{\frac{1}{2}}\ln 2$, of the isomeric state. Currently, there are two possibilities for phenomenological estimation of the reduced probability for the isomeric transition, $B(M1; \frac{3}{2}^{+}\frac{3}{2}[631] \rightarrow \frac{5}{2}^{+}\frac{5}{2}[633])$. The first

possibility is to use parameters of the similar 311.9 keV transition in the spectrum of the ^{233}U nucleus. The second is to take advantage of the available experimental data for the M1 transitions between the rotational bands K^{π} $[Nn_z\Lambda] = \frac{5}{2}^+[633]$ and $\frac{3}{2}^+[631]$ in the excitation spectrum of the ^{229}Th nucleus. The first method can be motivated, because transitions $\frac{3}{2}^+\frac{3}{2}[631] \rightarrow \frac{5}{2}^+\frac{5}{2}[633]$ at 311.9 keV in the ^{233}U nucleus and 7.8 eV in the 229Th nucleus look identical in terms of the rotational model and, in that context, should have the same reduced transition probabilities.

The reduced probability of the transition in the ^{233}U nucleus is known to be $B_{W.u.}$ (M1; $\frac{3}{2}^+\frac{3}{2}[631](311.9keV) \rightarrow \frac{5}{2}^+\frac{5}{2}[633](0.0)) = [0.33 \pm 0.05 \times 10^{-2}]$ [ST05]. Here, $B_{W.u.}$ denotes a reduced probability in Weisskopf units [BW79] (see Chapter 1 for details):

$$B_{W.u.}(M1; J_i \rightarrow J_f) = \frac{B(M1; J_i \rightarrow J_f)}{B(W; M1)} \quad \text{with} \quad B_{W.u.} = \frac{45}{8\pi}\mu_N^2 \tag{5.1}$$

. $B_{W.u.}$ is the reduced probability of the nuclear M1 transition in the Weisskopf model and μ_N is the nuclear magneton. Nonetheless, the ^{233}U and ^{229}Th nuclei are different and those differences could be crucial, which becomes evident when comparing to other nuclei with similar level structure.

For example, a $\frac{3}{2}^+\frac{3}{2}[631] \rightarrow \frac{5}{2}^+\frac{5}{2}[633]$ transition with an energy of 221.4 keV also exists in the ^{231}Th nucleus [BT13]. The half-life of the $\frac{3}{2}^+\frac{3}{2}[631]$ (221.4 keV) state in ^{231}Th is less than 74 ps and only one γ transition, namely, the transition to the ground state has been observed experimentally from this level, with an internal conversion coefficient of 1.96 [BT13]. This is not surprising since according to the level scheme [BT13], the quantum numbers of states lying between the $\frac{3}{2}^+\frac{3}{2}[631]$ (221.4 keV) level and the ground state are such that the intensity of other possible transitions must be orders of magnitude smaller than the $\frac{3}{2}^+\frac{3}{2}[631](221.4$ keV$) \rightarrow \frac{5}{2}^+\frac{5}{2}[633](0.0)$ transition. Therefore, the transition directly to the ground state should give the dominant contribution to the decay of the level in the ^{231}Th nucleus, and the other decay channels cannot significantly change the lifetime of the level. Using the data from Ref. [BT13] the reduced probability of this transition in the ^{231}Th nucleus is estimated

as $B_{W.u.}(M1; 3/2^+3/2[631](221.4\text{ keV}) \rightarrow 5/2^+5/2[633](0.0)) \geq 0.93 \times 10^{-2}$. This value is at least three times larger than would have been expected estimating it from the similar transition in ^{233}U. Accordingly, interpolation from the ^{233}U nucleus to the ^{229}Th nucleus could lead to similar results. In addition, it is not obvious that measurements of the nuclear lifetimes, γ-ray intensities, the probabilities of electronic conversion, and other characteristics of this transition in the ^{233}U nucleus are more accurate than for the ^{229}Th nucleus, where measurement errors, as we shall see below, are significant.

For these reasons, we prefer to use the second approach to determine an estimate of $B(M1; 3/2^+3/2[631](7.8\text{ eV}) \rightarrow 5/2^+5/2[633](0.0))$, which relies on available experimental data for the reduced probability of the $M1$ transitions between the rotational bands $K^\pi[Nn_Z\Lambda] = 5/2^+[633]$ and $3/2^+[631]$ in the ^{229}Th nucleus and the Alaga rules. Such a calculation assumes that the adiabatic condition is fulfilled (see [DT98] for a detailed analysis of the use of the adiabatic condition). Here, we do not consider the effects of nonadiabaticity because of the relatively large uncertainties and disagreements of the experimental data (see Fig. 5.1). Further, the well-expressed rotational structure of the bands in the ^{229}Th nucleus and a number of other factors [DT98] allow us to neglect the Coriolis interaction for a preliminary estimation of the reduced probability of the isomeric transition from the experimental data for the $9/2^+5/2[633](97.14\text{ keV}) \rightarrow 7/2^+3/2[631](71.83\text{ keV})$ transition in the ^{229}Th nucleus. In this limit, we can, however, provide an estimate of the effect of the Coriolis interaction, which is quite small, on the matrix element [DT98].

Experimental data for $B(M1; 9/2^+5/2[633](97.14\text{ keV}) \rightarrow 7/2^+3/2[631](71.83\text{ keV}))$ are, to our knowledge, available from four separate experiments [BMF88,GKA02,BAB03,RPZ06]. As can be seen in Fig. 5.1, the reported values for the $M1$ transition show considerable spread. For comparison, in the case of the $E2$ transition, there is consensus between three of the measurements.

Using the Alaga rules, it is straightforward to obtain the reduced probability of the

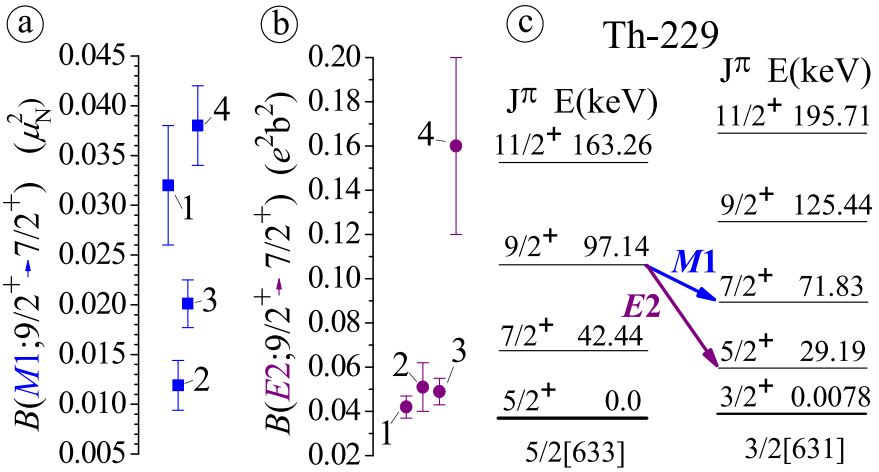

Figure 5.1: The experimental values for the reduced probability of the nuclear (a) $9/2^+(97.14$ keV$)\to 7/2^+(71.83$ keV), and (b) $9/2^+(97.14$ keV$)\to 5/2^+(29.19$ keV) transitions The relevant level scheme of the ^{229}Th nucleus is shown in part (c). Data for the transitions were taken from: 1 – [BMF88], 2 – [GKA02], 3 – [BAB03], and 4 – [RPZ06].

isomeric nuclear transition in terms of the measured $M1$ reduced probability:

$$\begin{aligned} &B(M1; 3/2^+(7.8 \text{ eV}) \to 5/2^+(0.0)) \\ &= \frac{15}{7} B(M1; 9/2^+(97.14 \text{ keV}) \to 7/2^+(71.83 \text{ keV})). \end{aligned} \tag{5.2}$$

The results of this calculation are shown in Table 5.1 for each measured value of

$$B(M1; 9/2^+5/2[633](97.14\text{keV}) \to 7/2^+3/2[631](71.83\text{keV})) \tag{5.3}$$

from Fig. 5.1(a).

Interestingly, the data of [BAB03] affords another means to obtain $B_{W.u.}(M1; 3/2^+(7.8\,\text{eV}) \to 5/2^+(0.0))$. In that work, the relative intensities of the transitions from the level $9/2^+3/2[631]$ (125.44 keV) were also measured to states $9/2^+(97.14$ keV) and $7/2^+(42.44$ keV) of the $5/2^+[633]$ rotational band. This allows us to calculate the reduced probabilities

$$B(M1; 9/2^+3/2[631](125.44 \text{ keV}) \to 9/2^+5/2[633](97.14 \text{ keV})) = (0.56 \pm 0.25) \times 10^{-2} \mu_N^2$$

and

$$B(M1; 9/2^+3/2[631](125.44 \text{ keV}) \to 7/2^+5/2[633](42.44 \text{ keV})) = (0.9 \pm 0.4) \times 10^{-3} \mu_N^2, \tag{5.4}$$

Table 5.1: Calculated reduced probabilities $B_{W.u.}(M1; 3/2^+(7.8\text{ eV}) \rightarrow 5/2^+(0.0))$ in ^{229}Th based on $B(M1; 9/2^+5/2[633](97.14\text{ keV}) \rightarrow 7/2^+3/2[631](71.83\text{ keV})$ from given references.

$B_{W.u.}$ (10^{-2})	based on
3.83 ± 0.72	Ref. [BMF88]
1.42 ± 0.30	Ref. [GKA02]
2.41 ± 0.29	Ref. [BAB03]
4.55 ± 0.48	Ref. [RPZ06]

Table 5.2: Reduced probabilities $B_{W.u.}(M1; 3/2^+3/2[631] \rightarrow 5/2^+5/2[633])$ for other nuclei or, for the case of ^{229}Th, calculated from reduced probabilities of other transitions (see text).

$B_{W.u.}$ (10^{-2})	nucleus	from/based on
0.33 ± 0.05	^{233}U	Ref. [ST05]
> 0.93	^{231}Th	Ref. [BT13]
0.74 ± 0.33	^{229}Th	Ref. [BAB03]

in the frame of the rotational model. Using the Alaga rules, we can then calculate the reduced probability of the $M1(7.8\text{ eV})$ isomeric transition. Both of the reduced probabilities give practically the same value $B_{W.u.}$ $(M1; 3/2^+(7.8\text{ eV}) \rightarrow 5/2^+(0.0)) = (0.74 \pm 0.33) \times 10^{-2}$. This result is shown in Table 5.2 along with the reduced probabilities of similar transitions in ^{233}U at 311.9 keV and ^{231}Th at 221.4 keV.

Thus, these estimates lead to a significant, more than an order of magnitude, range in the values for the reduced probability of the isomeric transition of the ^{229}Th nucleus. However, if, for the aforementioned reasons, we restrict the estimate to those values calculated from the $9/2^+5/2[633](97.14\text{ keV}) \rightarrow 7/2^+3/2[631](71.83\text{ keV})$ transitions the spread in mean values is within a factor of 3.

5.2 The Radiative Lifetime of the Isomeric Level

Currently, the generally accepted value for the energy of the isomeric state $3/2^+3/2[631]$ is 7.8 ± 0.5 eV [BBB07,BWB09]. Since the energy of the isomeric level exceeds, for example, the ionization potential of the isolated thorium atom, 6.08 eV, the radiative lifetime of the ^{229}Th isomeric state is highly dependent on the chemical environment and electronic conversion is the dominant decay channel [ST91]. It is very difficult to directly observe the transition in such environments, as both the excitation radiation is absorbed by the electrons and the energy of any conversion electron is very small (only a few electron volts), making it difficult to detect. Similarly, it is difficult to predict the lifetime of the isomeric state for thorium ions in the Th^{m+}, $m < 4$ charge state. Here, for example, the process of decay via the electronic bridge [ST91, PF10a, PF10b] can dominate, which cannot be calculated without precise knowledge of the nuclear transition energy and the wave functions of the valence electrons.

In the following, we only estimate the radiative half-life of the thorium isomeric state in the absence of any chemical effects based on the reduced probabilities discussed in the previous section. As discussed previously, we prefer the four reduced probabilities calculated from the four measurements for the $M1\ 9/2^+5/2[633](97.14\ \text{keV}) \rightarrow 7/2^+3/2[631](72.83\ \text{keV})$ transition in ^{229}Th (see Tab. 5.1), which appears most defensible, as this technique has shown to be accurate to within experimental error in cases where data exists [DT98]. Radiative half-lifes based on the reduced probabilities from other transitions in ^{229}Th or the similar transition in ^{233}U are only given for completeness (see Tab. 5.2). These results are directly applicable to trapped Th^{m+} ions with $m \geq 4$ and, with a minor modification, to Th in a large-bandgap crystal. The modification in the latter case is due to the polarization of the dielectric medium and leads to a reduction of the half-life by a factor of $1/n^3$ [RK95, Tka00], where n denotes the refractive index. The calculated half-lifes can further be used in the trapped ion approach with $m < 4$ to calculate e.g. the electron bridge process once the electronic spectra of the ions are known.

The results are shown in Fig. 5.2, first row, for $\omega = 7.8\,\text{eV}$. The range of half-lifes

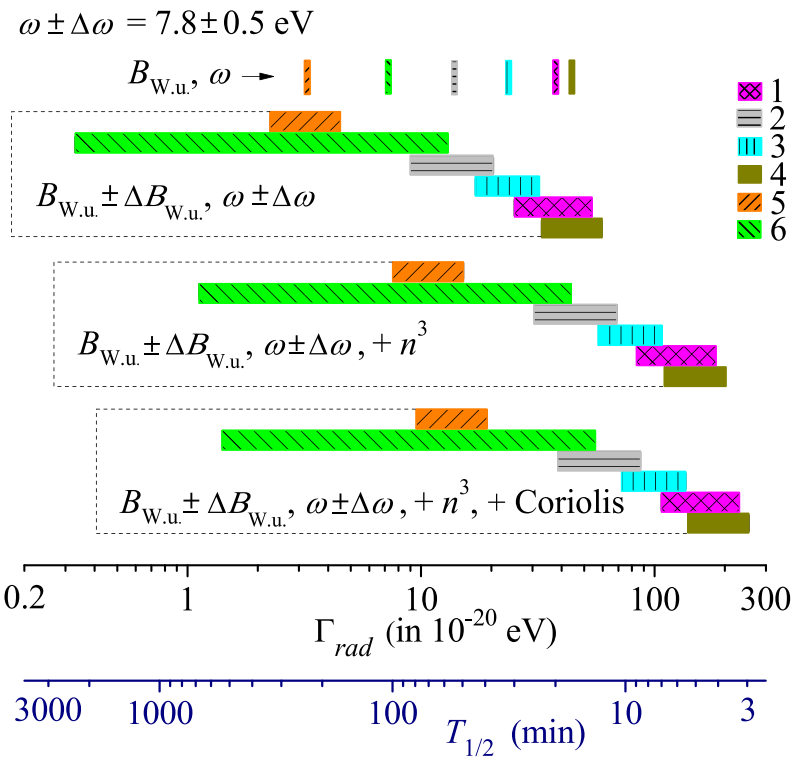

Figure 5.2: The range of possible radiative linewidths Γ_{rad} (upper scale) and half-lifes $T_{1/2}$ (lower scale) of the isomeric state $3/2^+3/2[631](7.8 \pm 0.5$ eV) in the ^{229}Th nucleus. Calculations are based on values for $B_{W.u.}(M1; 3/2^+3/2[631] \rightarrow 5/2^+5/2[633])$ from Tab. 5.1 (calculated from: 1 – [BMF88], 2 – [GKA02], 3 – [BAB03], 4 – [RPZ06]) and, for completeness, Tab. 5.2 (5 – [ST05]; 6 – [BAB03]). The refractive index $n \approx 1.5$ increases the probability of the $M1$ transition by a factor n^3 (third row). The Coriolis interaction can lead to a slight increase of the linewidth by a factor of 1.2–1.3 [DT98] (fourth row).

including one standard deviation in both the reduced probabilities and the currently accepted transition energy is given in the second row. The calculations for the case of a large-bandgap crystal with a typical refractive index $n \approx 1.5$ is shown in the third row. Lastly, the additional inclusion of the Coriolis interaction leads to only a small correction (fourth row).

Using these results, we construct a favored region for the radiative half-life as a function of the transition energy based only on the values for the reduced probabilities from Tab. 5.1, see Fig. 5.3. The center of this favored region is defined by the weighted average of the reduced probabilities. The bounds of the favored region are constructed as 1.96 standard deviations around the center of the favored region, which corresponds to roughly a 95% confidence level, however, considering that the individual reduced transition probabilities are not consistent within their errors, we increase the standard deviation by the Birge ratio of 3.4 [BE14]:

$$0.46 \times 10^6 \text{ s eV}^3/\omega^3 \leq T_{1/2} \leq 1.5 \times 10^6 \text{ s eV}^3/\omega^3.$$

Here, we did not include a crystal environment, as the inclusion of the refractive index n is straightforward. However, the small correction due to Coriolis interaction is included leading to an increase of the linewidth of the transition by a factor of 1.2–1.3 [DT98]. (These bounds are similar to those of Ref. [JSS15], but we consider them more accurate as they include e.g. the Birge ratio.)

Alternatively, a more conservative region can be constructed which is bound by the extreme values of the individual radiative lifetimes deduced from Tab. 5.1 ± 1.96 standard deviations (see Fig. 5.3). Its functional form is given as (again including correction due to Coriolis interaction, but without crystal environment):

$$0.31 \times 10^6 \text{ s eV}^3/\omega^3 \leq T_{1/2} \leq 2.1 \times 10^6 \text{ s eV}^3/\omega^3.$$

5.3 Energy of the Isomeric Level

The isomeric transition energy is equally as important as the isomeric transition radiative lifetime to current experiments. There have been several attempts [RH90, HR94, GH05]

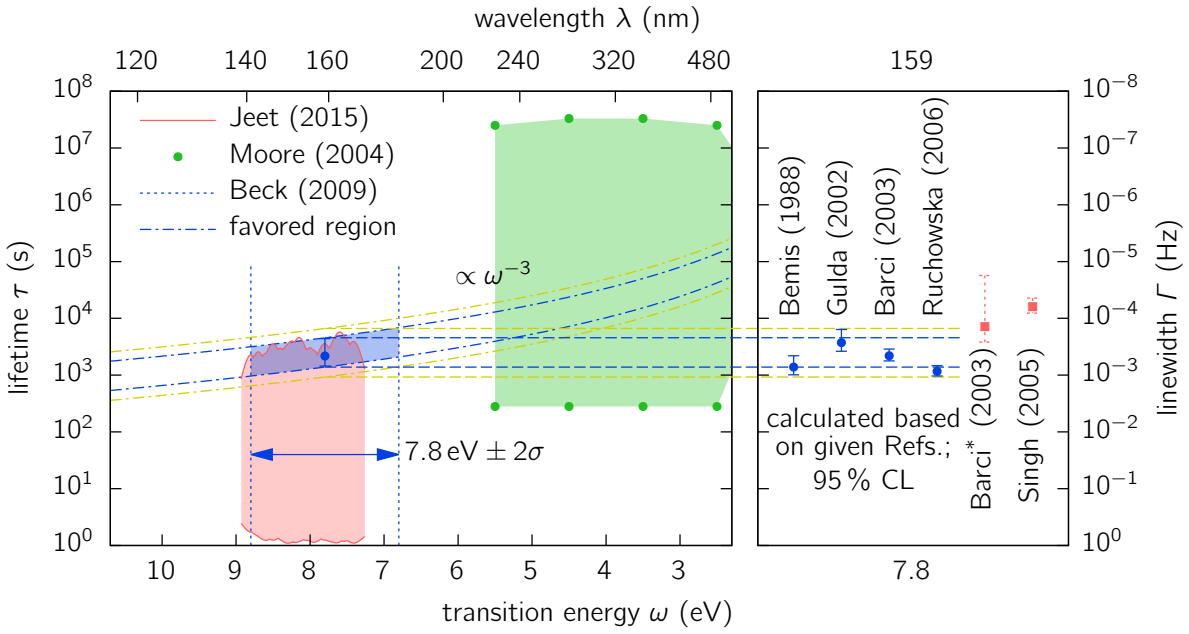

Figure 5.3: Favored region and experimentally excluded regions for the nuclear isomeric transition as a function of transition energy (wavelength) and radiative lifetime. (Left) The favored region (dash-dotted blue line; see text) and currently accepted energy of the isomeric transition (dotted blue lines) according to Ref. [BWB09] are recommended as primary region of interest for current searches (blue shaded area). Experimentally excluded areas according to Ref. [MAB04] (green shaded area between circles) and Ref. [JSS15] (red shaded area between solid red lines) exclude parts of the favored region. Also shown are the more conservative bounds (outer dash-dotted yellow lines; see text). The point at 7.8 eV (blue circle) shows exemplarily the weighted average of the radiative lifetimes from reduced transition probabilities in Tab. 5.1 with 1.96 standard deviations including a Birge ratio of 3.4. (Right) Radiative lifetimes at 7.8 eV for individual values of the reduced transition probability with 1.96 standard deviations according to Tab. 5.1 (circles, blue) and Tab. 5.2 (squares, red). (The latter are only shown for completeness and do not enter into the construction of the favored region.)

to infer the isomeric transition energy from indirect measurements of γ-ray transitions in the ^{229}Th nucleus. Though the recommended value for the isomeric transition energy has changed considerably over the last 40 years, the consensus in the field is to accept the value put forward in Ref. [BWB09] of $E_{is} = 7.8 \pm 0.5$ eV, which updates a previous measurement by the same group [BBB07] of $E_{is} = 7.6 \pm 0.5$ eV. In the following, we detail the dependence of this value on the assumed branching ratios of interband $E2$ transitions in the ^{229}Th nucleus. We find there is considerable spread in the available experimental data, which could have significant affect on the interpretation of the data of Ref. [BBB07].

In their original publication [BBB07], γ-ray energies of four transitions consisting of a doublet at 29 keV and a doublet at 42 keV, respectively, were measured with a state-of-the-art microcalorimeter (see Fig. 5.4, solid arrows). In their analysis, they made use of the relation $E_{is} = \Delta E_{29} - \Delta E_{42}$, where ΔE_{29} and ΔE_{42} are the differences between the transition energies in the corresponding doublets, which reduces the dependency of the measurement on the absolute calibration of the detector. The authors accounted for an admixture of the low-intensity $5/2^+3/2[631](29\text{ keV}) \rightarrow 5/2^+5/2[633](0.0)$ transition (see Fig. 5.4, green dashed arrow) to their measured signal of the transition, which could not be resolved due to the energy resolution of the detector (26 eV). This admixture lead to a correction of $\Delta E_{29} - \Delta E_{42} = 7.0 \pm 0.5$ eV to the value of the isomeric transition of $E_{is} = 7.6 \pm 0.5$ eV [BBB07]. Later, the authors included another unresolved weak interband transition, $7/2^+5/2[633](42.435\text{ keV}) \rightarrow 3/2^+3/2[631](7.8\text{ eV})$ (see Fig. 5.4, blue dashed arrow), in their analysis, which shifted the isomeric transition energy to the currently accepted value of $E_{is} = 7.8 \pm 0.5$ eV [BWB09].

Specifically, the authors showed that the value of the isomeric transition energy is shifted due to the unresolved transitions by [BWB09]

$$E_{is} = \frac{\Delta E_{29} - \Delta E_{42}}{1 - b_{29} - b_{42}}\,, \tag{5.5}$$

where the branching ratio b_{29} is given as [BBB07]

$$b_{29} = \frac{\Gamma^{tot}_{rad}(29.193\text{ keV})}{\Gamma^{tot}_{rad}(29.193\text{ keV}) + \Gamma^{tot}_{rad}(29.185\text{ keV})}\,, \tag{5.6}$$

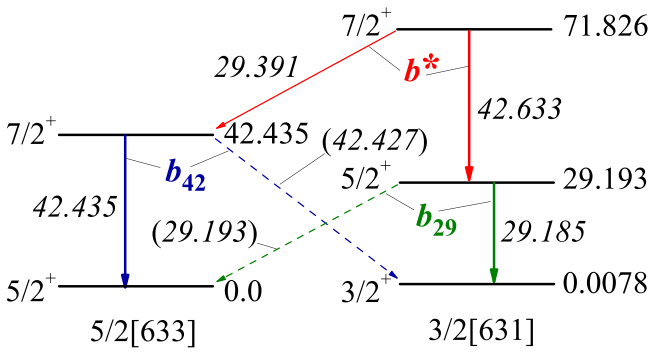

Figure 5.4: Relevant part of the level scheme of ^{229}Th with transitions and branching ratios b^*, b_{29}, and b_{42} used in the works [BBB07, BWB09] to determine the energy of the isomeric level. Energies of the levels and transitions are given in keV.

and the branching ratio b_{42} is given as [BWB09]

$$b_{42} = \frac{\Gamma^{tot}_{rad}(42.427 \text{ keV})}{\Gamma^{tot}_{rad}(42.427 \text{ keV}) + \Gamma^{tot}_{rad}(42.435 \text{ keV})} \,. \tag{5.7}$$

In order to determine b_{29}, the authors of Ref. [BBB07] conducted additional measurements of the branching ratio

$$b^* = \frac{\Gamma^{tot}_{rad}(29.391 \text{ keV})}{\Gamma^{tot}_{rad}(29.391 \text{ keV}) + \Gamma^{tot}_{rad}(42.633 \text{ keV})} = \frac{1}{37} \tag{5.8}$$

with a quoted measurement accuracy of 8%. (Here, $\Gamma^{tot}_{rad} = \Gamma_{rad}(M1) + \Gamma_{rad}(E2)$ and the designations of the transition energies correspond to those in Fig. 5.4.) Using the Alaga rules (see Ch. 1.1) the authors obtained $b_{29} \approx 1/13$. This led to the aforementioned increase of the energy of isomeric transition by 0.6 eV in accordance with the Eq. (5.5). In Ref. [BWB09], the authors performed an estimation of the value of the b_{42} coefficient, which is several times smaller (see in Tab. 5.3) than b_{29}, leading to a smaller shift of 0.2 eV and the currently accepted value of $E_{is} = 7.8 \pm 0.5$ eV.

Interestingly, the same branching ratios can be obtained from the experimental data [BMF88, GKA02, BAB03, RPZ06] for parameters of interband (see in Figure 5.1(a) and (b)) and inband transitions in the rotational bands $5/2^+[633]$ and $3/2^+[631]$ in the ^{229}Th nucleus. The corresponding results are given in Table 5.3, where the probabilities of the inband transitions were calculated using the internal quadrupole moment Q_{20} and the difference of the rotational and internal gyromagnetic ratio g_R and g_K, respectively (for the rotational band

Table 5.3: Branching ratios b_{29} and b_{42}. Results are based on the data of the given references.

Ref.	[BBB07]	[BWB09]	[BMF88]	[GKA02]	[BAB03]	[RPZ06]
b_{29}	1/13		1/3.5	1/7.8	1/5.0	1/3.1
b_{42}		1/50	1/324	1/439	1/214	1/123

Table 5.4: Coefficients b^* and b_{29} obtained from the data for the relative intensities of transitions in [BAB03].

Decaying level	$7/2^+$(71.826 keV)	$5/2^+$(29.193 keV)
b^*	1/17.5	
b_{29}	1/6.4	1/3.9

$5/2^+[633]$ — $Q_{20} = 7.1$ eb, $|g_K - g_R| = 0.176$; for the rotational band $3/2^+[631]$ — $Q_{20} = 7.1$ eb, $|g_K - g_R| = 0.56$, (see [BAB03])).

From Tab. 5.3, it is obvious that the branching ratios calculated by the Alaga rules show considerable spread. This fact is relatively unimportant for the coefficient b_{42}, as the relatively small value given in [BWB09] is the largest of the available in Table 5.3. Thus, if, for example, $b_{42} = 1/439$ the isomeric transition energy would effectively shift back to the previous result of $E_{is} = 7.6 \pm 0.5$ eV [BBB07]. The situation is more dramatic for the coefficient b_{29}. In the scenario $b_{29} \approx 1/3.1$, the energy of the isomer level would rise up to ~ 10.5 eV.

The data from Ref. [BAB03] allow for two additional estimates of the coefficient b_{29}. Specifically, Table VI of Ref. [BAB03] presents the intensities of gamma transitions from the levels $7/2^+$(71.826 keV) and $5/2^+$(29.193 keV); some of these data are experimental results, while others (namely, the relative intensities of the interband transitions) were calculated from the strong coupling rotational model. The branching ratios calculated from these data are presented in Tab. 5.4. In the case of the data for decays from the $7/2^+$(71.826 keV) level, we calculated the branching ratio b_{29} by the formula (5.15) using the coefficient b^*.

These branching ratios are in rough agreement with those calculated for Tab. 5.3, but

differ significantly from the measurement of Ref. [BBB07]. The resolution of this tension between experiments is of the upmost importance. This can be seen by, for example, taking b_{29} to be given by the statistical average of the values calculated here. In that case $b_{29} = 1/5 \pm 1/10$ and the isomeric transition energy becomes $E_{is} = 9.3 \pm 1.0$ eV. Despite this disagreement, we cannot reject the value of $b_{29} = 1/13$ found in Ref. [BBB07], since b^* is given directly from their experimental data and there is no proof this experiment, which used a state-of-the-art micro-calorimeter, is less reliable than the other measurements. Finally, we have performed Monte Carlo simulations of the Beck et al. experiments and if $b_{29} = 1/3$, an asymmetry in the 29 keV peak should be visible. Unfortunately, the size of this asymmetry is smaller than be confirmed by simply viewing the presented date in Ref. [BBB07]. In this regard, it would be interesting to reanalyze the experimental data.

5.4 Moving Forward

The results presented so far reveal that the current situation is far from desirable. There is considerable scatter in the experimental data leading to a large range of predictions for the $3/2^+(7.8$ eV$)$ ^{229}Th isomer radiative lifetime. And although the basic value of $\Delta E_{29} - \Delta E_{42} = 7.0 \pm 0.5$ eV obtained in [BBB07] is not currently in question, there is significant spread in the branching ratio of two unresolved transitions, which systematically shift the value of the isomeric state.

The situation could be made much less ambiguous with an improved measurement of the intensities of the gamma transitions and internal conversion coefficients between the rotational bands $5/2^+[633]$ and $3/2^+[631]$ in the ^{229}Th nucleus. Such experiments could ideally resolve the tension between the current results of Ref. [BMF88, GKA02, BAB03, RPZ06] and allow accurate values of b_{29} and b_{42} to be calculated. Using these values in Eq. (5.5) along with the value of $\Delta E_{29} - \Delta E_{42} = 7.0 \pm 0.5$ eV obtained in [BBB07], the isomeric state energy could be found with greater certainty. These same experiments could also give a definitive means to calculate the nuclear matrix element of the isomeric transition, and thus the radiative lifetime of the isomeric state.

Ideally, the measurements should be conducted for transitions from the rotational band $5/2^+[633]$ to the band $3/2^+[631]$, and vice versa, in the decay of states of the rotational band $3/2^+[631]$. Comparison of the data in Tables 5.1 and 5.2 indicates a systematic excess of the reduced probabilities obtained from the analysis of the decay data for the levels of the $5/2^+[633]$ rotational band. Reduced probabilities of interband transitions from the rotational band $3/2^+[631]$ to the band $5/2^+[633]$ are considerably less. This may indicate an error of measurements, as well as the inapplicability of the adiabatic approximation in the calculation using the Alaga rules.

These measurements, if performed, will considerably sharpen the region of interest that must be scanned in the search for the isomeric transition. This narrowing of the search space may prove to be a prerequisite for the completion of this decades old quest.

5.5 Appendix

5.5.1 Appendix A: Weisskopf Units

In modern nuclear spectroscopy a value of the reduced probability of transition between the nuclear states with the spins I_iM_i and I_fM_f

$$\begin{aligned} B(E/ML; i \to f) &= \sum_{M_f,M} |\langle I_f M_f | \hat{\mathcal{M}}^{E/M}_{LM} | I_i M_i \rangle|^2 \\ &= \frac{|\langle I_f \| \hat{\mathcal{M}}^{E/M}_{L} \| I_i \rangle|^2}{2I_i + 1}\,, \end{aligned} \tag{5.9}$$

where $\langle I_f \| \hat{\mathcal{M}}^{E/M}_{L} \| I_i \rangle$ is the reduced matrix element of the transition operator $\hat{\mathcal{M}}^{E/M}_{LM}$, usually is expressed in the Weisskopf units; see Eq. (5.1) and Ref. [Bla]. The nuclear wave functions are as a rule so complex that an exact calculation of the nuclear matrix elements becomes very difficult. The simplified single-particle Weisskopf model is convenient because it makes it easy to evaluate the nuclear matrix element of the electromagnetic transition. For this purpose the model uses the proton single-particle radial wave functions of the form $\varphi = \text{const.}$ inside the nucleus ($R \le R_0$) and $\varphi(R) = 0$ outside the nucleus ($R > R_0$). The normalization condition $\int_0^{R_0} |\varphi(R)|^2 R^2 dR = 1$ gives const. $= \sqrt{3/R_0^3}$. Thus the total wave function of the

proton has the form [Bla]

$$\Psi(\mathbf{R}) = \sqrt{\frac{3}{R_0^3}} Y_{LM}(\Omega_{\mathbf{R}})\chi_{1/2} \quad \text{for} \quad R \leq R_0\,, \tag{5.10}$$

where $\chi_{1/2}$ is the spin part, and $\Psi(\mathbf{R}) = 0$ for $R > R_0$.

The radial part of the matrix element of the EL proton transition operator $\hat{\mathcal{M}}^E_{LM} = eR^L Y_{LM}(\Omega)$ is easily calculated with the wave functions (5.10):

$$\langle \varphi_f(R)|R^L|\varphi_i(R)\rangle = \frac{3}{3+L} R_0^L\,.$$

From the angular part of the reduced matrix element in Eq. (5.9), $\langle f\|Y_L(\Omega)\|i\rangle$, only a factor $\sqrt{1/4\pi}$ is left, because $\sqrt{(2L_i+1)(2L+1)}C^{L_f 0}_{L_i 0 L 0}$ with the factor $1/\sqrt{(2I_i+1)}$ from (5.9) gives a value of about 1. (Here C^{ef}_{abcd} is the Clebsch-Gordan coefficient [VMK88].) As a result, the following expression is obtained in the Weisskopf model for the reduced probability of the EL single-particle transition

$$\begin{aligned} B(W;EL) &= \frac{e^2}{4\pi}\left(\frac{3}{3+L}\right)^2 R_0^{2L} \\ &= \frac{e^2}{4\pi}\left(\frac{3}{3+L}\right)^2 1.2^{2L} A^{2L/3}\ \mathrm{fm}^{2L}. \end{aligned}$$

Here, the value of $R_0 = 1.2A^{1/3}$ fm was used for the radius of the nucleus with the atomic number A.

For the magnetic ML transition the orbital (l) and the spin (σ) contributions leads to the relation

$$\frac{|\hat{\mathcal{M}}^M_{LM}(l) + \hat{\mathcal{M}}^M_{LM}(\sigma)|^2}{|\hat{\mathcal{M}}^E_{LM}|^2} \simeq \frac{10}{(M_p R_0)^2} \tag{5.11}$$

between multipole moments of transition [Bla]. (M_p in Eq. (5.11) is the proton mass.) This allows to write for the reduced probability of magnetic transitions in the Weisskopf model:

$$B(W;ML) = \frac{10}{(M_p R_0)^2} B(W;EL).$$

Now, one can express the real reduced probability of a nuclear transition, $B(M/EL; i \to f)$, through the single particle reduced probability of the Weisskopf model $B(W; M/EL)$ according

$$B(E/ML; i \to f) = B(W; E/ML) B_{W.u.}(E/ML; i \to f)\,,$$

where $B_{W.u.}$ is the reduced probability in Weisskopf units, which is commonly used in tables of nuclear transitions.

The γ emission probability in the Weisskopf model [Bla]

$$\Gamma_{rad}(W; E/ML) = \frac{8\pi}{[(2L+1)!!]^2}\frac{L+1}{L}\omega^{2L+1}B(W; E/ML)$$

satisfies the condition

$$\frac{\Gamma_{rad}(W; L+1)}{\Gamma_{rad}(W; L)} \sim (\omega R_0)^2 \sim \left(\frac{R_0}{\lambda}\right)^2$$

for the emission of $E(L+1)$ and EL (or $M(L+1)$ and ML) multipoles. This approximation is true if the nuclear radius R_0 is small compared to the wavelength of nuclear transition λ. The latter condition is certainly satisfied for nuclear transitions with the energies up to several MeV.

5.5.2 Appendix B: Branching Ratios

The section discussed the relation of the coefficients b^* and b_{29}. Simple algebraic transformation of the Eq. (5.8) enables us to express the ratio of the widths of the transitions with energies of 42.627 keV and 29.391 keV through coefficient b^*:

$$\frac{\Gamma^{tot}_{rad}(42.627 \text{ keV})}{\Gamma^{tot}_{rad}(29.391 \text{ keV})} = \frac{1-b^*}{b^*} \tag{5.12}$$

Using the rotational model, we can express the radiation widths of the 29.185 keV transitions through the widths of the 42.627 keV transitions:

$$\begin{aligned}
&\Gamma_{rad}(M1; 29.185 \text{ keV}) \\
&= \left(\frac{C^{3/2\,3/2}_{5/2\,3/2\,1\,0}}{C^{5/2\,3/2}_{7/2\,3/2\,1\,0}}\right)^2 \left(\frac{25.185}{42.627}\right)^3 \times \Gamma_{rad}(M1; 42.627 \text{ keV}) \\
&= 0.240\,\Gamma_{rad}(M1; 42.627 \text{ keV})
\end{aligned}$$

and

$$\begin{aligned}
&\Gamma_{rad}(E2; 29.185 \text{ keV}) \\
&= \left(\frac{C^{3/2\,3/2}_{5/2\,3/2\,2\,0}}{C^{5/2\,3/2}_{7/2\,3/2\,2\,0}} \right)^2 \left(\frac{25.185}{42.627} \right)^5 \times \Gamma_{rad}(E2; 42.627 \text{ keV}) \\
&= 0.241\, \Gamma_{rad}(E2; 42.627 \text{ keV}).
\end{aligned}$$

Due to the coincidental equality of the transformation coefficients for the $M1$ and $E2$ components we obtain

$$\Gamma^{tot}_{rad}(29.185 \text{ keV}) = 0.24\, \Gamma^{tot}_{rad}(42.627 \text{ keV}). \tag{5.13}$$

Using the rotational model once again, we obtain the following relations:

$$\Gamma_{rad}(M1; 29.193 \text{ keV}) = 0.735\, \Gamma_{rad}(M1; 29.391 \text{ keV})$$

and

$$\Gamma_{rad}(E2; 29.193 \text{ keV}) = 1.36\, \Gamma_{rad}(E2; 29.391 \text{ keV}),$$

or, for the total linewidth,

$$\begin{aligned}
\Gamma^{tot}_{rad}(29.193 \text{ keV}) = 0.735\, &\left(\Gamma^{tot}_{rad}(29.391 \text{ keV}) \right. \\
&\left. + 0.85\, \Gamma_{rad}(E2; 29.391 \text{ keV}) \right).
\end{aligned}$$

Let us estimate the additional part $0.85\, \Gamma_{rad}(E2; 29.391 \text{ keV})$ to the width $\Gamma^{tot}_{rad}(29.391 \text{ keV})$ using the mean values $B(M1)$ and $B(E2)$ for the interband transitions in Fig. 5.1 (a)–(b). The result is

$$\Gamma_{rad}(E2; 29.391 \text{ keV}) \simeq 2 \times 10^{-3}\, \Gamma_{rad}(M1; 29.391 \text{ keV}),$$

i.e. we really can neglect by the "extra" part $0.85\, \Gamma_{rad}(E2; 29.391 \text{ keV})$ in the width $\Gamma^{tot}_{rad}(29.391 \text{ keV})$ and use the estimation

$$\Gamma^{tot}_{rad}(29.193 \text{ keV}) \approx 0.735\, \Gamma^{tot}_{rad}(29.391 \text{ keV}). \tag{5.14}$$

Substituting expression (5.13), (5.14) and (5.12) in (5.6) we finally obtain

$$\begin{aligned} b_{29} &= \left(1 + \frac{0.24\,\Gamma^{tot}_{rad}(42.627\text{ keV})}{0.735\,\Gamma^{tot}_{rad}(29.193\text{ keV})}\right)^{-1} \\ &= \left(1 + \frac{0.24}{0.735}\frac{1-b^*}{b^*}\right)^{-1}. \end{aligned} \tag{5.15}$$

CHAPTER 6

Interrogation with A Pulsed VUV Laser System

Following the experiments at the Advanced Light Source, we realized that our sensitivity to lifetimes was limited by the synchrotron source. After being introduced to a tunable pulsed VUV laser system at the University of CA Davis, we decided to build one at UCLA. Pulsed VUV systems typically allow for a spectral irradiance that surpasses those of synchrotron sources. This can result in a finer scan, which when including experimental overhead requires more time to sweep an equivalent range of excitation energies as compared to the ALS, but with the benefit of enhanced sensitivity to longer lifetimes. We have constructed a VUV laser system at UCLA which outperforms all other systems known to us and is roughly 10,000x brighter than synchrotron sources. Through a few years of operation in search for the transition, we made many improvements to our VUV laser and spectroscopy systems, some of these will be discussed later. In brief, we have scanned from $\sim (6.8 - 8.3)$eV with no clear evidence of the transition. In this scan range, we exclude upper lifetime bounds that are about an order of magnitude improved over what was achieved at the ALS.

6.1 Nonlinear Polarizations and Four Wave Mixing

High intensity light can alter the optical properties of a material. This is achieved through the polarisation ($\vec{P}$) of the material, which is a vector quantity representing the density of dipole moments. The dipole moments arise from the electron clouds associated with individual atoms in the material. In response to an applied electric field, the electron cloud distribution can shift, inducing a dipole moment. With an applied external field of sufficiently

low intensity, the polarisation of a dielectric medium is related to the field as:

$$\vec{P} = \epsilon_0 \chi \vec{E}. \tag{6.1}$$

χ is the susceptibility of the material. For anisotropic medium, χ is represented by a tensor which can lead to induced polarizations whose orientations are different than that of the applied field. As the intensity of the applied field is increased, higher orders terms of the field can become relevant in describing the polarization:

$$\vec{P} = \epsilon_0 \big(\chi^{(1)} \vec{E} + \chi^{(2)} \vec{E}^{\,2} + \chi^{(3)} \vec{E}^{\,2} + ... \big). \tag{6.2}$$

$\chi^{(2)}$ and $\chi^{(3)}$ are the second and third order nonlinear susceptibilities. Intense oscillating electric fields, such as those in an intense laser beam, can induce oscillations of atomic charge distributions within the medium. This results in an oscillating polarization which can act as a source term in Maxwell's equation. The second order polarization describes several interesting nonlinear optical effects such as second harmonic generation, optical rectification, difference-frequency generation, and sum frequency generation.

Four wave mixing is a third-order nonlinear polarization effect. In the case of degenerate four-wave difference frequency mixing utilized to produce VUV, an expression for the intensity of the generated beam ($I_{2\nu_1 - \nu_2}$) is given by:

$$I_{2\nu_1 - \nu_2} = I_{\nu_1}^2 I_{\nu_2} \big[\chi^{(3)} \big] N^2 F \big(b \Delta k \big). \tag{6.3}$$

I_{ν_1} and I_{ν_2} are the respective intensities of the mixing beams. $\chi^{(3)}$ is the third-order non linear susceptibility which is enhanced by driving a two photon transition corresponding to the frequency $2\nu_1$. N^2 is proportional to the number density of the nonlinear medium gas. And F is a phase matching factor which depends on the confocal parameter of the beam (b) and the wave vector mismatch (Δk) [AHC11]. The relevant two photon transition in Xe utilized by our VUV laser system is shown in Figure 6.1. By tuning ν_2, a tuneable VUV is produced as shown in Figure 6.2.

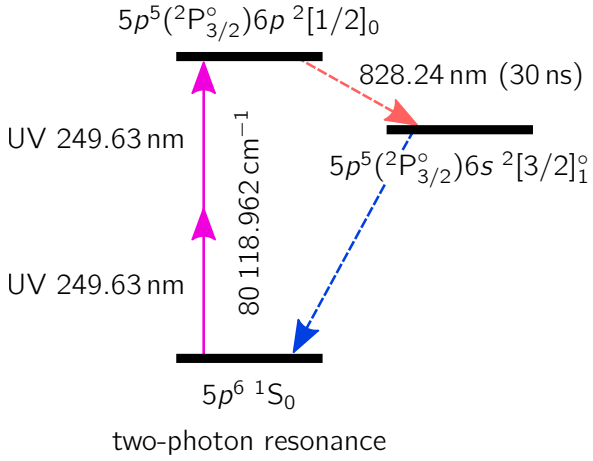

Figure 6.1: Two photon resonance line in Xe. This line is utilized in our VUV laser system. Driving it enhances the VUV production efficiency through enhancement of the third order polarizability.

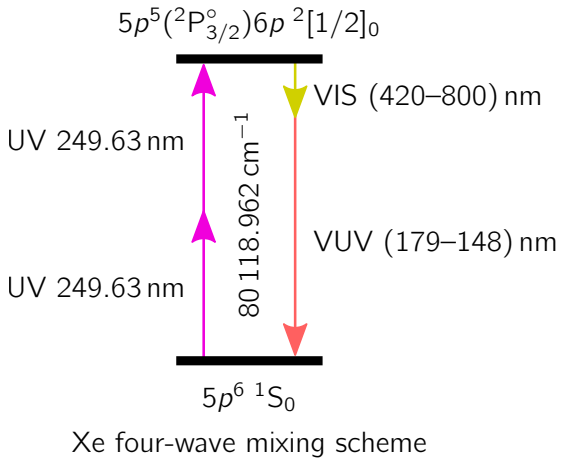

Figure 6.2: Difference frequency mixing in Xe. The generated VUV frequency is equivalent to the sum of 2 times that of the two-photon resonance shown in Figure. 6.1 minus the frequency of the second mixing beam.

6.2 UC Davis Collaboration

The pulsed VUV laser system at the University of CA Davis utilizes resonance-enhanced four-wave difference frequency mixing in Xe. A 30 Hz Spectra Physics Nd:YAG Quanta Ray Pro 270 laser is used to pump two Lambda Physiks dye lasers (LPD 3000). One of these dye lasers is fixed at a two-photon resonance line in Xe. See Fig. 6.1. The other pulsed dye laser is tunable and produces the change in the output VUV frequency. The two beams from the pulsed dye lasers (PDL's) are overlapped and focused into a Xe jet where the frequency mixing occurs. The Xe jet is composed of a Parker 9 Series pulsed valve housed inside of a capillary which is then put in vacuum with a relatively powerful turbo pump. The capillary aids in the overlapping of the mixing beams and is where the VUV is produced with an output frequency equivalent to the difference between two times the doubled frequency from the fixed PDL minus the tunable PDL frequency as can be seen in Fig. 6.2. Upon exit from the Xe jet, the three beams are then incident on an off-axis MgF_2 lens that allows separation of the beams. See Fig. 6.3. The VUV beam can then be directed into a spectroscopy chamber where it can interrogate the ^{229}Th:LiSrAlF$_6$ crystal. In the overlapping of the mixing beams, the sum frequency is also generated. However, this

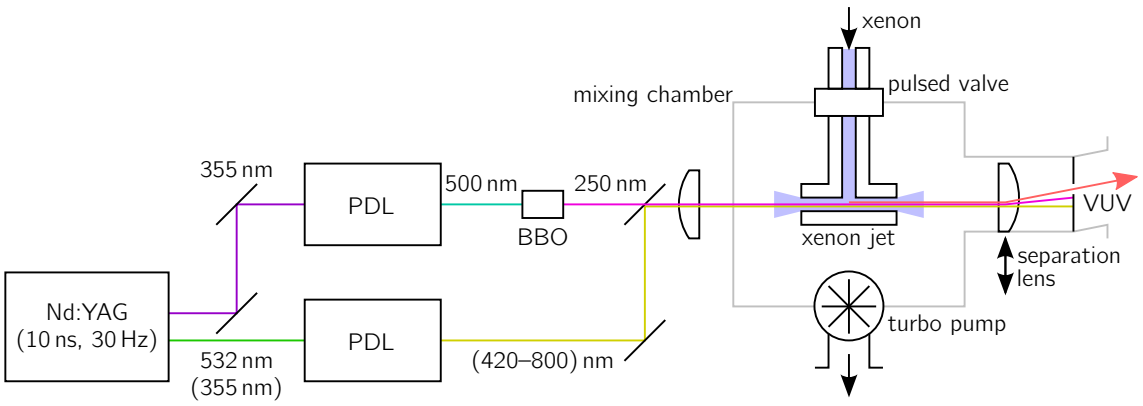

Figure 6.3: UCD VUV laser schematic. A pulsed Nd:YAG laser pumps two pulsed dye lasers (PDL's). One of the PDL outputs is fixed and doubled to the two photon resonance shown in Fig. 6.1. The other PDL output is tunable and will determine the VUV output frequency, as shown in Fig. 6.2. Both PDL outputs are overlapped and focused into a Xe jet where the frequency mixing occurs. And off-axis MgF_2 lens can the separate the mixing beams from the generated VUV beam.

should be mostly absorbed by the MgF_2 separation lens. Additionally, the sum frequency will exit the separation lens at a different angle then the difference frequency. And finally, the phase matching conditions can be different for the sum and difference frequencies, and we optimize the VUV pulse energies according to the latter. These steps should essentially reduce any residual sum frequency components in the output beam.

At UCD, our time with the laser system was limited. Much effort went into setting up the laser system for our experiment and properly characterizing the pulsed VUV energies. We were successful however and were able to further interrogate ^{229}Th:$LiSrAlF_6$ crystal B. We did not scan a large VUV range, however, improved longer lifetime exclusion bounds were obtained, as can be seen in Fig. 6.4. The gray shaded area represents the resulting longer lifetime exclusion bounds.

A huge thanks to Cheuk Ng for allowing us to spend some time in their lab and learn some things about their VUV laser systems. And also a huge thanks to Yih-Chung Chang for all his efforts in making the experiment at UCD possible.

6.3 A Pulsed VUV Laser System at UCLA

Construction of a pulsed VUV laser system at the University of CA Los Angeles began around February of 2015. Since that time, many changes and improvements have been made to our system. In the following, the major components of our experimental apparatus will be described. The pulsed VUV is generated in a very similar manner as was done at UC Davis. The laser system built at UCLA also utilizes resonance-enhanced four-wave difference frequency mixing in Xe. A 30 Hz Spectra Physics Nd:YAG Quanta Ray Pro 270 laser is used to pump two Lambda Physiks dye lasers (LPD 3002). One of the PDL outputs is fixed and doubled to drive the same two photon resonance in Xe, and the other is tunable. Instead of a Xe jet however, the output beams from the pulsed dye lasers (PDL's) are overlapped and focused into a Xe cell where the frequency mixing occurs. An off-axis MgF_2 lens once again separates the generated VUV beam from the mixing beams. The VUV beam can then be directed into the spectroscopy chamber for interrogation of the ^{229}Th:$LiSrAlF_6$ crystal. See

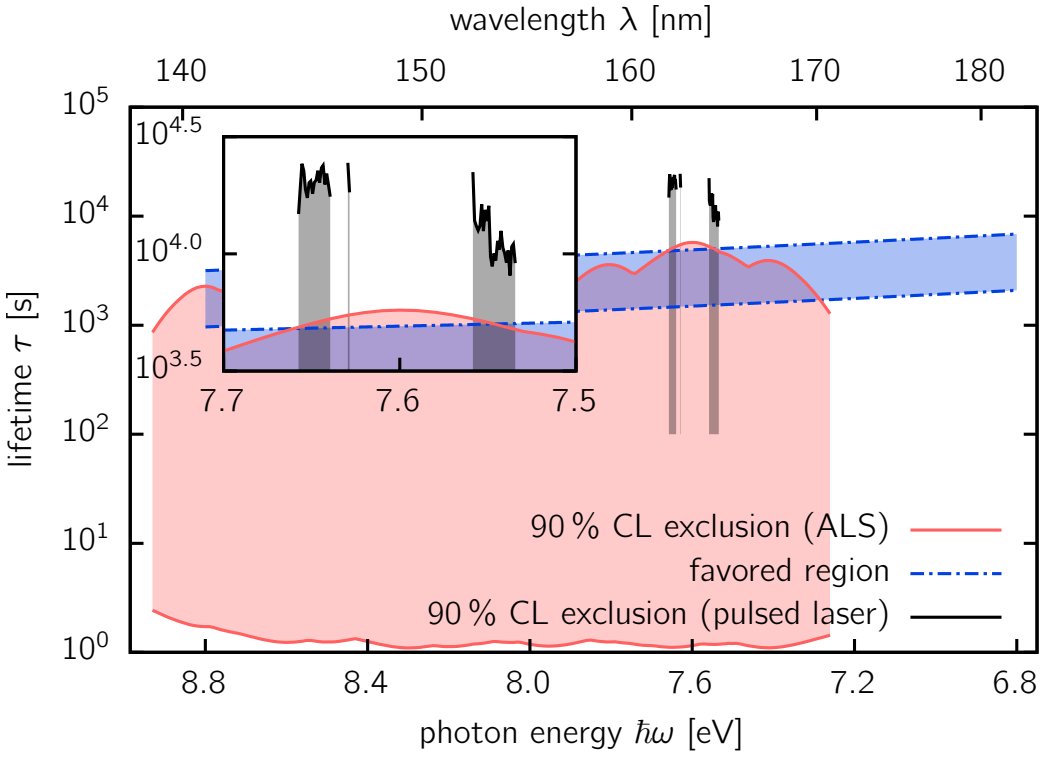

Figure 6.4: UCD longer lifetime exclusion bounds. These were obtained in a similar manner as to was done for the ALS data. The red shaded region is the exclusion region obtained from the ALS data. The blue shaded region is once again the favored region, or range of expected lifetimes, as described in chapter 4. And the gray shaded region depicts an upper lifetime exclusion bound obtained from utilizing the laser system at UCD.

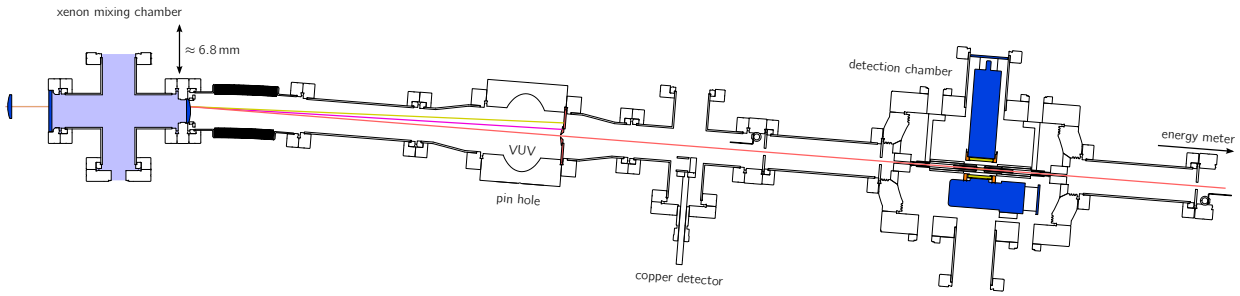

Figure 6.5: Experimental apparatus. An input lens along with the MgF_2 separation lens form a telescope for the PDL output beams. The input lens focuses the beams into the Xe cell (which promotes the difference frequency mixing), and the separation lens then separates the VUV from the mixing beams. The telescope produces a VUV beam of $\sim$ 1 mm in diameter. This beam is directed past a prism beam separator and into the spectroscopy chamber for interrogation of the ^{229}Th:$LiSrAlF_6$ crystal. Upon exiting the thorium crystal, the beam is then incident on a pyroelectric detector which characterizes the VUV pulse energies.

Fig. 6.5. Having our own VUV laser system has allowed us to push the limits of what these types of systems can achieve. The technologies we have developed and characterizations we have made have allowed successful operation of our system for a few years now.

6.3.1 Apparatus

The experimental apparatus is composed of a few major components which include the Nd:YAG laser system, the pulsed dye lasers, the mixing and reference cells, and the spectroscopy chamber. In the following, the current status of these components will be described in some detail.

6.3.1.1 Spectra Physics Nd:YAG

To generate VUV pulses, we require an Nd:YAG laser for pumping two different PDL's. For our YAG, we utilize the Quanta Ray Pro 270-30 Hz. The properties of neodymium-doped yttrium aluminum garnet (Nd:YAG) have been extensively studied over the years, and among solid-state lasers is perhaps the best understood. Commercial systems are typically built to

be rugged and powerful. The active medium of the laser is triply ionized neodymium and upon pumping with Xe flash lamps, emission at primarily 1064 nm is produced.

Typically, the flash lamps that pump the Nd:YAG gain medium are fired for relatively long durations (100's of usecs) at a time. If there was no mechanism to make the cavity lossy, the output pulse of the Nd:YAG laser will have the same duration as that of the flash lamp firing and with a relatively low peak intensity. The laser can be operated in this long-pulse mode which can be adequate for alignment purposes and particular experiments. If this light will undergo higher harmonic generation and subsequent PDL pumping, a shorter pulse width and higher peak intensity would be necessary to facilitate the task. To achieve shorter pulse widths and higher peak intensities, the Quanta Ray Pro models utilize an active Q-switch. This is a well-known technology and it is vital for higher harmonic generation and subsequent pumping of the PDL's, and ultimately VUV generation.

The Quanta Ray Pro models utilize an unstable resonator configuration. This allows larger beam diameters for better pumping of the Nd:YAG rods. The spectral distribution of the output of the laser depends on the laser gain profile of the Nd:YAG rods as well as the length of the cavity. A cavity in general can support an infinite number of longitudinal cavity modes. This is due to the fact that certain wavelengths can form standing waves in the cavity and these will constructively interfere. All other wavelengths are suppressed due to destructive interference. The frequency difference between successive supported modes is known as the free spectral range (FSR) of the resonator.

$$\nu_{\mathrm{m}} = \frac{\mathrm{mc}}{2\mathrm{L}} \quad \text{and} \quad \Delta\nu = \frac{\mathrm{c}}{2\mathrm{L}} \tag{6.4}$$

Here ν_{m} represents the supported frequencies of the cavity: m is an integer, c the speed of light, and L is the length of the cavity. And the spacing of these modes (or the FSR) is given by $\Delta\nu$. Taking into consideration the profile of the gain medium, the spectral output of the YAG looks like a 30 GHz Guassian envelope which contains evenly spaced discrete frequencies determined by the above equations. With a cavity length of 60 cm, this puts the

spacing between different longitudinal modes at ∼250 MHz.

Optionally, the Nd:YAG lasers from Spectra Physics can be equipped with an injection seeder unit (Model 6350). The benefit of a seeder is that it can significantly reduce the output bandwith of the Nd:YAG laser. This is achieved by coupling a narrowband CW laser into the resonator cavity. The cavity output coupling mirror is equipped with a piezo which can adjust the length of the cavity and the frequencies of all the longitudinal cavity modes. The nearest Nd:YAG output cavity mode can then be locked to the seeder frequency through modulation of the piezo, which will then dominate in lasing and steal power from the other modes. And in so, the bandwidth of the Nd:YAG laser is reduced to ∼90 MHz. By pumping with a single cavity mode of the Nd:YAG output, the PDL output pulses have less intensity variations in the different cavity modes. This helps minimize chirp and also promotes the production of a more uniform VUV spectrum. In addition, the doubling efficiency of the PDL output is improved when the pump laser is injection seeded.

Our Nd:YAG laser utilizes a custom-made high harmonic generation box which allows us to produce 355 nm and 532 nm light simultaneously for a dual PDL pumping scheme. Additionally, our flash lamps are powered by 4, instead of the typical 2, power supplies (the power supplies charge a capacitor which is then shorted across the flash lamps for pumping of the Nd:YAG rods). This modification has allowed us to operate the laser continuously and without failures. A big thanks to everyone at Spectra Physics including Adam Larson, Michael Crumb, Brant Jones, and others.

6.3.1.2 Pulsed Dye Lasers

The outputs from the Nd:YAG laser are sufficient to pump two different pulsed dye lasers. The PDL's we use were manufactured by Lambda Physik (model LPD 3002) in 1991. These pulsed dye lasers utilize a Littrow type grating configuration with 600 lines/mm. The grating equation can be derived from the use of the Huygens-Fresnel principle or simple ray diagrams and is given by:

$$\mathrm{d}(\sin\alpha + \sin\beta) = \mathrm{m}\lambda. \tag{6.5}$$

d is the line spacing, α is the angle of incident light, β is the angle of diffracted light, m is the diffraction order, and λ is the wavelength of the light. In the case of the Littrow configuration, α is equal to β. Then the grating equation reduces to:

$$2\mathrm{d}\sin\alpha = \mathrm{m}\lambda. \tag{6.6}$$

An advantage of the Littrow configuration is in the fact that the incident and diffracted angles are equal, which allows the grating to serve as an end mirror of an optical resonator. A given grating orientation will then fix the wavelength within the gain bandwidth of the particular laser dye. For optimal tunability, different diffraction orders can be used to accommodate for different lasing wavelengths.

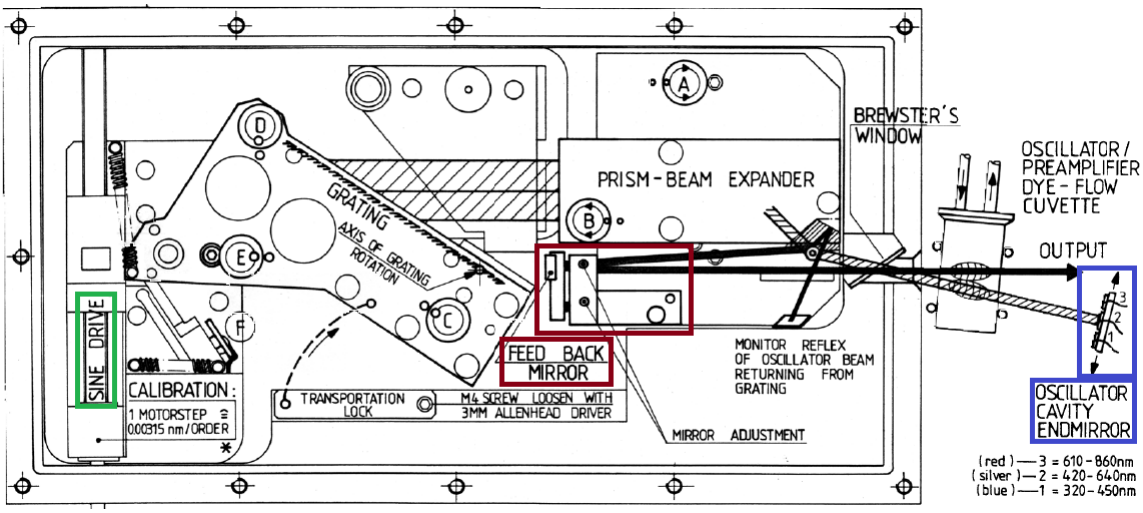

Figure 6.6: PDL oscillator cavity. The bulk of the cavity is enclosed inside of a air tight box allowing for pressure tuning of the output wavelength. The "feed back mirror" is outlined in dark red. A custom version of this was built in-house for our PDL's. The "oscillator cavity endmirror" is outlined in blue. A custom version of this was built which allows for the length of the cavity to be adjusted with a piezo. The "sine drive" shaft is outlined in green. The shaft is adjusted with a stepper motor, which is controlled with a microcontroller.

The LPD 3002 is operated between the 3rd and 8th diffraction orders with an output bandwidth that is less than 6 GHz. The bulk of the oscillator cavity is mounted inside an enclosed pressure tight box which also allows for pressure tuning. In Fig. 6.6, the oscillator cavity for the LPD 3002 is shown. For high energy Nd:YAG pumping, a "feedback mirror" is

required to minimize damage to the grating while pumping. Our PDL's were not equipped with feedback mirrors upon acquisition. We built our custom versions. The prism beam expander along with the grating promote a relatively narrow bandwidth from the output of the oscillator cavity. But as an optical cavity can support longitudinal cavity modes, the output spectrum of the PDL's are composed of discrete modes within an approximately gaussian envelope of < 6 GHz. More details on the PDL frequency spectrum will be discussed later. We equipped the oscillator "cavity end mirror" with a piezo such that the frequency of the cavity modes can be tuned by changing the length of the cavity. A picture is shown in Fig. 6.7. The electronics that drive the stepper motors, which then in turn control the

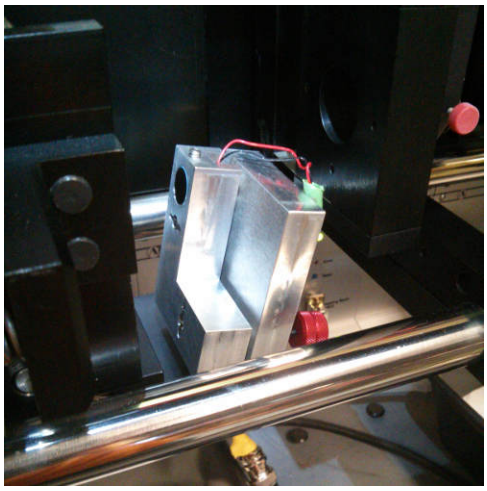

Figure 6.7: PDL oscillator cavity mirror. The original oscillator cavity endmirror is replaced with one that has a piezo attached such that the cavity length, and the therefore the cavity modes, can be dithered.

"sine drive" which changes the grating angle and ultimately the output wavelength of the oscillator cavity, were not functional. We developed a microcontroller solution which can drive our stepper motors and ultimately serve as new control unit for our PDL's. We also equipped our pulsed dye lasers with custom optics mounts which allow us to use standard circular optics for manipulation of the pump beams.

6.3.1.3 Spectroscopy Chamber

The spectroscopy chamber used in our experiment is essentially the same as that used at the Advanced Light Source. We use the same 8" spherical octagon from Kimball Physics. The photomultiplier tubes used in our experiment are both of the same type in the most current configuration and are of a head-on model, the R6835. There are some advantages of this PMT configuration that will be discussed in the next section. The PMT's are once again used in the cathode-grounded configuration. We no longer use the low-profile UniBlitz VS35

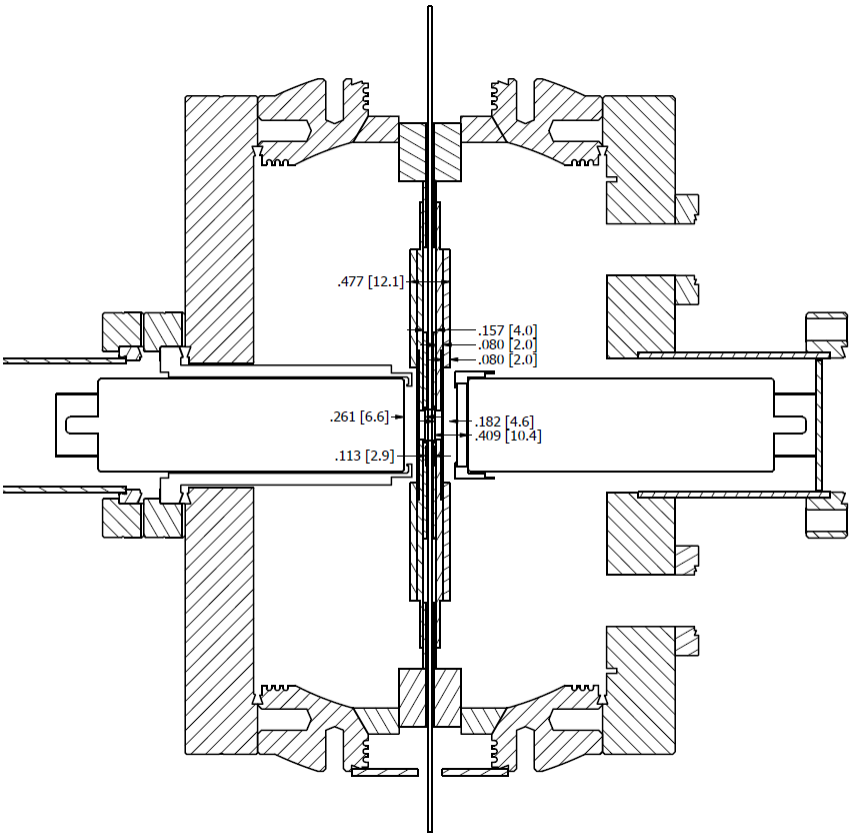

Figure 6.8: Current spectroscopy chamber layout. Two PMT's of the same type are used for fluorescence detection, the R6835. This setup has the advantage of an improved overall light collection efficiency. The PMT's are each mounted a little differently: one of the PMT's voltage divider board is in vacuum, while the other's is kept outside of vacuum.

shutters used at the Advanced Light Source. It was mentioned that these shutters are of unistable design and require a relatively large voltage across its actuator coils to keep them

open during fluorescence collection. Previously, we had discovered that this applied voltage causes some heating of the actuator coils which then produces black-body radiation which affected the dark count rate of our head-on photomultiplier tubes. In the past, we fixed this issue by attaching a heat sink to the actuator coils. In the current version of the spectroscopy chamber, a pneumatic linear motion vacuum feedthrough (MDC, part ABLM-275-2-01) is used to drive stainless steel shutter blades over a stainless steel mount referenced to the spherical octagon. When the blades are closed, a light tight enclosure is formed which is adequate for the photomultiplier tubes housed inside the spectroscopy chamber to remain powered on during illumination of the crystal. And with this pneumatic solution, the heat produced is negligible.

At the Advanced Light Source, the excitation source spectrum contained flux mostly where it was needed as the higher order harmonics are mostly absorbed in the differentially pumped gas filter. For VUV sources utilizing frequency mixing, the excess photon flux from the mixing beams may need to be adequately separated from the VUV beam. In our particular case, we would hope to minimize exposure of the ^{229}Th:LiSrAlF$_6$ crystals with intense UV light for various reasons including the formation of color centers. In addition to the separation lens for separation of the three beams, a prism beam separator is used to pick off the two mixing beams to dump them into a diffuser. This helps reduce scattered light from entering the spectroscopy chamber, see Fig. 6.9. Minimizing the scattered light from the mixing beams is necessary for reliable VUV pulse energy readings.

As the ^{229}Th:LiSrAlF$_6$ crystal is illuminated, the photon flux of the VUV beam must be monitored as was done at the ALS. While we were able to use VUV photodiodes for the nearly CW light generated by the synchrotron, the pulsed VUV laser at UCLA requires a modified pyroelectric detector. We utilize a QS5-IL pyroelectric detector manufactured by Gentec. The modifications made to the detector as well as the characterization of the VUV flux will be detailed in the following section. In addition to pyroelectric detectors, Cu detectors utilizing high voltages can also be used to detect pulsed UV and VUV light. As incident photons exceed the binding energies of conduction electrons in metals and other

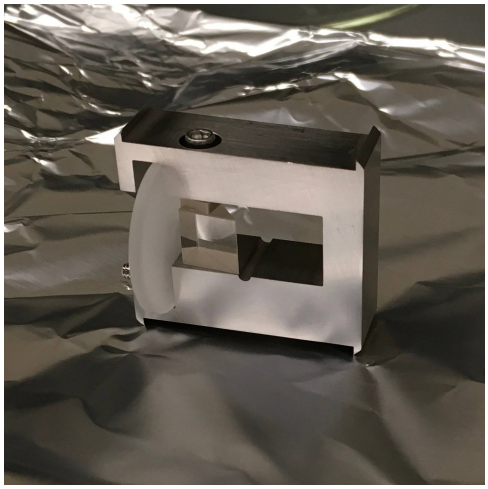

Figure 6.9: Prism beam separator. The separator is located downstream of the separation lens. The VUV beam passes near the edge of the prism and into the spectroscopy chamber. The mixing beams are incident on the prism causing refraction and reflection. These beams are then diffused with a UVFS ground glass diffuser, and then dumped into the chamber.

materials, electrons can be ejected from the bulk via the photo-electric effect:

$$\begin{gathered} K_{max} = hf - W \\ \text{with} \\ W = -e\phi - E_F. \end{gathered} \tag{6.7}$$

Here, K_{max} is the kinetic energy imparted to the electron due to the absorption of a photon with frequency f. W is the work function, which is defined as the minimum energy needed to remove an electron from inside of a material to immediately outside of it in vacuum, and is a material dependent property. e is the charge of an electron, ϕ is electric potential in vacuum near the surface of the material, and E_F is the Fermi level inside of the material. As pulses of light knock electrons out of the metal and into vacuum, an applied voltage can then be utilized to collect the ejected electrons onto another electrically isolated conductor, which in turn will generate a current pulse which can be detected and interpreted as a measure of the photon flux. In Fig. 6.10, our homemade Cu detectors are shown mounted to a $2\frac{3}{4}$ conflat flange. The detector itself is made of a Cu disk (emitter disk) which is incident with the pulsed VUV light. A surrounding electrically isolated Cu cylindrical tube (collection cylinder) at a high positive voltage collects the ejected photoelectrons. These Cu detectors

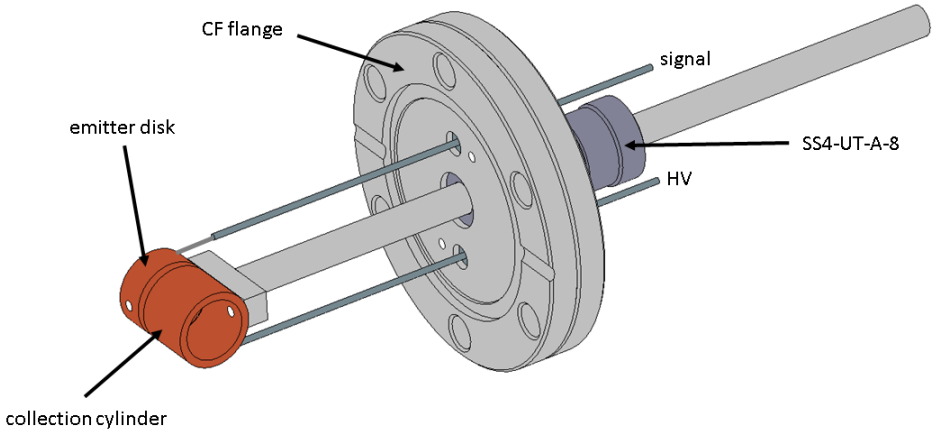

Figure 6.10: Cu VUV detector. The pulsed VUV is incident on the "emitter disk". The ejected electrons are collected by the "collection cylinder" which has a positive voltage applied to it. The electrons leaving the "emitter" to make their way to the "collector" constitute a current which can be measured and interpreted as a photon flux or pulse energy.

are very useful since they are relatively inexpensive and easy to operate. Attachment to a motion feedthrough allows for the detector to be moved in and out of the path of the beam. This can be especially useful for in situ crystal transmission measurements as well as for troubleshooting.

In addition to our Cu detectors which serve mostly as diagnostic tools, we built a special viewing and measurement chamber for the actual experimental data. This chamber houses our modified Gentec QS5-IL for ultimate VUV energy determination and also houses a quartz viewing optic which allows us to view the VUV beam. A translation stage attached to the chamber allows us to move the quartz viewing optic into the path of the beam. The fluorescence produced by the optic upon absorption of the VUV gives us an idea of our VUV beam size and is a useful tool for optimizing the overall collimation of the beam.

6.3.2 Characterizations

Meaningful interpretation of data requires knowledge of all the experimental parameters. As in the case at the Advanced Light Source, we do our best to characterize all of the

components in our experiment. This involves frequency characterization of the excitation source, detector calibrations, determination of light collection efficiencies, and some other additional information.

6.3.2.1 Pulsed Dye Laser Frequency Spectrum

It has been shown that the pulse-to-pulse frequency spectrum from the output of pulsed dye lasers can vary [KLS92]. In this work, a Fizeau Interferometer and an imaging system were utilized to characterize the frequency spectrum of PDL pulses. The pulsed dye laser model used was the Lambda Physik FL2002E, which has essentially the same oscillator cavity as our PDL's. Some useful information can be obtained from the results of these past works involving characterization of PDL's. We will summarize some of the results in the following:

- Single pulse measurements of the PDL frequency spectrum show distinct longitudinal modes and the intensities of the modes can vary significantly from pulse to pulse.
- The average of many pulses still results in distinguishable longitudinal cavity modes.
- There was also some asymmetry noticed in the spectrum when averaging over tens of pulses.
- By tabulating certain modes that are above a particular threshold, a pattern was established between the stronger lasing cavity modes. The stronger cavity modes seem to prefer a mode spacing of either 3 or 7.

In the work of [WRS84], this last effect is studied in depth. In general, lasers are systems that are driven far off from equilibrium. As the system will want to return to equilibrium through the fastest possible means, emission rates are maximized. Consider a single oscillating cavity mode. In the gain medium itself, there will be nodes and anitnodes of this standing waves. Roughly speaking, less than half the energy in the gain medium will be extracted by this mode due to the presence of the anitnodes. By the maximum emission principle, another oscillating cavity mode can steal the rest of the energy from the gain medium. Modes that

are $\pi/2$ radians out of phase with some arbitrary initial cavity mode will be most efficient at extracting the remaining energy. An overlap integral between different mode-intensity distributions within the gain medium can be constructed to obtain the mode competition coefficient C_{nm} given by:

$$C_{nm} = \frac{1}{l}\int_{xo}^{xo+l} \sin^2(k_n)\sin^2(k_m)dx, \tag{6.8}$$

where xo is the distance to the closest cavity mirror, l is the length of the oscillator dye cell, and k_m and k_n are the respective wavenumbers of the particular modes. It is expected that modes with minimum mode competition will have maximum cross correlation [WRS84].

To characterize the output spectrum from our pulsed dye lasers, we employ monitor etalons for both PDL's. The etalons are flat Fabry-Perot interferometers purchased from Light Machinery. Photons travelling through the etalon can constructively interfere with other photons making round trips through it. The result is an interference pattern which can be focused onto a camera for imaging. With these etalons, we can map the frequency spectrum of every single pulse. The high finesse allows us to map out the frequency of individual PDL cavity modes. Our etalon imaging system consists of a diffuser to scatter the incoming light. An iris then picks off a certain amount of the scattered light so that it can be incident on mainly the effective area of the etalon optic. Upon exiting the etalon, a 150 mm FL plano-convex lens is used to focus the interference fringes onto a CCD camera (PixeLink PL B959U). See Figure. 6.11. The etalons we use are custom made. They have a thickness of 14.935 mm ($\sim$ 6 GHz FSR in the visible range) and a calculated finesse, based on the measured reflectivity and surface flatness, of greater than 40.

We can correlate the fringe positions on an imaging plane to actual frequency measurements. Given an etalon of thickness d, and with given index of refraction n, an expression can be derived for the constructive interference condition using simple ray diagrams. Considering the difference in phase accumulated by rays that make successive round trips in the etalon, an expression can be derived that ensures the constructive interference case:

$$\lambda m = 2dsqrt(n^2 - \sin^2\theta). \tag{6.9}$$

In the above equation, λ is the wavelength of the light, m is an integer that describes the

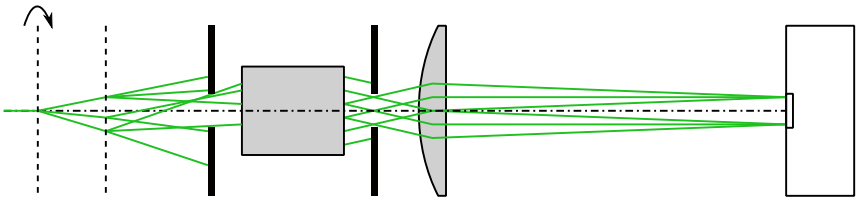

Figure 6.11: Etalon imaging system schematic. A rotating diffuser diffuses the PDL output and an iris then introduces some of this light to the clear aperture of the etalon optic (custom from Light Machinery). Light rays at the exit face of the etalon optic can interfere with other rays making rounds trips through it. The produced interference pattern is then focused onto a CCD camera for imaging.

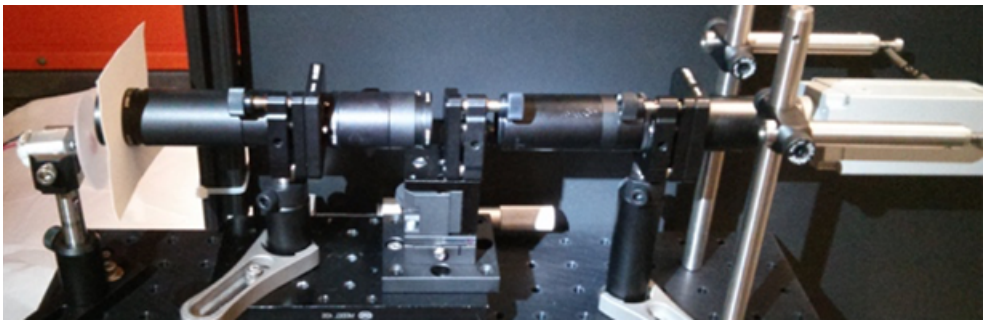

Figure 6.12: Etalon imaging system picture. The picture depicts the actual imaging system shown in the schematic of Fig. 6.11. The etalon is 14.93 mm thick and is made of UVFS. The lens used to focus the image onto the CCD camera is a PCX lens with a 150 mm focal length. The CCD camera used is the PixeLink PL B959U.

order of the interference fringe, and θ is the angle at which the ray (with a given frequency and interference order) exits the etalon. Further, with knowledge of the imaging system, an expression can be derived that relates frequency to the position of the fringe on the imaging plane. The following equation is the result derived from applying the paraxial approximation:

$$\nu = \frac{mc}{2d} \frac{1}{\sqrt{n^2 - \frac{r^2}{F^2}}}. \tag{6.10}$$

It relates the frequency of the spectrum (ν) to positions on the image plane (r). F is focal length of the lens used to focus the interference pattern onto the CCD camera. This allows the etalon images to be mapped into frequency distributions.

In our analysis of the PDL output frequency spectrum, we were able to confirm much of the findings of previous works ([KLS92, WRS84]) discussed earlier. The frequency spacing of longitudinal cavity modes is confirmed to be 450 MHz which is consistent with what is expected from the oscillator cavity length. We have also seen that the overall bandwidth of the PDL depends on the lasing wavelength as well as the grating order and can vary in between 2 and 6 GHz. A surprising discovery that was made in analyzing the PDL frequency spectrum was that the mode structure in the output pulses are very stable. Even after averaging over 100's of laser pulses of the PDL output, the individual laser cavity modes could be resolved as can be seen in the images taken by our etalon imaging system. By dithering a piezo on the oscillator cavity mirror in one of the PDLs, the length of the cavity is changed as are the frequencies of all the longitudinal modes. By applying a voltage ramp to the piezo, the resonant cavity modes can be effectively scanned over an FSR of the stationary PDL oscillator cavity. And by doing so, the frequency spectrum of the output is smeared out, which produces a more uniform frequency spectrum when averaged over time. See Fig. 6.13. Etalon images were taken where the interference fringes are radially binned and analyzed to determine the frequency spacing of adjacent cavity modes as well as the overall bandwidth. The Fourier limit for the individual cavity modes, based on a pulse width of 10 nsec, is expected to be around tens of MHz. Based on the radially binned etalon images, the individual cavity modes seem to have a width of $\sim$ 150 MHz, and this is roughly the resolution width of the etalon. We expect that the actual cavity modes are broader than

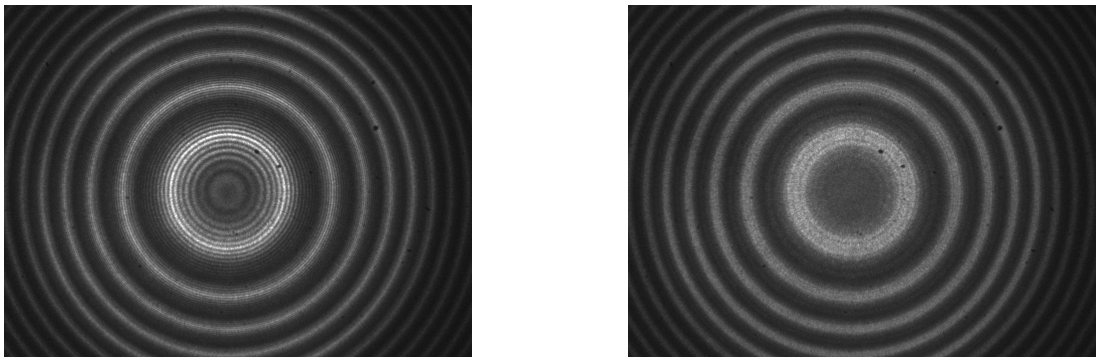

(a) Without Dither. **(b)** With Dither.

Figure 6.13: Etalon Images taken with the imaging system. (a) Images taken with the piezo dither off, an average of ~ 30 shots. (b) Images taken with the piezo dither on, an average of ~ 30 shots.

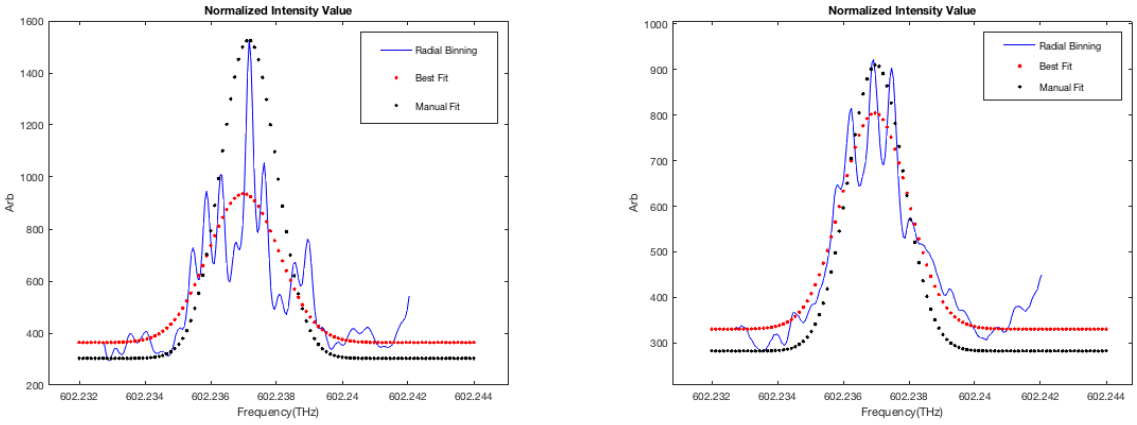

(a) Without Dither. **(b)** With Dither.

Figure 6.14: Radially binned etalon images. (a) Radially binned image with the piezo dither off, an average of ~ 30 shots. (b) Radially binned image with the piezo dither on, an average of ~ 30 shots.

the Fourier limit due to the optics in the oscillator cavity, however, we have not determined the actual width of these individual modes.

These images show that the frequency dither does in fact make a difference in the PDL output spectrum. To scan over VUV frequencies, the undoubled PDL (tuning PDL) is scanned in finite time intervals equal to 1 second, while the doubled PDL remains fixed at the particular two-photon resonance in Xe. For a given one second interval of illumination, the grating position of the tuning PDL is held constant while the piezo on the oscillator cavity mirror is dithered. The ramp applied to the piezo is a 1 Hz sawtooth voltage with a fifty percent duty cycle. It is adequate to cover two FSR's of the stationary oscillator cavity, one FSR is scanned on an up sweep and another on a down sweep of the voltage ramp. In this manner, 30 dithered pulses are distributed over an FSR per second. In any subsequent 1 second time interval, the tuning PDL grating is changed by a single grating step. This shifts the center of the tuning PDL spectrum by approximately 500 MHz. And for every step of the tuning PDL grating, each of the cavity modes are effectively walked back and forth over an FSR of the PDL oscillator cavity. This method of stepping the tuning PDL grating and dithering the oscillator cavity modes helps ensure a more uniform VUV production over the scan range.

It was previously mentioned that the seeded pump for the PDL's can have some benefits. It has been noticed that the shot-to-shot frequency spectrum of the output from the pulsed dye lasers seem to have less intensity variations in the different cavity modes when pumped with the seeded laser. It has also been noticed that when doubling this PDL output, an increase by roughly 20 percent in the doubling efficiency is possible. This can be attributed to a narrower bandwidth of the PDL with more power in the center cavity modes which results in more efficient doubling of the light. And finally, these effects do seem to propagate and eventually affect the VUV production. VUV pulse intensities are much more stable with the seeded pump.

6.3.2.2 VUV Pulse Energies

To measure the photon flux of the pulsed VUV light we utilize a pyro-electric detector, the Gentec QS5-IL. Pyroelectric detectors operate on the principle of pyroelectricity. Materials with a given natural dipole orientation can store large internal electrical fields. When a sudden change in temperature is produced, the orientations of the dipoles can change slightly which can lead to potential differences across the material. A general design of a pyroelectric detector can be seen in Fig. 6.15. A light absorbing material is thermally coupled to a

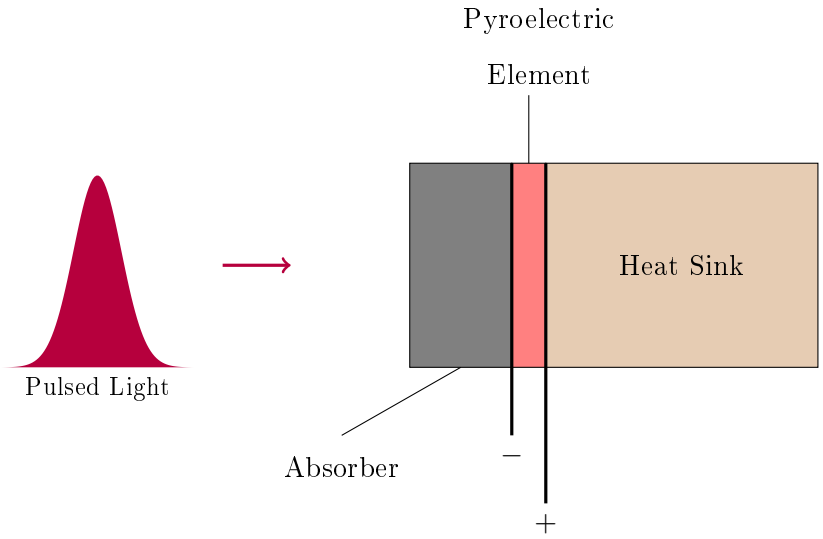

Figure 6.15: Pyroelectric detector general schematic. A pulse of light is absorbed by the absorber. This produces a change in temperature which affects the orientation of the dipoles in the pyroelectric element, and this in turn produces a voltage across the element. As the heat dissipates via the heat sink, the pyro element recovers and is ready to register another pulse of light.

pyroelectric element encased by electrodes. As pulses of light are absorbed by the absorber, a temperature change is induced which then produces a voltage across the pyroelectric element and the electrodes. The generated current can then be fed into a load circuit. As the heat sink dissipates the heat away, the absorber and pyroelectric elements recover and become available to register another pulse. The current (I) produced by the pyroelectric element can be described by a simple model.

$$I = p(T)A\frac{dT}{dt} \tag{6.11}$$

In the above equation, p(T) is the temperature dependent pyroelectric coefficient, A is the area of the front electrode, and $\frac{dT}{dt}$ is the induced temperature change.

The QS5-IL detector is very desirable for our application. These models of pyroelectric detectors involve the integration of a low-noise amplifier to the pyroelectric element which results in a high gain and high performance detector suitable for pulsed light with energies as low as tens of nJ. Pyroelectric detectors are not typically manufactured for operation in the VUV. Some work was involved in getting the detector working properly for our application. It was mentioned earlier that pulsed UV and VUV light can typically knock electrons off of metal surfaces via the photoelectric effect. When pulsed VUV or even scattered UV light is incident on the detector housing, the generated photoelectrons produce a false negative signal which prevents accurate energy measurements of the VUV pulses. To remedy this, we added a Cu iris very close and just upstream of the detector surface and housing. The iris diameter is slightly smaller than the detector housing diameter. A negative voltage can be applied to the Cu iris which prevents the ejection of photoelectrons from the detector housing. Additionally, we added a BK7 iris just upstream and very close to the Cu iris. It has a slightly smaller diameter than that of the Cu iris and serves to absorb any scattered VUV and UV light that may be incident on either the Cu iris or the detector housing surfaces. The BK7 iris is typically sufficient in reducing the scattered light on the detector housing which in turn prevents the production of photoelectrons, and has eliminated the need for the applied voltage to the Cu iris.

Unfortunately, these detectors are not calibrated by the manufacturers in the VUV. We attempted to contact NIST in an effort to get these detectors NIST traceable, but at the time the facilities they had available were not equipped for calibrating detectors with pulsed VUV light. Instead, we conducted our own conservative calibration. The manufacturer was able to provide data on the absorption of the detector surface at different wavelengths. Using CW and pulsed laser sources, we confirmed the absorption of the surface at select visible wavelengths. The manufacturer also provided an energy calibration of the detector near 600 nm. We confirm this energy calibration by cross checking the energy readings with another model Gentec, the QE25. With a confirmed energy calibration at visible wavelengths along

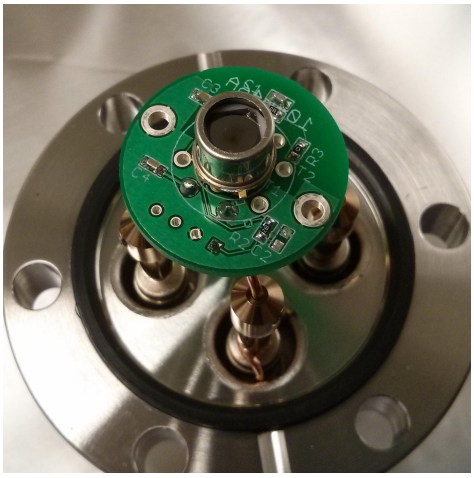

(a) Without Shield.

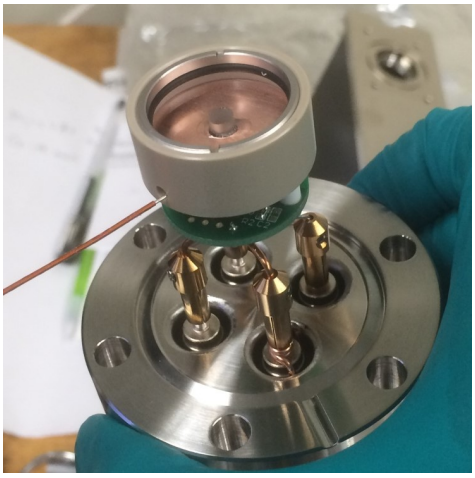

(b) With Shield.

Figure 6.16: Modified Gentec QS5IL. (a) An image of the bare detector. (b) An image of the detector with the necessary modifications for proper VUV calibrations. These include the Cu iris and a BK7 iris.

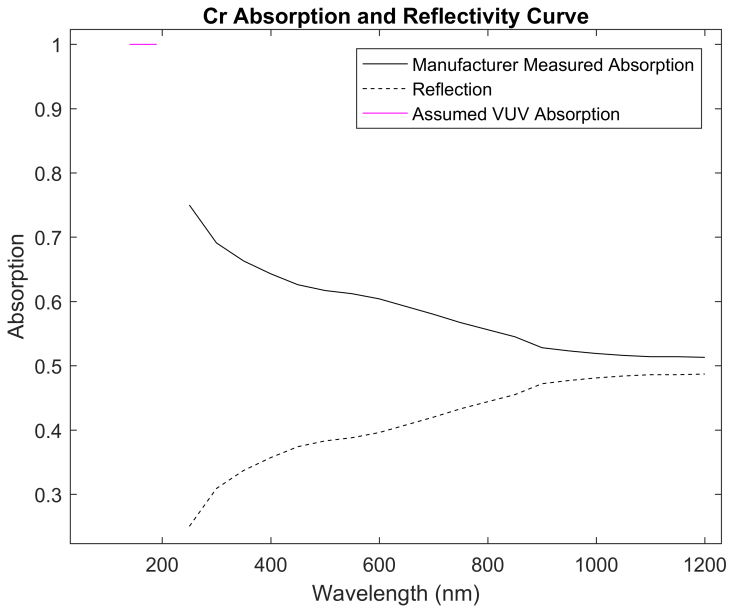

Figure 6.17: Gentec QS5-IL surface absorption curve. With a confirmed detector surface absorption and detector sensitivity at known visible wavelengths, the sensitivity in the VUV can be determined by scaling with respect to the given absorption curve. The most conservative VUV pulse energies are given by assuming 100% absorption at VUV wavelengths.

with the absorption curve for the detector surface, we can determine the detector sensitivity at VUV wavelengths. The most conservative value to use for the detector absorption at VUV wavelengths is 100%. This means that no VUV is reflected from the surface and all incident photons are converted to heat, which would produce the maximal response signal. This ensures that the most conservative values for the VUV pulse energies are reported.

It was mentioned previously that we utilize homemade Cu detectors for pulsed UV and VUV detection. Besides being relatively inexpensive and simple to operate, these detectors can also be calibrated. In Fig. 6.18, a typical response of the Gentec QS5-IL and the Cu detector are shown for pulsed VUV light. For the Cu detector response, there is an initial

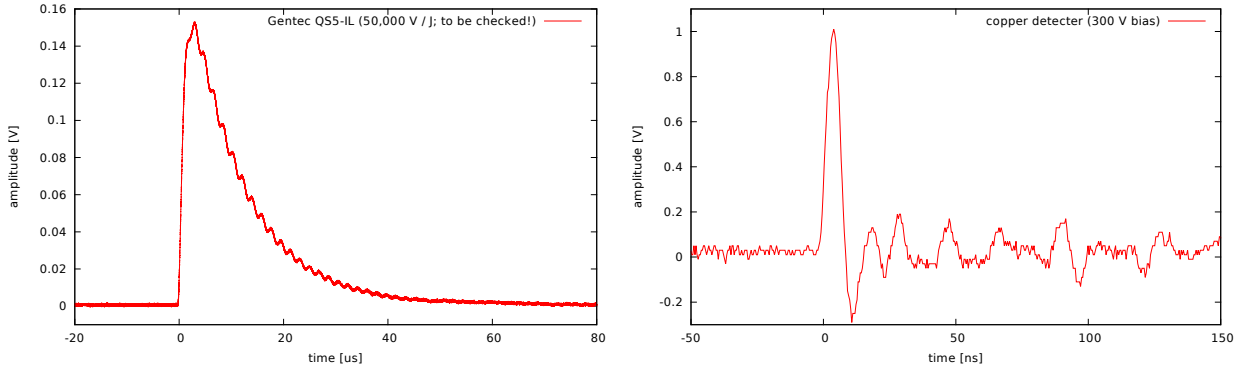

(a) QS5-IL Response.

(b) Cu Detector Response.

Figure 6.18: Detector response to pulsed VUV light. (a) The Gentec QS5-IL response. (b) The homemade Cu detector response. There is the possibility to calibrate the homemade Cu detectors against the Gentec QS5-IL.

sharp increase in amplitude due to the photoelectrons being effectively captured by the positively biased Cu "collection cylinder" surrounding the incident "emitter disk". The ringing in the tail can be attributed to secondary emissions of photoelectrons from the "collection cylinder". The pulse heights of both the Cu detector and the Gentec QS5-IL can be measured over a range of pulse energies to test for linearity in the Cu detector response.

Our laser system has been able to achieve pulse energies in excess of 40 uJ. For normal day-to-day operations and during typical data runs, we operate at VUV pulse energies of 10 uJ.

6.3.2.3 Light Collection Efficiencies

As in the experiments at the Advanced Light Source, we perform similar calibrations to the detectors used in the current experiment at UCLA. The solid angle fractions are once again determined by using Zemax as well as homemade softwares. The photomultiplier tubes utilized in the current experimental configuration are of the same type, they are of the head on design, model R6835. Due to the large photocathode area and relative insensitivity to wavelengths red of 200 nm, these PMT's are ideal given our experimental parameters. The large photocathodes are advantageous as they can collect more fluorescence photons eliminating the need for additional optics and complicated alignments. The photocathode material (Cs-I) is solar blind, eliminating the need of bandpass filters which also significantly reduce the overall transmission of potential signal photons. And by being mostly insensitive to the Cherenkov spectrum shown in Fig. 4.6 along with an optimized light collection efficiency, we become sensitive to longer lifetimes for the decay from the isomeric level.

The quantum efficiencies are measured similar to before. A deuterium lamp and monochromator setup along with the NIST calibrated AXUV100 photodiode (manufactured by Opto-Diode Corporation) provide a means for determination of the detector quantum efficiencies. The quantum efficiency of the PMT photocathode is determined by applying a positive voltage (typically +100V) to all the dynodes and the anode, and then reading a current signal from the cathode as ejected electrons are attracted away from it. The current is measured with a Keithley 6485 picoammeter. The two photomultiplier tubes are mounted differently inside the spectroscopy chamber. The respective solid angle fractions along with the detector quantum efficiencies then allow us to determine the total light collection efficiency for each detector. There is an underlying assumption here which is that all of the photoelectrons produced by the photocathode are efficiently amplified in the dynode chain and produce a current signal which we can undeniably detect. To prove this, we can begin with some known amount of CW VUV photons, from the deuterium lamp for example, and the absolute flux can be confirmed with a calibrated detector such as our AXUV100 photodiode. This light can then be attenuated by a known amount with the use of measured filters to a level that is

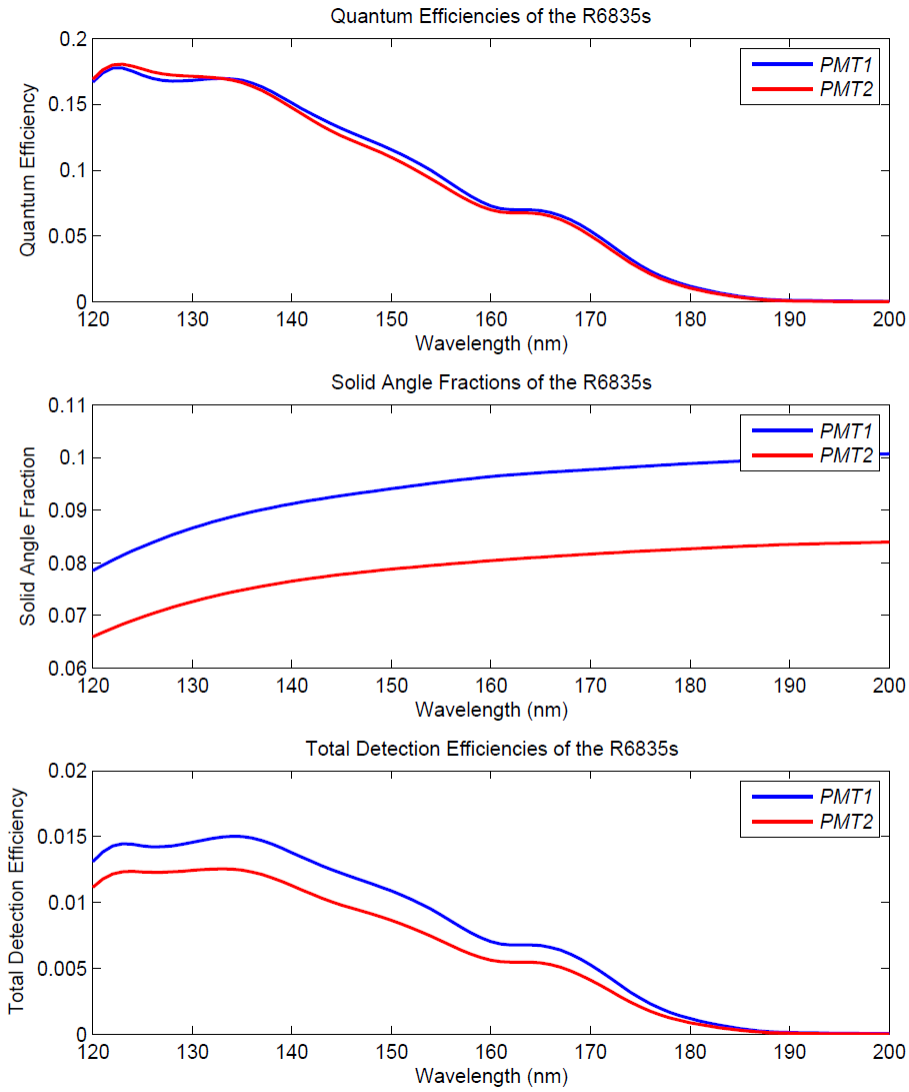

Figure 6.19: R6835 detector efficiencies. The figure on top displays the QE's for the two different PMT's utilized in fluorescence detection. The middle figure shows the solid angle fractions for the different orientations of the two different PMT's. And the bottom figure displays the overall detection efficiencies.

sufficient for photon counting. Then the number of detected pulses can be compared to the number of photons which are expected. As we have not yet conducted this measurement, we instead rely on the fact that the R6835 utilizes a linear-focused dynode structure which is very efficient in amplification of the initially produced photoelectron. With the application of higher voltages across the dynodes, we increase the overall gain of the PMT which promotes the production of adequate electrical response pulses.

6.3.2.4 Absolute Frequencies

In addition to flux and bandwidth, we must also monitor the absolute frequencies of both PDL's. For the tuning PDL, we use the WaveMaster wavemeter manufactured by Coherent. And for the fixed PDL, we have constructed a Xe reference cell, which ensures that we are in fact at the two-photon resonance of interest in Xe. The WaveMaster wavemeter is ideal for determining the location of the most intense cavity modes from the PDL output. This helps us identify the center of the output spectrum with a 1 pm resolution. Additional information of the frequency spectrum is provided by the etalon images. The reference cell scans provide an absolute calibration for the WaveMaster readings. Our Xe cell consists of gas at room temperatures so we can at least expect a Doppler broadened linewidth upon scanning the line. Considering the classical Doppler shift along with the Maxwell-Boltzmann distribution of particle velocities in an ideal gas, an expression can be derived for the Doppler broadened width:

$$\Delta f = \sqrt{\frac{8kT \ln 2}{mc^2}} f_o \tag{6.12}$$

where Δf is the full width at half maximum, k is the Boltzmann constant, T is the temperature of the gas, m is the mass of the emitter, and f_o is the rest frequency of the emitted light. For a reference cell at room temperature and a rest frequency corresponding to the emitted IR light upon relaxation after the two photon excitation, we can expect a broadening of a few hundred MHz. Actual scans of the reference cell were performed at different pressures and UV intensities. See Fig. 6.20. In these scans, we find that the broad lineshape feature is consistent with the width expected from the doubled PDL output.

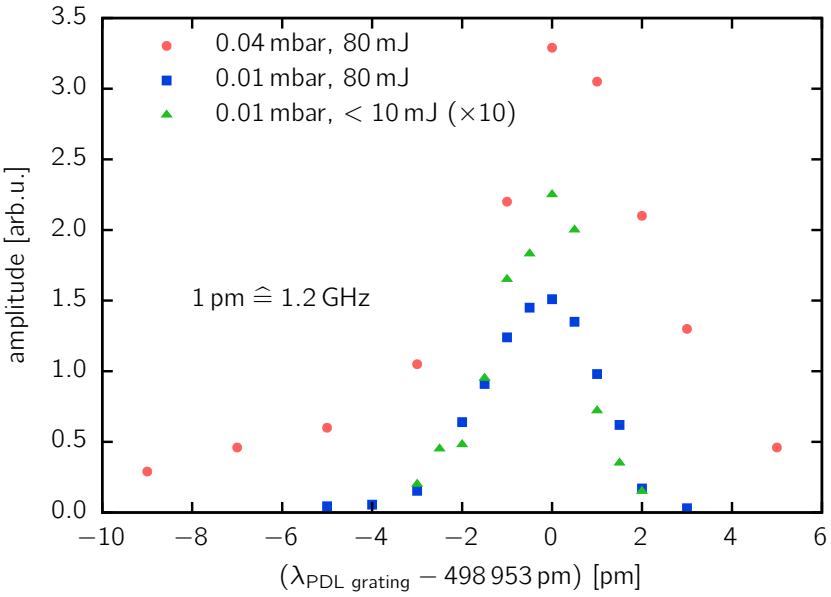

Figure 6.20: Xe reference cell scans. The scans are performed at different Xe pressures and pump intensities. At lower Xe pressures and pump intensities, the width of the feature is consistent with the doubled PDL output.

6.3.2.5 Polarization of the VUV

We measured the polarizations of the mixing beams as well as that of the generated VUV. According to the literature found on these older pulsed dye lasers, a vertical (or S) polarization is expected. We have confirmed this with the use of standard cube polarizers. For the doubled output from the PDL fixed at the two photon resonance in Xe, we use an MgF_2 window for a first attempt at determining its polarization. According to theory and software such as SNLO, we can expect a horizontally polarized UV output from Type I mixing and S polarized input beams. By orientating the MgF_2 window in the S and P configurations and at Brewster's angle, the intensity of the reflected UV can be measured to determine the polarization. This confirmed a horizontal polarization for the doubled PDL output. An attempt was made to utilize this same method to determine the VUV polarization, however this was not a simple measurement to conduct in vacuum. Instead we purchased an MgF_2 Rochon polarizer from Edmund Optics (item 68-825). As can be seen in Fig. 6.21, a Rochon polarizer will accept light of any polarization. It consists of two separate birefringent prisms

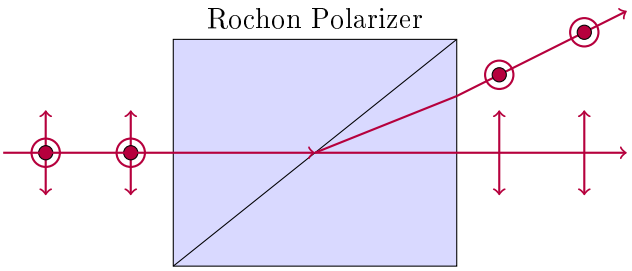

Figure 6.21: Rochon polarizer schematic. Two prisms are glued or optically contacted to one another. At the interface, the ordinary component in the beam is unaffected, while the extraordinary component undergoes refraction.

in optical contact with one another. Upon entrance into the second prism, the ordinary component of the incident light will experience no refraction, while the extraordinary component will refract. This causes an angle of separation between the different polarization components of the beam which allows them to be measured separately. Through this measurement, we learned that the VUV polarization is in fact horizontal.

6.3.2.6 Waveform Digitization and Post Processing

Since our most recent experiment at the Advanced Light Source, we have been using waveform digitization for capturing the signal responses from the output of the photomultiplier tubes. We utilize the DT5751 digitizer manufactured by CAEN. It has 4 independent input channels, each capable of a 1 Gs per second sampling rate. Additionally, we utilize the Digital Pulse Processing Pulse Shape Discrimination (DPP-PSD) firmware. The firmware allows us to set different threshold values for each channel. When an event leads to a trigger, a finite number of points of the waveform are sampled near the triggering event. The DPP-PSD firmware provides a nanosecond resolution time tag for every registered event. In addition, the numerically integrated "charge" of every digitized waveform is provided by default along with other useful information. This can be very advantageous for post-processing of data.

In Fig. 6.22, a histogram is constructed for all of the integrated charges that were registered in a single data point (typically 1000 sec of fluorescence collection after 2000 sec of illumination of the crystal). This can be recognized as the differential pulsed height spectrum

(PHS). In actuality, the PHS should be a histogram of the pulse-heights, but these typically have a linear relationship with the integrated charge. Much can be learned from these figures. There are several factors that can generally affect the pulsed height distribution of a photomultiplier tube. One of them is the gain or voltage at which the PMT is operated. Another factor that can potentially affect the pulsed height spectrum is the temperature at which the PMT is operated. By analysing the PHS of our photomultiplier tube output, we

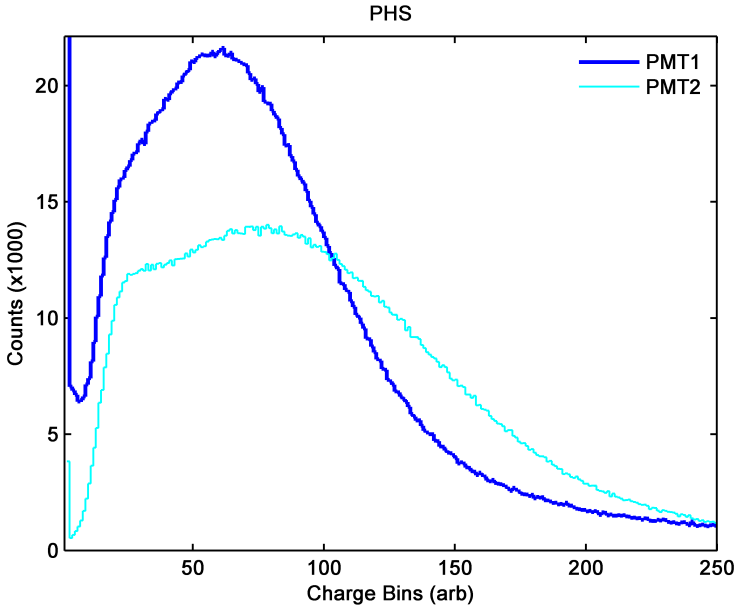

Figure 6.22: PMT pulsed height spectra (PHS). The area under each pulse is determined via the CAEN digitizer firmware and the resulting histogram of pulse areas, or equivalently pulse heights, for a single data point is shown in the plot. Fluctuations in temperature or voltage across the dynodes, and ultimately the gain of the PMT, will affect the PHS. Additionally, the response of the PMT's to VUV photons is typically well-behaved. Events that register very large pulses are not typical of VUV photons and can be attributed to radiation induced events such as scintillation or photoelectron emissions due to high energy gamma's incident on the photocathode and/or dynodes. The tails noticed in the PHS plots at high charge values are indicative of such radiation induced events.

have a means of monitoring the stability of the PMT's. If there is some issue with the high voltage power supply powering the PMT's, or if there is some significant temperature change in the lab, these pulsed height spectra will be affected.

The pulse height spectra can also provide some insight about the types of events that are being detected by the PMT's. The background fluorescence emitted from the crystal can be primarily attributed to radiation induced events. Radioactive decays events in the crystal can promote scintillation and the release of many photons. Additionally, a γ can directly interact with the photocathode or even the dynodes to yield a PMT response. The pulsed height spectra due to radioactive events versus CW photons can look different. For the case of CW photons, the PMT response is well-behaved. In comparison, the PHS from the crystal background has a large tail at higher charge values, as can be seen in Fig. 6.22. The large tail is indicative of larger pulses being registered by the PMTs. This can be attributed to multiple photons striking the detectors at once, or gammas interacting with the photocathodes and dynodes. In the search for fluorescence photons from the crystal, these larger PMT pulses should be very rare and we can often discriminate against them.

In addition to the pulsed height spectra, we can also use the time tags of all the detected events as a powerful tool to help post process the data. The background fluorescence from the crystal produces an overall count-rate of $\sim$2 kHz. As the number of counts within an arbitrary time interval is expected to have a Poissonian distribution; the distribution of time differences between consecutive events, or equivalently the inter-arrival time distribution, will be exponential. Given a count-rate Γ, the inter-arrival times should have a distribution defined by:

$$\mathrm{p(t)} = \Gamma \exp\left(-\Gamma \mathrm{t}\right), \tag{6.13}$$

where p(t) is the probability density function. And

$$\mathrm{P(t)} = 1 - \exp\left(-\Gamma \mathrm{t}\right) \tag{6.14}$$

is the corresponding cumulative distribution, which is the probability that an event will occur within a time t of a preceding event, given an overall count-rate Γ. For a truly Poissonian process with $\Gamma \sim 2$ kHz, a distribution of the binned inter-arrival times (using the nanosecond time tags generated by the digitizer for every event) should show and exponential with a 2 kHz rate. It can be seen in Fig. 6.23 that there is a large accumulation of events with inter-arrival times (IATs) of less than 10 usec. This accumulation of events cannot be

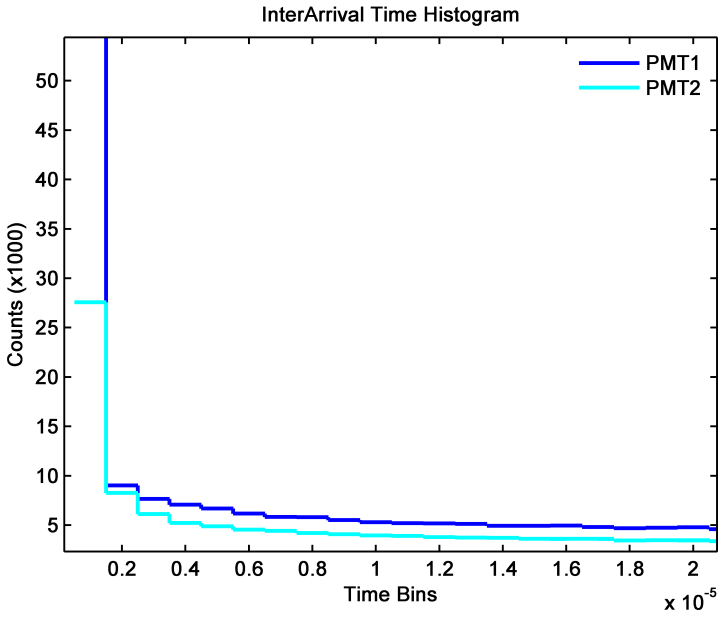

Figure 6.23: PMT inter-arrival time (IAT) distributions. The plot represents the histogram of time differences between consecutive events. For a well-behaved overall count-rate on the detectors, due to a Poissonian process, the IAT distribution should be exponential with decay constant indicative of the background count-rate. Although this is true for larger inter-arrival times, there is a pile up of events with very short inter-arrival times. This can be attributed to radiation induced scintillation producing many photons in a short time interval, which are then detected by the PMT's.

representative of a Possionian process with a 2 kHz countrate, and certainly not a signature from a long-lived decay from the isomeric level in ^{229}Th. For the given overall count-rate, the number of expected events with inter-arrival times less than 10 usec is negligible relative to the total number of collected events and therefore we can discriminate against these events when considering the longer lifetime exclusion bound. The pile up of events with short inter-arrival times can be a result of several different effects. We have seen that noise, which can occur spuriously, can result in multiple events being registered within very short times. The excess of events with short IATs may also be attributed to radiation induced scintillation within the ^{229}Th:LiSrAlF$_6$ crystal. A single radioactive decay occurring in the crystal can potentially generate lots of photons which can lead to consecutive detections by the PMT's within very short time intervals. These events are not desirable and certainly not indicative of long-lived fluorescence, and we can therefore safely reject them.

An advantage of having two similar PMT's is that we can look for coincident events. All of the digitizer channels are initialized with a common trigger and therefore they can be used to look for events which occur within very short time periods. By looking at the nearest neighbor time tags between events on the different channels of the digitizer and binning their differences, a coincidence histogram can be produced. In Fig. 6.24, it can be seen that there is a large pile of events on the different channels which were detected within just a few nanoseconds of each other. The number of events in this pile up accounts for 10 percent of the total number of events in both channels. Once again, this can be explained by the production of numerous photons following radioactive decay events in the crystal. This is similar to the previous case described except that our ability to reject events is improved with the second photomultiplier tube. It should be noted that the width of the coincidence histogram may be significantly affected by the electron transit times of the PMT's. And while it can be argued that such fluorescence can be due to superradiance from the decay of the isomeric level, considering the broadening of the transition in the crystal due to nearest neighbor magnetic dipole interactions, such a radiative decay is not expected.

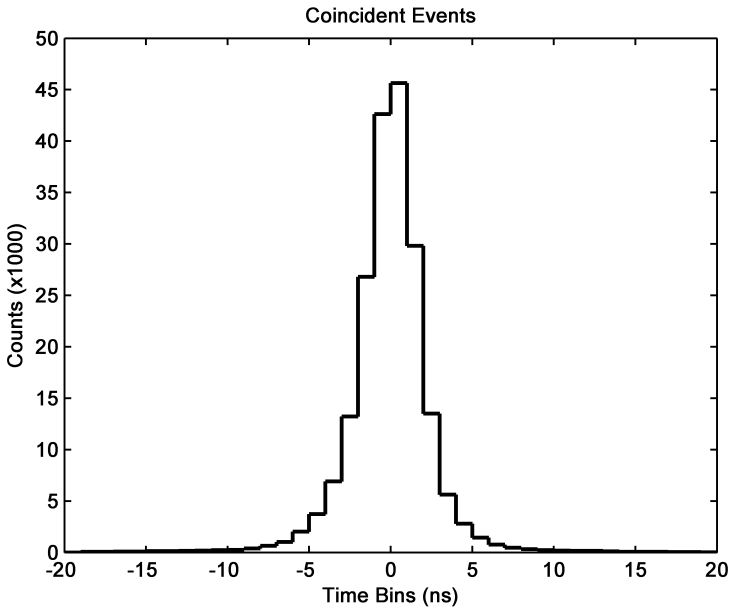

Figure 6.24: PMT coincident counts. A binning of the nearest neighbor time-tags, between the two different detectors, results in the following plot. A significant amount of events are being detected at effectively the same time by the different PMT's, as is indicated by the pile up of events at a time difference of zero. These events are not indicative of random fluorescence upon de-excitation from the isomeric level and can be attributed to radiation induced scintillation.

6.4 Implementation and Maintenance

As we scan over VUV frequency ranges in search of the transition, we do our best to maintain precision and consistency in the scans. In addition to reliable hardware and software for data acquisition, this requires a well-maintained VUV laser system. One of the cons of a tuneable and pulsed VUV laser system is that it requires laser dyes. Laser dyes are often carcinogenic and always messy. Some laser dyes have relatively long lifetimes while others may only last a few hours of intense pumping. For our pump powers, we typically operate at less than 150 mJ per pulse for the 355 nm output and less than 120 mJ for the 532 nm output. We've found that the 532 nm pumped laser dyes are generally more efficient at lasing and have longer lifetimes. For the 355 nm pumped dyes, the addition of 1, 4-diazabicyclo[2.2.2]octane (DABCO) has proven to enhance the lifetimes for certain dyes significantly. Over the last few years of operation, we have scanned over 400 nm with our tuning PDL, almost the entire visible spectrum. In this time, the laser has consumed over a quarter kilogram of laser dye powder and hundreds of gallons of solvents. Some solvents such as p-dioxane are also carcinogenic and must be handled with great caution. Depicted in Fig. 6.25(a) shows an accumulation of empty containers of various dye laser powders. Fig. 6.25(b) shows gallons of laser dye waste accumulated in just a couple weeks of time during continuous operation of the VUV laser system. Laser dyes and solvents are not the only items that our VUV laser consumes.

The intense powers that we push our system to causes damage to many optics. The outputs from the PDL's tend to eat away at mirror coatings as the beams are not always Gaussian and may contain hot spots. Similarly, anti-reflection coatings on optics also degrade with continued exposure to the beams. In addition to surface damage, the intense pulsed UV light of the frequency doubled PDL causes damage in the bulk material of optics. A bright fluorescence can be noticed from optics such as the input lens, input window, and separation lens as color centers are produced with continued exposure. The bright fluorescence is often accompanied by a reduction in transmission through the optic. While some of the optics used are easy enough to rotate, others must be replaced. Figure 6.26, (a) and (b), show color

(a) Empty laser dye containers.

(b) Laser dye waste.

Figure 6.25: Laser dye waste. (a) This waste consists of empty dye laser containers for various laser dye powders. (b) The gallons of waste shown is representative of the laser dye consumed in just a couple weeks of continuous operation.

center formation in the UVFS input window and the MgF_2 separation lens, respectively. With prolonged exposure to the UV beam, the fluorescence from the color centers becomes brighter.

A known issue for optical components in vacuum which are incident with UV and higher energy photon beams is hydro-carbon build-up. This tends to occur on most surfaces in vacuum that are incident with such beams. Optical components in our laser and spectroscopy chambers which suffer from hyrdo-carbon build-up include the separation lens, the ^{229}Th:lisaf crystal, and the Gentec QS5-IL detector. A brown build-up accumulates on the respective surfaces over time. UV and higher energy photons can break up residual gas molecules in a vacuum chamber. Due to the low pressures in the chamber and the radiation pressure exerted by the laser beams, the by-products of the broken-down molecules can find their way to optical surfaces. Reactions between by-products can occur to form non-volatile molecules which remain on the surface, and eventually form into hydro-carbon build-up.

To remedy this, we constructed a plasma cleaner. The plasma cleaner utilizes intense RF fields with low oxygen pressures to produce a plasma which emits UV light and produces oxygen radicals. The UV light breaks up the hydro-carbons on the surface of the affected

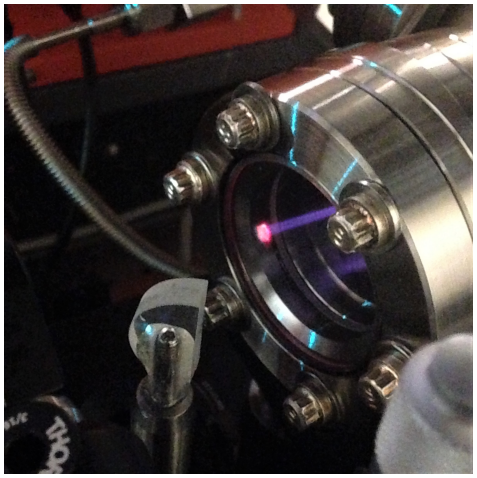

(a) Input window damage.

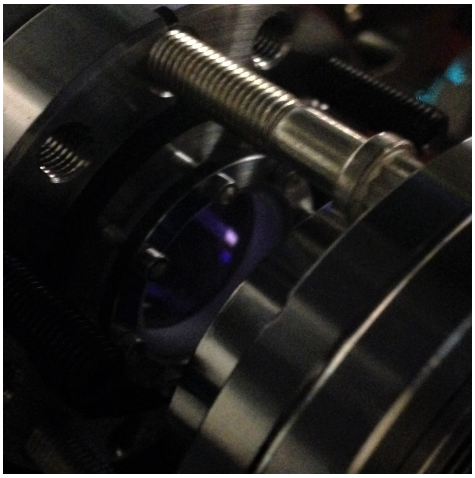

(b) Separation lens damage.

Figure 6.26: Color center formation in the bulk. (a) Intense pulsed UV light causes color-center formation in UVFS. The red fluorescence due to the color centers grows more intense with prolonged exposure to the UV beam. (b) Intense pulsed UV light causes color-center formation in MgF_2. The white-blue fluorescence due to the color centers grows more intense with prolonged exposure to the UV beam.

optics allowing the oxygen radicals to react with the formed by-products to form volatile molecules. These volatile molecules are removed with a roughing pump. We employ periodic plasma cleaning of our MgF_2 separation lens as well as the thorium crystal. Our plasma cleaning chamber consists of a 4.5" 6-way conflat cross. One of the ports is equipped with a leak valve (Duniway Stockroom, part 10671) through which oxygen is flowed. The opposite port is attached to a roughing pump (Agilent scroll pump SH-110). A sinusoidal wave of $\sim$ 900 kHz is produced with an Agilent function generator (model 33220A) and amplified with an HD17216 RF amplifier, as can be seen in Fig. 6.27. The output of the HD17216 is coupled to an RF plate in the 6-way cross via a power transformer. In parallel with the RF plate is a high impedance input scope for monitoring of the RF waveform and determining the resonant frequency of the RF plate in the chamber. The RF plate is placed roughly 14 mm above a grounded stainless steel mesh inside the 6-way cross. A ceramic boat is used to hold the crystal and is placed just underneath the mesh plate below the generated plasma. The cleaning process typically last 24 hours and the results on ^{229}Th:LiSrAlF$_6$ crystal B is

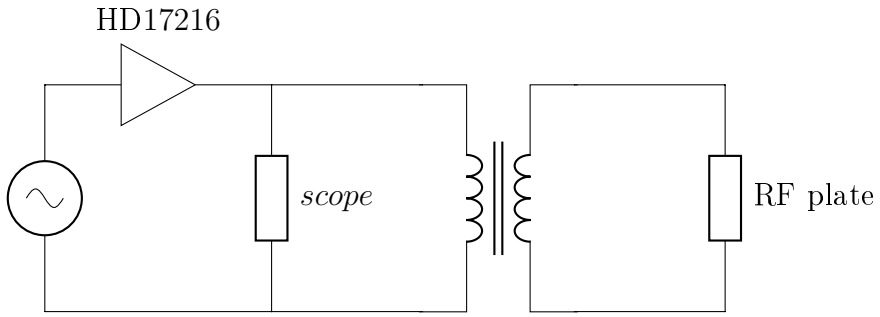

Figure 6.27: Plasma cleaner circuit. A sinusoidal waveform ($\sim$ 900 kHz)is generated with a function generator (Agilent 33220A) and amplified with the HD17216 RF amplifier. The output from this amplifier is coupled to the RF plate in the plasma cleaning chamber via a power transformer. The output of the transformer is impedance matched to the RF plate in the chamber. A high input impedance scope monitors the RF waveform and aids in determining the resonant frequency of the RF plate in the chamber.

shown in Figure 6.28.

In addition to the plasma cleaner, we also constructed a downstream asher which operates under the same principles and with the same hardware as the plasma cleaning chamber. A 2.75" 4-way cross is equipped with an RF rod, whose surface is $\sim$ 14 mm in distance from the grounded walls of the 4-way cross, as can be seen in Fig. 6.29. A similar leak valve (Duniway Stockroom, part 10671) is connected to a port opposite of the roughing line. The power is supplied to the rod in exactly the same way as was done with the RF plate in the plasma cleaning chamber. The ultimate goal of the downstream asher will be to attach it to our spectroscopy chamber such that all of the surfaces which were incident with the VUV beam can be properly cleaned and removed of hydro-carbon build-up.

6.5 Analysis and Results

For interrogation of the ^{229}Th:LiSrAlF$_6$ crystals, we utilize crystal B as described previously. The scans are conducted in a similar manner as was done at the ALS. Illumination of the crystal is followed by fluorescence detection. An illumination cycle is typically 2000 seconds or greater followed by 1000 seconds of detection. As we scan, we continue to produce

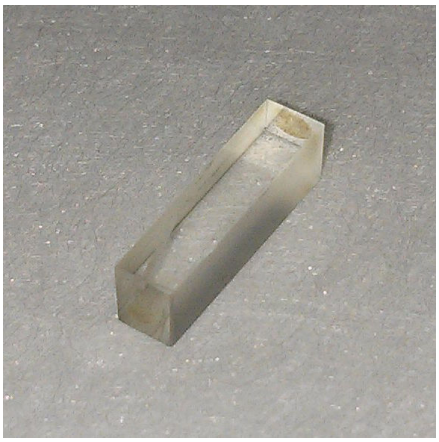

(a) HC deposits on thorium crystal.

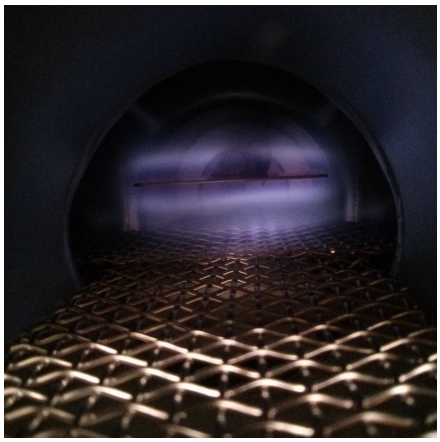

(b) Oxygen plasma in RF fields.

(c) Ceramic boat with thorium crystal.

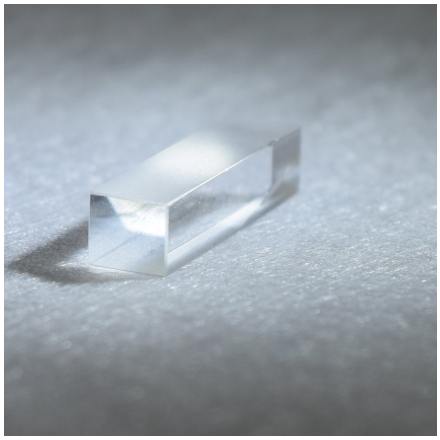

(d) Cleaned thorium crystal.

Figure 6.28: Plasma cleaning of the ^{229}Th:LiSrAlF$_6$ crystal. (a) The crystal is shown just after the most recent experiments at the ALS. The hydro-carbon build-up is clearly visible. (b) The oxygen plasma is shown to form between the ground mesh and RF plate. The ambient pressure in the chamber, the RF frequency, and the RF power are all important factors in generating an adequate plasma. (c) The thorium crystal is contained in a ceramic boat which is placed underneath the ground mesh just below the generated plasma. (d) The resulting "clean" crystal is shown after $\sim$ 24 hours of continuous plasma cleaning.

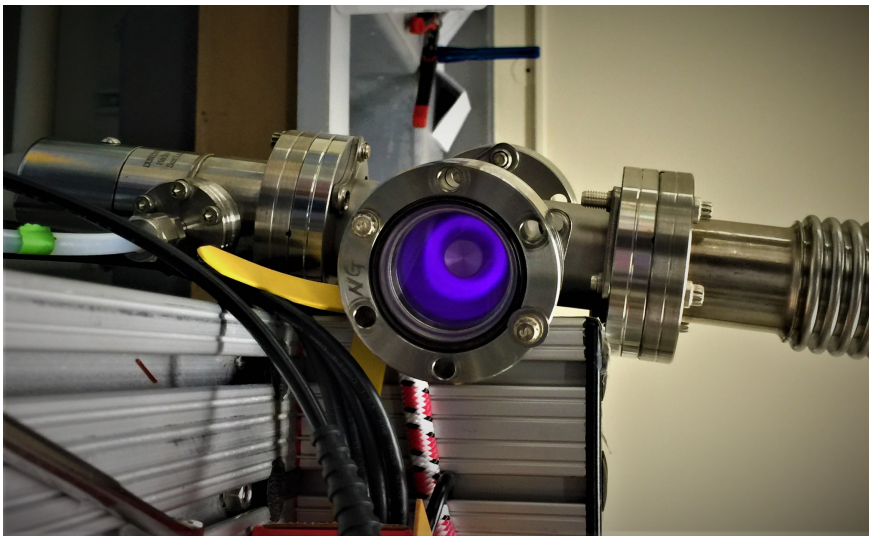

Figure 6.29: Downstream asher. The operation of the asher is similar to that of the plasma cleaning chamber. The goal of the asher will be to attach it to our spectroscopy chamber such that it can be removed of hyrdro-carbons which may have built over time and with exposure to the VUV beam.

exclusion bounds in the same manner as was done with the ALS data. There are some subtle differences in the excitation scheme and analytical model.

6.5.1 Excitation Model

If we refer back to the excitation model described in chapter 3, and in particular to the 2-level system rate equation describing the population in the excited state (4.1), we can simply replace the ALS excitation source with one described by our VUV laser system. $\Phi(\omega)$ in this rate equation is represented by an inhomogeneously broadened lineshape function. We have shown that the frequency spectrum of the pulsed dye lasers are Gaussian with a bandwidth in between $\sim 2-6$ GHz, see Fig. 6.14. There are resolvable cavity modes present in the spectrum. The tuning PDL's output is dithered over an FSR of the PDL oscillator cavity every second, effectively smearing out the spectrum. The PDL fixed at the two photon resonance in Xe is not dithered however, but through doubling, mixing of the different cavity modes should result in a more homogenous output spectrum. The actual frequency spectrum of the VUV will be more complicated and we have yet to adequately characterize it. For

now, we approximate the VUV lineshape as it will be rather complicated in actuality due to the pulse-to-pulse variations in the PDL frequency spectrums. The overall VUV lineshape, averaged over many shots, should be approximately Gaussian with a bandwidth given by the quadrature sum of the bandwidths of the individual beams involved in the mixing process. The VUV is generated with 4 photons from the fixed PDL output (2 photons double to generate the UV beam from which two photons are involved in the VUV generation) and one photon from the tuning PDL. The bandwidth of the VUV (Γ_{VUV}) is then given by:

$$\Gamma_{VUV} = \sqrt{4\Gamma_{fixed}^2 + \Gamma_{tuning}^2}, \tag{6.15}$$

where Γ_{fixed} is the bandwidth of the PDL which is fixed at the 2 photon resonance (499.257 nm) and Γ_{tuning} is the bandwidth of the tuning PDL.

The scan over VUV frequencies is done according to the method described earlier. The tuning PDL center frequency is "stepped" in $\sim$ 500 MHz increments at a rate of 1 Hz. This is accomplished with single grating steps toward shorter wavelengths. The number of grating steps in a given illumination cycle can vary from a couple hundred and above. All of the "steps" combine to form a "sweep" over some particular range of VUV frequencies. And for a given data point, several sweeps over the same range of VUV frequencies are taken. Given this description, we can describe a legitimate excitation scheme. Let us call the frequency traversed in a step Γ_{step} and let the actual transition frequency (ω_o) lie somewhere in the scan range. In a single sweep, we can assume that the transition sees a number of pulses (n_P) given by:

$$n_P = 30\text{FLOOR}\left(\frac{\Gamma_{VUV}}{\Gamma_{step}}\right), \tag{6.16}$$

where FLOOR is just the floor function and a factor of 30 represents the YAG repetition rate. As the tuning PDL's grating is stepped every second, FLOOR($\frac{\Gamma_{VUV}}{\Gamma_{step}}$) represents the number of seconds that the transition is exposed to the VUV laser, and still lie within its bandwidth. To be conservative, we can assume that for each of these pulses, the transitions frequency is detuned from the center VUV frequency by $\Gamma_{VUV}/2$. We can assume that the pulse duration is 10 ns, and lets call this Δt_P. Neglecting the $\sim$ 33 ms delay between pulses (this is a valid approximation given the lifetimes that we are sensitive to) results in an effective illumination

time (Δt_{ill}) given by:

$$\Delta t_{ill} = n_P \Delta t_P. \tag{6.17}$$

The sweep time is considerable and will need to be accounted for. The excitation of ^{229}Th can then be modeled with the bandwidth, detuning, and effective illumination time as just described. But this excitation will occur for every sweep with delays given by its duration. In our experiment, this is approximately equivalent to the number of steps taken by the tuning PDL per sweep. The solution is numerically solved to get the total number of excited thorium nuclei given the experimental parameters.

6.5.2 Exclusions

To obtain the most conservative exclusion, we must consider the transition frequency ω_o to lie at the beginning of every sweep. This means that there is a delay in between excitation and the subsequent fluorescence detection. We obtain the long and short lifetime limits in exactly the same way as done with the ALS data utilizing the Maximum Likelihood method, delta chi-squared statistics, and the Feldman Cousins prescription to compare against. For every single data point, which lasts about an hour or longer, an analysis report is automatically generated and emailed to us for our viewing pleasures. These can be seen in Figures 6.30 and 6.31. The reports include significant experimental parameters such as the VUV pulse energies during illumination, the PDL wavelengths over the scan, and of course the long and short lifetime exclusion bounds. We also monitor the PHS, the IAT distribution, and coincident count histogram for every single data point.

We have scanned from $\sim 6.8 - 8.3$ eV in the course of the last couple years with no clear signature of fluorescence decay that could be due to the relaxation from the isomeric level. We have over 6 terabytes of data collected. The resulting preliminary exclusion region is shown in Fig. 6.32. The gray shaded region represents the current exclusion bounds generated from the scans conducted with the VUV laser at UCLA (the dip in the long lifetime exclusion bound near 8 eV is not real and should be corrected), and the red shaded region represents the exclusion bounds obtained from the scans conducted at the ALS synchrotron.

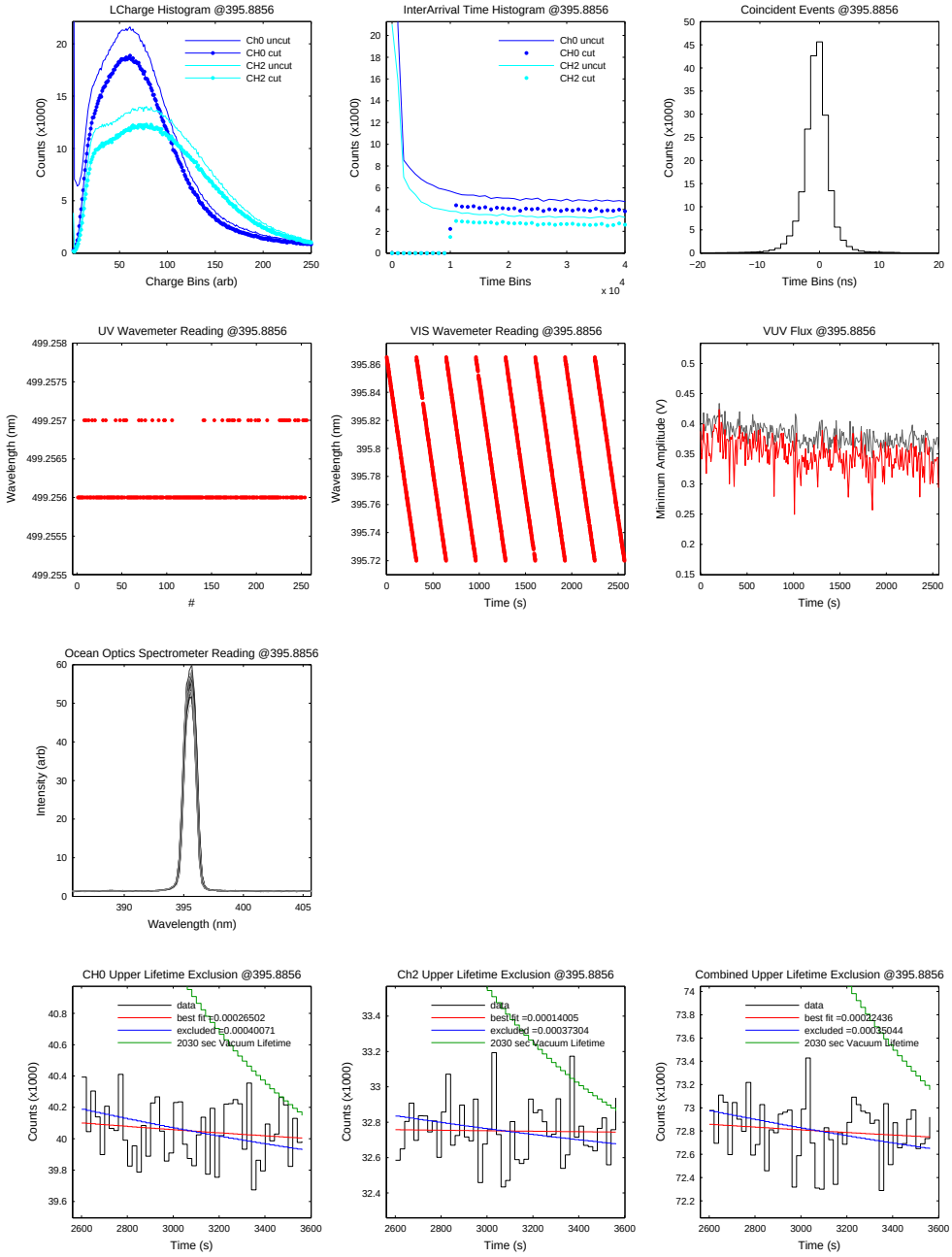

Figure 6.30: Jeet's analysis report. The report shows some relevant parameters of the scan for a single data point which include the VUV pulse energies and the wavelengths of the center of the PDL output spectrums over the course of the scan.

^{229}Th Search with Pulsed VUV Laser: 395.8856 nm

Hudson Group, Department of Physics and Astronomy, University of California, Los Angeles, California 90095, USA[1]

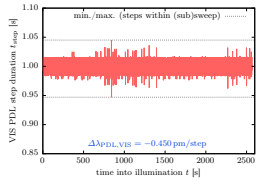

Figure 1: VIS PDL wavelength sweeps.

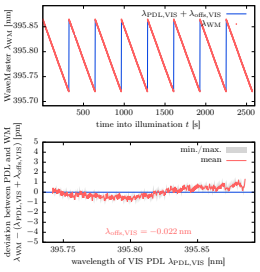

Figure 2: VIS PDL wavelength during illumination.

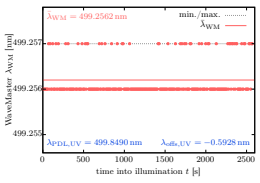

Figure 3: UV PDL wavelength during illumination.

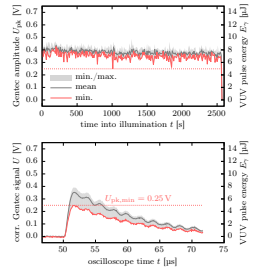

Figure 4: Pulse energies recorded with Gentec QS5.

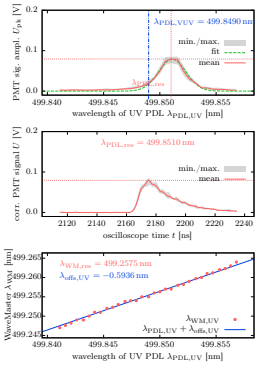

Figure 5: Xenon reference spectroscopy.

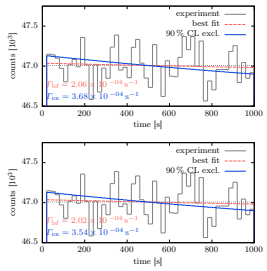

Figure 6: Long-lived isomeric linewidth bounds. The transition frequency is assumed to be close to the VUV start (top) and stop (bottom) frequency of a sweep, respectively.

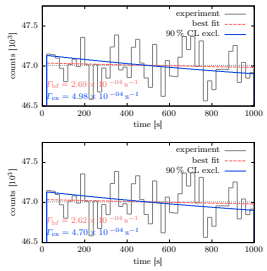

Figure 7: Long-lived isomeric linewidth bounds assuming a reduced photon flux.

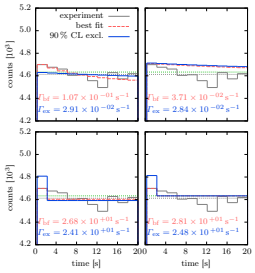

Figure 8: Short-lived isomeric linewidth bounds.

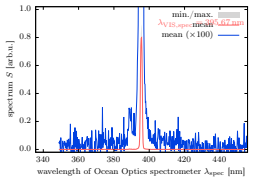

Figure 9: VIS PDL frequency spectrum.

mean UV wavelength [nm]:	499.2562
min. UV wavelength [nm]:	499.2560
max. UV wavelength [nm]:	499.2570
min. VIS wavelength [nm]:	395.7200
max. VIS wavelength [nm]:	395.8650
VUV start wavelength [nm]:	182.28870
VUV stop wavelength [nm]:	182.31940
VUV start frequency [THz]:	$2\pi \times 1644.6029$
VUV stop frequency [THz]:	$2\pi \times 1644.3254$
VUV frequency step [MHz]:	$2\pi \times (-870)$

Table 1: Summary of parameters.

[1]date of analysis: April 6, 2018; source directory: `/data/cwrsync/data/2018-04-06_data_run`

Figure 6.31: Schneider's analysis report. The analysis report is automatically generated and emailed to us at the end of every single data point. The report shows relevant parameters of the scan such as the reference cell scan over the two-photon resonance in Xe as well as the long and short lifetime exclusion bounds.

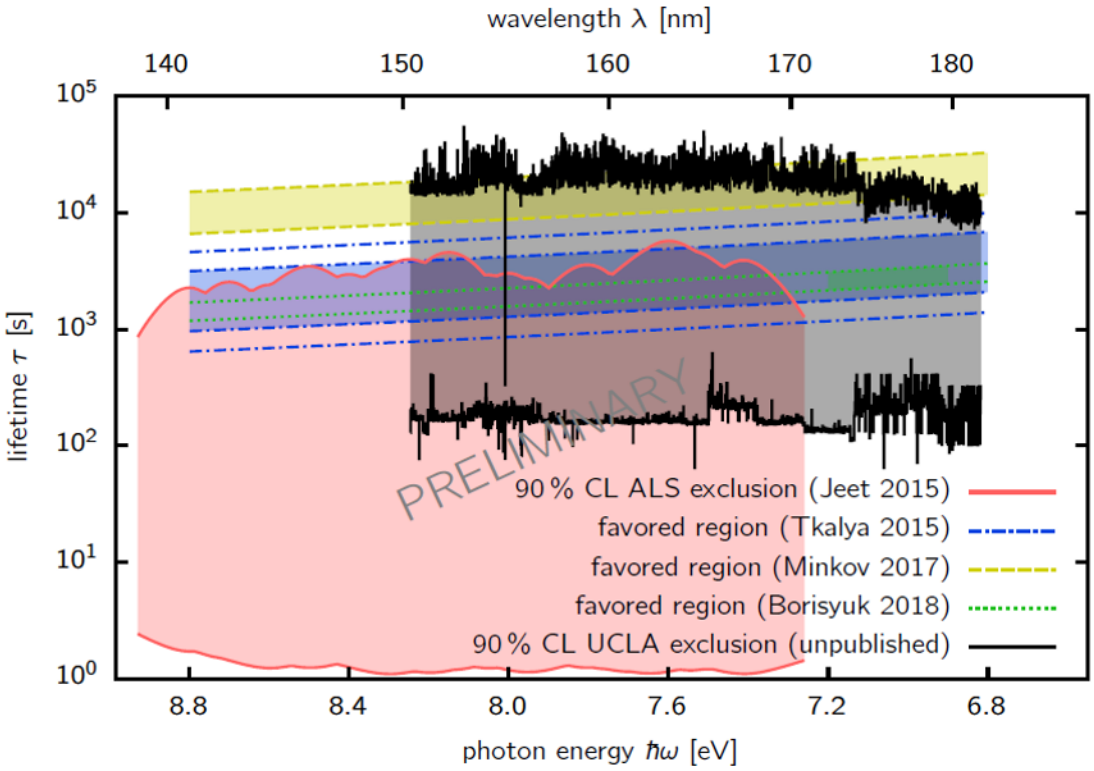

Figure 6.32: Current exclusion region. The gray shaded region represents current exclusion bounds (the dip in the long lifetime exclusion bound near 8 eV is not real), and the red shaded region represents the exclusion bounds obtained from the scans conducted at the ALS. The blue shaded region represents the "favored region" as described previously. The yellow shaded region represents an alternative "favored region", described in [MP17]. And finally, the green shaded region represents the search results from a recent experiment involving excitation of ^{229}Th through inverse internal conversion (IIC) [BCK18].

The blue shaded region represents the "favored region", or range of expected lifetimes for the decay from the isomeric level, as described previously. The yellow shaded region represents an alternative "favored region", described by a Hamiltonian including the effects of a quadrupole-octopole deformed nuclear core and the single-particle motion of the unpaired nucleon, as well as the Coriolis and pairing interactions [MP17]. And finally, the green shaded region represents the search results from a recent experiment involving excitation of ^{229}Th through inverse internal conversion (IIC) [BCK18]. More on this experiment in the next chapter.

CHAPTER 7

SNSPDs and the Utilization of the Internal Conversion Decay Channel

Internal conversion is a process in which a nucleus undergoes a non-radiative relaxation, which instead of producing a gamma ray equivalent to the energy difference between the transitioned levels, causes the ejection of a bound electron, resulting in an ionized nuclei. For isolated nuclei, a valence electron can then fall into the hole produced by the ejected electron, yielding an x-ray photon or Auger electrons. The mechanism which enables this involves the coupling of the inner shell electronic wavefunctions with the excited state nuclear level. This allows the electron to take energy away from the nuclear excited state without the emission of an intermediate γ. Recently, there have been many experiments conducted involving the IC channel available to the isomeric level in ^{229}Th. These experiments confirm theoretical predictions on the lifetime of the IC decay and also constrain the isomer energy level in between the 1st and 3rd ionization potentials (6.3-18.3 eV) [WSL16, SWT17]. We hope to conduct an experiment that is sensitive to the IC decay channel in which detection is carried out with the use of superconducting nanowire single photon detectors (SNSPD's). The chief advantage of the experiment involving SNSPD's is that it may be able to provide significantly tighter constraints on the isomeric energy level.

In the following chapter, some details about the IC decay channel in ^{229}Th will be discussed along with some recent experiments. I will then briefly discuss superconductivity in brief and provide some information regarding SNSPD's including operation and performance. Finally, the details of the experiments conducted at UCLA will be discussed along with some preliminary results.

7.1 Importance of the IC Channel

The chemical environment of ^{229}Th can significantly affect the half-life of the isomeric state [ST91]. It most likely explains why, given the currently accepted value for the isomeric transition energy, that many previous experiments performed in powders, solids and solutions produced null results [BNC01, KKH09, MHO03, Zim10, Swa12]; similarly, non-VUV sensitive measurements could have been affected by internal conversion [UBB99, SYC99]. The internal conversion process could also have strong implications for the experiments reported in Refs. [ZER12] and [YKK15]. Though crystalline material is used as host in these experiments, the charge state of the thorium atom is not known, since the thorium atoms are either implanted into [ZER12] or chemically adsorbed onto the surface of [YKK15] the crystal. Therefore, it is likely that some, if not all, of the thorium atoms are in a local chemical environment that experiences electronic conversion. As we will see in the following, it is unlikely the isomeric transition can be detected in such a system, if internal conversion is present. Thus, as aptly pointed out in Ref. [YKK15], any conclusions drawn from experiments of this type should be considered preliminary until the thorium chemical environment is known.

If the energy of the isomeric level $3/2^+3/2[631]$ in the ^{229}Th exceeds the binding energy of electrons in the local chemical environment, the main channel of decay is electronic conversion [ST91]. Therefore, the lifetime of the isomeric state can be significantly reduced compared to the radiative lifetime only. In the following, we consider electronic conversion of the isomeric state in the neutral Th atom as an example to give a rough estimate of the lifetime for the ^{229}Th isomeric state in such a chemical environment.

Electronic $M1$ and $E2$ conversion from the valence $6d$ and $7s$ shells of the thorium atom is possible for the nuclear isomeric transition. The ratio of radiation widths of the $E2$ and $M1$ transitions with energy of 7.8 eV in the ^{229}Th nucleus is $\Gamma_{rad}(W; E2)/\Gamma_{rad}(W; M1) \simeq 10^{-13}$ in the Weisskopf model, i.e. when the nuclear reduced probabilities are $B_{W.u.}(M1) = 1$ and $B_{W.u.}(E2) = 1$. Therefore, we can neglect the $E2$ contribution to the radiation width of the level for true values in the ranges $B_{W.u.}(M1; 3/2^+(7.8\text{ eV}) \rightarrow 5/2^+(0.0)) \simeq 10^{-1}$–$10^{-3}$ and

$B_{W.u.}(E2; 3/2^+(7.8\,\text{eV}) \to 5/2^+(0.0)) \simeq 1$–$10$, respectively. As for the conversion decay channel, our calculations for the thorium atom give the relation $\Gamma_{conv}(W; E2)/\Gamma_{conv}(W; M1) \simeq 10^{-6}$ in the Weisskopf model. Accordingly, for the true range of values for the reduced probabilities we find $\Gamma_{conv}(E2)/\Gamma_{conv}(M1) \leq 10^{-3}$ for a transition with energy of 7.8 eV in the ^{229}Th nucleus. Thus, we neglect the contribution of electronic $E2$ conversion to the isomeric state conversion lifetime.

The calculation of the probability Γ_{conv} was performed using code developed in [Sol] on the basis of known code in [BF79], and then advanced in [ST91]. The calculated electronic $M1$ conversion probability for the energy range 7.3 eV – 8.3 eV, using the reduced probabilities from Tables 5.1 and 5.2, are presented in Figure 7.1. Taking into account the uncertainties on the magnitude of the nuclear matrix element of the transition, the characteristic lifetime of the isomer in an atom is $\sim 10\,\mu$s. As a result, electronic conversion completely quenches the isomeric state non-radiatively. Thus, experiments looking for the emitted photons as a signal of the isomeric transition must ensure that the local chemical environment of the thorium atom does not support electronic conversion.

However, this is only one side of the issue. The $M1$ isomeric transition like the other $M1$ transitions between states of the bands $K^\pi[Nn_Z\Lambda] = 5/2^+[633]$ and $3/2^+[631]$, is first-order forbidden by the asymptotic quantum numbers of the Nilsson model [Nil55]. Indeed, we are considering $M1$ transitions where $\Delta K = 1$, $\Delta N = 0$, $\Delta n_Z = 0$, and $\Delta\Lambda = 2$, while the selection rules for the $M1$ transition allow the following change for the asymptotic quantum numbers for the case $\Delta K = 1$: $\Delta N_a = 0, \pm 2$, $\Delta n_{Z_a} = 0, \pm 1$, and $\Delta\Lambda_a = 0, \pm 1$ [Nil55] (the index a means "allowed"). Thus, the interband $M1$ transitions $K^\pi[Nn_Z\Lambda] = 5/2^+[633] \leftrightarrow 3/2^+[631]$ are weakly forbidden transitions by the number Λ. Phenomenology shows that the intensity of such $M1$ interband transitions are weakened by a factor 10^{-2n}, where $n = |\Delta N_a - \Delta N| + |\Delta n_{Z_a} - \Delta n_Z| + |\Delta\Lambda_a - \Delta\Lambda|$ for K-allowed transitions. In our case $n = 1$ and we can expect that such transitions have reduced probabilities $B_{W.u.}(M1; 5/2^+[633] \leftrightarrow 3/2^+[631]) \simeq 10^{-2}$.

The so-called anomalous internal conversion or the dynamic nuclear volume effect in internal conversion [CW56] is possible in transitions forbidden by the asymptotic selection

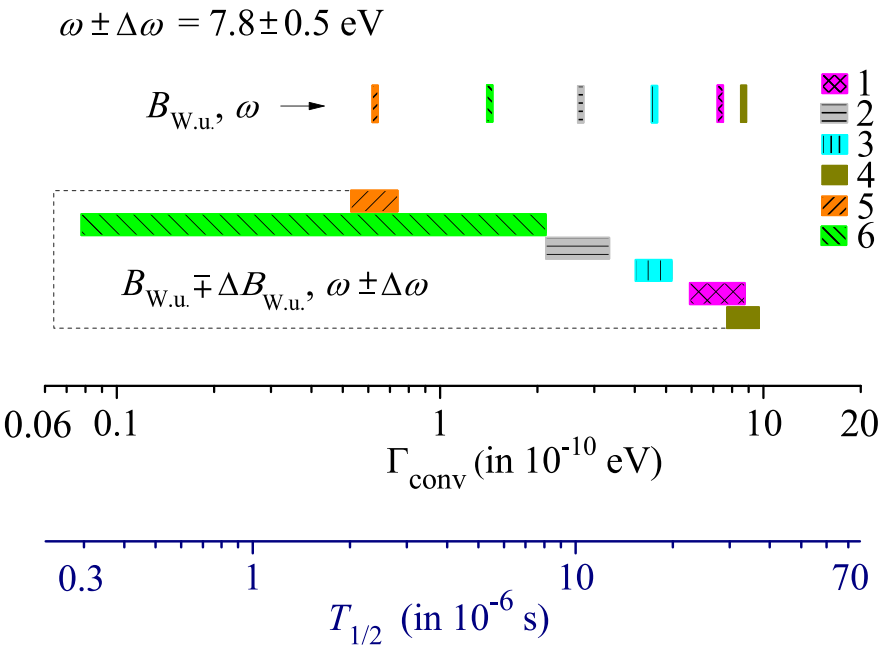

Figure 7.1: The ranges of possible conversion widths (the upper scale) and lifetimes (the lower scale) of the isomeric nuclear state in a neutral isolated Th atom. The designations are identical with designations in Fig. 5.2.

rules. Its essence is as follows. Amplitudes of the electron wave functions for the $ms_{1/2}$ ($m = 1, 2, 3...$) and $lp_{1/2}$ ($l = 2, 3, 4...$) (or K, $L_{I,II}$, $M_{I,II}...$) shells inside the nucleus differ from zero: $|\psi_{ms_{1/2},lp_{1/2}}(0)| > 0$. In internal conversion via these shells, the electron current effectively penetrates into the nucleus, and an "intranuclear'" internal conversion becomes possible. The new phenomenon arises if the coordinates of the electron current $j_e(r)$ and nuclear one $J_N(R)$ satisfy the condition $r < R < R_0$ (where R_0 is a nuclear radius). In this case, the intranuclear matrix element is changed. The new nuclear matrix element is not forbidden by the asymptotic quantum numbers [Voi], and the intranuclear anomalous conversion becomes possible. Usually, intranuclear electron conversion is very small and amounts to $(R_0/a_B)^3$, where a_B is the Bohr radius, as compared with the usual internal conversion that is gained in the atomic shell outside the nucleus. But, in the case where the normal nuclear matrix element is forbidden by the asymptotic quantum numbers of the Nilsson model and anomalous intranuclear matrix element is allowed by the asymptotic quantum numbers, the smallness introduced by the function $(R_0/a_B)^3$ is compensated since

the factor 10^{-2n} is absent for the anomaly, and anomalous internal conversion becomes observable.

In this sense, significant difference in the internal conversion coefficients with the M shell for the $M1$(29.19 keV) transitions in the ^{229}Th nucleus, if they really exist, may indicate a strong anomaly. As aforementioned, the interband transition provides less than 10% of the total intensity of the 29.19 keV transitions. If this transition provides the observed difference in the internal conversion coefficients, the anomaly probably exists. And in this case, it will manifest itself in the conversion decay of the isomeric state $3/2^+$(7.8 eV), because the $7s_{1/2}$ shell is involved in the process. The amplitudes of course obey the condition $\psi_{7s_{1/2}}(0) \ll \psi_{2s_{1/2},3s_{1/2}}(0)$. However, the factor $(\lambda_{is}/a_B)^2$, where $\lambda_{is} = 2\pi/E_{is}$, is included in the formula for the probability of the dynamic effect of penetration [Tka94], compensates the smallness of the amplitude of the $7s_{1/2}$ wave function inside the nucleus. Thus, if the dynamic effect of penetration really exists in the $M1$ interband transitions, it can also have an impact on the range of the lifetimes of the $3/2^+$(7.8 eV) isomer in the conversion decay.

Currently, we can only speculate of the possibility of anomalous internal conversion, since the accuracy of the measurements [GKA02] were not sufficient. Therefore, it would be extremely useful if precise measurements of the internal conversion coefficients for interband magnetic dipole transitions between the bands $K^\pi[Nn_Z\Lambda] = 5/2^+[633]$ and $3/2^+[631]$ especially at the K and L atomic shells were performed.

7.2 Recent Experiments Utilizing the IC Channel

There have been many recent experiments utilizing the IC channel in ^{229}Th. The following list mentions some of these and provides some brief info regarding the experiments:

- [WSL16, SWT17]: A source of ^{233}U is utilized to generate excited ^{229}Th ions through α decay. An RF quadrupole and quadrupole mass separator are utilized to isolate different charge states of ^{229}Th. Bunches of these ions are then implanted onto an MCP detector where they can become neutral and undergo internal conversion. The

results of these experiment confirm that the IC channel does exist and bounds the isomeric level between the first and third ionization energies. In addition, they are able to measure a lifetime for the IC decay at 7 ± 1 usec.

- [BCL18, BCK18]: In these experiments, laser ablation of a ^{229}Th target are investigated. The laser ablation, with intense pulsed light, produces a plasma which then stimulates the excitation of the ^{229}Th ions to the isomeric level through inverse internal conversion. The ions are then quickly accelerated and embedded into an SiO2 substrate, where they can undergo radiative decay. This leads to emission of photoelectrons from the substrate, on which spectroscopy is performed to determine the electron energies. The results suggest that the isomeric energy level is $7.1^{+0.1}_{-0.2}$ eV, with a vacuum half life of 1880 ± 170 sec. Although these results are subject to controversy.

- [SSR18]: A layer of ^{233}U is coated with thin layers of gold and placed in between an α detector and an electron detector. Coincidence measurements are performed against retarding field potentials in an attempt to gain an energy resolution on the electrons. The IC signal is unfortunately masked by low energy electrons from the gold layers.

The results of experiments [WSL16, SWT17] show that the IC channel does exist and the lifetime measurements are in agreement with theoretical predictions [ST91, KT07]. Many research groups are showing interest in this decay channel, particularly due to the fact that the IC decay has a much shorter lifetime which can be advantageous over detection of long-lived fluorescence from the radiative decay. Our experiments utilizing a ^{233}U source along with SNSPD's provide another avenue in the search for the energy of the low lying isomeric level and can hopefully provide tighter energy constraints than other recent experiments.

7.3 Superconductivity

Superconductivity was discovered over a century ago. On April 8, 1911, Heike Kamerlingh Onnes was studying the resistance of solid mercury at cryogenic temperatures. He observed that the resistance suddenly vanished below 4.2 K. Since then, a host of materials have been

discovered which can exhibit superconductivity. The unique properties of these materials have been studied extensively and have allowed its integration into several modern technologies. These include powerful electromagnets for partcile accelerators, Josephson junctions, and even the "ubiquitous" SQUID [CB06]. A primary standard for the volt is achieved through the use of Josephson junctions [Ham00].

In the superconducting state, the direct current (DC) electrical resistivity is essentially zero such that persistent electrical currents have been observed to circulate in superconducting loops for very long periods of time with little attenuation. As bulk superconductors are cooled towards zero Kelvin, there exists a transition temperature (T_C) under which they behave as perfect diamagnets to expel all the magnetic flux from its interior. This is known as the Meissner effect. Superconductivity occurs in many metallic elements, alloys, intermetallic compounds, and doped semiconductors. The range of transition temperatures varies wildly in different materials from temperatures of 0.001 to over 100 Kelvin.

With strong external magnetic fields, superconductivity is destroyed. The critical field (H_C) is the temperature dependent field over which superconductivity ceases. The critical field at the critical temperature (T_C) is zero. There are characteristic magnetization curves for superconductors as a function of the applied field and these differ for type 1 and type 2 superconductors. For type 1 superconductors at a fixed and sufficiently low temperature, the Meissner effect is complete up until some critical field (H_C). Above this critical field, the magnetization is destroyed and magnetic fields can permeate into the bulk of the specimen. In type 2 superconductors, the Meissner effect is complete up until the applied field reaches H_{C1}. Then from H_{C1} to H_{C2}, magnetic flux lines and vortices can exist in the bulk and the Meissner effect is said to be incomplete. Upon exceeding H_{C2}, the magnetization is completely destroyed.

In all superconductors, the entropy decreases significantly upon cooling below the critical temperature. This represents the fact that the superconducting state has more order than the normal. Other unique properties of superconductors include the heat capacity, free energy, and energy gap; all of which display characteristic features when transitioning from the normal to the superconducting state.

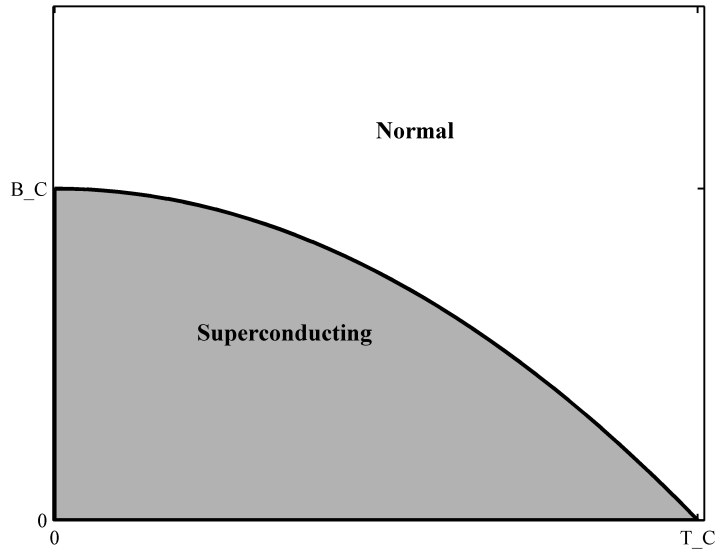

Figure 7.2: The superconducting regime for type I superconductors. Beyond certain temperatures and with adequately strong applied fields, a superconductor will revert to the normal state, depicted by the white region in the figure.

To motivate the theory behind superconductivity, we can approach it from a historical standpoint. The London theory is a simple phenomenological approach to explain superconductivity. It involves an argument requiring that the current density $\vec{j}_s$ be directly proportional to the vector potential $\vec{A}$:

$$\vec{j}_s = -\frac{1}{\mu_o \lambda_L}\vec{A}. \tag{7.1}$$

λ_L is the London penetration depth. The curl of the vector potential yields the magnetic field. Requiring that Maxwell's equation for the curl of the magnetic field be proportional to the current density as described, results in the following relation:

$$\boldsymbol{\nabla}^2\vec{B} = \frac{1}{\lambda_L^2}\vec{B}$$

$$\text{with} \tag{7.2}$$

$$\lambda_L = \sqrt{\frac{m}{\mu_0 \mathrm{n_s q^2}}}.$$

n_s is associated to the density of superconducting carriers and q is their individual charge. The solution for the field inside a superconductor is a decaying exponential, which can

explain the penetration of magnetic fields in thin superconducting films and the depth of penetration in bulk medium, which is the characteristic London penetration depth. The theory is oversimplified.

The Ginzburg-Landau Theory is another phenomenological approach to superconductors which involves an order parameter $\psi(\vec{r})$ with the relation:

$$\psi^*(\vec{r})\psi(\vec{r}) = \mathrm{n}_s(\vec{r}). \tag{7.3}$$

An expression for the free energy density $\mathrm{F}_S(\vec{r})$ in a superconductor can be constructed in terms of the order parameter which is valid near the transition temperature:

$$\mathrm{F}_S(\vec{r}) = \mathrm{F}_N - \alpha \mid \psi \mid^2 + \frac{\beta}{2} \mid \psi \mid^4 + \frac{1}{2\mathrm{m}} \mid (-\mathrm{i}\hbar\boldsymbol{\nabla} - q\vec{A})\psi \mid^2 - \int_0^{B_a} \vec{M} \cdot \mathrm{d}\vec{B}_a. \tag{7.4}$$

α, β, and m are phenomenological constants. F_N is the normal state free energy density. $-\int_0^{B_a} \vec{M} \cdot \mathrm{d}\vec{B}_a$ represents the increase in $\mathrm{F}_S(\vec{r})$ due to the expulsion of the magnetic fields within the bulk, with $\vec{M}$ representing the fictitious magnetization that can associated with the Meissner effect ($\vec{M} = -\frac{\vec{B}_a}{\mu_o}$ with $\vec{B}_a$ being the applied field). We will not get into the details of the other terms in the superconducting free energy density, but minimizing the total superconducting free energy with respect to variations in $\psi(\vec{r})$ yields the Ginzburg-Landau equation:

$$-\alpha\psi + \beta \mid \psi \mid^2 \psi + \frac{1}{2\mathrm{m}}(-\mathrm{i}\hbar\boldsymbol{\nabla} - q\vec{A})^2\psi = 0, \tag{7.5}$$

and minimization of this quantity with respect to variations in the vector potential yields an expression for the current density:

$$\vec{j}_s = \frac{\mathrm{q}}{\mathrm{m}}\Re\{\psi^*(-\mathrm{i}\hbar\boldsymbol{\nabla} - \mathrm{q}\vec{A})\psi\}. \tag{7.6}$$

An advantage of the Ginzburg-Landau theory is that it can be derived from the more formal BCS theory, which we will mention shortly, and it provides a quantum behavior to the superconducting state, in terms of the order parameter. In addition, an intrinsic coherence length can be derived for superconductors which describes the distance in which the superconducting carrier density should not change appreciably within a spatially varying magnetic field. It can be considered as the minimum thickness of a transition layer between

the normal and superconducting states, or the length scale in which the vector potential should be averaged to obtain the local current density. The coherence length ξ is derived in the Ginzburg-Landau theory and is given by:

$$\xi = \sqrt{\frac{\hbar^2}{2\mathrm{m} \mid \alpha \mid}}. \tag{7.7}$$

And the penetration depth is given by:

$$\lambda = \sqrt{\frac{m}{\mu_0 \mathrm{q}^2 \psi_0^2}}, \tag{7.8}$$

where ψ_o is the order parameter deep within the superconductor where there is no field present. The value $\kappa = \lambda/\xi$ is a dimensionless quantity that divides type 1 and 2 superconductors with $\kappa < 1/(\sqrt{2})$ describing the former and $\kappa > 1/(\sqrt{2})$ the latter.

The order parameter arises naturally from the Bardeen-Cooper-Schrieffer theory (BCS theory). This is the first successful microscopic theory of superconductivity. It involves a wavefunction description for pairs of electrons with opposite wavevectors $(\vec{k}^+, -\vec{k}^-)$ which are called Cooper pairs. In this theory, superconductivity is established through an attractive interaction between electrons near the Fermi surface. The attraction between electrons is made possible through an effective screening of the Coulomb repulsion which arises from the ionic motion of the electrons in the lattice. The mechanism can be simply described by an electron interacting with the lattice, via an electron-phonon interaction, causing it to deform. A second electron can then take advantage of this deformation and become correlated with the initial electron forming a Cooper pair. As many electron pairs become correlated, the Cooper pairs can then form a condensate. Much of the described characteristics of superconductors are derived through the BCS theory in a natural way. It has successfully provided an expression for the critical temperature measured in superconductors:

$$\mathrm{k}_B \mathrm{T}_C \approx 1.13 \mathrm{E}_D \exp\left(\frac{-1}{\mathrm{N}_o \mathrm{V}_o}\right). \tag{7.9}$$

E_D is the Debye energy ($\mathrm{k}_B \Theta_D$), with Θ_D representing the Debye temperature. N_o is related to the density of electronic levels , and V_o is a parameter of the model Hamiltonian.

While the BSC theory may not accurately describe exotic superconductors, it has had

much success over the decades. The BCS theory can also be applied to nuclear physics in describing the pairing interaction between nucleons [RS04]!

[Cyr73, AM05]

7.4 SNSPDs

7.4.1 Introduction

The superconducting nanowire single photon detector (SNSPD) has recently emerged as a promising photon counting technology. These detectors are based on current biased superconducting nanowires. By applying a bias current just under the critical current of the superconducting nanowire, an incident photon can interact with superconducting Cooper pairs to produce a local resistive hot spot. Fig. 7.3 depicts the cross section of a nanowire and the process of photon absorption and recovery. The local hot spot causes the current to flow around it leading to increased current densities and more resistive areas in the nanowire cross section. Joule heating will ultimately cause the entire cross section and an adequate length of the nanowire to become resistive such that its high resistivity causes the current to be redirected across some load impedance connected in parallel. As the current is shunted across the load resistor, which defines the detector response to the absorbed photons, the nanowire is allowed to cool down and relax and in so becomes available to repeat the process and register another photon. Typically nanowires are fabricated to be relatively thin with a meandering pattern layout which promotes an improved efficiency for light collection. In general, there are several desirable properties of SNSPDs that make them a very suitable detector technology. Some of these benefits include a high detection efficiency, a low dark count rate, low timing jitter, and potentially quick recovery times [NTH12]. The materials used for fabrication and the geometries of the device can have a significant effect on performance of the detector. Although SNSPD's have been used mostly in IR detection, these devices can be fabricated for improved detection at UV and VUV wavelengths.

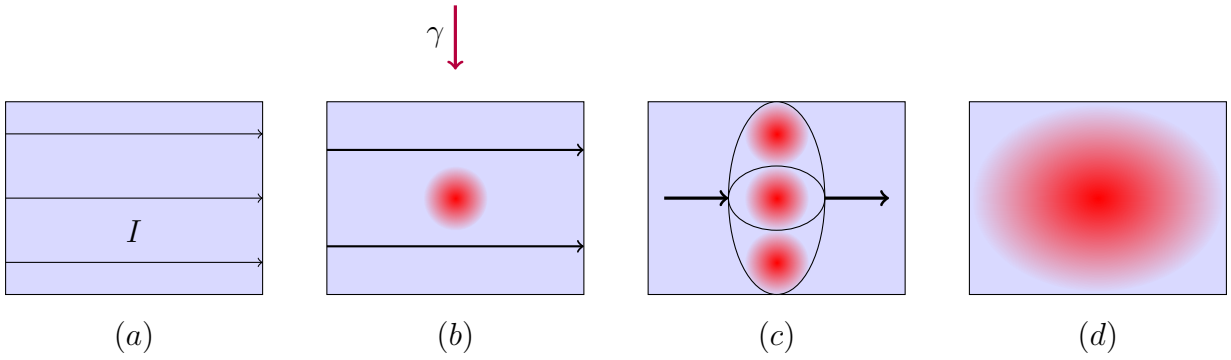

Figure 7.3: Hot spot generation in an SNSPD. The figure depicts a small cross section of the meandering nanowire feature. (a) At sufficiently low temperatures, the nanowire is in the superconducting state with current flowing through its entire length. (b) The absorption of a photon produces a local hot spot in the nanowire. This causes redirection of current to avoid the hot spot. (c) The redirection of current produces an increased current density in the remaining superconducting cross-section of the nanowire. This leads to the generation of further hot spots. (d) Joule heating ultimately causes the entire cross section of the nanowire to become resistive. The large resistance of the nanowire then causes the flowing current to be redirected across a load, which constitutes the detected signal. This redirection of current allows the nanowire to recover in temperature such that current can once again flow through it, returning to the state depicted in (a).

7.4.1.1 Detector Model

A simple electro-thermal model is sufficient to describe the SNSPD. It involves two coupled differential equations. One of which describes the hot spot temperature in the nanowire:

$$\mathrm{cd}(\frac{\partial \mathrm{T}}{\partial \mathrm{t}}) = \mathrm{J}^2\rho\mathrm{d} + \kappa\mathrm{d}\nabla^2\mathrm{T} + \alpha(\mathrm{T_o} - \mathrm{T}). \tag{7.10}$$

c is the specific heat per volume of the nanowire film, which is the sum of the electronic and phononic specific heats. T_o is the equilibrium or reservoir temperature, d is the thickness of the nanowire, and κ is its thermal conductivity. α is the conductance between the nanowire film and substrate boundary, J is the current density through the nanowire, and ρ is its electrical resistivity. The generated heat in the SNSPD is dissipated through electron-phonon interactions in the nanowire and then through phonon-phonon interactions at the film-substrate interface.

In a simple circuit model, the absorption of a photon by the detector is simulated with an opening of the switch shown in Fig. 7.4. The corresponding differential equation describing

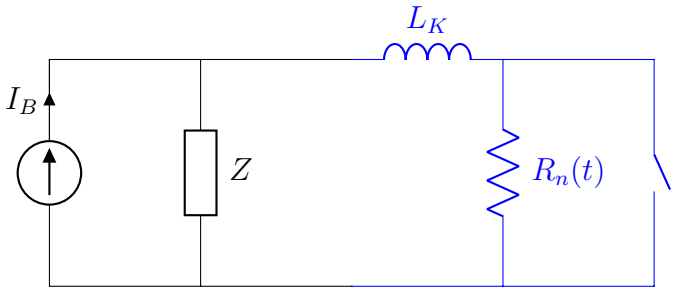

Figure 7.4: SNSPD generic circuit schematic. The absorption of a photon is simulated in the circuit by the opening of the switch. This forces the bias current to flow across the load resistor (with impedance Z), constituting the detected signal. $\mathrm{R_N}$ represents the hot spot resistance in the nanowire and $\mathrm{L_K}$ is its kinetic inductance.

this circuit model is given by:

$$C\left[\frac{d^2}{dt^2}L_K I + \frac{d}{dt}(IR_N) + Z\frac{dI}{dt}\right] = I_B - I. \tag{7.11}$$

C is the coupling capacitor of the readout amplifier (a part of the load circuit in the schematic) and Z is the load impedance. L_K is the kinetic inductance of the nanowire, due to the inertia

of the charge carriers, and I_B is the bias current supplied by some source. I is the time dependent current flowing through the nanowire which has a time dependent resistance R_N.

The two different differential equations in the electro-thermal model are coupled via the hot spot resistance in the nanowire. The model is sufficient to describe many of the characteristics observed in SNSPD's such as detector response and recovery times [YKD07].

7.4.1.2 Detector Performance

The system detection efficiency (SDE) for any detector can be represented by:

$$\mathrm{SDE} = (\eta_{\mathrm{coupling}})(\eta_{\mathrm{absorption}})(\eta_{\mathrm{internal}})(\eta_{\mathrm{trigger}}). \tag{7.12}$$

η_{coupling} is the coupling efficiency and will be dependent on the experimental setup. $\eta_{\mathrm{absorption}}$ will be dependent upon the material properties of the detector and represents the probability that an incident photon will get absorbed. η_{internal} represents the probability that an absorbed photon will result in an electrical response. And finally, η_{trigger} describes the efficiency of the counting electronics to register the electrical response produced from the absorbed photon. These independent efficiencies are typically lumped together and reported as an overall SDE, as the individual efficiencies may be difficult to isolate and characterize.

Another useful metric for detectors in general is the dark count rate (DCR). This can be represented by:

$$\mathrm{DCR} = \mathrm{R}_{\mathrm{intrinsic}} + \mathrm{R}_{\mathrm{background}} + \mathrm{R}_{\mathrm{electronic}}. \tag{7.13}$$

$\mathrm{R}_{\mathrm{intrinsic}}$ is the intrinsic dark count rate and represents the detector response rate in the absence of absorbed photons. $\mathrm{R}_{\mathrm{background}}$ represents the count-rate due to detection of unwanted photons, such as due to scattered external light and blackbody radiation. And finally, $\mathrm{R}_{\mathrm{electronic}}$ is the electronic contribution to the overall count-rate and can be attributed to noise in the detection and counting electronics. As in the case of the SDE, the individual rates that comprise the DCR can be hard to isolate and quantify, and so typically an overall DCR is reported.

For SNSPD's, proper materials can be chosen for the superconducting film such that

$\eta_{\text{absorption}}$ and η_{internal} are large. With efficient coupling of light and with reliable electronics for registering of the signal response, a high SDE can be achieved. In terms of the DCR, $R_{\text{intrinsic}}$ can be low. As long as background and electronic contributions to the noise can be minimized, a large signal-to-noise ratio (SNR) can be achieved. This makes SNSPD's very desirable for many different applications.

A typical SNSPD signal response is shown in Figure 7.5 for one of the detectors used in our experiments at UCLA. The rise time (τ_1) of the response is given in the following

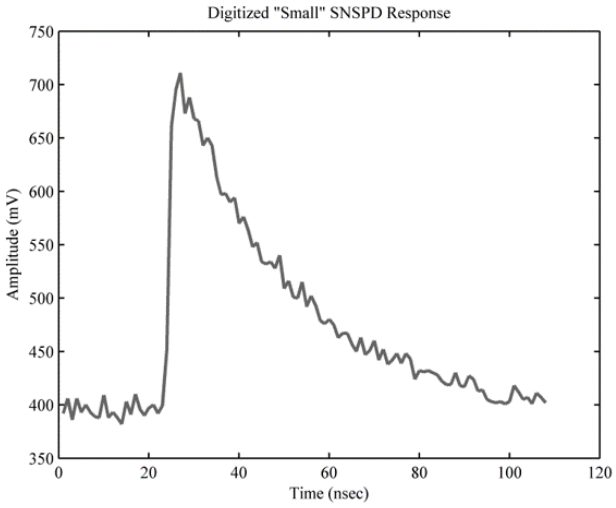

Figure 7.5: Small SNSPD waveform. The waveform was acquired via the CAEN DT5751 digitizer.

expression:

$$\tau_1 = \frac{L_k}{Z_o + R_n(t)}, \tag{7.14}$$

with L_k representing the kinetic inductance of the nanowire, $R_n(t)$ its hot spot resistance, and Z_o the impedance of the load circuit which is typically 50 Ohms. As the hot spot resistance in the nanowire tends to be very high, the rise time of the signal response is fast. An expression for the recovery time (τ_2) of an SNSPD is given by:

$$\tau_2 = \frac{L_k}{Z_o}. \tag{7.15}$$

The kinetic inductance of a nanowire scales with its length and is lower for shorter (smaller area) nanowires, resulting in a faster recovery time. Small area nanowires are therefore suitable for high speed applications. Certain experiments may require a larger detector area

for improved collection efficiencies. Large area nanowires, typically achieved with a longer meander feature, will have a large kinetic inductance which will result in longer recovery times [HJ16].

In general, the SDE curve as a function of the bias current should be sigmoidal, if the response is measured against a monochromatic light source. Figure 7.6 shows such a response curve for one of the detectors used in our experiments. The calibration was done at NIST against 375 nm photons. As the bias current is increased, the hot spot generated in response

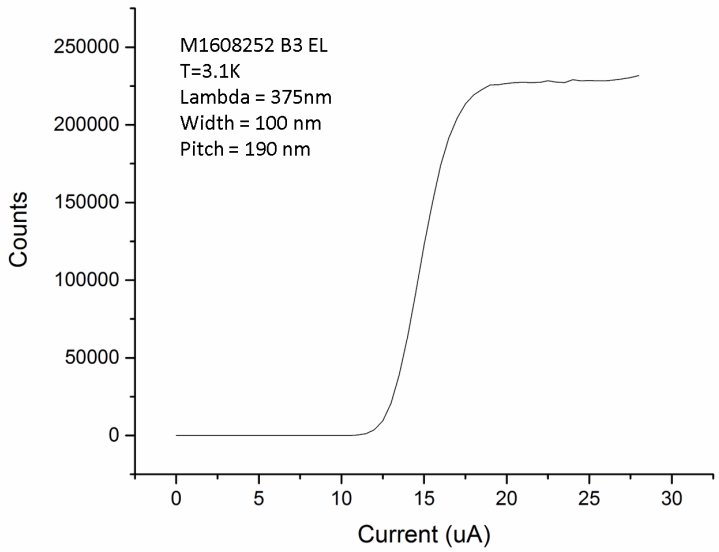

Figure 7.6: "Small" SNSPD counts vs bias current curve. The properties of the "Small" SNSPD's are described in table 7.1. This calibration was performed at NIST against 375 nm photons at a temperature of 3.1 K.

to photon absorption becomes adequate to make the nanowire go resistive, which results in detected signals. As the bias is increased further, the sensitivity to the photons of a particular energy continues to increase. Eventually, an optimal sensitivity to the photons is reached and a saturation plateau is observed in which the detected signal is constant over some range of bias currents. As the bias current is increased even further, the current density can no longer be sustained at the given system temperature, and the nanowire switches to the normal state. The detector no longer has any response to absorbed photons in the resistive

state.

We can expect that photons with wavelengths less than 375 nm would saturate at smaller bias currents in Figure 7.6. The ability to vary the bias current to achieve sensitivity to different wavelength photons can be very advantageous in certain experiments. This sigmoidal relationship between the detector sensitivity and bias current, if compared at different wavelengths and at a fixed system temperature, can provide a means for photon energy calibrations.

Given a superconducting material, narrower nanowires will typically yield larger saturation plateaus and with increased sensitivity to lower energy photons. While such an SNSPD will detect higher energy photons, its resolution at higher energies can diminish as the bias currents necessary for saturation could be small making detection of the amplified signal response difficult. This can make a clear characterization of the sigmoidal response curve problematic, and would make it difficult to distinguish the saturation plateaus of different high energy photons. Thicker nanowires on the other hand, may provide better energy resolution to higher energy photons as larger hot spots and bias currents will be necessary to make the nanowire become resistive.

7.4.1.3 Detector Fabrication

Constrictions in the SNSPD, non-uniformities and defects along the length of the nanowire that can be generated in the fabrication process, do not allow the detector to be biased at a high current. With longer meander features, uniformity becomes difficult to maintain. Reducing the area of the nanowire meander and utilizing an ultra-narrow geometry can improve the nanowire uniformity, however, coupling light efficiently to such small detectors could be challenging.

Amorphous materials such as WSi and MoSi are particularly desirable for the fabrication of SNSPD's. The lack of a well-defined crystal structure allows amorphous superconductors to be deposited on virtually any substrate without significant degradation in material properties. In addition, longer meander features can be fabricated while maintaining uni-

formity [VKB15]. The reduced carrier density in WSi and the formation of larger hot spots allows fabrication of wider nanowire features than other typical superconducting substrates such NbN and NbTiN [HJ16]. With longer and thicker meander features, large area detectors are realized with improved collection efficiencies.

Another means to improve signal detection with SNSPD's is to utilize a SNAP configuration. The superconducting nanowire avalanche photodetector (SNAP) involves two or more SNSPD's in an electrically parallel connection. The meander features can be vertically stacked (3D SNAP) such that the effective area of the detector is increased. Polarization effects can be reduced in this configuration [VMH12]. The nanowires can also be placed side-by-side to produce a larger surface promoting improved collection efficiencies. Such a configuration can lead to faster recovery times compared to a standard SNSPD with the same detection area, due to an effective reduction in the kinetic inductance of the parallel nanowire configuration. A SNAP operating in the "avalanche" regime requires that a single detection event in one of SNSPD's leads to all nanowires in parallel becoming resistive, which is achieved when the current redistribution across the other parallel nanowires exceeds what can be sustained. This is required such that the bias current is properly shunted to the load for a signal response. The parallel nanowire configuration operated in the "avalanche" regime has an effect on the cutoff current (I_{CO}), which is the inflection point of the sigmoidal counts vs. bias current curve in Fig. 7.6. At a fixed temperature and incident photon energy, I_{CO} is typically higher for a SNAP compared to a standard SNSPD. There are different configurations and regimes in which SNAPs can be operated [HJ16], which can be advantageous for different applications.

7.5 Experiments at UCLA

A ^{233}U source is placed very close to SNSPD's and the whole system is cooled down to approximately 3.3 to 3.8 K with the use of a cryostat. As the ^{233}U undergoes α decay, energetic daughter ^{229}Th nuclei can collide into the SNSPD. These collisions are very energetic and expected to cause the detector to produce a signal response or "click". The ^{229}Th ions

should undergo charge exchange and become neutral almost immediately upon impact with the detector. A fraction of these nuclei should remain embedded in the SNSPD substrate and 2 percent are expected to be at the excited isomeric level. For neutral thorium nuclei, the relaxation from this level will favor internal conversion over radiative decay. For those ^{229}Th nuclei which get embedded in the detector and which are at the excited isomeric level, an IC decay should occur at a time scale indicative of the IC lifetime. The decay from the isomeric level via the IC channel should deposit energy into the SNSPD resulting in another "click". It is these correlated events, an initial collision event followed by an IC decay, that we wish to isolate and characterize. The basic experimental setup can be seen in Fig. 7.7. An advantage utilizing SNSPD's for IC detection is in its potential to provide bounds on the

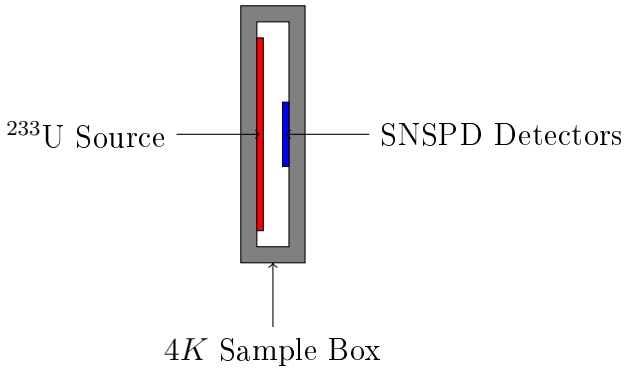

Figure 7.7: SNSPD experimental setup schematic. The red disk represents the ^{233}U source while the blue disk, exaggerated in size, represents the SNSPD. Both source and detectors are housed inside of a Cu sample box which is mounted to the 4K stage of a cryostat. As α decay occurs, daughter ^{229}Th ions are produced an ejected from the disk source. 2% of the produced ^{229}Th ions are expected to be at the excited isomeric level. The SNSPD can capture some of these nuclei which will result in a detector response. Collisions with the SNSPD's should yield neutral ^{229}Th atoms almost immediately upon impact. The neutral ^{229}Th atoms at the excited isomeric level can then undergo IC decay, depositing the energy into the SNSPD, which should yield another detector response. It is these correlated events, a collision with the detector followed by an IC decay, that we isolate and characterize.

energy that the IC decay event deposits into the detectors. By characterizing the detectors response against IC events and VUV photons at different bias currents, useful information

detector	pixel area	thickness	width	pitch	fill factor	substrate
Large SNSPD	1mm x 1mm	10 nm	~ 250 nm	~ 500 nm	~ 0.5	WSi
Small SNSPD	16μm x 16μm	10 nm	90 nm	180 nm	0.5	MoSi
SNAP SNSPD	200μm x 200μm	10 nm	140 nm	260 nm	0.54	WSi
Thick SNSPD	100μm x 100μm	17 nm	140 nm	280 nm	0.5	WSi

Table 7.1: The SNSPD's utilized at UCLA. Some properties of each detector are listed such as its dimensions and the material of the nanowire.

may be learned about the energy of the IC event and the isomeric level.

AT UCLA, we have characterized and performed experiments on several detectors over the time period from $2017-02$ up until the present. In the following, these characterizations and experiments will be described in more detail.

7.5.1 Apparatus

Experiments were conducted at UCLA using several different SNSPD's, a ^{233}U source, and a crysostat. The ^{233}U source was purchased from Eckert and Ziegler. It is electroplated onto a stainless steel disk with a 19 mm active diameter and is NIST traceable with an activity of 21.22 kBq. There is a ^{232}U contamination which was measured to be $\sim$18 Bq and additionally there is some other α impurities measured to be $\sim$42 Bq.

A total of four different types of devices have been used at UCLA whose properties are described in Table 7.1. For each type of SNSPD mentioned in the table, two similar detectors are simultaneously utilized in the experiments. The actual devices are shown in Fig. 7.8.

The devices are mounted inside of a Cu sample box which is mounted to the 4 K stage of the cryostat (Sumitomo coldhead model SRDK-101D, and compressor model CNA-11C), as depicted in Fig. 7.9. Two signal cables extend from the sample box and down to the 40 K stage and finally to a feedthrough port leading to external connectors. By routing the signal and other cables through the 40 K stage, a tolerable temperature gradient is produced in the cables which is adequate to produce a low enough load on the cryostat system such that

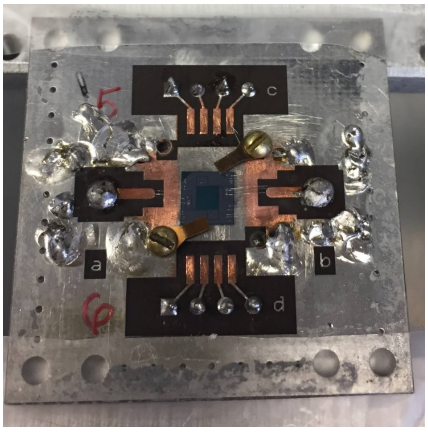

(a) Large SNSPD Device.

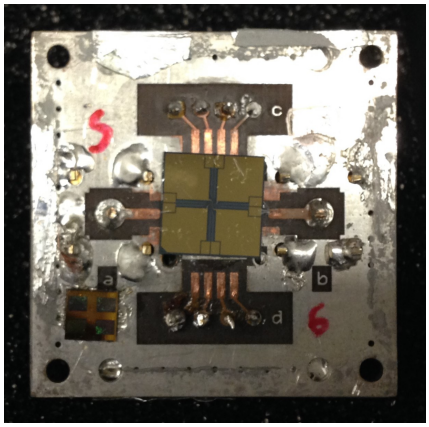

(b) Small SNSPD Device.

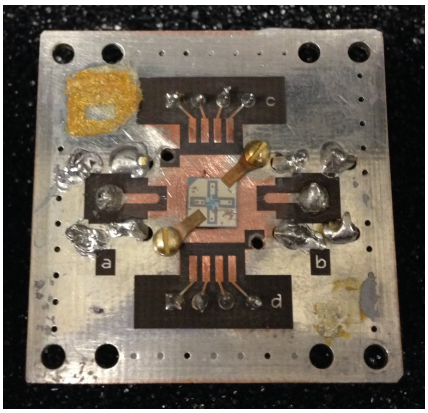

(c) SNAP SNSPD Device.

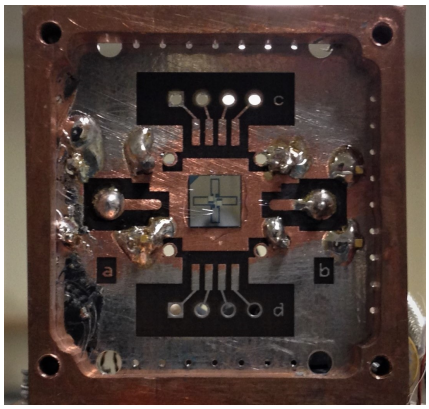

(d) Thick SNSPD Device.

Figure 7.8: SNSPD devices used for the experiments conducted at UCLA. A picture of the corresponding detectors are shown.

temperatures below 4 K can be achieved. The temperatures of both the 40 K stage and the sample box (mounted to the 4K stage) are monitored throughout the experiments.

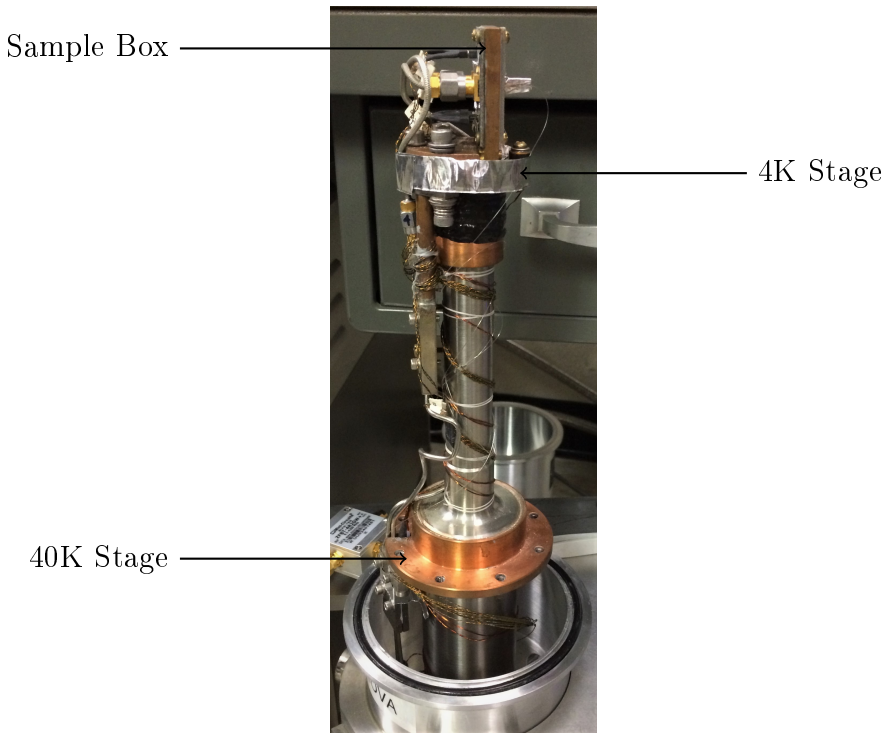

Figure 7.9: Sumitomo cryostat. The inside of the cryostat is shown along with the 40K and 4K stages, as well as the sample box containing the source and detectors.

The current bias' used for the SNSPD's are usually on the order of micro Amps. This is provided with a Keithley 213 Quad Voltage source in series with a resistor (200 and 270 kOhm resistors are used in our setup). As the nanowire goes resistive, the current flowing through it is shunted to the load. The load circuit typically amplifies and reads out the SNSPD responses. See Fig. 7.4 for a basic schematic of the setup. The bias current is coupled to the SNSPDs via a bias tee (Mini-Circuits, model ZFBT-4R2GW+). The bias tee allows DC current flow through the devices and also directs any RF currents, produced via the SNSPD's going resistive followed by a recovery of the temperature and current through the nanowire, into a pair of daisy-chained amplifiers (Mini-Circuits, models ZFL-500LN+ and ZFL-1000LN+). The output from the amplifiers can then produce an adequate voltage signal into 50 Ohms input impedance. The CAEN DT5751 digitizer is utilized for processing

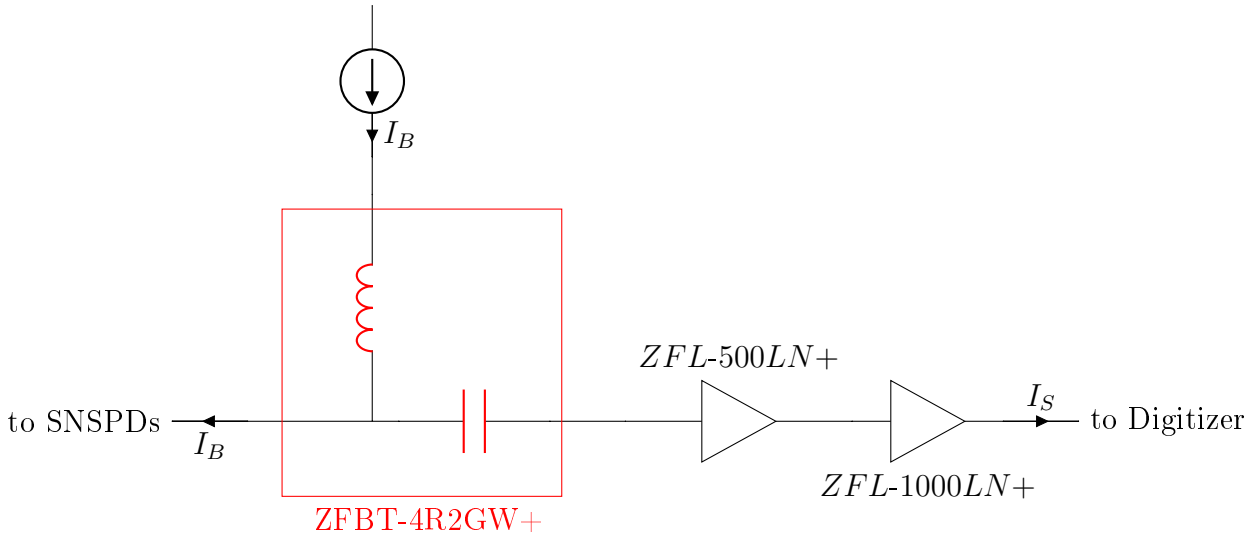

Figure 7.10: SNSPD readout circuit schematic. A DC current is coupled to the SNSPD's via a bias tee. The bias tee also allows for the fast current response of the detectors to be coupled to a pair of daisy-chained amplifiers. The amplifiers then output an adequate signal which can be read with 50 Ohm input impedance devices.

of the detected signals. For this experiment we will be interested primarily in the events with short inter-arrival times as theory [ST91] and recent experiments [SWT17] suggest a lifetime of microseconds for the IC decay.

7.5.2 Characterizations

Some basic characterizations were performed on the detectors. IV curves were taken to determine the switching currents at the lowest temperatures achieved, and additionally the recovery times of the SNSPD responses are measured. The IV curves assure that the detectors are superconducting and they also help determine the range of bias currents that could be used for experiments. In Figure 7.11, the relevant IV curve measurements are shown, taken at temperatures between 3.3 and 3.8 K. The dates of each measurement vary.

The amorphous superconductors, MoSi and WSi, are used in the fabrication of the detectors for our experiments. They help produce larger and more uniform meander features for improved collection efficiencies of ^{229}Th ions produced in the α decay of ^{233}U. The stopping

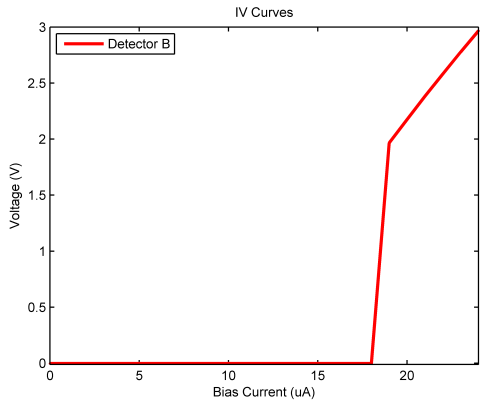

(a) Large SNSPDs

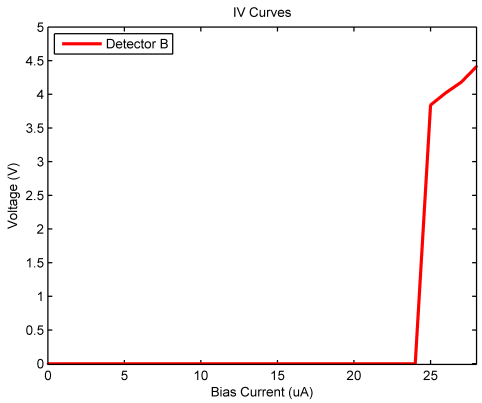

(b) Small SNSPDs

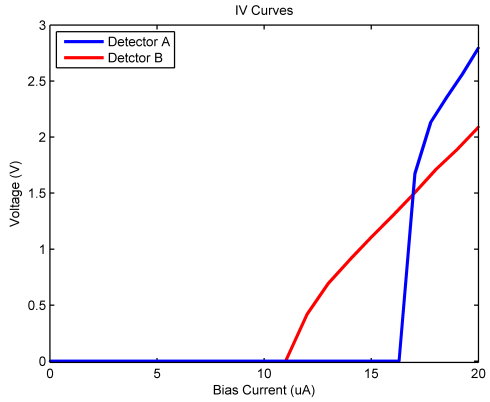

(c) SNAP SNSPDs

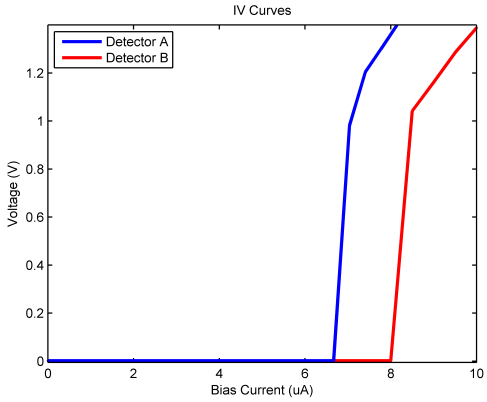

(d) Thick SNSPDs

Figure 7.11: Voltage versus bias current response curves. The representative IV curves are shown for each of the SNSPD's utilized in experiments at UCLA.

distances in these substrates were calculated for $\sim$ 100 keV ^{229}Th ions using SRIM software. The results can be seen in Figure. 7.12. These results help estimate the fraction of incident

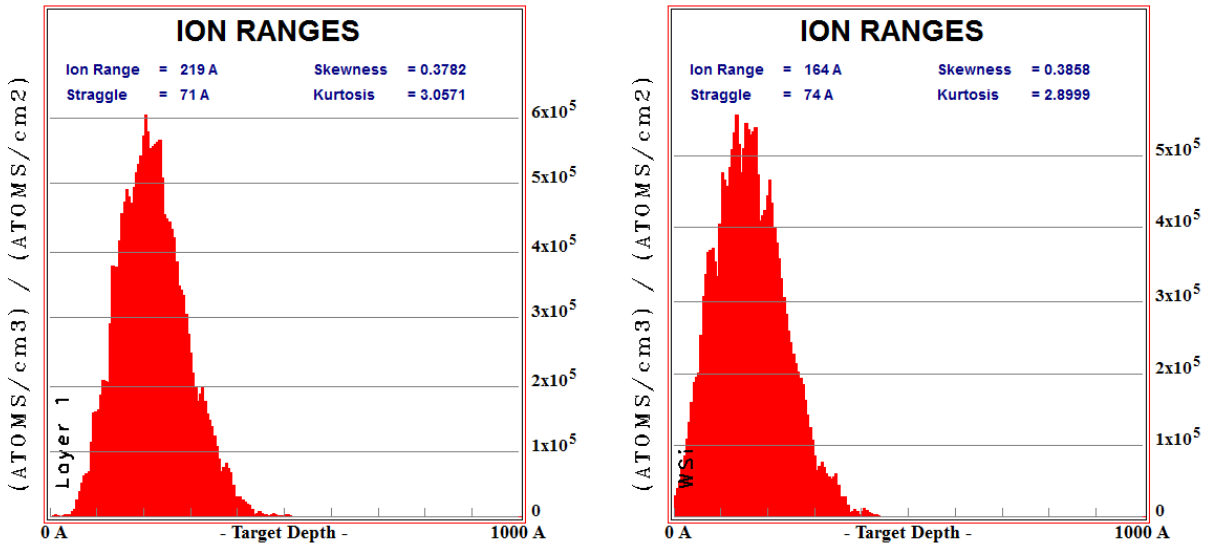

(a) SRIM simulation for MoSi.

(b) SRIM simulation for WSi.

Figure 7.12: SRIM calculations for the capture fractions η_{capture} of the different nanowire substrates. The substrate along with the thickness will determine the fraction of incident 100 keV ^{229}Th ions that can be expected to embed into the SNSPD.

^{229}Th ions expected to embed into the SNSPD's (η_{capture}), which will be dependent on the detector substrate and thickness. 2% of the embedded ^{229}Th atoms will be expected to be at the isomeric level from which can expect IC decays.

The SRIM software was also utilized to simulate ^{229}Th ions escaping a UO_2 layer. A 10 nm thick UO_2 layer is expected in the electroplating of ^{233}U onto stainless steel. The SRIM simulations help determine the fraction of 89 keV ^{229}Th ions, produced in the α decay of ^{233}U, that are expected to escape this layer to find their way to the SNSPD's. The simulations confirm that most of the ions should escape the UO_2 layer.

Characterization of the SNSPD's against VUV light were also performed for the "Large and "Thick" detectors. This was accomplished using a Deuterium lamp, a McPherson 234/302 monochromator, and modified shields to the Sumitomo cryostat. The setup is shown in Fig. 7.14. The modified 40 K and outer shields have ports which allow for cou-

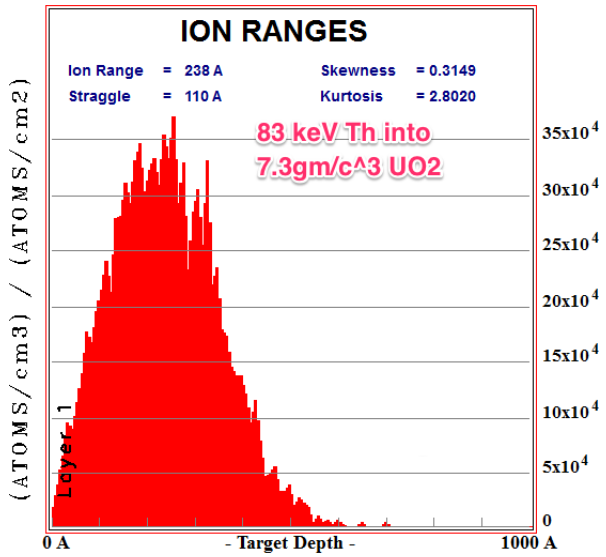

Figure 7.13: Stopping range of ^{229}Th ions in UO_2. A 10 nm thick UO_2 layer is expected for the electroplating of ^{233}U onto the stainless steel disk. The SRIM software is utilized to confirm that 89 keV ^{229}Th ions, produced in the α decay of ^{233}U, will escape this layer.

pling of light. The outer shield has a KF port which was adapted to a $2\frac{3}{4}$" conflat (CF) MgF_2 window to isolate the monochromator and cryostat chambers. The output of the monochromator is directed towards apertures in the 40 K shield and sample box which allow for some of the incident light to enter the latter for detection with the SNSPD's. The results of the characterizations involving the "Thick" detector will be discussed later in which the calibrations were performed in situ with the ^{233}U source. But in brief, a clear sigmoidal relationship between the efficiency (or total counts) and bias current was not observed as shown in Fig. 7.6 for either of the detector types. This can be attributed to the large nanowire cross sections which make it more difficult to obtain a saturation plateau. Another reason for the lack of an observed saturation plateau may be attributed to UV fluorescence. VUV photons from the deuterium lamp impinging on unwanted surfaces may cause water and other frozen molecules to fluoresce. As the bias current is increased against a fixed monochromator output VUV wavelength, the SNSPD's may become sensitive to the UV fluorescence photons. This would also prevent a clear sigmoidal feature from being observed.

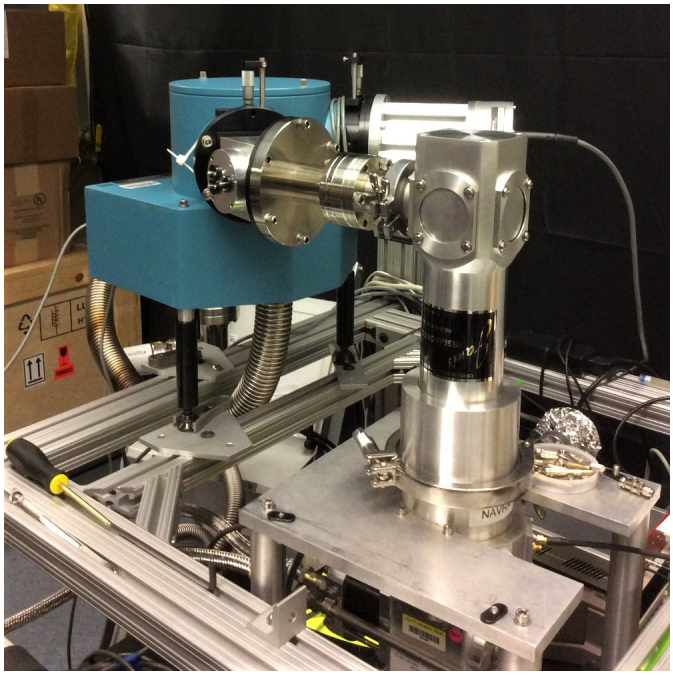

Figure 7.14: SNSPD VUV calibration setup. The output from a deuterium lamp and McPherson 234/302 monochromator allows coupling of VUV light into the cryostat. Apertures in the 40 K shield and sample box pick off a portion of the light for detection via the SNSPD's.

7.5.3 IC Experiments

The IC experiments conducted here at UCLA have been relatively simple in practice. The ^{233}U source and SNSPD pixel array are mounted inside of the sample box with the respective surfaces separated by just a few mm. The cryostat chamber is pumped down for a couple days to pressures of $\sim 5e-7$ mbar and then cooled down to temperatures between $3.3-3.8$ K. The IV response of the devices are measured and then the appropriate bias currents determined. The DT5751 is configured accordingly based on the signal response from each particular detector and then the system is allowed to run for several days and weeks at a time. The digitizer time tags and records the waveforms produced from the collisions of the ^{229}Th ions with the detectors, and other potential events such as the IC decay.

For any given detector, it is important to know how many IC events to expect. In our setup, the SNSPD array is placed a very close distance (ℓ) from the ^{233}U disk source. Each detector has an area (a) defined by a square, and a fill factor (f) due the meander pattern.

The active area (A) of the ^{233}U source is define by a circle with a diameter of 2R = 19 mm. Both detector and source center axis are approximately aligned as can be seen in Figure 7.15. We can begin by writing an expression for the solid angle fraction (SAF) subtended

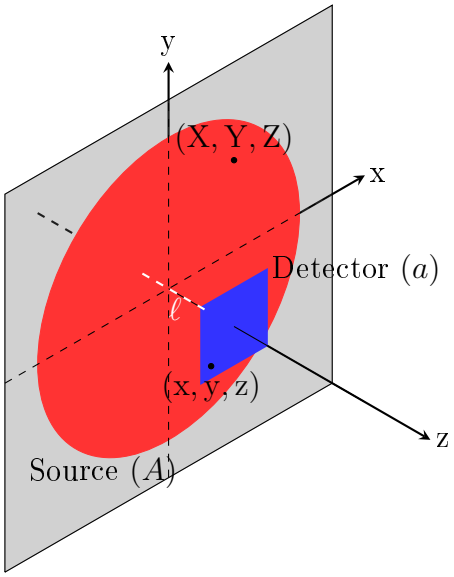

Figure 7.15: SNSPD IC measurement layout schematic. The red circle represents the source and the blue square represents the SNSPD. The center axis of each are approximately aligned in the experiments. The source and detector surfaces are roughly parallel and placed millimeters apart from one another. (X,Y,Z) represents an arbitrary point on the source surface while (x,y,z) represents an arbitrary point on the detector surface.

by some surface given a point source. Let (S_d) define the detector surface for which we wish to determine the SAF, (d$\vec{a}$) is the corresponding infinitesimal area vector at any arbitrary point given by (x, y, z). And let (X, Y, Z) be an arbitrary point on the source surface with $\vec{R}$ representing a vector pointing from (X, Y, Z) to (x, y, z). The SAF of the detector due to an arbitrary point at (X, Y, Z) on the source is just:

$$\mathrm{SAF}_{\text{arbitrary point}} = \int_{S_d} (\mathrm{f}) \frac{\vec{R} \cdot \mathrm{d}\vec{a}}{2\pi \mathrm{R}^3}, \tag{7.16}$$

with the integral conducted over S_d. A factor of two is included to account for the fact that radiation from the source is not distributed evenly over 4π radians. It is actually directional and primarily on one side of the disk, and therefore distributed over 2π radians. Additionally, a factor of f is also included to account for the fill factor of the detector. Let us define the

activity density of the ^{233}U source:

$$\sigma_{\text{activity}} = \frac{\Gamma_{\text{source}}}{\text{A}}, \tag{7.17}$$

with Γ_{source} being the activity in Bq, assumed to be uniform over the corresponding source area (A). Given the setup and defined quantities, R^3 can be re-written as $(\text{R}^2)^{\frac{3}{2}}$ with $\text{R}^2 = (\Delta\text{X})^2 + (\Delta\text{Y})^2 + (\ell)^2$. With $(\Delta\text{X})^2 = (\text{X} - \text{x})^2 \approx (\text{X})^2$ and similarly $(\Delta\text{Y})^2 \approx (\text{Y})^2$, since the dimensions of the detectors are a couple orders of magnitude smaller than that of the source. With $(\text{d}\vec{a})$ along the z-axis, and the distance between the source and detector fixed at (ℓ), the SAF due to a single point on the source simplifies significantly:

$$\text{SAF}_{\text{arbitrary point}} = \int_{S_d} (\text{f}) \frac{(\ell)\text{dxdy}}{2\pi(\text{X}^2 + \text{Y}^2 + \ell^2)^{\frac{3}{2}}}. \tag{7.18}$$

This can be easily integrated under our assumptions. We can also define the rate of total expected events incident upon the detector due to the entire source as Γ_{detBG}:

$$\Gamma_{\text{detBG}} = \int_{S_s} (\text{SAF}_{\text{arbitrary point}})(\sigma_{\text{activity}})\text{dA}, \tag{7.19}$$

with the integral conducted over the source surface (S_s). Substituting and solving yields:

$$\Gamma_{\text{detBG}} = (\Gamma_{\text{source}})(\text{f})(\frac{\text{a}}{\text{A}})(1 - \frac{\ell}{\sqrt{\text{R}^2 + \ell^2}}). \tag{7.20}$$

From the background count-rate, we can determine the expected IC event count-rate. Any particle passing through or deflected from the nanowire substrate can potentially contribute to the overall background count-rate. For every ^{229}Th ion incident on the detector surface; (η_{capture}), determined by the SRIM simulations shown in Figure 7.12, represents the probability that it will embed into the SNSPD. Only 2 percent of the embedded ^{229}Th atoms will be at the excited isomeric level. Considering these factors, an expression for the expected IC signal rate (Γ_{detIC}) is given by:

$$\begin{gathered} \Gamma_{\text{detIC}} = (0.02)(0.5)(\eta_{\text{capture}})\Gamma_{\text{detBG}} \\ \rightarrow \\ \Gamma_{\text{detIC}} = (0.02)(0.5)(\eta_{\text{capture}})(\Gamma_{\text{source}})(\text{f})(\frac{\text{a}}{\text{A}})(1 - \frac{\ell}{\sqrt{\text{R}^2 + \ell^2}}). \end{gathered} \tag{7.21}$$

The factor of 0.02 accounts for the isomeric level population expected from the α decay of ^{233}U. There is also a factor of 0.5 included in the expression to account for the fact that half of the background events detected could potentially be due to α-particle collisions with the detectors from which an IC decay event should not be expected.

To identify the IC events, we will look at the waveforms recorded by the DT5751 digitizer along with their nanosecond time-tags. The number of radioactive decays from the source, and also the number of detected events in a given amount of time, is described by a Poisson distribution. This means that the time interval between consecutive detected events is a memoryless process. And so the distribution of inter-arrival times will be exponential:

$$\begin{gathered} \mathrm{f}(\mathrm{t};\Gamma) = \Gamma \exp(-\Gamma \mathrm{t}) \\ \text{and} \\ \mathrm{F}(\mathrm{t};\Gamma) = 1 - \exp(-\Gamma \mathrm{t}). \end{gathered} \tag{7.22}$$

In these equations, f represents the probability distribution and F the cumulative distribution function. t is the time (the random variable) and Γ is the rate parameter. In our experiments, we expect at least two different parameterizing rates which are Γ_{detBG} and Γ_{detIC}. A histogram of the binned inter-arrival times for the captured events should reflect these rates. By collecting large numbers of events at different bias currents and looking at the events with short inter-arrival times, we attempt to identify and characterize the IC decay.

7.5.3.1 "Small" SNSPD IC Measurements

The "Small" SNSPDs were not originally designed for the IC experiment but for testing against UV photons. The widths of the wires are less narrow than typical promoting an increased sensitivity to higher energy photons. The detector area is rather small however and this would require data collection for long periods of time in order to obtain good statistics on the IC events. As a benefit, the shorter nanowire lengths result in reduced recovery times of the detector at ~ 100 ns, which is sufficient to resolve an expected lifetime of the IC decay at around 7 usec [SWT17].

Data was taken with the "Small" SNSPD's at a temperature of $\sim 3.3 - 3.4$ K. The

switching current was ~ 24 uA for the device that we label "Detector B", see Figure 7.11b. Due to noise from the amplifier setup shown in Figure 7.4, acquisition of data at lower bias currents, where the SNSPD pulse heights become comparable to the noise amplitudes, is not possible. The results from "Detector B" are reported in the following. Experiments were conducted at several different bias currents. For each bias current, a certain number of data points were taken, with each data point consisting of a 1000-second collection interval. We will consider the results from a couple of different particular bias current settings in more detail.

Figure 7.16 shows some relevant data taken at a bias of 10 uA. Over the course of the experiments conducted at UCLA, we have learned that captured noise events can be devastating in the analysis of the data. Noise events can be spurious and fast, in the respect that it can lead to detected events with very short inter-arrival times, and this can produce misleading results when interpreting the inter-arrival time distributions. For an accurate interpretation of the data, all noise events must be removed. The charge and amplitude histograms of all the recorded waveforms at each particular current bias can provide some insight in regards to the real SNSPD response signals and potential noise events. An example is shown in Figure 7.16(a,b). The charge values were described previously and result from numerical integration of the digitized waveforms, which is performed by default via the DPP-PSD firmware. The amplitudes of the waveforms are determined in post processing of the data. The histograms of these charge and amplitude distributions provide a quick and effective way to distinguish the real SNSPD response signals from potential noise events. In Figure 7.16(a,b), a large distribution of events can be seen at lower values of charge and amplitude. These represent noise events. The distributions at the larger values of charge and amplitude are representative of the real SNSPD responses. In situations in which the noise amplitude is large or when data must be taken at lower bias currents, additional software filters can be applied that further analyze the individual waveforms to help discriminate noise events. To verify that all the noise events have been removed, we inspect all of the recorded waveforms within 20 usec inter-arrival time of another event. A plot of these events can be seen in Figure 7.16(c). With verification that the noise events have been successfully

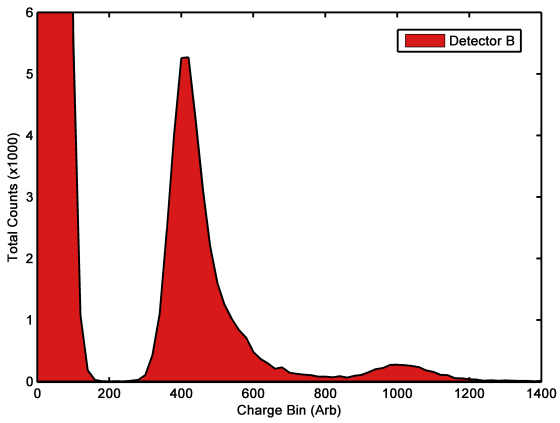

(a) Charge Histogram

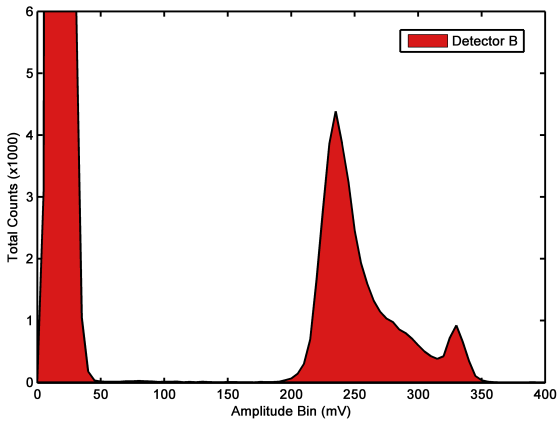

(b) Amplitude Histogram

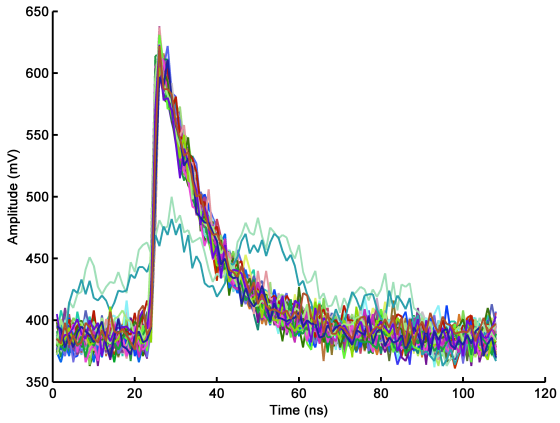

(c) SNSPD Waveforms

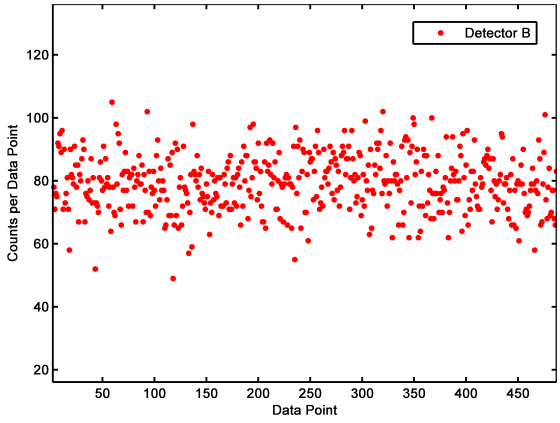

(d) Counts per 1000 sec collections

Figure 7.16: "Small" SNSPD data taken at a 10 uA bias current. The data is representative of detector "B". (a) The charge values are generated by the CAEN digitizer DPP-PSD software through numerical integration of the digitized waveforms. (b) The amplitudes are determined in post-processing of the data. (c) A sample of SNSPD waveforms are shown. These are actually a set of all of the waveforms that occurred within 20 usec of an initial event, potentially a ^{229}Th ion or α particle collision with the detector. (d) The total counts per 1000 sec of data collection, which constitutes a single data point, provides the overall count-rate of each detector.

removed, we can plot the total counts per data point (1000 sec of collection each) to get an idea of the total measured background count-rate (Γ_{meas}), seen in Figure 7.16(d). The data taken at this particular bias did show a pile up of events at shorter inter-arrival times. At a first glance, this looks promising. It should be noted however that the measured background count-rate is significantly larger than what is expected for these detectors ($\Gamma_{\text{meas}} > \Gamma_{\text{detBG}}$). This may just be a dark count rate on the detector, or this could be due to real photons and electrons which are produced from radioactive decay events and collisions inside of the sample box.

Similar analysis is conducted at a bias current of 17 uA. The appropriate plots can be seen in Figure 7.17. In Figure 7.17(a), the charge histogram is shown. It is clear that the SNSPD response distribution is pushed further away from the noise at this larger bias current setting, making it easier to distinguish the SNSPD responses from the noise events. Figures 7.17(b,c) show two sets of waveforms, the impact collisions in (b) and the subsequent correlated events in (c). If these "impact" and "correlated" waveforms were actually due to IC events, we should expect both waveform plots to look similar to that in Figure 7.16(c) in which there is only one correlated event for every single collision event. The impact collision waveforms in Figure 7.17(b) suggest that a single collision event with the substrate may be causing a cascade of detected events. The number of events with short inter-arrival times is significantly larger than what is expected with IC decay from the isomeric level in ^{229}Th. Most radioactive decay events due to the presence of the ^{233}U source will lead to an ejected particle that is not incident upon the detector but elsewhere in the sample box. These collisions may cause the ejection of photons and/or electrons that can potentially be detected by the SNSPD's. This is likely the source of the larger-than-expected measured background count-rate (Γ_{meas}). The large number of correlated events may also be attributed to the particle collisions in the sample box. It is possible that a single particle collision event in the sample box can yield many photons and electrons of varying energies. In cases where the collisions are near the detector surface, the probability of detecting the produced photons and/or electrons increases. And with a larger bias current applied to the SNSPD's, sensitivity to lower energy photons and electrons is increased. The cascading events shown

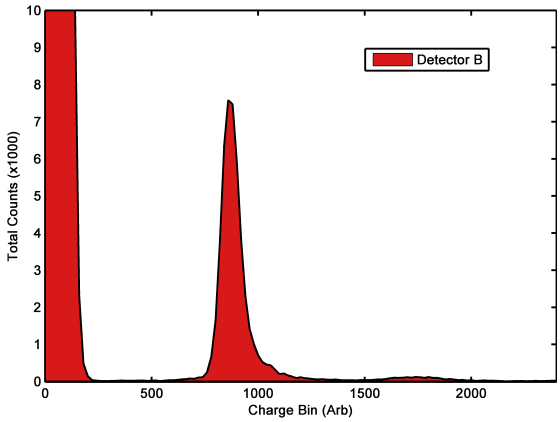

(a) Charge Histogram

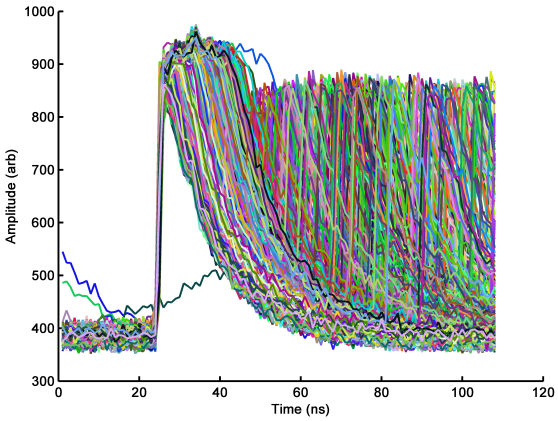

(b) SNSPD Impact Waveforms

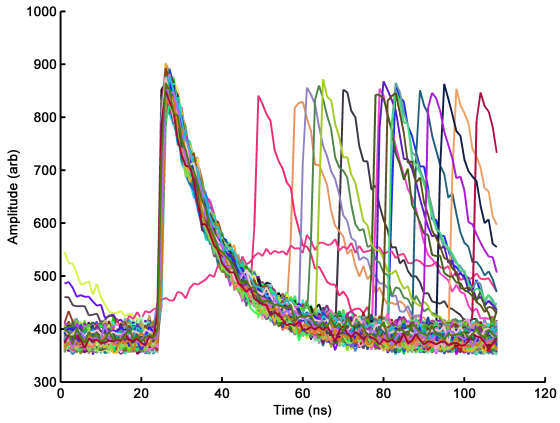

(c) SNSPD Correlated Waveforms

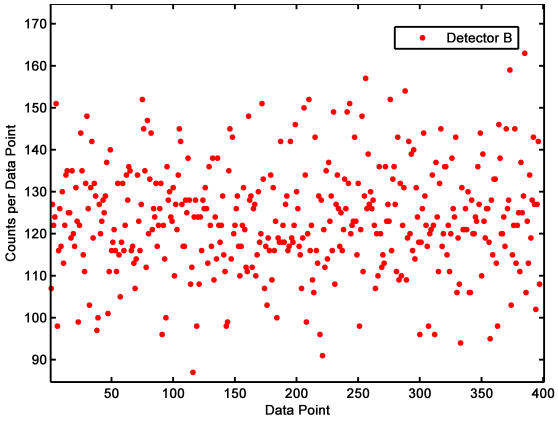

(d) Counts per 1000 sec Collections

Figure 7.17: Small SNSPD data at 17 uA bias. The data is representative of detector "B". (b) The potential "impact" waveforms are shown which could represent initial collision events with the SNSPD's, such as with ^{229}Th ions and α particles. (c) The "correlated" events are shown. These are events that occurred within 20 usec of an "impact" event shown in (b) and could be representative of IC decay events. However, the "impact" waveforms in (b) suggest that the initial collision event could be leading to a cascade of other detected events, which could mask potential IC decay events.

in Figure 7.17(b) are only observed at larger bias currents and may be indicative of particle collision events near the SNSPD surface which produce multiple photons and electrons of varying energies, some of which are detected.

In addition to the mentioned plots, we can also look at the inter-arrival time (IAT) distributions at the various bias current settings. These are shown in Figure 7.18. The exponentials at the highest bias settings seem to reflect different parameterizing rates, one that is on the order of ~ 0.2 MHz and another faster rate > 1 MHz. It should be noted that any single digitized event containing multiple SNSPD response pulses only get counted as a single event with a single time tag. Many of the events shown in Figure 7.17(b) display multiple responses in a single digitized record. If these "extra" events could be properly accounted for, a more accurate inter-arrival time distribution would result which may provide more insight on the true nature of the process governing the faster decay rate.

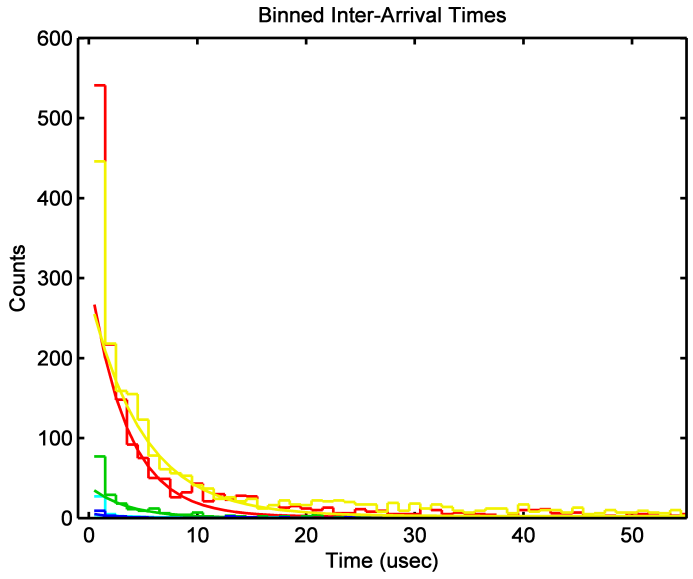

;

Figure 7.18: Binned inter-arrival times for the "Small" detector. The inter-arrival time distribution is shown for data collections at different bias currents. An excess of events can be seen at short inter-arrival times, which increases with larger bias currents.

It is possible that an SNSPD with different properties, such as a wider nanowire feature, may be better suited for this experiment and would provide less sensitivity to lower energy photons and electrons.

7.5.3.2 "SNAP" SNSPD IC Measurements

The IC experiment was also conducted utilizing the "SNAP" SNSPD's. These detectors do have a wider nanowire feature as compared to the "Small" SNSPD's, see Table. 7.1. Data was taken with the detectors cooled down to temperatures in between $3.4 - 3.6$ K. Similar techniques were used in the analysis. The waveforms were confirmed to be legitimate SNSPD responses and then the background count-rate (Γ_{meas}) is determined from the number of counts per data point, shown in Figure 7.19(a). In these experiments however, we did not see any signature of the IC decay. An excess of events with short inter-arrival times was not observed. In fact, the inter-arrival time distribution is reflective of the measured background count rate. The histogram of binned inter-arrival times is shown in Figure 7.19(b).

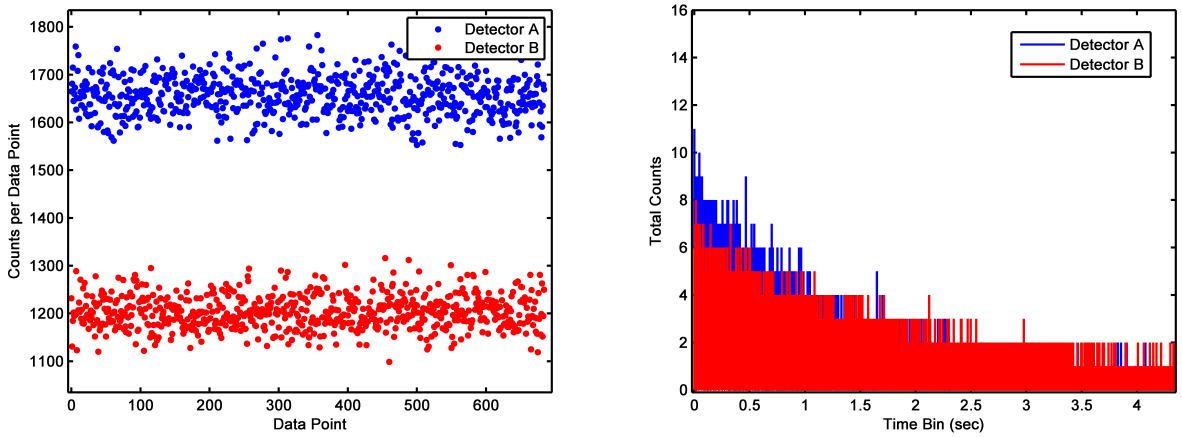

(a) Counts per 1000 seconds of collection.

(b) Binned Inter-Arrival times histogram.

Figure 7.19: "SNAP" SNSPD data. The counts per 1000 sec of data collection (a) and the inter-arrival time histogram (b) are shown. There was no evidence of correlated events in the experiments with these detectors.

Based on the experimental parameters, we should have expected a significant detection of IC events. Its possible that the SNAPs utilized in our experiments were insensitive to the IC events. The bias currents necessary to achieve sensitivity to the IC decay in ^{229}Th may have exceeded the effective switching current for the parallel connection of SNSPD's. Constrictions or other defects in either of the nanowires in parallel could promote a reduced

switching current in the entire configuration, through redirection of the current and subsequent switching of the other SNSPD's. Another explanation for the lack of observation of potential IC events is that the detectors are not thick enough to capture enough of the incident ^{229}Th ions. The SRIM simulations shown in Figure 7.12 suggests a capture fraction (η_{capture}) of ~ 0.2 for these particular detectors, which should have been adequate to see IC events. These detectors were not characterized against VUV light unfortunately. If there are no unknown systematic effects which would prevent the "SNAP" SNSPD's from detecting the IC decay events, the VUV calibration may provide an upper bound on the isomeric energy.

7.5.3.3 "Thick" SNSPD IC Measurements

The "Thick" SNSPD's have been used in experiments only as of relatively recently. These detectors utilize a non-"SNAP" design and a thicker WSi nanowire to help capture more incident ^{229}Th ions. The capture fraction (η_{capture}) is expected to be ~ 0.5 for these detectors. Although the switching current is small compared to the other SNSPD's, as seen in Figure 7.11(d), we were able to take data with bias currents as low as ~ 3 uA. This was made possible through some measures taken to reduce external as well as the amplifier noise mentioned previously. For the readout circuit shown in Figure 7.4, it was found that low pass filters with stopbands in the tens of MHz range were very effective in reducing the amplifier noise. As the recovery time of these particular detectors is long, ~ 400 nsec, the lowpass filters do not limit our detection of events with short inter-arrival times. In addition, cables with better shielding were used to help reduce the effects of external noise. Data was taken at different bias currents. As was done in previous analysis, we verify that all the recorded events are in fact SNSPD responses. Figure 7.20 shows example data taken with the "Thick" SNSPD's at a bias current of 7.5 uA. The charge histogram in Figure 7.20(a) shows that the distribution of real SNSPD responses for "Detector B" is well separated from the noise events at the lower charge values. The "impact" and "correlated" waveform plots are shown in Figures 7.20(b,c) for events within 20 usec inter-arrival time. There is a clearly an excess of events with short inter-arrival times. While there seems to be no strange cascading

effects as was noticed in the case of the "Small" SNSPD's at the higher bias currents, the recovery times for these "Thick" detectors are significantly longer than those of the "Small". This may prevent the detection of events with very short inter-arrival times. The measured

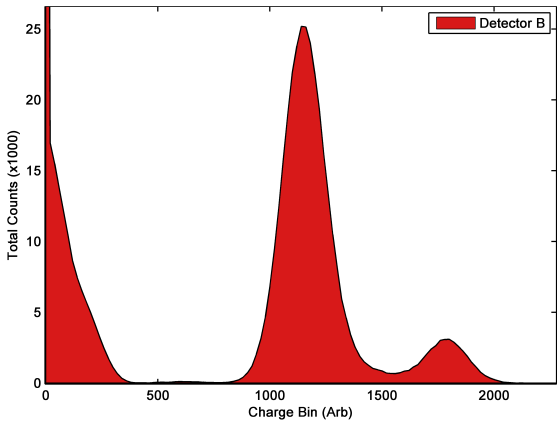

(a) Charge Histogram

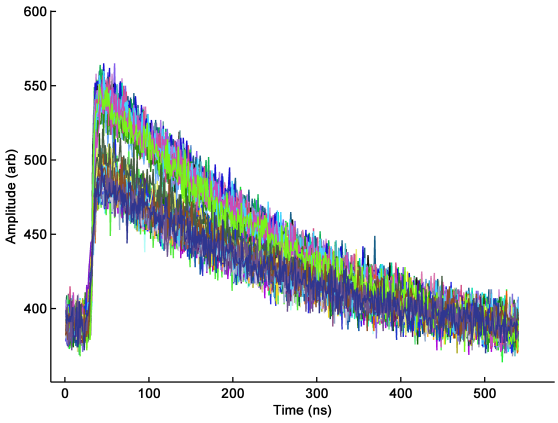

(b) SNSPD Impact Waveforms

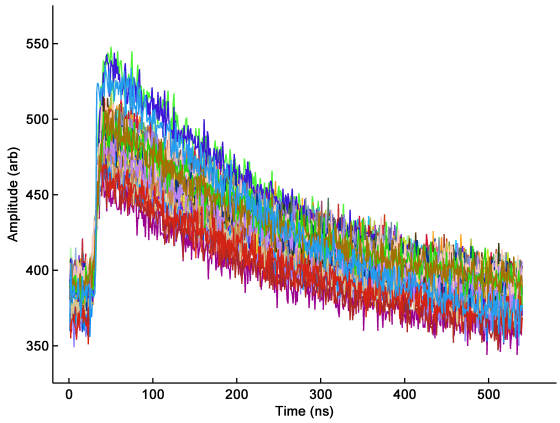

(c) SNSPD Correlated Waveforms

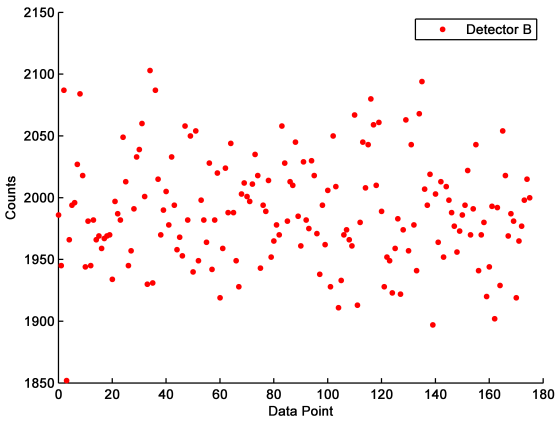

(d) Counts per 1000 sec Collections

Figure 7.20: Thick SNSPD data at 7.5 uA bias. The data is representative of detector "B". The potential "impact" waveforms (b) and "correlated" events (c) do not show cascading events and could be representative of the IC decay. The waveforms are significantly longer in duration as compared to the signal response of the "Small" SNSPD's. This is attributed to the larger detector area (longer meander) which increases the kinetic inductance of the nanowire and its recovery time.

background count-rate seen in the data, as shown in Figure 7.20b(d), is larger than what is expected (Γ_{detBG}). This is once again attributed to the detection of photons and electrons produced in the collisions between the radioactive decay products and contents of the sample

box.

A histogram of the binned inter-arrival times for "Detector A" and "Detector B" can be seen in Figures 7.21(a) and 7.22(a). These look promising, an increase in the bias current seems to reflect an increase in events with short inter-arrival times. To get an idea of Γ_{detIC} at different bias currents, we can consider its expression in terms of the expected background count-rate (Γ_{detBG}) given in (7.21). The ratio of Γ_{detIC} to Γ_{detBG}, which we will call the "expected" IC event fraction, should saturate at ~ 0.005 (since $\eta_{capture}$ for the "Thick" SNSPD's is ~ 0.5 from SRIM simulations). Ideally, we can sweep the bias current such that $\frac{\Gamma_{\mathrm{detIC}}}{\Gamma_{\mathrm{detBG}}}$ increases in a characteristic sigmoidal manner until it reaches a value of ~ 0.005. The following function can represent the "expected" IC event fraction as a function of the bias current:

$$\frac{\Gamma_{\mathrm{detIC}}}{\Gamma_{\mathrm{detBG}}} = \frac{0.005}{2}\left(1 + \mathrm{erf}\left(\frac{\mathrm{I_{bias}} - \mathrm{I_{CO}}}{\sigma_{\mathrm{f}}}\right)\right). \tag{7.23}$$

In this equation $\mathrm{I_{bias}}$ is the bias current, $\mathrm{I_{CO}}$ is the cutoff current parameter, and σ_{f} is the fano-fluctuation parameter [KLM17]. The ratio of Γ_{detIC} to Γ_{detBG} is determined by the excess counts within 20 usec inter-arrival time divided by the total number of expected events. The cutoff current and fano-fluctuation parameters can be approximated from fits performed to the data. Figures 7.21(b) and 7.22(b) show the resulting IC event fractions at different bias currents for detectors "A" and "B", respectively. The corresponding gray lines represent the fits. As can be seen, the IC event fraction does not saturate in our experiments. And unfortunately, the high end of the bias current spectrum has been exhausted as the devices switch at a little over ~ 7 and ~ 8 uA for "Detector A" and "Detector B" respectively. If these are actually IC events and colder temperatures could be reached with the cryostat system, then it may be possible to saturate the IC events.

7.5.3.4 In Situ VUV Calibrations and a Control Source

The next steps in the experiment involve characterization of the "Thick" SNSPD's against VUV light. This was performed in situ along with the ^{233}U source. The coupling of VUV light was accomplished in a "brute force" method which involved drilling a 1 mm diameter

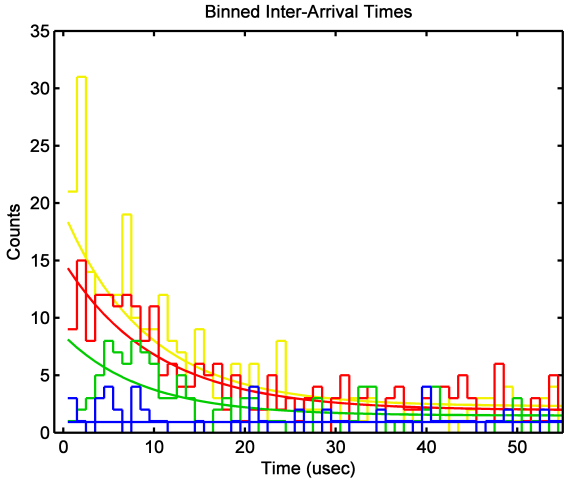

(a) Binned Inter-Arrival Times.

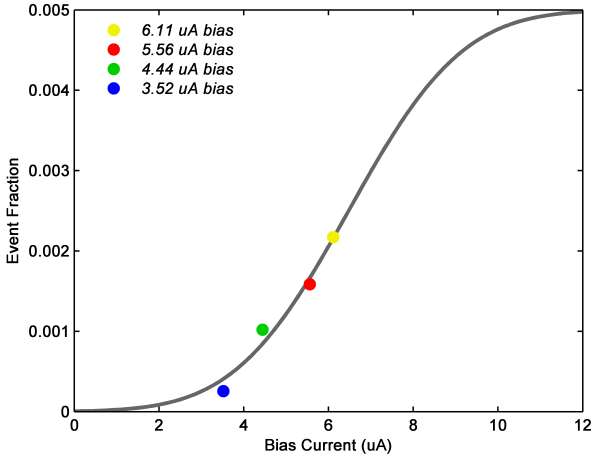

(b) "Expected" Event Fraction vs Bias.

Figure 7.21: "Thick" SNSPD detector "A". (a) The inter-arrival time distributions are shown at different bias currents. (b) The event fraction vs current bias curve is shown. The event fraction is proportional to the number of excess measured events within 20 μsec inter-arrival time divided by the total number of expected events, which is dependent on the total collection time at each particular bias current.

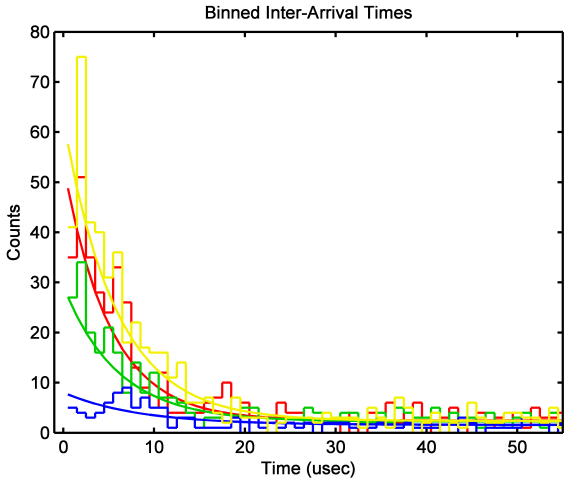

(a) Binned Inter-Arrival Times.

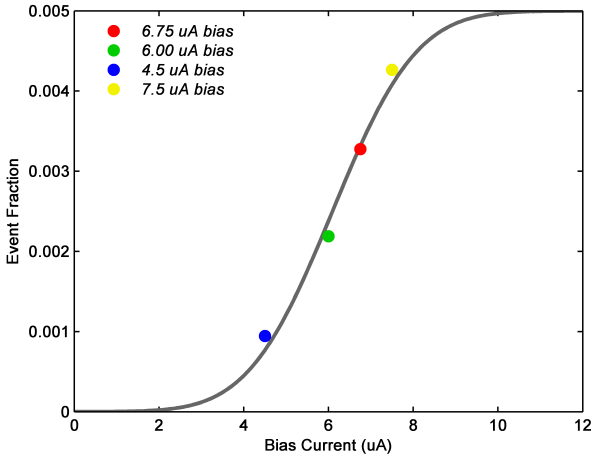

(b) Event Fraction vs Bias.

Figure 7.22: "Thick" SNSPD detector "B". (a) The inter-arrival time distributions are shown at different bias currents. (b) The resulting event fraction vs current bias curve is shown.

hole through the NIST calibrated ^{233}U source. The hole serves as an aperture and allows for coupling of the VUV photons directly through it. A half inch MgF_2 window covers the hole in the ^{233}U source and its mount, which helps significantly reduce the rate at which residual atoms and molecules can freeze onto the SNSPD surfaces. The setup is similar to that shown in Figure 7.14 in which the deuterium lamp and monochromator provide photons for coupling into the sample box housing the detectors. The results of the in-situ calibrations are shown in Figures. 7.23, (a) and (b), for detectors "A" and "B" respectively. These are

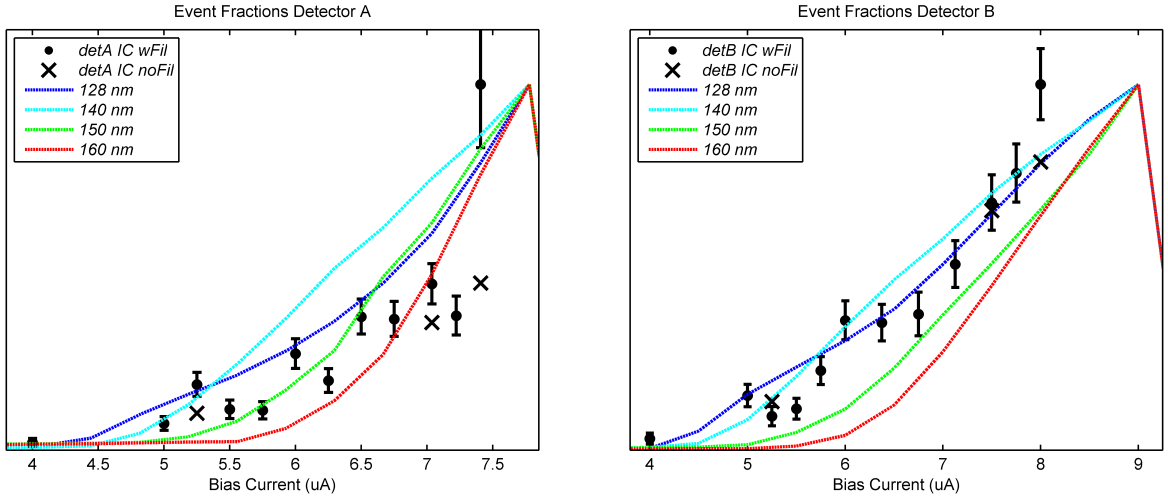

(a) "Thick" detector A.

(b) "Thick" detector B.

Figure 7.23: In situ VUV calibrations compared to IC event fractions. The dashed curves represent the VUV calibration measurements with (blue, cyan, green, and red) representing the response from photons of wavelengths (128, 140, 150, and 160) nm. The black dots represent the "expected" event fractions taken with low pass filters (BLP-10.7+ and BLP-21.4+ from Mini-Circuits) and the black x's represent data taken for comparison without the filters.

preliminary results. All VUV and IC measurement curves are normalized to unity in these figures. It can be noticed that the detectors become sensitive to higher energy photons at lower bias currents, as expected. A saturation plateau may be difficult to achieve with wider and thicker nanowire features. UV fluorescence, resulting from the absorption of VUV photons by molecules frozen on surfaces in the cryostat, could lead to extraneous detection of events at larger bias currents. These factors may be responsible for the lack of a distinct

sigmoid and saturation plateau in the VUV response curves. The IC event fraction increases with the bias current to numbers which agree with the model. Unfortunately, there is no clear saturation plateau for these correlated events either.

In addition to calibration against light, a ^{241}Am source was used as a control against ^{233}U. The α decay of ^{241}Am will yield ^{237}Np with energies of $\sim$ 5.6 MeV, comparable to the energies of ^{229}Th ions produced in the α decay of ^{233}U. While the half life of ^{237}Np is $\sim$ 2.144 million years, it is known to have an isomeric level with a lifetime of $\sim$ 0.7 usecs. The decay from the level should yield γ's with energies of hundreds of keV however, and we should expect correlated events with such a lifetime over the entire range of bias currents that yield detectable signal responses. As before, data is taken at different bias currents. The resulting "expected" and "measured" event fractions for both the ^{241}Am and ^{233}U sources can be compared in Figures 7.24a and 7.24b, respectively. The "expected" event fraction is as described earlier. The "measured" event fraction represents the excess counts within

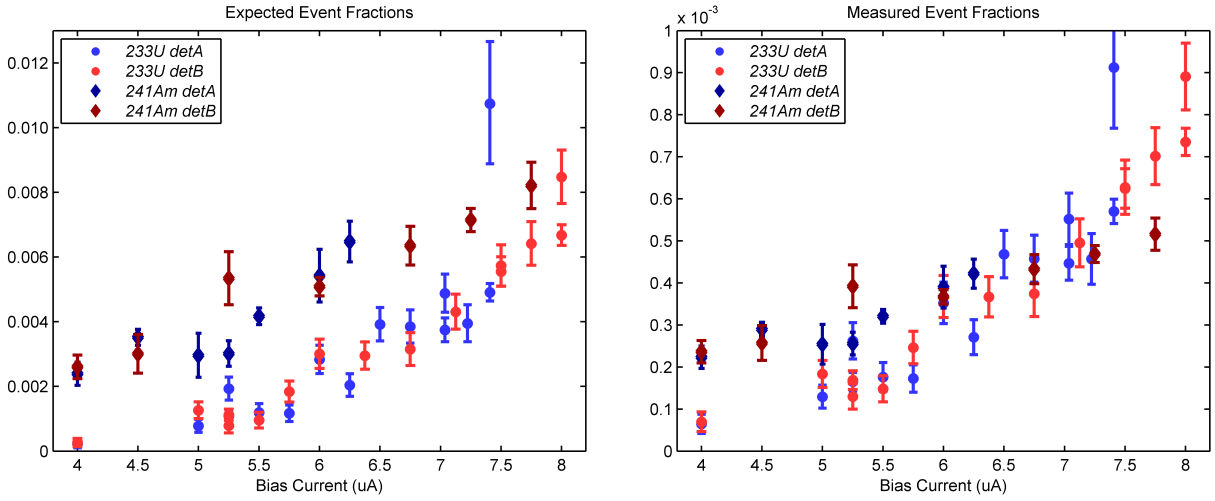

(a) Expected event fraction vs bias.

(b) Measured event fraction vs bias.

Figure 7.24: Comparison of the expected and measured event fractions for ^{233}U and ^{241}Am. The bright blue and red dots represent measurements with ^{233}U for detectors "A" and "B" respectively. The dark blue and red diamonds represent measurements with ^{241}Am for detectors "A" and "B" respectively.

20 μsec inter-arrival time divided by the total number of measured events. Although the

^{241}Am and ^{233}U source activities are approximately similar, the overall count-rate due to the former is twice as large as that due to the latter. This may simply be due to a non-uniform electroplating process which yields a non-uniform source activity. The binned inter-arrival time plots resulting from the ^{233}U and ^{241}Am sources have noticeably different lifetimes and features. More data is being collected with the ^{233}U and ^{241}Am sources, and other control sources will be tested in the future. In addition, the inter-arrival time distributions for the different sources will be examined more carefully at different bias currents. This may help distinguish different processes, with potentially different lifetimes and energies, that may be occurring. These results are not clearly conclusive for IC detection. There is still much work to be done.

A huge thanks to folks at NIST involved in this work: Sae Woo Nam, Varun Verma, and Galen O'Neil.

References

[AHC11] W Al-Basheer, M Hedén, ZJ Cai, and YJ Shi. "Study of two-photon resonant four-wave sum mixing in xenon in the spectral region of 105–110 nm." *Chemical Physics*, **381**(1-3):59–66, 2011.

[AHJ07] N. Ashby, T. P. Heavner, S. R. Jefferts, T. E. Parker, A. G. Radnaev, and Y. O. Dudin. "Testing Local Position Invariance with Four Cesium-Fountain Primary Frequency Standards and Four NIST Hydrogen Masers." *Phys. Rev. Lett.*, **98**:070802, Feb 2007.

[AM05] Neil W Ashcroft and N David Mermin. "Solid state physics (holt, rinehart and winston, new york, 1976)." *Google Scholar*, **403**, 2005.

[ARM02] D. Alexiev, M.I. Reinhard, L. Mo, A.R. Rosenfeld, and M.L. Smith. "Review of Ge detectors for gamma spectroscopy." *Australas. Phys. Eng. Sci. Med.*, **25**(3):102–109, 2002.

[ATV05] D Alderighi, G Toci, M Vannini, D Parisi, and Mauro Tonelli. "Experimental evaluation of the cw lasing threshold for a Ce: LiCaAlF 6 laser." *Optics express*, **13**(19):7256–7264, 2005.

[ATV06] D Alderighi, G Toci, M Vannini, D Parisi, S Bigotta, and Mauro Tonelli. "High efficiency UV solid state lasers based on Ce: LiCaAlF 6 crystals." *Applied Physics B*, **83**(1):51–54, 2006.

[BAB03] V. Barci, G. Ardisson, G. Barci-Funel, B. Weiss, O. El Samad, and R. Sheline. "Nuclear structure of^{229}Th from γ-ray spectroscopy study of^{233}U α-particle decay." *Phys. Rev. C*, **68**:034329, September 2003.

[BBB07] B. R. Beck, J. A. Becker, P. Beiersdorfer, G. V. Brown, K. J. Moody, J. B. Wilhelmy, F. S. Porter, C. A. Kilbourne, and R. L. Kelley. "Energy Splitting of the Ground-State Doublet in the Nucleus ^{229}Th." *Phys. Rev. Lett.*, **98**(14):142501, April 2007.

[BCK18] PV Borisyuk, EV Chubunova, NN Kolachevsky, Yu Lebedinskii, OS Vasiliev, EV Tkalya, et al. "Excitation of ^{2}29Th nuclei in laser plasma: the energy and half-life of the low-lying isomeric state." *arXiv preprint arXiv:1804.00299*, 2018.

[BCL18] PV Borisyuk, EV Chubunova, Yu Yu Lebedinskii, EV Tkalya, OS Vasilyev, VP Yakovlev, E Strugovshchikov, D Mamedov, A Pishtshev, and S Zh Karazhanov. "Experimental studies of thorium ion implantation from pulse laser plasma into thin silicon oxide layers." *Laser Physics Letters*, **15**(5):056101, 2018.

[BE14] O. Bodnar and C. Elster. *Metrologia*, **51**:516, 2014.

[Bel14] K. Beloy. "Hyperfine Structure in $^{229g}Th^{3+}$ as a Probe of the ^{229g}Th $\rightarrow^{229m}$ Th Nuclear Excitation Energy." *Phys. Rev. Lett.*, **112**:062503, Feb 2014.

[BF79] I. M. Band and V. I. Fomichev. *At. Data Nucl. Data Tabl.*, **23**:295, 1979.

[BGQ90] D. G. Burke, P. E. Garrett, Tao Qu, and R. A. Naumann. "Additional evidence for the proposed excited state at $\leq$5 eV in ^{229}Th." *Phys. Rev. C*, **42**:R499–R501, Aug 1990.

[Bla] J. M. Blatt and V. F. Weisskopf, *Theoretical Nuclear Physics*. John Wiley & Sons, Inc. NY, 1952.

[BMF88] C. E. Bemis, F. K. McGowan, J. L. C. Ford, Jr., W. T. Milner, R. L. Robinson, P. H. Stelson, G. A. Leander, and C. W. Reich. "Coulomb excitation of states in ^{229}Th." *Phys. Scr.*, **38**(5):657–663, 1988.

[BNC01] E. Browne, E. B. Norman, R. D. Canaan, D. C. Glasgow, J. M. Keller, and J. P. Young. *Phys. Rev. C*, **164**:014311, 2001.

[BPP18] Pavlo V Bilous, Ekkehard Peik, and Adriana Pálffy. "Laser-induced electronic bridge for characterization of the 229mTh 229gTh nuclear transition with a tunable optical laser." *New Journal of Physics*, **20**(1):013016, 2018.

[BT13] E. Browne and J.K. Tuli. "Nuclear Data Sheets for A = 231." *Nuclear Data Sheets*, **114**(6):751 – 840, 2013.

[BW79] John M. Blatt and Victor F. Weisskopf. *General Properties of the Nucléus*, pp. 1–47. Springer New York, New York, NY, 1979.

[BWB09] B. R. Beck, C. Y. Wu, P. Beiersdorfer, G. V. Brown, J. A. Becker, J. K. Moody, J. B. Wilhelmy, F. S. Porter, C. A. Kilbourne, and R. L. Kelley. "Improved Value for the Energy Splitting of the Ground-State Doublet in the Nucleus ^{229m}Th." Conference LLNL-PROC-415170, Lawrence Livermore National Laboratory, Livermore, CA, July 2009.

[CB06] John Clarke and Alex I Braginski. *The SQUID handbook: Applications of SQUIDs and SQUID systems*. John Wiley & Sons, 2006.

[CC00] R Casten and Richard F Casten. *Nuclear structure from a simple perspective*, volume 23. Oxford University Press on Demand, 2000.

[CM04] David W Coutts, Andrew JS McGonigle, et al. "Cerium-doped fluoride lasers." 2004.

[Cow98] Glen Cowan. *Statistical data analysis*. Oxford university press, 1998.

[CRK11] C. J. Campbell, A. G. Radnaev, and A. Kuzmich. "Wigner Crystals of ^{229}Th for Optical Excitation of the Nuclear Isomer." *Phys. Rev. Lett.*, **106**:223001, Jun 2011.

[CRK12] C. J. Campbell, A. G. Radnaev, A. Kuzmich, V. A. Dzuba, V. V. Flambaum, and A. Derevianko. "Single-Ion Nuclear Clock for Metrology at the 19th Decimal Place." *Phys. Rev. Lett.*, **108**:120802, March 2012.

[CSC09] C. J. Campbell, A. V. Steele, L. R. Churchill, M. V. DePalatis, D. E. Naylor, D. N. Matsukevich, A. Kuzmich, and M. S. Chapman. "Multiply Charged Thorium Crystals for Nuclear Laser Spectroscopy." *Phys. Rev. Lett.*, **102**:233004, Jun 2009.

[CW56] E. L. Church and J. Weneser. *Phys. Rev.*, **104**:1382, 1956.

[Cyr73] M Cyrot. "Ginzburg-Landau theory for superconductors." *Reports on Progress in Physics*, **36**(2):103, 1973.

[Dav96] Hananel Davidowitz. "A novel technique for temperature stabilization very near a phase transition: Results for He2." *Review of Scientific Instruments*, **67**(1):236–239, 1996.

[DET96] A. M. Dykhne, N. V. Eremin, and E. V. Tkalya. "Alpha decay of the first excited state of the Th-229 nucleus." *Journal of Experimental and Theoretical Physics Letters*, **64**(5):345–349, Sep 1996.

[Dic53] R. H. Dicke. "The Effect of Collisions upon the Doppler Width of Spectral Lines." *Phys. Rev.*, **89**:472–473, Jan 1953.

[Dic54] R. H. Dicke. "Coherence in Spontaneous Radiation Processes." *Phys. Rev.*, **93**:99–110, Jan 1954.

[DSL] Schroeer D., Kuo Ch. S., and Lambe R. L. "Isomer shift of Eu2+ in fluorites." *physica status solidi (b)*, **92**(2):565–572.

[DT98] A. M. Dykhne and E. V. Tkalya. "Matrix element of the anomalously low-energy (3.5±0.5 eV) transition in ^{229}Th and the isomer lifetime." *JETP Lett.*, **67**(4):251–256, February 1998. [Pis'ma Zh. Éksp. Teor. Fiz. 67, 233–238 (1998)].

[FC98] Gary J. Feldman and Robert D. Cousins. "Unified approach to the classical statistical analysis of small signals." *Phys. Rev. D*, **57**:3873–3889, April 1998.

[Fla06] V. V. Flambaum. "Enhanced Effect of Temporal Variation of the Fine Structure Constant and the Strong Interaction in ^{229}Th." *Phys. Rev. Lett.*, **97**:092502, August 2006.

[GCS09] Eduardo Granados, David W Coutts, and David J Spence. "Mode-locked deep ultraviolet Ce: LiCAF laser." *Optics letters*, **34**(11):1660–1662, 2009.

[GH05] Z. O. Guimaraes-Filho and O. Helene. *Phys. Rev. C*, **71**:044303, 2005.

[Gib76] T. C. Gibb. *The Mössbauer Effect*, pp. 1–21. Springer US, Boston, MA, 1976.

[GKA02] K. Gulda, W. Kurcewicz, A. J. Aas, M. J. G. Borge, D. G. Burke, B. Fogelberg, I. S. Grant, E. Hagebø, N. Kaffrell, J. Kvasil, G. Løvhøiden, H. Mach, A. Mackova, T. Martinez, G. Nyman, B. Rubio, J. L. Tain, O. Tengblad, and T.F. Thorsteinsen. "The nuclear structure of 229Th." *Nucl. Phys. A*, **703**(1–2):45–69, May 2002.

[GL74] S Gerstenkorn and P Lue. "Gerstenkorn, S., P. Lue, J. Verges, DW Engelkemeir, JE Gindler, and FS Tomkins, 1974, J. Phys.(Paris) 35, 483." *J. Phys.(Paris)*, **35**:483, 1974.

[GNJ14] R. M. Godun, P. B. R. Nisbet-Jones, J. M. Jones, S. A. King, L. A. M. Johnson, H. S. Margolis, K. Szymaniec, S. N. Lea, K. Bongs, and P. Gill. "Frequency Ratio of Two Optical Clock Transitions in $^{171}Yb^{+}$ and Constraints on the Time Variation of Fundamental Constants." *Phys. Rev. Lett.*, **113**:210801, November 2014.

[Ham00] Clark A Hamilton. "Josephson voltage standards." *Review of scientific instruments*, **71**(10):3611–3623, 2000.

[HCA09] Hsiu-Sheng Hsu, Can Cai, and Andrea M Armani. "Ultra-low-threshold Er: Yb sol-gel microlaser on silicon." *Optics Express*, **17**(25):23265–23271, 2009.

[Her65] R. H. Herber. "Introduction to Mossbauer spectroscopy." *Journal of Chemical Education*, **42**(4):180, 1965.

[HGR13] Markus P. Hehlen, Richard R. Greco, Wade G. Rellergert, Scott T. Sullivan, David DeMille, Robert A. Jackson, Eric R. Hudson, and Justin R. Torgerson. "Optical spectroscopy of an atomic nucleus: Progress toward direct observation of the ^{229}Th isomer transition." *J. Lumin.*, **133**:91–95, January 2013.

[HJ16] Robert H Hadfield, Göran Johansson, et al. *Superconducting Devices in Quantum Optics*. Springer, 2016.

[HKH97] P. A. Heimann, M. Koike, C. W. Hsu, D. Blank, X. M. Yang, A. G. Suits, Y. T. Lee, M. Evans, C. Y. Ng, C. Flaim, and H. A. Padmore. "Performance of the vacuum ultraviolet high-resolution and high-flux beamline for chemical dynamics studies at the Advanced Light Source." *Rev. Sci. Instrum.*, **68**(5):1945–1951, 1997.

[HLT14] N. Huntemann, B. Lipphardt, Chr. Tamm, V. Gerginov, S. Weyers, and E. Peik. "Improved Limit on a Temporal Variation of m_p/m_e from Comparisons of Yb^{+} and Cs Atomic Clocks." *Phys. Rev. Lett.*, **113**:210802, November 2014.

[HNO13] O. A. Herrera-Sancho, N. Nemitz, M. V. Okhapkin, and E. Peik. "Energy levels of Th^{+} between 7.3 and 8.3 eV." *Phys. Rev. A*, **88**:012512, Jul 2013.

[HOZ12] O. A. Herrera-Sancho, M. V. Okhapkin, K. Zimmermann, Chr. Tamm, E. Peik, A. V. Taichenachev, V. I. Yudin, and P. Głowacki. "Two-photon laser excitation of trapped $^{232}Th^{+}$ ions via the 402-nm resonance line." *Phys. Rev. A*, **85**:033402, Mar 2012.

[HR94] R. G. Helmer and C. W. Reich. "An excited state of ^{229}Th at 3.5 eV." *Phys. Rev. C*, **49**:1845–1858, April 1994.

[IK97] G. Irwin and K. Kim. "Observation of Electromagnetic Radiation from Deexcitation of the ^{229}Th Isomer." *Phys. Rev. Lett.*, **79**(6):990–993, August 1997.

[JAV09] Robert A Jackson, Jomar B Amaral, Mario E G Valerio, David P DeMille, and Eric R Hudson. "Computer modelling of thorium doping in LiCaAlF 6 and LiSrAlF 6 : application to the development of solid state optical frequency devices." *Journal of Physics: Condensed Matter*, **21**(32):325403, 2009.

[JSS15] J. Jeet, Christian Schneider, Scott T. Sullivan, Wade G. Rellergert, Saed Mirzadeh, A. Cassanho, H. P. Jenssen, Eugene V. Tkalya, and Eric R. Hudson. *Phys. Rev. Lett.*, **114**:253001, 2015.

[Kim10] Ki Young Kim. *Advances in Optical and Photonic Devices*. Sciyo. com, 2010.

[KKH09] H. Kikunaga, Y. Kasamatsu, H. Haba, T. Mitsugashira, M. Hara, K. Takamiya, T. Ohtsuki, A. Yokoyama, T. Nakanishi, and A. Shinohara. "Half-life estimation of the first excited state of ^{229}Th by using α-particle spectrometry." *Phys. Rev. C*, **80**:034315, September 2009.

[KLM17] AG Kozorezov, C Lambert, F Marsili, MJ Stevens, VB Verma, JP Allmaras, MD Shaw, RP Mirin, and Sae Woo Nam. "Fano fluctuations in superconducting-nanowire single-photon detectors." *Physical Review B*, **96**(5):054507, 2017.

[KLS92] T. T. Kajava, H. M. Lauranto, and R. R. E. Salomaa. "Mode structure fluctuations in a pulsed dye laser." *Appl. Opt.*, **31**(33):6987–6992, Nov 1992.

[KPR75] OSVALD Knop, EM Palmer, and RW Robinson. "Arrangements of point charges having zero electric-field gradient." *Acta Crystallographica Section A: Crystal Physics, Diffraction, Theoretical and General Crystallography*, **31**(1):19–31, 1975.

[KR76] L.A. Kroger and C.W. Reich. "Features of the low-energy level scheme of ^{229}Th as observed in the α-decay of ^{233}U." *Nucl. Phys. A*, **259**(1):29–60, March 1976.

[KT07] F. F. Karpeshin and M. B. Trzhaskovskaya. "Impact of the electron environment on the lifetime of the ^{229}Th^m low-lying isomer." *Phys. Rev. C*, **76**:054313, Nov 2007.

[LSC08] H Liu, DJ Spence, DW Coutts, H Sato, and T Fukuda. "Broadly tunable ultraviolet miniature cerium-doped LiLuF lasers." *Optics Express*, **16**(3):2226–2231, 2008.

[MAB04] I.D. Moore, I. Ahmad, K. Bailey, D. L. Bowers, Z.-T. Lu, T. P. O'Connor, and Z. Yin. "Search for a low-lying 3.5-eV isomeric state in ^{229}Th." Physics Division Report PHY-10990-ME-2004, Argonne National Laboratory, Argonne, IL, December 2004.

[MHO03] T. Mitsugashira, M. Hara, T. Ohtsuki, H. Yuki, K. Takamiya, Y. Kasamatsu, A. Shinohara, H. Kikunaga, and T. Nakanishi. "Alpha-decay from the 3.5 eV isomer of ^{229}Th." *J. Radioanal. Nucl. Chem.*, **255**(1):63–66, January 2003.

[MP17] Nikolay Minkov and Adriana Palffy. "Reduced Transition Probabilities for the Gamma Decay of the 7.8 eV Isomer in Th 229." *Physical review letters*, **118**(21):212501, 2017.

[MSA90] Mitsuo Maeda, Takashi Sibata, and Hideharu Akiyoshi. "Optimum wavelengths in solar-blind UV ozone lidars." *Japanese journal of applied physics*, **29**(12R):2843, 1990.

[MSP94] CD Marshall, JA Speth, Stephen A Payne, William F Krupke, Gregory J Quarles, V Castillo, and Bruce HT Chai. "Ultraviolet laser emission properties of Ce 3+-doped LiSrAlF 6 and LiCaAlF 6." *JOSA B*, **11**(10):2054–2065, 1994.

[MSS07] AB Matsko, AA Savchenkov, D Strekalov, VS Ilchenko, N Yu, and L Maleki. "Fabrication, Characterization and Applications of Crystalline Whispering Gallery Mode Resonators." In *Transparent Optical Networks, 2007. ICTON'07. 9th International Conference on*, volume 3, pp. 50–54. IEEE, 2007.

[MV00] S. A. Murphy and A. W. van der Vaart. "On Profile Likelihood." *J. Am. Stat. Assoc.*, **95**(450):449–465, June 2000.

[Nil55] S. G. Nilsson. *Mat.-fys medd. danske selskab*, **Bd. 29**:n. 16, 1955.

[NTH12] Chandra M Natarajan, Michael G Tanner, and Robert H Hadfield. "Superconducting nanowire single-photon detectors: physics and applications." *Superconductor science and technology*, **25**(6):063001, 2012.

[OMP15] M. V. Okhapkin, D. M. Meier, E. Peik, M. S. Safronova, M. G. Kozlov, and S. G. Porsev. "Observation of an unexpected negative isotope shift in $^{229}Th^{+}$ and its theoretical explanation." *Phys. Rev. A*, **92**:020503, Aug 2015.

[OV09] Eric P Ostby and Kerry J Vahala. "Yb-doped glass microcavity laser operation in water." *Optics letters*, **34**(8):1153–1155, 2009.

[PBB09] F S Porter, P Beiersdorfer, G V Brown, M F Gu, R L Kelley, S Kahn, C A Kilbourne, and D B Thorn. "Evolution of X-ray calorimeter spectrometers at the Lawrence Livermore Electron Beam Ion Trap." *Journal of Physics: Conference Series*, **163**(1):012105, 2009.

[PDF09] Elisabeth Peters, Scott A Diddams, Peter Fendel, Sascha Reinhardt, TW Hänsch, and Th Udem. "A deep-UV optical frequency comb at 205 nm." *Optics express*, **17**(11):9183–9190, 2009.

[PF10a] S. G. Porsev and V. V. Flambaum. "Effect of atomic electrons on the 7.6-eV nuclear transition in $^{229}Th^{3+}$." *Phys. Rev. A*, **81**:032504, Mar 2010.

[PF10b] S. G. Porsev and V. V. Flambaum. "Electronic bridge process in $^{229}Th^{+}$." *Phys. Rev. A*, **81**:042516, Apr 2010.

[Pre90] H Preston-Thomas. "The International Temperature Scale of 1990 (ITS-90)." *Metrologia*, **27**(1):3, 1990.

[PRF] Roesch L. Ph., Kulessa R., and Horber F. "Electric Field Gradients in Hexagonal Crystals of Cd, Zn, Gd, and Te Acting on Sm, W, and Os Impurities." *physica status solidi (b)*, **71**(1):389–394.

[PT03] E. Peik and Chr. Tamm. "Nuclear laser spectroscopy of the 3.5 eV transition in Th-229." *Europhys. Lett.*, **61**(2):181–186, January 2003.

[PZ13] Ekkehard Peik and Kai Zimmermann. "Comment on "Observation of the Deexcitation of the ^{229m}Th Nuclear Isomer"." *Phys. Rev. Lett.*, **111**(1):018901, July 2013.

[Ram66] J. Ramakrishna. "Electric field gradients in ionic crystals III. nuclear quadrupole resonance in thorium tetrachloride." *The Philosophical Magazine: A Journal of Theoretical Experimental and Applied Physics*, **13**(123):515–519, 1966.

[RBE98] D. Richardson, D. Benton, D. Evans, J. Griffith, and G. Tungate. "Ultraviolet Photon Emission Observed in the Search for the Decay of the ^{229}Th Isomer." *Phys. Rev. Lett.*, **80**(15):3206–3208, April 1998.

[RCK12] A. G. Radnaev, C. J. Campbell, and A. Kuzmich. "Observation of the 717-nm electric quadrupole transition in triply charged thorium." *Phys. Rev. A*, **86**:060501, Dec 2012.

[RDG10] Wade G. Rellergert, D. DeMille, R. R. Greco, M. P. Hehlen, J. R. Torgerson, and Eric R. Hudson. "Constraining the Evolution of the Fundamental Constants with a Solid-State Optical Frequency Reference Based on the ^{229}Th Nucleus." *Phys. Rev. Lett.*, **104**(20):200802, May 2010.

[RH90] C. W. Reich and R. G. Helmer. *Phys. Rev. Lett.*, **64**:271, 1990.

[RHS08] T. Rosenband, D. B. Hume, P. O. Schmidt, C. W. Chou, A. Brusch, L. Lorini, W. H. Oskay, R. E. Drullinger, T. M. Fortier, J. E. Stalnaker, S. A. Diddams, W. C. Swann, N. R. Newbury, W. M. Itano, D. J. Wineland, and J. C. Bergquist. "Frequency Ratio of Al^+ and Hg^+ Single-Ion Optical Clocks; Metrology at the 17th Decimal Place." *Science*, **319**(5871):1808–1812, 2008.

[RK95] G. L. J. A. Rikken and Y. A. R. R. Kessener. "Local Field Effects and Electric and Magnetic Dipole Transitions in Dielectrics." *Phys. Rev. Lett.*, **74**(6):880–883, February 1995.

[RPZ06] E. Ruchowska, W. A. Płóciennik, J. Żylicz, H. Mach, J. Kvasil, A. Algora, N. Amzal, T. Bäck, M. G. Borge, R. Boutami, P. A. Butler, J. Cederkäll, B. Cederwall, B. Fogelberg, L. M. Fraile, H. O. U. Fynbo, E. Hagebø, P. Hoff, H. Gausemel, A. Jungclaus, R. Kaczarowski, A. Kerek, W. Kurcewicz, K. Lagergren, E. Nacher, B. Rubio, A. Syntfeld, O. Tengblad, A. A. Wasilewski, and L. Weissman. "Nuclear structure of ^{229}Th." *Phys. Rev. C*, **73**:044326, Apr 2006.

[RS83] M. Rohde and D. Salomon. "Temperature dependence of the Isomer Shift and electric field gradient of181Ta in Re-metal." *Hyperfine Interactions*, **15**(1):257–260, Dec 1983.

[RS04] Peter Ring and Peter Schuck. *The nuclear many-body problem.* Springer Science & Business Media, 2004.

[RSD10a] Wade G Rellergert, Scott T Sullivan, D DeMille, R R Greco, M P Hehlen, R A Jackson, J R Torgerson, and Eric R Hudson. "Progress towards fabrication of 229 Th-doped high energy band-gap crystals for use as a solid-state optical frequency reference." *IOP Conference Series: Materials Science and Engineering*, **15**(1):012005, 2010.

[RSD10b] Wade G. Rellergert, Scott T. Sullivan, D. DeMille, R. R. Greco, M. P. Hehlen, R. A. Jackson, J. R. Torgerson, and Eric R. Hudson. "Progress towards fabrication of ^{229}Th-doped high energy band-gap crystals for use as a solid-state optical frequency reference." *IOP Conf. Ser.: Mater. Sci. Eng.*, **15**(1):012005, 2010.

[San96] V Sandoghdar. "V. Sandoghdar, F. Treussart, J. Hare, V. Lefèvre-Seguin, J.-M. Raimond, and S. Haroche, Phys. Rev. A 54, R1777 (1996)." *Phys. Rev. A*, **54**:R1777, 1996.

[Sla61] Glen A. Slack. "Thermal Conductivity of CaF_2, MnF_2, CoF_2, and ZnF_2 Crystals." *Phys. Rev.*, **122**:1451–1464, Jun 1961.

[Sol] A. A. Soldatov and D. P. Grechukhin, Kourchatov Institute of Atomic Energy Report-3174, Moscow, 1979.

[SSR18] Simon Stellmer, Yudai Shigekawa, Veronika Rosecker, Georgy A. Kazakov, Yoshitaka Kasamatsu, Yuki Yasuda, Atsushi Shinohara, and Thorsten Schumm. "Toward an energy measurement of the internal conversion electron in the deexcitation of the ^{229}Th isomer." *Phys. Rev. C*, **98**:014317, Jul 2018.

[ST91] V. F. Strizhov and E. V. Tkalya. *Sov. Phys. JETP*, **72**:387, 1991.

[ST05] Balraj Singh and Jagdish K. Tuli. "Nuclear Data Sheets for A = 233." *Nuclear Data Sheets*, **105**(1):109 – 222, 2005.

[Swa12] Erik Lars Swanberg Jr. *Searching for the Decay of ^{229m}Th.* Dissertation, University of California, Berkeley, 2012.

[SWT17] Benedict Seiferle, Lars von der Wense, and Peter G Thirolf. "Lifetime Measurement of the Th 229 Nuclear Isomer." *Physical review letters*, **118**(4):042501, 2017.

[SYC99] R. Shaw, J. Young, S. Cooper, and O. Webb. "Spontaneous Ultraviolet Emission from ^{233}Uranium/^{229}Thorium Samples." *Phys. Rev. Lett.*, **82**(6):1109–1111, February 1999.

[SZF07] Siyka I Shopova, Hongying Zhou, Xudong Fan, and Po Zhang. "Optofluidic ring resonator based dye laser." *Applied physics letters*, **90**(22):221101, 2007.

[Tka94] E. V. Tkalya. *JETP Lett.*, **78**:239, 1994.

[Tka00] E. V. Tkalya. *JETP Lett.*, **71**:311, 2000.

[Tka11] E. V. Tkalya. "Proposal for a Nuclear Gamma-Ray Laser of Optical Range." *Phys. Rev. Lett.*, **106**:162501, April 2011.

[TSJ15] EV Tkalya, Christian Schneider, Justin Jeet, and Eric R Hudson. "Radiative lifetime and energy of the low-energy isomeric level in Th 229." *Physical Review C*, **92**(5):054324, 2015.

[TVL96] E. V. Tkalya, V. O. Varlamov, V. V. Lomonosov, and S. A. Nikulin. "Processes of the nuclear isomer ^{229m}Th($3/2^+$, 3.5 ± 1.0 eV) resonant excitation by optical photons." *Phys. Scr.*, **53**(3):296–299, 1996.

[UBB99] S. Utter, P. Beiersdorfer, A. Barnes, R. Lougheed, J. Crespo López-Urrutia, J. Becker, and M. Weiss. "Reexamination of the Optical Gamma Ray Decay in ^{229}Th." *Phys. Rev. Lett.*, **82**(3):505–508, January 1999.

[VKB15] Varun B Verma, Boris Korzh, Felix Bussieres, Robert D Horansky, Shellee D Dyer, Adriana E Lita, Igor Vayshenker, Francesco Marsili, Matthew D Shaw, Hugo Zbinden, et al. "High-efficiency superconducting nanowire single-photon detectors fabricated from MoSi thin-films." *Optics express*, **23**(26):33792–33801, 2015.

[VMH12] Varun B Verma, Francesco Marsili, S Harrington, Adriana E Lita, Richard P Mirin, and Sae Woo Nam. "A three-dimensional, polarization-insensitive superconducting nanowire avalanche photodetector." *Applied Physics Letters*, **101**(25):251114, 2012.

[VMK88] D. A. Varshalovich, A. N. Moskalev, and V. K. Khersonslii. *Quantum Theory of Angular Momentum.* World Scientific Publ., London, 1988.

[VNM14] Zsolt Varga, Adrian Nicholl, and Klaus Mayer. "Determination of the ^{229}Th half-life." *Phys. Rev. C*, **89**:064310, June 2014.

[Voi] M. E. Voikhansky, M. A. Listengarten, and I. M. Band, Penetration effects in internal conversion. In: (Internal Conversion Processes), Ed. by J.H. Hamilton, Academic Press, NY, 1966, p.581.

[Wil11] Philip Willmott. *An introduction to synchrotron radiation: techniques and applications.* John Wiley & Sons, 2011.

[WRS84] L. A. Westling, M. G. Raymer, and J. J. Snyder. "Single-shot spectral measurements and mode correlations in a multimode pulsed dye laser." *J. Opt. Soc. Am. B*, **1**(2):150–154, Apr 1984.

[WSL16] Lars von der Wense, Benedict Seiferle, Mustapha Laatiaoui, Jürgen B Neumayr, Hans-Jörg Maier, Hans-Friedrich Wirth, Christoph Mokry, Jörg Runke, Klaus Eberhardt, Christoph E Düllmann, et al. "Direct detection of the 229 Th nuclear clock transition." *Nature*, **533**(7601):47, 2016.

[WWT12] Nan Wang, Rui Wang, Hao Teng, Dehua Li, and Zhiyi Wei. "Tunable deep UV narrow linewidth laser by frequency converted Ti: sapphire Laser at 5kHz repetition rate." In *Advanced Solid-State Photonics*, pp. AM4A–27. Optical Society of America, 2012.

[YKD07] Joel KW Yang, Andrew J Kerman, Eric A Dauler, Vikas Anant, Kristine M Rosfjord, and Karl K Berggren. "Modeling the electrical and thermal response of superconducting nanowire single-photon detectors." *IEEE transactions on applied superconductivity*, **17**(2):581–585, 2007.

[YKK15] A. Yamaguchi, M. Kolbe, H. Kaser, T. Reichel, A. Gottwald, and E. Peik. *New J. Phys.*, **17**:053053, 2015.

[ZER12] Xinxin Zhao, Yenny Natali Martinez de Escobar, Robert Rundberg, Evelyn M. Bond, Allen Moody, and David J. Vieira. "Observation of the Deexcitation of the ^{229m}Th Nuclear Isomer." *Phys. Rev. Lett.*, **109**:160801, October 2012.

[Zim10] Kai Zimmermann. *Experiments Towards Optical Nuclear Spectroscopy With Thorium-229*. Dr. rer. nat., Gottfried Wilhelm Leibniz Universität Hannover, 2010.